A Theory for Magnetic Fluctuations in Strongly Correlated Electron-Systems

Vom Fachbereich Physik
der Technischen Universität Darmstadt

zur Erlangung des Grades
eines Doktors der Naturwissenschaften
(Dr. rer. nat.)

genehmigte

Dissertation

von

Dipl.-Phys. Torben Jabben
aus Frankfurt am Main

Referent:	Prof. Dr. N. Grewe
Korreferent:	Prof. Dr. J. Berges
Tag der Einreichung:	2.03.2010
Tag der mündlichen Prüfung:	03.05.2010

Darmstadt 2010
D17

Abstract

Strongly correlated electron systems show a rich variety of astonishing physical phenomena. However, the strong interactions make the theoretical description of these systems a highly non-trivial task. Even the simplest models cannot be solved exactly, and one has to reside to approximative solutions, which often cover only certain aspects of the physics contained in these models. In recent years progress has been made in the theoretical description of correlated lattice systems through the mapping of lattice models onto effective impurity models. The most prominent example is the mapping of the Hubbard model onto an effective single impurity Anderson model (SIAM). Within this description both models feature the prominent Kondo effect, which leads to the emergence of low energy quasiparticles. The occurrence of such excitations is a result of the dynamical screening of local magnetic moments and the corresponding formation of a low temperature Fermi liquid phase. On the other hand these theories usually fail in the description of non Fermi liquid behavior, which is for example observed in the normal state of high temperature superconductors and some Heavy-Fermion systems. Strong nonlocal fluctuations drive the dynamics of these systems. In the theoretical treatment, due to the mapping of the lattice problem to an effective single impurity problem, these fluctuations are not adequately described.

In this thesis a new self-consistent approach for the inclusion of spatial correlations is presented for the Hubbard model. In contrast to existing quantum cluster theories in this field, the approach allows for the simultaneous description of short and long range pair correlations. Due to the intimate connection of this new lattice theory with the two impurity Anderson model (TIAM) a thorough numerical investigation of the TIAM is undertaken in this thesis. The competition of the Kondo effect with the RKKY interactions is studied in great detail. Furthermore two new solvers for the TIAM are introduced, which extend existing non crossing approximations for the SIAM.

Zusammenfassung

Stark korrelierte Elektronensysteme zeigen eine Vielzahl interessanter physikalischer Phänomene. Aufgrund der vorhandenen starken Wechselwirkung ist ihre theoretische Beschreibung jedoch ein höchst nichttriviales Problem. Selbst die einfachsten Modelle lassen sich nicht exakt lösen und man ist daher auf Näherungen angewiesen, die jedoch oft nur ein Teil der in diesen Modellen enthaltenen Physik gut beschreiben.

In den letzten Jahren wurden bei der Beschreibung stark korrelierter Gittersysteme enorme Fortschritte erzielt. Möglich wurde dies durch die näherungsweise Abbildung des Gitterproblems auf effektive Störstellenprobleme. Das bekannteste Beispiel hierfür ist die Abbildung des Hubbard Modells auf ein effektives Ein-Störstellen Anderson Modell (SIAM). Innerhalb dieser Beschreibung weisen beide Modelle einen Kondo-Effekt auf, der zu Niederenergie-Quasiteilchen führt. Das Auftreten solcher Anregungen ergibt sich aus der dynamischen Abschirmung lokaler magnetischer Momente und dem damit einhergehenden Auftreten einer Tieftemperatur Fermiflüssigkeitsphase.
Auf der anderen Seite sind diese Theorien gewöhnlich nicht in der Lage Nicht-Fermiflüssigkeitsverhalten zu beschreiben. Solches Verhalten wird zum Beispiel in der normalleitenden Phase von Hochtemperatursupraleitern und einigen Schwere-Fermionen Systemen beobachtet. Starke nichtlokale Korrelationen bestimmen das Verhalten solcher Systeme. In der theoretischen Behandlung werden, durch die Abbildung auf ein effektives Ein-Störstellen System, diese Fluktuationen nicht adäquat beschrieben.

In dieser Arbeit wird eine neue selbstkonsistente Theorie am Beispiel des Hubbard Modells vorgestellt. Im Gegensatz zu den existierenden Quanten Kluster Theorien auf diesem Gebiet, erlaubt dieser neue Ansatz die simultane Beschreibung von kurz- und langreichweitigen Paarkorrelationen. Aufgrund der engen Verwandtschaft dieser Gittertheorie mit dem Zwei-Störstellen Anderson Modell (TIAM), ist in dieser Arbeit ebenfalls eine detaillierte numerische Auswertung des TIAM zu finden. Der Wettbewerb zwischen dem Kondo-Effekt und der RKKY-Wechselwirkung wird ausgiebig untersucht. Weiterhin werden zwei neue Verfahren zur Lösung des TIAM eingeführt, die bestehende “non-crossing” Näherungen für das SIAM auf die Beschreibung von Zwei-Störstellen erweitern.

Contents

1 Introduction

The theoretical description of interacting many-particle systems is one of the great challenges in modern condensed-matter physics. The discovery of heavy fermion compounds and high-temperature superconductors has greatly revived the interest in this field of physics. In recent years it has become of even more relevance through the progress in nano-technology. Quantum-dots systems are direct experimental realizations of N-impurity models. Apart from the interesting physics of these models on their own, they constitute - as effective models - the main building block in the modern theoretical description of highly correlated lattice systems, e.g. high T_c-materials. Quantum-dots systems on the other hand show transport properties, that could be utilized for a range of electronical and optical applications. Arrays of densely packed dots could be used to build computers of unprecedented power. Quantum dots could also constitute materials capable of absorbing and emitting light at whatever wavelengths their designers specify.

Strongly correlated systems usually involve atoms with partially filled $d-$ or $f-$ shells. They can for example be found in transition-metals, rare-earth elements and actinides. When embedded in a crystalline environment the valence electrons of the d- or f-orbitals remain quite localized, which leads to very narrow valence-bands. On the other hand the Coulomb-interaction in these localized shells is strong and plays a vital role for the properties of these materials. In these systems the strength of the interactions between particles is comparable to or larger than their kinetic energy. Therefore any theory based on a perturbation expansion around the non-interacting limit is at least questionable. The theoretical description of such systems is therefore faced with extreme difficulties, due to the non-perturbative nature of the problem.

A major advance in the theoretical description of strongly correlated lattices came with the introduction of extended mean-field schemes. In the limit of infinite dimension or coordination number it is possible to map the dynamics of the lattice model onto an effective impurity model. The complexity of the lattice problem is thereby reduced to the complexity of a single impurity model, which nowadays can be solved to a high degree of accuracy. These extended mean-field schemes, namely the Dynamical Mean Field Theory (DMFT), are e.g. quite successful in the description of Mott-insulators and the correct description of the Fermi-liquid phase for many heavy-fermion materials. One of the striking features of the DMFT is its ability to describe to the formation of quasiparticles below a coherence temperature T^* connected to the occurrence of a Fermi-liquid phase.

Despite its successes the DMFT is critically flawed by the fact that it neglects the influence of spatial correlations. The DMFT self-energy is a $\underline{k}$-independent quantity. The correct description of inter-site correlations is however crucial for many correlated fermion problems. Among these are the formation of Luttinger-liquids in low dimensional systems or more generally the occurrence of non Fermi-liquid behavior in various materials. DMFT fails to describe non-local order parameters such as the order parameter in high-T_c materials, which has a d-wave symmetry, or the occurence of magnetic correlation of limited range as well as exotic magnetic phases. Furthermore DMFT is incapable to describe the behavior of a system towards a classical or quantum critical point where long range spatial fluctuations of the order parameter occur. Another example is the Mott-transition in cuprate materials, where short range magnetic correlations due to an effective exchange-coupling J lead to a strong tendency towards the formation of singlet-bonds. In situations, where the effective J becomes comparable to the coherence temperature T^* one can expect that the DMFT-picture of the Mott-transition is deeply modified.

In recent years cluster extensions of the DMFT tried to incorporate the effects of these spatial correlations. In essence the lattice problem in these schemes is mapped to a generalized impurity problem. The impurity in these schemes consists of a cluster of sites embedded in an effective non-interacting host-lattice. These approaches capture very well the influence of short range spatial correlations but offer no way to describe spatial correlations beyond the spatial extent of the cluster.

In this thesis a different approach is proposed. The basic idea is to map the lattice problem onto an effective N-impurity problem. As simplest example the two-impurity model is chosen in this work. The impurities can be placed at arbitrary distances in the lattice. The solution of the two-impurity problem then contains spatial correlations for this distance. This work tries to show a way to map these correlations to the lattice problem and a large part of this thesis is devoted to the solution and a precise understanding of the physical properties of such systems. The focus in this thesis is on the Two-Impurity Anderson-Model (TIAM), which is, apart from its application as an effective two-impurity-model in a lattice theory, very interesting on its own behalf. It is the first of the (multi-)impurity models which contain the competition between the Kondo-effect and the RKKY-interaction. In the Kondo-effect local magnetic correlations are manifested, while via the RKKY-interaction the non-local aspects of these magnetic correlations come into play. The RKKY-interaction favors a magnetic order between impurity-spins, while the Kondo-effect screens the impurity-spins. In the TIAM both effects originate from the same hybridization to the band and the competition of these effects makes the TIAM much more complex than the SIAM. Additional direct coupling matrix-elements between the two-impurities, such as a direct hopping or a direct exchange J, make the situation even more complicated. A good understanding of the physics of the TIAM is therefore necessary in order to understand the influence of spatial correlations in more complicated systems, e.g. correlated lattices.

This thesis is organized as follows:

- In Chapter 2 two new solvers for the TIAM the ENCATI and the SNCATI are presented. First the TIAM is introduced, then it is shown how the setup of direct-perturbation theory for the SIAM can be generalized to the TIAM. Especially it will be shown how the self-consistent diagrammatic approach in the SNCA/ENCA can be extended to the TIAM, and which new diagram rules come into play. Furthermore it is shown how direct-matrix elements between the impurities can be included in this type of theories. The chapter concludes with some comments on the numerical implementation of the new solvers.

- In Chapter 3 numerical solutions of the TIAM will be presented. The aim of this chapter is two-folded. On the one hand the quality of the two new TIAM approximations needs to be approved, and one the other hand these solvers are used to investigate the physics of the TIAM. In the first two sections of this chapter the focus is more on the quality of the new approximations. There the solution of the TIAM-solvers is compared to the exactly solvable resonant-level limit and the SIAM limit of the TIAM, where the numerical results are compared to results from established SIAM-solvers.

  The following investigation of the physics of the TIAM is then undertaken in two-steps:

  1. The TIAM properties are investigated in the absence of the RKKY-interaction mediated by the band-electrons. The two-impurities are coupled only by direct inter-impurity matrix elements.
  2. The TIAM is not coupled by direct inter-impurity matrix elements, but the two impurities are dynamically coupled by RKKY-processes for various distances.

- In Chapter 4 a new theory for the lattice problem, the DMFT2S, is derived. The Chapter gives also a short review on some existing lattice theories from the viewpoint and in the language of the DMFT2S approximation.

- In Chapter 5 some results of the DMFT2S approximation for the Hubbard-model in two-dimensions are presented.

- This thesis concludes with a summary and an outlook in Chapter 6.

Appendix C contains magnifications of all Figures from numerical calculations presented in this thesis within the text. In order to set Figures near the place they are described in the text, it was often necessary to reduce the size of the Figures to an extent which makes details barely visible. Nevertheless, the smaller Figures in text suffice for a quick overview and increase the readability. For a more detailed inspection the reader is advised to consult the corresponding figure in appendix C.

2 Two impurity Anderson model(s) (TIAM)

In order to investigate the spatial correlations between two s-shell impurities with arbitrary distance embedded in an uncorrelated medium a minimal model needs to be defined and solved. The model must simultaneously contain - in the right parameter regime - the Kondo effect for each impurity and also the description of the coupling of the two impurities via the medium and in cases of small distances also the inclusion of direct hybridization and/or interaction matrix elements. The solver for this model therefore needs to be sufficiently elaborate to include not only the Kondo-scale but also in the right proportions the inter-impurity interactions to allow for a proper description of the competition of these effects.

The key model which contains all the physics described is the extended two impurity Anderson model (TIAM):

$$H = H_0 + V \tag{2.1}$$

$$H_0 = \sum_{\underline{k},\sigma,i} \epsilon_{\underline{k}\sigma} c^\dagger_{\underline{k}\sigma} c_{\underline{k}\sigma} + \sum_{i\sigma} \epsilon^f_{i\sigma} f^\dagger_{i\sigma} f_{i\sigma} + \sum_i U_i f^\dagger_{i\uparrow} f_{i\uparrow} f^\dagger_{i,\downarrow} f_{i\downarrow} + \hat{F}^D \tag{2.2}$$

$$V = \sum_{i,\underline{k},\sigma} \Big(V_{\underline{k},i,\sigma}\, c^\dagger_{\underline{k},\sigma} f_{i\sigma} + h.c. \Big) + \hat{F}^{ND} \tag{2.3}$$

where $f^\dagger_{i\sigma}/f_{i\sigma}$ creates/annihilates an electron with spin σ at impurity site $i = \{1, 2\}$. Correspondingly the $c^\dagger_{\underline{k}\sigma}/c_{\underline{k}\sigma}$ operators create/annihilate electrons with host lattice crystal impulse $\underline{k}$. $V_{\underline{k},i,\sigma}$ is the hybridization matrix element and U_i describes the local Coulomb matrix element at site i.
In the further context equal spin degenerated impurity sites are assumed and the index i is dropped in some quantities, i.e. $U \equiv U_i$ and $\epsilon^f \equiv \epsilon^f_{i\sigma}$. With the operators $\hat{F}^D = \hat{F}^{ND} = 0$ the Hamiltonian in equation (2.1) describes the model commonly referred to as TIAM [Ale64].

The split-up of equation (2.1) in a part H^0, which is diagonal in the ionic f-states and the host c-states, and the part V mixing these states, already indicates the perturbation expansion of the model, which will be presented in the following sections.

2.1 Direct perturbation theory

In this work the two-impurity problem will be treated within the framework of direct perturbation theory. In this framework an approximative solution of the TIAM will be constructed by infinite order summations of diagrams from integral-equation solutions.
These methods date back to the early works of Keiter and Kimball [Kei70, Kei71a, Kei71b]

for the Anderson- and the related s-d-model and later to works by [Gre83, Kur83, Kur85b, MH84] where the terminus Non-Crossing Approximation or short NCA was coined for this kind of approximation.

This work follows closely the route of [Pru89], where the “classical” NCA for the Anderson model was extended to include finite U contributions (SNCA) and additionally some vertex corrections (ENCA) were included. Here the SNCA/ENCA will be generalized to the TIAM.
In the following the direct-perturbation theory will be presented very briefly with the focus on the specialties arising from the inclusion of a second impurity site in the SNCA/ENCA. For a more general introduction on this topic the reader is advised to consult one of the following references [Kei84, Bic87]. A more recent and detailed overview of the SNCA/ENCA and further extensions of this approximations in comparison with other methods for the Anderson-model can be found in [Gre08] and the references therein.

In direct- or resolvent perturbation theory the partition function and Greenfunctions are expressed as contour integrations in the complex plane with traces over resolvent operators and operators in the integrand,

$$\mathcal{Z} = Tr\left(exp(-\beta H)\right) = \oint_{\mathcal{C}} \frac{dz}{2\pi i} e^{-\beta\, z} Tr\left([z-H]^{-1}\right) \tag{2.4}$$

$$G_{A,B}(i\omega_n) = \frac{1}{\mathcal{Z}} \oint_{\mathcal{C}} \frac{dz}{2\pi i} e^{-\beta\, z} Tr\left([z-H]^{-1} A\, [z+i\omega_n - H]^{-1} B\right). \tag{2.5}$$

The contour $\mathcal{C}$ encircles in a mathematically positive sense all singularities of the integrands, which in case of equation (2.4) are situated at $Im(z) = 0$ and respectively for equation (2.5) at $Im(z) = 0$ and $Im(z + i\omega_n) = 0$. Depending on the type of operators $\hat{A}$ and $\hat{B}$, $i\omega_n$ is either the fermionic or bosonic Matsubara frequency.

Splitting the Hamilton operator $H = H_0 + V$, as for the TIAM already undertaken in equation (2.1), allows for the expansion of the resolvent operator $[z-H]^{-1}$ in powers of V

$$[z - H_0 - V]^{-1} = [z-H_0]^{-1} + [z-H_0]^{-1} \sum_{n=1}^{\infty} \left(V\,[z-H_0]^{-1}\right)^n . \tag{2.6}$$

For the TIAM H_0 can now be further divided in two distinct parts $H_0 = H_c + H_f$ with H_c the diagonal Hamiltonian describing the unperturbed band electrons and the H_f describing the unperturbed two-impurity sites. Introducing the Eigenstates $|M,c\rangle = |M\rangle|c\rangle$ of H_0 with

$$H_c|c> = E_c|c> \qquad \text{and} \tag{2.7}$$

$$H_f|M,c> = E^f_M|M,c>, \tag{2.8}$$

it is possible in the partition function $\mathcal{Z}$ to trace out the band electron part and investigate only the reduced f partition function $\mathcal{Z}_f$

$$\mathcal{Z}_f = \frac{\mathcal{Z}}{\mathcal{Z}_c} \tag{2.9}$$

$$\mathcal{Z}_c = Tr\left(e^{-\beta H_c}\right) \tag{2.10}$$

$$\mathcal{Z}_f = \oint \frac{dz}{2\pi i} e^{-\beta z} Tr_f \left(\frac{1}{\mathcal{Z}_f} \left[z - H\right]^{-1} \right) = \sum_M \oint \frac{dz}{2\pi i} e^{-\beta z} Tr_f \left(P_{M,M}(z)\right) \tag{2.11}$$

with

$$P_{M,M'}(z) \equiv \frac{1}{\mathcal{Z}_c} \sum_c e^{-\beta E_c} < c, M| \left[z + E_c - H\right]^{-1} |M', c> . \tag{2.12}$$

The calculation of the the partition function is thereby reduced to the calculation of the ionic propagators $P_{M,M'}(z)$, which describe the time evolution of the ionic two-impurity state M to the ionic two-impurity state M'.

As H_0 conserves the ionic quantum number M and the Tr_f-operator is diagonal, it might at this point look dispensable, and in comparison with the standard literature on this issue, nonstandard to introduce non-diagonal ionic propagators. But with the series expansion defined in equation (2.6) in mind it soon becomes clear, that such non-diagonal propagations happen as intermediate processes in multi impurity site systems. In the scheme presented here they are absolutely vital in order to describe inter-impurity correlations.

After resolving the impurity f-operators A and B in terms of Hubbard transfer operators

$$A = \sum_{M,M'} \alpha^A_{M,M'} |M >< M'| \equiv \sum_{M,M'} \alpha^A_{M,M'} \chi_{M,M'} \tag{2.13}$$

$$B = \sum_{M,M'} \alpha^B_{M,M'} |M >< M'| \equiv \sum_{M,M'} \alpha^B_{M,M'} \chi_{M,M'} \tag{2.14}$$

the A, B Greenfunction in equation (2.5) can easily be expressed in terms of ionic propagators

$$\begin{aligned} G_{A,B}(i\omega_n) = \frac{1}{\mathcal{Z}_f} \sum_{\substack{M',M'',\\ M''',M}} \alpha^B_{M''',M} \times \\ \oint_{\mathcal{C}} \frac{dz}{2\pi i} e^{-\beta z} P_{M,M'}(z) \Lambda^A_{M',M''}(z + i\omega_n, z) P_{M'',M'''}(z + i\omega_n) \, . \end{aligned} \tag{2.15}$$

$\Lambda^A_{M',M''}(z, z')$ represents a vertex function with incoming frequency z and outgoing frequency z', the superscript A indicates that the proportionality factors $\alpha^A_{M,M'}$ defined in equation (2.13) are absorbed in the vertex function.
The vertex function itself will be defined later on in the proceeding. At this point it suffices to mention that the inclusion or exclusion of specific processes in $\Lambda^A_{M',M''}$ defines the different approximation levels in the context of the direct perturbation theory presented here.

2.2 One-particle Greenfunction

In the further context the general formula (2.5) is specialized for the spin-diagonal one-particle Greenfunctions

$$\underline{\underline{G}}_{\sigma} = \begin{pmatrix} G_{f_{1\sigma},f^\dagger_{1\sigma}} & G_{f_{1\sigma},f^\dagger_{2\sigma}} \\ G_{f_{2\sigma},f^\dagger_{1\sigma}} & G_{f_{2\sigma},f^\dagger_{2\sigma}} \end{pmatrix} \equiv \begin{pmatrix} G_{1\sigma,1\sigma} & G_{1\sigma,2\sigma} \\ G_{2\sigma,1\sigma} & G_{2\sigma,2\sigma} \end{pmatrix},$$

where the matrix structure combines all possible ionic one-particle Greenfunctions.

More generally for an ionic state vector $|M>$ the notation $|M> \equiv |n_1\sigma^1_z; n_2\sigma^2_z\rangle$ is introduced, where n_i denotes the occupation at site i and $\frac{\hbar}{2}\sigma^i_z$ the projection of the spin vector parallel to the z-axis at site i. Therefore the ionic two impurity Hilbert space is spanned by 16 base vectors

$$\begin{aligned} \mathcal{B} = \{ &|0;0>, |\sigma;0>, |2;0>, |0;\sigma>, |0;2>, \\ &|\sigma;\sigma'>, |\sigma;2>, |2;\sigma>, |2;2> \}, \end{aligned} \tag{2.16}$$

with $\sigma, \sigma' = \pm 1$. This notation is used whenever it is necessary to specify a distinct ionic state. With the convention

$$|2;2> = f^\dagger_{1\uparrow} f^\dagger_{1\downarrow} f^\dagger_{2\uparrow} f^\dagger_{2\downarrow} |0;0> \tag{2.17}$$

the decomposition of the f operators in Hubbard transfer operators according to equation (2.13) and equation (2.14) is as follows:

$$\begin{aligned} f^\dagger_{1\sigma} =& |\sigma;0 >< 0;0| + |\sigma;2 >< 2;0| + \sum_{\sigma'} |\sigma;\sigma' >< \sigma';0| \\ &+ \sigma \left(|2;0 >< 0;-\sigma| + |2;2 >< 2;-\sigma| + \sum_{\sigma'} |2;\sigma' >< \sigma';-\sigma| \right) \end{aligned} \tag{2.18}$$

$$\begin{aligned} f^\dagger_{2\sigma} =& |0;\sigma >< 0;0| + |2;\sigma >< 0;2| - \sum_{\sigma'} |\sigma';\sigma >< 0;\sigma'| \\ &+ \sigma \left(|0;2 >< -\sigma;0| + |2;2 >< -\sigma;2| \right). \end{aligned} \tag{2.19}$$

Substituting the series expansion in equation (2.6) into equation (2.12), the ionic propagators $\underline{\underline{P}}(z) \equiv (P_{M,M'})(z)$ in a skeleton expansion can be expressed in terms of unperturbed ionic propagators $\underline{\underline{P}}^0$, the non-diagonal ionic matrix elements of the Hamiltonian $\underline{\underline{W}}$, $\underline{t}$ and the irreducible self-energy $\underline{\underline{\Sigma}}_{W,t}$(z) in form of a Matrix Dyson equation:

$$\underline{\underline{P}}(z) = \underline{\underline{P}}^0(z) + \underline{\underline{P}}^0(z) \left(\underline{\underline{\Sigma}}_{W,t}(z) + \underline{\underline{W}} + \underline{t} \right) \underline{\underline{P}}(z). \tag{2.20}$$

The subscript at $\underline{\underline{\Sigma}}_{W,t}$ indicates that in the extended TIAM models the self-energy also depends on the ionic matrix elements $\underline{\underline{W}}$ and $\underline{t}$.
Noticing that

$$\underline{\underline{P_0}}(z) = \left(\frac{1}{z - E_M} \delta_{M,M'} \right) \tag{2.21}$$

is diagonal, equation (2.20) can be formally solved and brought into a form which closely resembles the shape of the scalar solution of this equation known from the SIAM [Gre08]

$$\underline{\underline{P}}(z) = \left[\left(\underline{\underline{P}}^0(z)\right)^{-1} - \underline{\underline{\Sigma}}_{W,t}(z) - \underline{\underline{W}} - \underline{\underline{t}}\right]^{-1}. \tag{2.22}$$

The direct matrix elements $\underline{\underline{W}}$ and $\underline{\underline{t}}$ persist even if the two impurities are not coupled to the host and the self-energy, which is at least proportional to one the hybridization matrix element $V_{\underline{k,i}}$, vanishes in this limit. So by

$$\underline{\underline{\Sigma}}_{W,t}(z) \longrightarrow 0.$$

the exact solution of the ionic propagators for two isolated impurities

$$\underline{\underline{P}}(z) = \left[z - \underline{\underline{E}} - \underline{\underline{W}} - \underline{\underline{t}}\right]^{-1} \qquad \text{with} \qquad \left(\underline{\underline{E}}\right)_{M,M'} = E_M \delta_{M,M'} \tag{2.23}$$

is reproduced. This handy feature of the Dyson-equation (2.22) guarantees that, no matter how the self-energy $\underline{\underline{\Sigma}}_{W,t}$ is calculated, the exact ionic limit given by equation (2.23) is contained in any TIAM approximation.

Starting with equation (2.22) the only task left is the specification and the calculation of the processes contained in the self energy. The introduction of Hubbard operators in equation (2.13) and equation (2.14) leads to a diagrammatic visualization of the perturbation theory in terms of families of time ordered Goldstone diagrams, describing the dynamics of the ionic f-states.
An other widely used approach avoids this by enlarging the degrees of freedom of the system via the introduction of auxiliary bosons (slave-bosons) representing the empty state [Col84, Kro05, Kro97]. With this “trick” Wick’s theorem becomes applicable which leads to a standard Feynman perturbation theory. But by the introduction of auxiliary particles this method must fulfill the constraint to stay in the physical Hilbertspace. In the context of this work this approach will not be used, diagrams have to be read in the sense described before.

The different analytic contributions to the self energy can to the best advantage be visualized in a diagrammatic language. The diagram rules used in standard direct perturbation theory for the SIAM are, apart from some modifications which will be discussed here, also applicable to the TIAM. The reader may consult [Kei84] for an introduction on this topic. For the TIAM the diagrammatic symbols needs to be adapted in order to deal with the following requirements:

- The enlarged ionic Hilbertspace of two impurities and the occurrence of non-diagonal processes between the two impurities need to be clearly represented in order to cope with the wealth of possibilities.
- Band electrons can propagate from one to the other ionic site. There are also two different diagonal propagation forms in the band, i.e. from site 1 to site 1 and from site 2 to site 2.
- As a consequence of the large number of different ionic states to be taken into account, there is also a large number of different vertex functions which must be clearly distinguishable.

Therefore some new graphical elements need to be introduced.

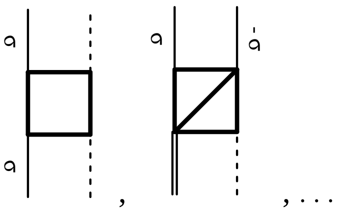

Figure 2.1: ionic propagators: $P_{1\sigma\,0;\,si\,0}$, $P_{2\,0;\sigma\,-\sigma}$

The graphical representation of the two-impurity ionic propagator has two legs at the bottom. The line on the left depicts the incoming ionic state of site 1, a dashed line for the empty state, a full line with spin index the singly occupied state, and the double line represents the doubly occupied state. Analogously the two lines at the top indicate the outgoing two-impurity state. The rectangle in the middle indicates that the propagator contains self energy processes in the sense of equation (2.22). As a further aid to the eye a diagonal line connecting site 1 with site 2 in the self energy rectangle is drawn if the propagator is non-diagonal.

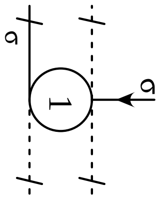

Figure 2.2: bare vertex $\tilde{\Lambda}^{1}_{0\,0;\sigma\,0}$

This symbol depicts a naked vertex function where in analogy the the ionic propagator the lines at top and bottom represent the incoming and outgoing ionic two-impurity state. The leg on the right side connects the vertex with an electron or hole band propagator. In case of Figure 2.2 this denotes a band electron with spin σ which is annihilated at site 1 and recreated as an f-electron with the same spin also at site 1. The number in circle always refers to the impurity-site where the band electron or hole is annihilated. The thin lines diagonal to the propagator lines indicate an amputation, i.e the propagator lines are a part of the ionic propagator attached to the vertex.

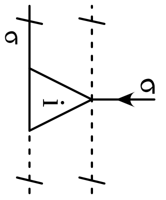

Figure 2.3: full vertex $\Lambda^{i}_{0\,0;\sigma\,0}$

Figure 2.3 depicts an irreducible vertex function including vertex corrections. The other elements are the same as in Figure 2.2 with the following difference: here the site where the band electron is annihilated in the vertex is unspecified, which is indicated by the variable i.

Using the above defined graphical elements, the equations for the irreducible ionic propagator self energies can now be stated in a diagrammatic form.

In equation (2.24) this is done for the empty state self-energy $\Sigma_{0\,0;0\,0}$ and in equations

(2.28), (2.29) for $\Sigma_{\sigma\ 0;0\ \sigma}$ and $\Sigma_{\sigma\ -\sigma;\sigma\ -\sigma}$.

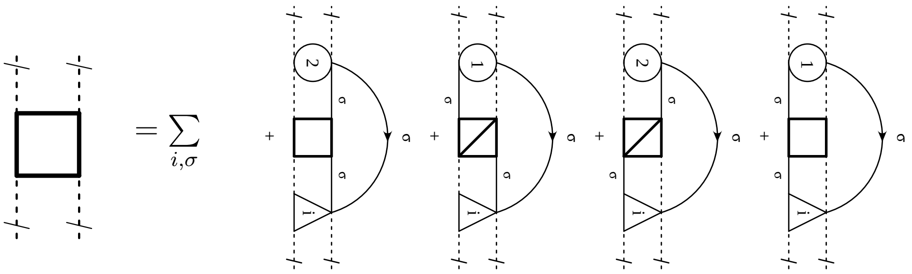

(2.24)

Equation (2.24) translates into the following analytical expression:

$$\begin{aligned}\Sigma_{0\ 0;0\ 0}(z) = \sum_{i,\sigma}\Bigg(&\int_{-\infty}^{\infty}\frac{d\epsilon}{\pi}\Delta_{i,2}(\epsilon)f(\epsilon)\Lambda^{i}_{0\ 0;0\ \sigma}(z,z+\epsilon)P_{0\ \sigma;0\ \sigma}(z+\epsilon)+\\ &\int_{-\infty}^{\infty}\frac{d\epsilon}{\pi}\Delta_{i,1}(\epsilon)f(\epsilon)\Lambda^{i}_{0\ 0;0\ \sigma}(z,z+\epsilon)P_{0\ \sigma;\sigma\ 0}(z+\epsilon)+\\ &\int_{-\infty}^{\infty}\frac{d\epsilon}{\pi}\Delta_{i,2}(\epsilon)f(\epsilon)\Lambda^{i}_{0\ 0;0\ \sigma}(z,z+\epsilon)P_{\sigma\ 0;0\ \sigma}(z+\epsilon)+\\ &\int_{-\infty}^{\infty}\frac{d\epsilon}{\pi}\Delta_{i,1}(\epsilon)f(\epsilon)\Lambda^{i}_{0\ 0;0\ \sigma}(z,z+\epsilon)P_{\sigma\ 0;\sigma\ 0}(z+\epsilon)\Bigg)\end{aligned} \tag{2.25}$$

with $f(x)$ the Fermi function, $\Lambda^{i}_{M;M'}(z,z')$ the full vertex function from state M to M', where the electron/hole band propagator internally ends at site i, and $\Delta_{i,j}(x)$ are the hybridization functions for band propagations connecting site i with site j. The diagonal hybridization function $\Delta_{i,i}(x)$ directly corresponds to the Anderson hybridization function known from the SIAM, i.e.

$$\Delta_{i,i}(w) = -\frac{1}{N}Im\left(\sum_{\underline{k}}\frac{|V_{\underline{k},i}|^2}{\omega+i\delta-\epsilon_k}\right). \tag{2.26}$$

The non-diagonal hybridization function is given by

$$\Delta_{i,j}(w) = -\frac{1}{N}Im\left(\sum_{\underline{k}}\frac{V_{\underline{k},i}V^{*}_{\underline{k},j}}{\omega+i\delta-\epsilon_k}\right). \tag{2.27}$$

and only occurs if both impurities couple to the same band. The explicit calculation of this function for a given lattice structure will be undertaken in section 3.4.

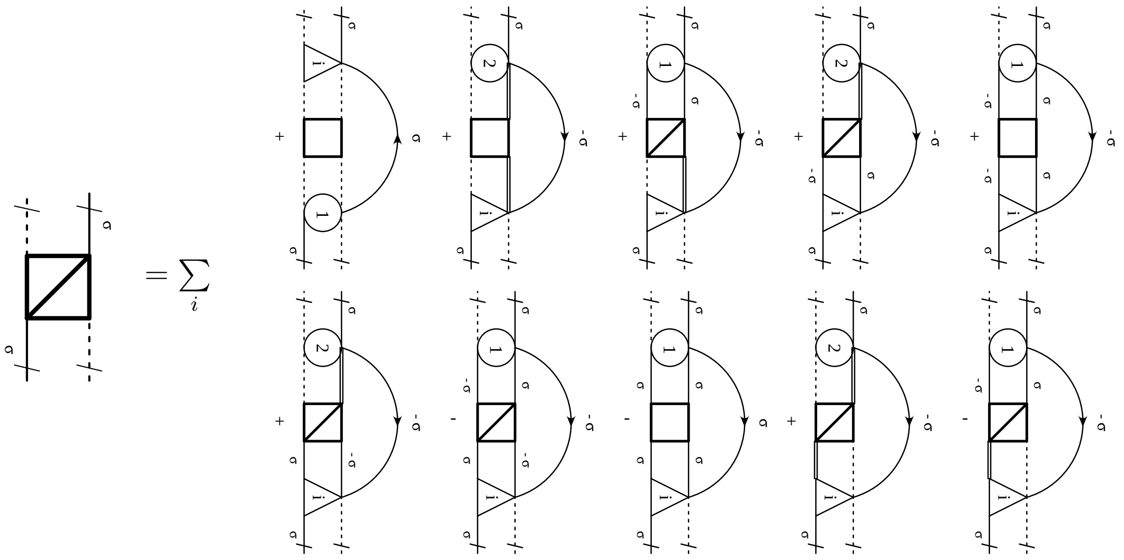

(2.28)

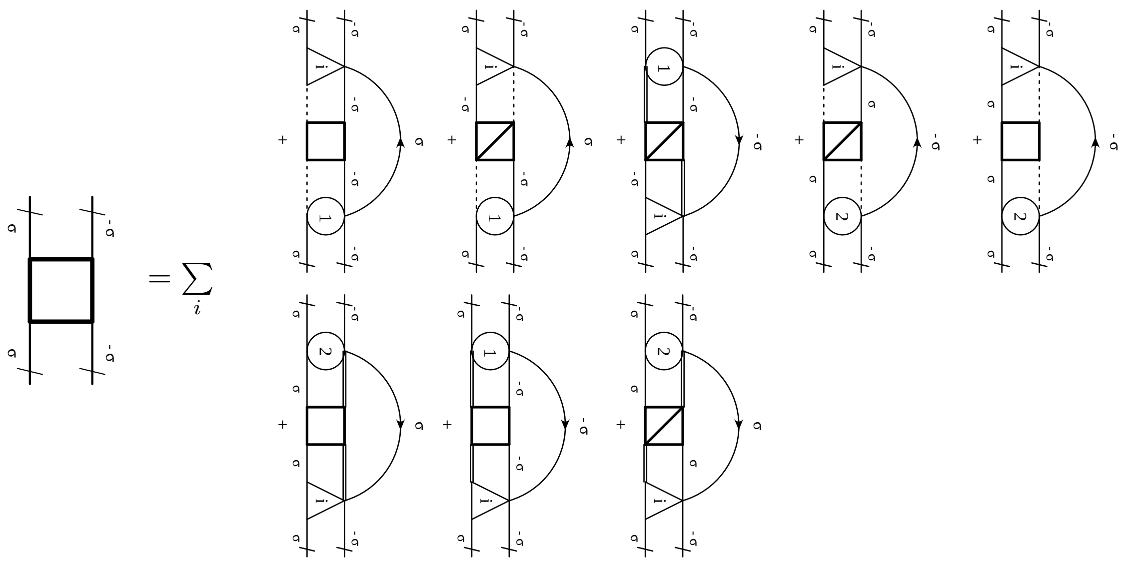

(2.29)

The full set of equations for all self energies can be found in appendix A.

Another important detail, that is of great practical relevance in order to setup the correct equations for the self energies, is that some contributions to the self energy may have an overall symmetry factor -1 relative to other contributions. Inspect here for example the seventh and eighth diagram in equation (2.28). The prefactors, always follow from the specific order of $c, f, c^\dagger, f^\dagger$ operators and the sign convention used in the decomposition of the ionic $f, f^\dagger$ operators given in equation (2.18).

In NCA-like theories for the SIAM which contain only diagonal propagators and self energies these prefactors always cancel to one, as long as there are no diagrams with crossing fermion lines explicitly included. For the TIAM this rule becomes obsolete when non-diagonal processes are involved.

Take for illustration the seventh diagram in equation (2.28). Here the initial ionic state is $|\sigma;0\rangle$, then a band electron with spin $-\sigma$ enters at site i and leaves the vertex at site 2 leading to the ionic state $-|\sigma;-\sigma\rangle$.

The minus sign stems from the convention that diagrams with vertex functions must be read as if the outgoing state is the consequence of the direct application of a creation or annihilation operator. Note, that it is irrelevant for this convention whether the vertex function $\Lambda^1_{M;M'}$ or $\Lambda^2_{M;M'}$ is meant; sign changes which occur from the two different internal attachments of the band electron line are absorbed in the vertex function.

In the example the vertex function $\Lambda^i_{\sigma\ 0;\sigma\ -\sigma}$ has to be read as if $|\sigma;0\rangle$ is changed to $|\sigma;-\sigma\rangle$ by the operation

$$f^\dagger_{2,-\sigma}|\sigma;0\rangle = -|\sigma;-\sigma\rangle, \tag{2.30}$$

where the minus sign directly follows from the convention defined in equation (2.18).

Following the example, the ionic state is then changed from $-|\sigma;-\sigma\rangle$ to $-|-\sigma;\sigma\rangle$ by the ionic propagator $P_{\sigma\ -\sigma;-\sigma\ \sigma}$, this operation involves no explicit change in the overall sign factor, as those are absorbed in the propagator. Finally the ionic state is changed from $-|-\sigma;\sigma\rangle$ to $-|0;\sigma\rangle$ by an outgoing band electron line attached to a naked vertex function, which in that specific case does not lead to an additional sign factor

$$f_{1,-\sigma}\left(-|-\sigma;\sigma\rangle\right) = -|0;\sigma\rangle \tag{2.31}$$

and explains the overall (-1) factor of the whole diagram.

It is a rather unfortunate situation, that probably no fast way exists to decide whether a diagram enters with positive or negative sign factor. At least, as long as only diagonal ionic propagators and band electron lines are involved, the statement of the NCA-like SIAM approximations stays valid, that only crossing electron lines have to be accounted for by a factor -1. For this reason, the whole set of diagrams used in this work is explicitly stated in detail appendix parts A and B. In order to reduce the possibility of any errors the diagrams printed there where deduced algorithmically and carefully checked for mistakes in the sign factor.

2.3 The vertex functions $\Lambda^i_{M,M'}$

Up to this point the theory presented is exact in the sense that all processes generated by the power series expansion in equation (2.6), which are not explicitly stated in the self energy equations, can formally be absorbed in the vertex functions $\Lambda^i_{M,M'}(z,z')$. Therefore the type of approximation is solely determined by the specification of the processes included in the vertices. The most simple self-consistent approximation in the frame of a skeleton expansion is to substitute bare vertices for the full ones.

In the context of the SIAM this approximation is termed SNCA and, specialized to infinite local Coulomb repulsion ($U \longrightarrow \infty$), NCA. In analogy this type of approximation generalized to the **T**wo **I**mpurity problem is referenced to as SNCATI and NCATI in the further context.

For SNCATI a lot of contributions to the self energies drop out of the equations due to the fact that not every full vertex function has the bare vertex as lowest order term. More specifically every full vertex where the transition of the incoming to the outgoing ionic state at a site cannot directly be caused by the incoming electron/hole vanishes in SNCATI. In close analogy to the NCA the NCATI can be obtained by further neglecting all ionic propagators which contain a double occupancy at one or both sites and the self energy contributions containing these propagators.

A nontrivial approximation for the vertices can be achieved if the FNCA [Pru89] are generalized to the two impurity problem (FNCATI). This effort is not undertaken in this work. In this work only the ENCA equations, which can be obtained by keeping only vertex corrections of second order, i.e. the ones with only one band electron line over the bare vertex, is generalized to the TIAM (ENCATI). As example the resulting contributions to $\Delta^{i}_{0\,0;\sigma\,0}$ are shown in the following equations:

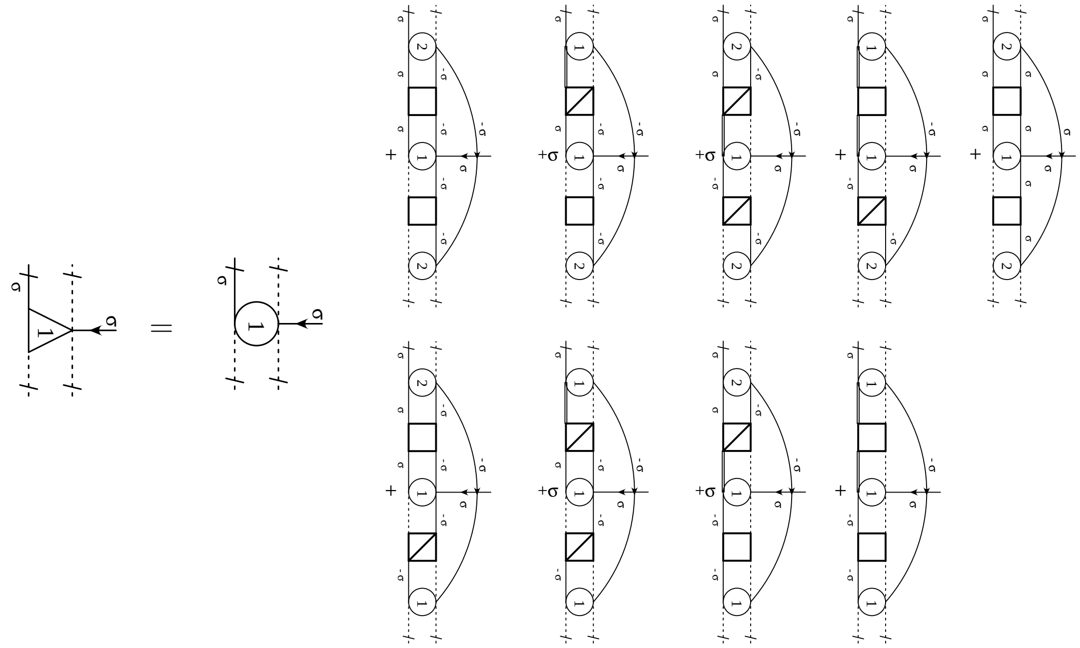

(2.32)

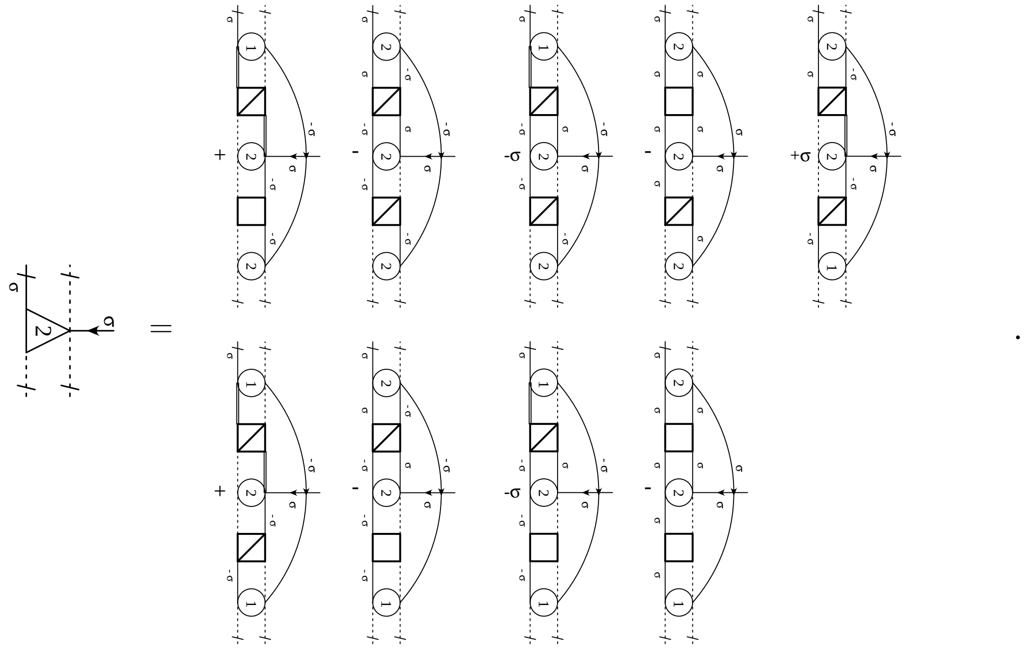

(2.33)

The full set of vertex equations can be found in Appendix B.

Notice, that the vertex terms also contribute with different sign factors for the same reasons as given in the discussion of the self energy equations; these have to be deduced on the same footage.

Apart from the sign factors which are caused by the presence of non-diagonal processes, an additional -1-factor contributes in each of the vertex correction diagrams because the incoming or outgoing electron line crosses an other band-electron line. This diagram rule from the SIAM NCA-theories exists also in the two-impurity extension.

As an example the analytical contributions of the two first, i.e. the top left, diagrams in equation (2.33) are explicitly given by

$$
\begin{aligned}
\Delta^2_{0\ 0;\sigma\ 0}(z, z+i\omega) =& \sigma \int\limits_{-\infty}^{\infty} \frac{d\epsilon}{\pi} \Delta_{2,2}(\epsilon) f(\epsilon) P_{0\ -\sigma;0\ -\sigma}(z+\epsilon) P_{0\ 2;\sigma\ -\sigma}(z+i\omega+\epsilon) \\
&+ \int\limits_{-\infty}^{\infty} \frac{d\epsilon}{\pi} \Delta_{1,2}(\epsilon) f(\epsilon) P_{0\ -\sigma;0\ -\sigma}(z+\epsilon) P_{0\ 2;2\ 0}(z+i\omega+\epsilon) \\
&+ \ldots \text{"other terms"}
\end{aligned}
\qquad (2.34)
$$

The $\sigma = \pm 1$ prefactor for the first term stems from the incoming external σ-electron at the second vertex changing the ionic state from $|0;\ -\sigma\rangle$ to $|2;0\rangle$, which involves via $f^\dagger_\sigma|0\ -\sigma\rangle = \sigma|0;2\rangle$ the factor σ. The (-1)-sign factor due to the crossing electron line in this diagram is canceled by the annihilation of the $-\sigma$ electron at the third vertex. There the ionic state is changed from $|\sigma;-\sigma\rangle$ to $|\sigma;0\rangle$, which according to the discussed sign rules for the vertices involves by $f_{-\sigma}|\sigma;-\sigma\rangle = -|\sigma;0\rangle$ an additional -1 sign factor.

Equation 2.33 contains no lowest order term, as here the electron enters the vertex at site 2 and leaves at site 1. This can only be caused by higher order processes, which necessarily involve at least one non-diagonal propagator.

The FNCA/ENCA was originally designed in order to incorporate the correct exchange coupling in the Kondo regime for finite U

$$J = \frac{V^2}{|\epsilon^f|} + \frac{V^2}{|\epsilon^f + U|}, \tag{2.35}$$

which can be obtained by a Schrieffer-Wolff transformation [Sch66], and to reproduce the right magnitude of the Kondo scale. The ENCATI - in difference - not only contains the terms which lead to the exchange given by equation 2.35 but also RKKY-terms favoring magnetic order between two impurities. Depending on the relative strength, these processes can destroy or significantly alter the characteristics of the SIAM Kondo-effect.
For the TI-approximations it is important, that the processes generating the Kondo-effect and the processes generating the RKKY-interaction enter the theory in a balanced way. The critical discussion of the processes included in SNCATI/ENCATI, undertaken in section 2.5, shows that the ENCATI - contrary to the SNCATI - contains not only the correct exchange given by equation (2.35) but also the correct leading order ($\propto J^2 = V^4$) RKKY processes. For more details on this issue consult section 2.5 and chapter 3, where numerical results are presented.

2.4 Symmetries

The equations specified for propagators, self energies and vertices represent the most general case, in the sense that no additional symmetries of the underlying Hamiltonian are taken into account. Especially if the Hamiltonian is spin degenerate - which is the case for the one stated in equation (2.1) - and/or if the two impurities have the same structure and energy parameters and couple to the same host states, the number of equations and terms for a given self energy and vertex can be considerably reduced.

In practice the reduction of equations according to symmetries must be undertaken with great care. The problem which arises here is that symmetry relations for non-diagonal propagators sometimes involve an symmetry factor -1. These factors can be deduced in a similar way as the sign factors which arise in non-diagonal diagrams due to vertices. Concerning the symmetry factor, propagators must be a read as generalized transfer operators

$$P_{M;M'}(z) \longrightarrow |M' >< M|. \tag{2.36}$$

Take for example the propagator $P_{\sigma\ -\sigma;0\ 2}$ and assume spin degeneracy. This propagator is then certainly symmetry-related to $P_{-\sigma\ \sigma;0\ 2}$. In order to obtain the symmetry factor between this pair on starts with the identification

$$P_{-\sigma\ \sigma;0\ 2}(z) \longrightarrow |0\ ;2\rangle\langle\sigma\ -\sigma| = f^\dagger_{2,\uparrow} f^\dagger_{2,\downarrow}|0\rangle\langle 0| f_{2,\sigma} f_{1,-\sigma}. \tag{2.37}$$

The spin symmetry related propagator is then given by interchanging

$$f^\dagger_{i,\sigma} \longrightarrow f^\dagger_{i,-\sigma} \tag{2.38}$$

$$f_{i,\sigma} \longrightarrow f_{i,-\sigma}. \tag{2.39}$$

This leads for equation (2.37) to

$$f^\dagger_{2,\downarrow} f^\dagger_{2,\uparrow} |0\rangle\langle 0| f_{2,-\sigma} f_{1,\sigma}. \tag{2.40}$$

According to the convention in equation (2.18) this can also be written as

$$-|0\ 2\rangle\langle -\sigma\ \sigma|. \tag{2.41}$$

So the symmetry relation for a spin degenerate Hamiltonian is

$$P_{-\sigma\ \sigma;0\ 2} = -P_{\sigma\ -\sigma;0\ 2}. \tag{2.42}$$

If both impurity sites are equal and couple to the same host, two further symmetries can be derived from the example. The symmetry operation is now

$$f^\dagger_{1,\sigma} \underset{\longrightarrow}{\longleftarrow} f^\dagger_{2,\sigma} \tag{2.43}$$

$$f_{1,\sigma} \underset{\longrightarrow}{\longleftarrow} f_{2,\sigma}, \tag{2.44}$$

and it directly follows

$$|0\ 2\rangle\langle \sigma\ -\sigma| = f^\dagger_{2,\uparrow} f^\dagger_{2,\downarrow} |0\rangle\langle 0| f_{2,\sigma} f_{1,-\sigma} \longrightarrow f^\dagger_{1,\uparrow} f^\dagger_{1,\downarrow} |0\rangle\langle 0| f_{1,\sigma} f_{2,-\sigma} = -|2\ 0\rangle\langle -\sigma\ \sigma| \tag{2.45}$$

$$-|0\ 2\rangle\langle -\sigma\ \sigma| = f^\dagger_{2,\downarrow} f^\dagger_{2,\uparrow} |0\rangle\langle 0| f_{2,-\sigma} f_{1,\sigma} \longrightarrow f^\dagger_{1,\downarrow} f^\dagger_{1,\uparrow} |0\rangle\langle 0| f_{1,-\sigma} f_{2,\sigma} = |2\ 0\rangle\langle \sigma\ -\sigma|. \tag{2.46}$$

So in case of spin- and impurity symmetry only one of the four propagators in the example needs to be calculated and the three others are then given by the relation

$$P_{\sigma\ -\sigma;0\ 2} = P_{-\sigma\ \sigma;2\ 0} \quad = \quad -P_{-\sigma\ \sigma;0\ 2} = P_{\sigma\ -\sigma;2\ 0}. \tag{2.47}$$

The above procedure must in principle be undertaken for each propagator, and no simpler rule to deduce the symmetry factor has so far come to the authors mind. The only simple rule one can state is, that for diagonal propagators sign factors in the procedure described above always cancel, and symmetries in that case are simple identities.

In order to reduce the set of equations according to symmetries a strategy can be formulated as follows:

- Define a minimal set of propagators, self energies and vertices which are not related by symmetry operations.
- Deduce from the minimal set of non-diagonal propagators the correct sign factor for the symmetry related non-diagonal propagators.
- Substitute in the equations all quantities with the corresponding quantity from the minimal set with the correct sign factor
- Sum up the terms and calculate the minimal set.

As it is very tedious and error-prone to do the procedure described above by hand, the numerical implementation of the SNCATI/ENCATI developed for this work automates this procedure. In a first step the program generates abstract representations of all self energies, vertices, propagators and the defining diagrammatic equations of these quantities. In a second step they are mapped according to the specified symmetries to a minimal set and reduces the abstract set of equations algorithmically. The third step is then the actual calculation of the diagrams. More details on the numerical implementation will be given in section 2.6.

2.5 Critical inspection of SNCATI and ENCATI

With the definition of SNCATI and ENCATI in the previous section it is now appropriate to discuss some potential benefits and shortcomings which can be deduced from the specific selection of diagrams in the approximations. One topic of great relevance in this thesis is the question:
How well behave SNCATI/ENCATI in the uncoupled limit in relation to SNCA/ENCA ?

The physics of this situation is very clear in the sense that the dynamic evolution of the two impurities are independent processes and can for each impurity be described by the solution of a calculation from a SIAM solver, for example SNCA or ENCA. In the following, it will be explained that it is a nontrivial task in the design of a TIAM-solver to correctly reproduce this limit and why SNCATI/ENCATI fail at this point.

Speaking in terms of exact Greenfunctions the one particle Greenfunction for impurity i can be obtained when the dynamics of the other impurity site is integrated out in the exact two particle Greenfunction

$$G_1(i\omega_1) = \frac{-1}{\beta}\sum_{i\omega_2} G_{1,2}(i\omega_1, i\omega_2) = G_1(i\omega_1)\ \frac{1}{\beta}\sum_{i\omega_2} G_2(i\omega_2) \tag{2.48}$$

The independence of the two sites is here manifested in the product form of the two-particle Greenfunction after the second equal sign. Stated differently, each impurity has its own independent timeline or energy variable $i\omega_i$.
The one particle Greenfunction obtained from SNCATI/ENCATI or from any other solver describes the dynamics of both impurities with one energy variable $i\omega$ or equivalently along one time-line, an ansatz in the form of equation (2.48) is therefore not possible.
From this point of view it is a very complicate task to design analytical approximations which on the one hand are capable of correctly reproducing the uncoupled limit[1] and on the other hand contain a proper description of the coupled impurities. Even more, when the physical origin of the coupling terms are the same which lead to the Kondo effect in the SIAM. Equation 2.48 gives a clear hint how two-impurity diagrams need to be selected for an approximation, which preserves the SIAM limit. Equation 2.48 condenses two time-lines - one for each impurity - in one time-line by allowing every process to happen on one site, no matter what is happening at that moment on the other site. Any selection of diagrams, where in the uncoupled limit processes on a site have to wait or are less likely to happen because of processes on the other site therefore introduce artificial correlations and lead to

---

[1] one has to remember that the SIAM solution itself is a highly nontrivial task

the failure in reproducing this limit.

Unfortunately in SNCATI/ENCATI the uncoupled limit is not correctly reproduced , i.e. they do not reduce to the ENCA/SNCA approximation. Figure 2.4 shows two 4'th order diagrams, without explicit coupling processes between the two-impurities. The left diagram is contained in the SNCATI/ENCATI, while the right diagram is only contained in the ENCATI. In this order the correct limit of uncoupled impurities is destroyed in SNCATI. The inner band electron propagation from site two to two must end inside the band propagation from site 1 to site 1. SNCATI contains no diagrams which include the crossing of band propagation electron lines. The necessary crossings for the correct uncoupled limit are generated by shifting the time-line of the second site and include all distinct diagrams which arise thereby in the approximation.

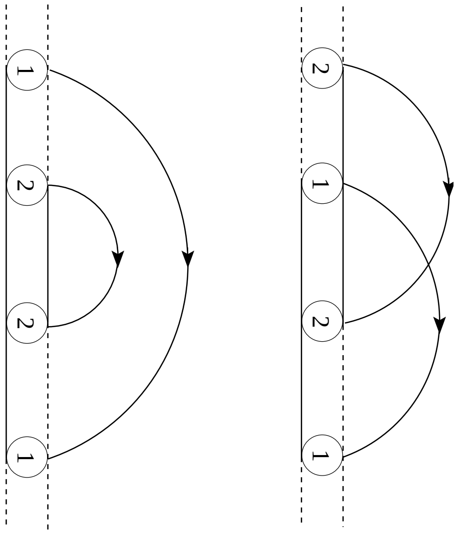

Figure 2.4: Two 4'th order diagrams, with no direct coupling between the two impurities. The diagram on the left is contained in the SNCATI/ENCATI, while the diagram on the right is only contained in the ENCATI and restores in this order the correct limit of uncoupled impurities.

In case of the SNCATI diagram on the left, by shifting the time axis for site 2 the right diagram in Figure 2.4 is generated. The ENCATI contains the first order corrections towards the uncoupled limit, the first terms which violate this limit are of order $O(V^6)$. So in difference to the ENCA in ENCATI there exist vertex correction processes which do not involve the local Coulomb interaction U, i.e. double occupations at one impurity site, and therefore do not vanish in this limit $U \longrightarrow \infty$. They would only vanish if additional to U an infinite large inter-impurity Coulomb interaction $\tilde{V}$ is switched on.

It is quite interesting in the ENCATI/SNCATI diagrams to notice, that if one looks only at the time evolution of one impurity site, i.e. the sequence of ionic states for one site, then this sequence is indistinguishable from the corresponding SIAM approximation. For the SNCATI this is very easy to see, take for example a look in equation (2.24) at the last diagram and replace the full vertices with the bare ones and focus only on the sequence of ionic states on the first impurity-site . The result looks like the SNCA for the unoccupied self energy Σ_0.

However, as stated before, this finding does not mean that the single impurity dynamics in SNCATI/ENCATI is described as good as in a corresponding SIAM solver. The unphysical inter-impurity correlations influence the single impurity dynamics and eventually can lead to a drastically altered behavior. It will be further investigated in chapter 3, how strong these artificial correlations are. At least one can expect that the ENCATI by the inclusion of the lowest order corrections behaves significantly better than the SNCATI at this point, especially for the case with switched off or weak impurity-impurity Coulomb interaction $\tilde{V}$.

Another important question which must be critically inspected for the SNCATI/ENCATI approximation concerns the quality in the treatment of inter-impurity processes. This question must be answered in a twofold way, on the one hand there are the indirect impurity-impurity couplings mediated by hybridization with and electrons and on the other hand there can also be direct matrix elements, e.g. a direct hopping t, connecting the impurities. It was already shown in the discussion of equation (2.22) that the ionic limit, i.e. the case with switched off hybridization V, is exactly contained in any approximation within the present framework. The situation for the direct couplings is a little bit more complicated to judge with switched on hybridization V. In that case, the self energy $\underline{\underline{\Sigma}}_{W,t}$ in equation (2.22) does not vanish and depends on the direct couplings W, t. In SNCATI/ENCATI the dependence of the self energy from W and t originates from the self-consistent calculation

$$\begin{tikzcd} \underline{\underline{P}}(z) = \left[\left(\underline{\underline{P}}^0(z)\right)^{-1} - \underline{\underline{\Sigma}}(z) - \underline{\underline{W}} - \underline{\underline{t}}\right]^{-1} \arrow[d, bend left] \\ \underline{\underline{\Sigma}}[\underline{\underline{P}}](z) \arrow[u, bend left] \end{tikzcd} \tag{2.49}$$

of the self energy as functional of the propagator. This self-consistent scheme thereby involves, in connection with the hybridization V direct W and t processes up to infinite order. In that sense the treatment of the direct couplings in the self-energy is only as good as the treatment of hybridization processes,

and enter the theory in a balanced way.

The indirect impurity-impurity couplings arise in the theory, due to the presence of off-diagonal elements in the self-energy matrix. By construction in SNCATI/ENCATI these non-diagonal processes are treated on the same footage as the diagonal ones. From that point of view, it can be expected that the V mediated inter-impurity coupling is equally well described as the uncoupled single impurity behavior of the approximations. Especially the approximations contain the V^4 and higher order terms, from impurity i to j and back, which mediate the RKKY interaction. A typical RKKY contribution to the self energy is shown in Figure 2.5. There a σ-electron from site 1 enters the lower vertex and leaves at site 2 and is transferred back to site 1 via the non-diagonal propagator between the two vertices. In effect, this contribution correlates the dynamics of the σ-electron on site 1 with the $-\sigma$-electron on site 2. Unfortunately such irreducible self energy contributions do not exist in

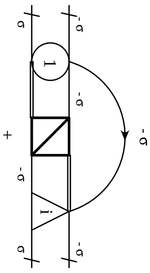

Figure 2.5: RKKY self energy diagram. The σ-electron propagates from site 1 to site 2 and back, thereby correlating its dynamics with the dynamics from the $-\sigma$-electron at the other site.

the SNCATI approximation. In SNCATI the lower full vertex has to be replaced by a bare vertex and as the full vertex involves at least one non-diagonal internal propagation process it has no lowest order contribution. The ENCATI in the vertex correction terms contains non-diagonal propagations. In lowest order contributions like the one depicted in Figure 2.5 are contained correctly in the ENCATI. The SNCATI contains irreducible V mediated couplings only by the insertion of the full propagator in the self energy (2.49). A typical irreducible V^4 process contained in the SNCATI is shown in Figure 2.6. Here, by two non-

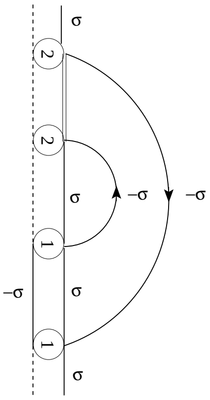

Figure 2.6: $O(V^4)$ irreducible impurity-impurity coupling process contained in the SNCATI.

diagonal band propagations, the $-\sigma$-electron propagates from site 1 to site 2 and back. In the inner band propagation the electron is transfered from site 1 to site 2, there it gets correlated with the σ-electron on that site and finally propagates back to site 1.

In conclusion, from the pure virtue of the diagrammatics, the ENCATI is expected to perform considerably better than the SNCATI. It contains in lowest order the correct RKKY couplings and - from the authors point of view even more important - the leading order corrections towards the limit of two uncoupled impurities. Concerning the last point, one has to keep in mind that the original NCA for the SIAM was designed for infinite Coulomb interactions and the SNCA for finite U is known to behave very badly for small or switched off U. The selection of non-crossing diagrams has proven to be only favorable if the largest scale is set by U. It tends most prominently for vanishing U, to develop a small pathological spike at the Fermi level, which is a completely unphysical result.

The ENCA is known to behave much better (but still not too good) in this limit. Without nearest neighbor Coulomb interaction $\tilde{V}$ the two impurity approximations have, concerning the inter-impurity coupling, no scale set by $\tilde{V}$ and there is no ab-initio reason to believe that non-crossing inter-impurity diagrams should be more important than crossing ones. The inclusion of lowest order inter-impurity crossing diagrams in the ENCATI is therefore, in the authors perception, of even more relevance than in the corresponding theory for the SIAM. It will be an important focus in the results of chapter 3 to investigate, how much of the mentioned here flaws in the theory show up in numerical calculations.

2.6 Defect equations and numerical implementation

Like NCA theories for the SIAM it also for SNCATI/ENCATI from a practical point of view is not sufficient to consider solely the ionic propagators and the vertices in order to calculate the Partitionfunction $\mathcal{Z}$ and the Greensfunctions. The problem is hidden in the exponential $\frac{e^{-\beta x}}{\mathcal{Z}}$ term in equation (2.5), which is even for relatively high temperatures very hard to handle numerically. The trick which circumvents this problem, originally proposed by Kuramoto [Kur84], is to define an auxiliary function, the so called defect propagator

$$\left(\zeta_{M.M'}\right)(x) \equiv -\frac{e^{-\beta x}}{\pi \mathcal{Z}_f} Im\left(\underline{\underline{P}}(x+i\delta)\right) = -\frac{e^{-\beta x}}{2\pi \mathcal{Z}_f}\left(\underline{\underline{P}}(x+i\delta) - \underline{\underline{P}}^*(x+i\delta)\right), \tag{2.50}$$

which absorbs the exponential factor. The procedure is then to setup a closed set of equations for $\underline{\underline{\zeta}}$ which can be solved self consistently. With the representation of the ionic propagator in terms of the unperturbed propagator $\underline{\underline{P}}_0$ and the irreducible ionic propagator self-energy $\underline{\underline{\Sigma}}$ given in equation (2.22), the imaginary part of the ionic propagator can be expressed by the imaginary part of the ionic self-energy via

$$\begin{aligned}
\underline{\underline{P}} - \underline{\underline{P}}^* =& \underline{\underline{P}}_0\left(\underline{\underline{I}} + \underline{\underline{\Sigma P}}\right) + \underline{\underline{P}}_0^*\left(\underline{\underline{I}} + \underline{\underline{\Sigma}}^*\underline{\underline{P}}^*\right) \\
=& \left(\underline{\underline{P}}_0 - \underline{\underline{P}}_0^*\right)\underbrace{\left(\underline{\underline{I}} + \underline{\underline{\Sigma}}\ \underline{\underline{P}}\right)}_{\underline{\underline{P}}_0^{-1}\underline{\underline{P}}} + \underline{\underline{P}}_0^*\left(\underline{\underline{\Sigma}}\ \underline{\underline{P}} - \underline{\underline{\Sigma}}^*\ \underline{\underline{P}}^*\right) \\
=& \left(\underline{\underline{I}} - \underline{\underline{P}}_0^*\left(\underline{\underline{P}}_0^{-1} - \left[\underline{\underline{\Sigma}} - \underline{\underline{\Sigma}}^*\right]\right)\right)\underline{\underline{P}} + \underline{\underline{P}}_0^*\underline{\underline{\Sigma}}^*\left(\underline{\underline{P}} - \underline{\underline{P}}^*\right) \\
=& \underbrace{\left[\underline{\underline{I}} - \underline{\underline{P}}_0^*\ \underline{\underline{\Sigma}}^*\right]^{-1}}_{\underline{\underline{P}}^*\ \underline{\underline{P}}_0^{*\ -1}}\left[\underline{\underline{I}} - \underline{\underline{P}}_0^*\left(\underline{\underline{P}}_0^{-1} - \left(\underline{\underline{\Sigma}} - \underline{\underline{\Sigma}}^*\right)\right)\right]\ \underline{\underline{P}} \\
=& \underline{\underline{P}}^*\underbrace{\left(\ \underline{\underline{P}}_0^{*\ -1} - \underline{\underline{P}}_0^{-1}\right)}_{\lim\limits_{i\delta\to 0}......=0}\underline{\underline{P}} + \underline{\underline{P}}^*\left(\underline{\underline{\Sigma}} - \underline{\underline{\Sigma}}^*\right)\underline{\underline{P}} \\
=& \underline{\underline{P}}^*\left(\underline{\underline{\Sigma}} - \underline{\underline{\Sigma}}^*\right)\underline{\underline{P}} = 2i\underline{\underline{P}}^*\mathrm{Im}(\underline{\underline{\Sigma}})\underline{\underline{P}}.
\end{aligned} \tag{2.51}$$

The defect propagator can therefore be written as

$$\underline{\underline{\zeta}}(x) = -\frac{e^{-\beta x}}{\pi \mathcal{Z}_f}\underline{\underline{P}}^*(x+i\delta) Im(\underline{\underline{\Sigma}}(x+i\delta))\underline{\underline{P}}(x+i\delta). \tag{2.52}$$

In the calculation the subscript $\underline{\underline{W}}, \underline{\underline{t}}$ of the self-energy is omitted for brevity. The exponential factor $-\frac{e^{-\beta x}}{\pi \mathcal{Z}_f}$ can then be absorbed in the imaginary part of the self-energy

$$\underline{\underline{\zeta}}^{\Sigma}(x) \equiv -\frac{e^{-\beta x}}{\pi \mathcal{Z}_f} Im(\underline{\underline{\Sigma}}(x+i\delta)), \tag{2.53}$$

where $\underline{\underline{\zeta}}^{\Sigma}$ is termed the defect self-energy. The analytic expressions for the self-energy contain Fermi functions $f(\pm x)$, which can absorb the explicit exponential factor by the useful relation

$$e^{\pm\beta x} f(\pm x) = f(\mp x), \tag{2.54}$$

if the equations for the defect self-energy are written in terms of defect-propagators. The defect self-energy thereby becomes a functional of the defect-propagators $\underline{\underline{\zeta}}^{\Sigma}\left[\underline{\underline{\zeta}}\right]$, which is in turn via equation (2.52) and equation (2.53) a functional of the defect self-energy $\underline{\underline{\zeta}}\left[\underline{\underline{\zeta}}^{\Sigma}\right]$. This constitutes a closed set of equations for the defect-propagators, which must be solved self-consistently.

Similar to the corresponding defect-equations for the SIAM, it turns out that the self-consistent solution of the TIAM defect-equations leads to no unique solution concerning the norm of the defect-propagators $\underline{\underline{\zeta}}$. This can be fixed by imposing the relation

$$\sum_M \int_{-\infty}^{\infty} dx\ \zeta_{M,M}(x) = \frac{1}{\mathcal{Z}_f} \underbrace{\sum_M \int_{-\infty}^{\infty} dx\ \rho_{M,M}(x) e^{-\beta x}}_{\mathcal{Z}_f} = 1 \tag{2.55}$$

for the diagonal defect propagators with $\rho_{M,M}(x) \equiv -\frac{1}{\pi} Im\left(P_{M,M}(x+i\delta)\right)$ the spectrum of the ionic propagator. The non-diagonal defect propagators $\zeta_{M,M'}$ with $M \neq M'$ do not fulfill any sum-rule, because the spectrum of the non-diagonal propagators have no definitive sign and valid relations like

$$\int_{-\infty}^{\infty} dx \rho_{M,M'}(x) = 0 \qquad \text{with } \ M \neq M' \tag{2.56}$$

for the ionic propagators are not valid for the defect propagators, due to the additional $e^{-\beta\, x}$ factor.

In the practical numerical iterative solution of the defect equations the fastest convergence is reached, if after each iteration the diagonal and the off-diagonal defect propagators are rescaled by

$$\zeta^{n'}_{M,M'}(x) = \frac{\zeta^{n}_{M,M'}(x)}{\sum_M \int dx\ \zeta^{n}_{M,M}(x)} \tag{2.57}$$

where $\zeta^{n}_{M,M'}$ denotes the solution of equation (2.52) after n iterations.

Due to the large number of self-energies and different terms in the self-energy it is a tedious and error-prone procedure to write down the whole set of defect self-energy equations by hand. The inclusion of vertex correction terms in the ENCATI makes this work even more cumbersome. The number of different terms is larger than for the self-energy and vertex equations itself, as in the defect equations the real and imaginary part of the propagators have to be made explicit. It is for a numerical implementation much more advantageous to generate these terms algorithmically.

Therefore, the full set of defect equations will not be presented in this work. Instead solely the generic analytic form of these equations will be analyzed and discussed. Furthermore, some practical advise in the algorithmic generation of these equations will be given and how a possible reduction according to the symmetries (see subsection 2.4) can be implemented.

The SNCATI contributions to the defect self-energies, which are also present in ENCATI, have the generic form

$$\zeta^{\Sigma}_{(gen)}(x) \equiv -\frac{e^{-\beta\omega}}{\pi\mathcal{Z}_f}\int\frac{d\epsilon}{\pi}f^{(s)}_{i,j}(\epsilon)Im(P_A(\omega+i\delta+s\;\epsilon)), \tag{2.58}$$

where $s=\pm1$ indicates a particle/hole band-propagation, A is an abbreviation for the ionic indices of the propagator $P_A\equiv P_{M,M'}$. Furthermore $f^{(s)}_{i,j}(\epsilon)$ is defined as

$$f^{(s)}_{i,j}(\epsilon) = f(s\;\epsilon)\Delta_{\underline{R}_i,\underline{R}_j}(\epsilon), \tag{2.59}$$

where $\Delta_{\underline{R}_i,\underline{R}_j}$ denotes the hybridization function from the impurity situated at $\underline{R}_i$ to the impurity at $\underline{R}_j$. Compare e.g. with equation (2.25) for examples. Equation (2.58) can then expressed in term of defect propagators by

$$\begin{aligned}\zeta^{\Sigma}_{(gen)}(x) &= -\frac{e^{-\beta\omega}}{\pi\mathcal{Z}_f}\int\frac{d\epsilon}{\pi}f^{(s)}_{i,j}(\epsilon)(-\pi)\mathcal{Z}_f e^{\beta(\omega+s\;\epsilon)}\zeta_A(\omega+s\;\epsilon)\\ &= \int\frac{d\epsilon}{\pi}f^{(-s)}_{i,j}(\epsilon)\zeta_A(\omega+s\;\epsilon).\end{aligned} \tag{2.60}$$

For the SNCATI each possible contribution to the defect self-energy is therefore uniquely identified with the specification of four quantities $(A,s,\underline{R}_i,\underline{R}_j)$. If both impurities couple to the same band, the hybridization function depends only on the distance vector

$$\Delta_{i,j}\longrightarrow\Delta_{\underline{d}} \qquad \text{with} \qquad \underline{d}=\underline{R}_j-\underline{R}_i \tag{2.61}$$

and it suffices to specify only a 3-tuple $u=(A,s,\underline{d})$ in order to identify a self-energy contribution.

For the numerical implementation of the defect equations it is useful to organize the N different contributions u_i in a set $\mathcal{M}=\{u_1,\ldots,u_N\}$. With additional symmetries $\mathcal{M}$ contains up to symmetry sign-factor (see section 2.4) many identical contributions. For the numerics it is advantageous to calculate these contributions only once. Therefore in the implementation according to the specified symmetries a second set $\mathcal{M}'=\{u'_1,\ldots,u'_{N'}\}$ is generated, which contains the $N' \leq N$ different contributions not related by symmetry. The two sets $\mathcal{M}'$ and $\mathcal{M}$ are then connected by a mapping function

$$f(u_i) \longrightarrow \beta_i \; u'_j \tag{2.62}$$

with $\beta_i = \pm 1$ the already mentioned symmetry sign-factor. With this notation the contributions to a defect self-energy can then expressed by a linear combination in the form

$$\zeta^{\Sigma}_{M,M'} = \sum_i \alpha_i u_i = \sum_i \alpha_i f(u_i), \tag{2.63}$$

where $\alpha_i = \pm 1$ is an additional symmetry sign-factor representing the sign-factor for the corresponding contribution to the self-energy $\Sigma_{M,M'}$ (see text below equation (2.29) for reference on this issue).

For the numerical implementation it is advantageous to calculate first the numerically costly contributions in $\mathcal{M}'$ and then evaluate the sum in equation (2.63). The defect-propagators are then calculated via equation (2.52). The matrix multiplications in equation (2.52) are numerically easy to handle.

For the numerical calculation of the ENCATI defect self-energies the same strategy as for the SNCATI can be implemented. Only the costly convolution integrals for a minimal set of contributions need to be numerically integrated, the defect self-energy itself is then again given by linear combinations of these precalculated contributions.
The ENCATI defect equations contain the SNCATI contributions, but calculated with the ENCATI ionic propagators. For these contributions the numerical apparatus described for the SNCATI can be reused. Furthermore the ENCATI defect self-energy contains terms due to the vertex corrections, which differ in the generic analytical form from the SNCATI contributions. These contributions will be examined in the following.

The generic term for the corrections in the defect self-energy due to vertex corrections is

$$\begin{aligned}
\tilde{\zeta}^{\Sigma}_{(gen)}(x) &= -\frac{e^{-\beta\omega}}{\pi \mathcal{Z}_f} \int \frac{d\epsilon}{\pi} f^{(s)}_{i,j}(\epsilon) Im(\tilde{\Lambda}^i_A(\omega + i\delta, \omega + i\delta + s\;\epsilon) P_C(\omega + i\delta + s\;\epsilon)) \qquad (2.64) \\
&= -\frac{e^{-\beta\omega}}{\pi \mathcal{Z}_f} \int \frac{d\epsilon}{\pi} f^{(s)}_{i,j}(\epsilon) Im(\tilde{\Lambda}^i_A(\omega + i\delta, \omega + i\delta + s\;\epsilon)) Re(P_C(\omega + s\;\epsilon)) \\
&\quad + \int \frac{d\epsilon}{\pi} f^{(-s)}_{i,j}(\epsilon) Re(\tilde{\Lambda}^i_A(\omega + i\delta, \omega + i\delta + s\;\epsilon)) \zeta_C(\omega + s\;\epsilon), \qquad (2.65)
\end{aligned}$$

where $\tilde{\Lambda}^i_A$ shall be defined to contain solely vertex corrections. The contributions from the bare vertex are included in the SNCATI contributions and can be handled with the setup described for this theory.
The second line in equation (2.65) already has the desired form, contrary to the first line where the exponential factor is still explicit. In order to resolve this, the analytic expression for the vertex corrections must be inserted and imaginary parts of propagators need then to be expressed in terms of defect propagators. In general the vertex correction function consists of many different terms. The structure of such a term in the vertex function is

generic and has the form

$$\tilde{\Lambda}^{(gen)}(z, z + s\ x) = \int \frac{dy}{\pi} f_{l,m}^{(s')}(y) P_A(z + s'\ y) P_B(z + s'\ y + s\ x), \tag{2.66}$$

Substituting the generic vertex function $\tilde{\Lambda}^{(gen)}$ in equation (2.65) one gains

$$\begin{aligned}
\tilde{\zeta}^{\Sigma}_{(gen)}(x) = \iint \frac{d\epsilon}{\pi} \frac{dy}{\pi} \Bigg[& \\
& f_{i,j}^{(s)}(\epsilon) f_{l,m}^{(-s')}(y)\ \zeta_A(\omega + s'y) Re\left(P_B(\omega + s'y + s\epsilon)\right) Re(P_C(\omega + s\epsilon)) + \quad (2.67) \\
& f_{i,j}^{(-s)}(\epsilon) f_{l,m}^{(-s')}(y)\ \zeta_B(\omega + s'y + s\epsilon) Re(P_A(\omega + s'y)) Re(P_C(\omega + s\epsilon)) + \quad (2.68) \\
& f_{i,j}^{(-s)}(\epsilon) f_{l,m}^{(s')}(y)\ \zeta_C(\omega + s\epsilon) Im(P_A(\omega + s'y)) Im(P_B(\omega + s\epsilon + s'y)) \Bigg] . \quad (2.69)
\end{aligned}$$

A contribution due to the vertex corrections in the ENCATI defect self-energy is therefore uniquely identified by the specification of 9 quantities $(A, B, C, s, \underline{R}_i, \underline{R}_j, s', \underline{R}_l, \underline{R}_m)$. If the impurities couple to the same band, i.e. the hybridization function depends only on the distance vector, it suffices to specify a 7-tuple $\tilde{u} = (A, B, C, s, \underline{d}, s', \underline{d}')$ with $\underline{d} = \underline{R}_i - \underline{R}_j$ and $\underline{d}' = \underline{R}_l - \underline{R}_m$. In the same fashion as for the SNCATI contributions, all $\tilde{N}$ contributions to $\underline{\underline{\tilde{\zeta}}}^{\Sigma}$ can be organized in a set $\tilde{\mathcal{M}} = \{\tilde{u}_1, \ldots, \tilde{u}_{\tilde{N}}\}$ of 7-tuples $\tilde{u}_i$. In presence of additional symmetries the contributions in $\tilde{\mathcal{M}}$ are again connected to the contributions not related by symmetry in the set $\tilde{\mathcal{M}}' = \{\tilde{u}'_1, \ldots, \tilde{u}'_{\tilde{N}'}\}$ with $\tilde{N}' \leq \tilde{N}$ by a mapping function

$$\tilde{f}(\tilde{u}_i) \longrightarrow \tilde{\beta}_i\ \tilde{u}'_j, \tag{2.70}$$

where $\tilde{\beta}_i = \pm 1$ accounts for the symmetry sign-factor between these contributions. The vertex corrections in the defect self-energy can then be expressed by a linear combination of the form

$$\tilde{\zeta}^{\Sigma}_{M,M'} = \sum_i \tilde{\alpha}_i \tilde{u}_i = \sum_i \tilde{\alpha}_i \tilde{f}(\tilde{u}_i), \tag{2.71}$$

where equivalent to α_i in Equation (2.63) $\tilde{\alpha}_i = \pm 1$ is the symmetry sign-factor of the corresponding contribution to the self-energy $\Sigma_{M,M'}$. With Equation (2.71) the calculation of the vertex-corrections to the defect self-energy is reduced to the minimal set.

But within the ENCATI a further reduction of the numerical effort is achievable. The evaluation of a contribution $\tilde{u}'_i$ involves the calculation of a double integral in each iteration of the self-consistent calculation scheme, which is numerically very costly as up to $10 - 20$ iterations are necessary until convergence is reached. The numerical effort can be significantly reduced by the calculation of two-dimensional kernel-functions, which do not depend on the defect-propagators, in advance of the iterative scheme. This has the advantage, that during the iterations only "simple" convolutions of these kernel-functions with the defect propagators from the previous iteration need to be numerically evaluated. For the kernel function Equation (2.67) is therefore rewritten as

$$\begin{aligned}&\int \frac{dy}{\pi} f_{l,m}^{(-s')}(y)\ \zeta_A(\omega+s'y) \int \frac{d\epsilon}{\pi} f_{i,j}^{(s)}(\epsilon) Re\left(P_B(\omega+s'y+s\epsilon)\right) Re(P_C(\omega+s\epsilon))\\ &= \int \frac{dy}{\pi} f_{l,m}^{(-s')}(y)\ \zeta_A(\omega+s'y) K^1_{\substack{B,C,\\ s,i,j}}(\omega, s'y), \qquad (2.72)\end{aligned}$$

where the Kernel $K^1_{\substack{B,C,\\ s,i,j}}$ is defined as

$$K^1_{\substack{B,C,\\ s,i,j}}(z,z') = \int \frac{d\epsilon}{\pi} f_{i,j}^{(s)}(\epsilon) Re\left(P_B(z+z'+s\epsilon)\right) Re(P_C(z+s\epsilon)). \qquad (2.73)$$

The second contribution in equation (2.68) after a shift in the integration variable $\epsilon \longrightarrow \epsilon - ss'y$ can be written as

$$\begin{aligned}&\int \frac{d\epsilon}{\pi} \zeta_B(\omega+s\epsilon) \int \frac{dy}{\pi} f_{i,j}^{(-s)}(\epsilon - s'y) f_{l,m}^{(-s')}(y)\ Re(P_A(\omega+s'y)) Re(P_C(\omega+s\epsilon-s'y))\\ &= \int \frac{d\epsilon}{\pi} \zeta_B(\omega+s\epsilon) K^2_{\substack{A,C,\\ s,i,j,\\ s',l,m}}(\omega,\epsilon) \qquad (2.74)\end{aligned}$$

with the kernel

$$K^2_{\substack{A,C,\\ s,i,j,\\ s',l,m}}(z,z') = \int \frac{dy}{\pi} f_{i,j}^{(-s)}(z'-s'y) f_{l,m}^{(-s')}(y)\ Re(P_A(z+s'y)) Re(P_C(z+s-s'y)). \qquad (2.75)$$

Equation (2.69) is written as

$$\begin{aligned}&\int \frac{d\epsilon}{\pi} f_{K^2 i,j}^{(-s)}(\epsilon) \zeta_C(\omega+s\epsilon) \int \frac{dy}{\pi} f_{l,m}^{(s')}(y)\ \Im(P_A(\omega+s'y)) Im(P_B(\omega+s\epsilon+s'y))\\ &= \int \frac{d\epsilon}{\pi} f_{i,j}^{(-s)}(\epsilon) \zeta_C(\omega+s\epsilon) K^3_{\substack{A,B,\\ s',l,m}}(\omega, s\epsilon) \qquad (2.76)\end{aligned}$$

with

$$K^3_{\substack{A,B,\\ s',l,m}}(z,z') = \int \frac{dy}{\pi} f_{l,m}^{(s')}(y)\ Im(P_A(z+s'y)) Im(P_B(z+z'+s'y)). \qquad (2.77)$$

The kernel-functions K^i remain constant during the iterative solution of the defect propagators and need to be calculated only once.

The here described symmetry-mapping procedure for the defect-equations and the introduction to two-dimensional kernel functions is naturally also applicable for the whole set of self-energy- and vertex-equations given in the Appendix A and B. The numerical effort can thereby be further reduced. The algorithmic reduction of the symmetry related terms has the great advantage, that the numerical implementation of the SNCATI/ENCATI can stay as general as possible without sacrificing the performance and memory consumption for situations with higher symmetries. The numerical implementation of the ENCATI in this work, makes dynamically reduces all possible symmetries in the self-energy and defect-equations. Even the set of different kernel-functions K^i is further reduced for situations with additional symmetries.

The computation time for a particle-hole symmetric and spin-degenerate TIAM can thereby be reduced by about a factor 10 against the most general solution. Further performance gains can be achieved by the numerical implementation of two-dimensional functions, which interpolate the function value from a discrete set of samples on an adaptively optimized mesh. These numeric functions are necessary for the precalculation of the described defect kernel-functions K^i, but can also with great benefit be used to calculate the vertex-functions before they enter the self-energy equations. By extensive use of these presampled two-dimensional functions, e.g. via the kernels in the defect-equations, the computation time for the ENCATI can be further reduced by an additional factor 10. With all these optimizations and the extensive use of parallel programming a high quality ENCATI solution for a particle-hole symmetric and spin-degenerate situation consumes on a modern Quad-Core CPU less than an hour. The memory consumption, due to the use of the presampled two-dimensional functions, for such a calculation is in the range of 1-2 GB and increases for less symmetric situations to about 8 GB.

3 TIAM results

3.1 Introduction

The two-impurity Anderson model (TIAM) is a classical problem in solid state physics. It is the first of the (multi-)impurity models which contain the competition between the Kondo-effect and the RKKY interaction. The RKKY exchange favors the formation of non-local magnetic correlations, while the Kondo effect is based on purely local magnetic correlations. The competition between these two effects is believed to be the key mechanism for the understanding of the magnetic properties in Heavy Fermion materials [Don71, Gre91].

In recent years, spectacular advances in nano-technology made it possible to construct direct experimental realizations of these models in quantum dot systems [Ree93, THO98, Jeo01, Cha04]. These developments have greatly revived the interest in multi-impurity models in general and especially the two-impurity model [Izu00, Zit06]. Since its first proposal in 1964 by Alexander and Anderson [Ale64] the TIAM and the related two-impurity Kondo model (TIKM) have been investigated with various methods.

The first systematic classification of the different regimes in these two models by the application of renormalization methods was given in the classical papers by Jayaprakash, Krishna-Murty and Wilkins [Jay81, Jay82]. Later the model was e.g. investigated by perturbation theory [Iva00, San94], variational methods [Sim06], Quantum Monte Carlo (QMC) [Fye87], Numerical Renormalization Group (NRG)[Jon88, Sak90, Sak93] and most recently with the Density Matrix Renormalization Group (DMRG) [Nis06]. Nevertheless, the dynamic properties at low temperatures and the influence of direct impurity-impurity matrix elements in extended models is far from well understood. Only some methods allow for a reliable calculation of the spectral density. The NRG, for example, is hard to implement for the two impurity case and the results obtained with this method are controversial [Fye94].

Only some efforts have so far been made to investigate the TIAM with direct perturbation theory. An attempt was made by [Sch96, Sch93], but there only the NCA at infinite $U = \infty$ was extended to the TIAM and only diagonal ionic propagators where calculated. To the authors knowledge, the SNCATI/ENCATI is the first implementation of the full TIAM in direct perturbation theory and the first method at all which is able to incorporate the full set of possible inter-impurity matrix elements.

In the following discussion the TIAM is restricted to the case of two equal ($\epsilon^f_{i\sigma} \equiv \epsilon^f$) spin degenerate impurity sites, which hybridize with the host lattice with a matrix element of the form $V_{\underline{k}i,\sigma} = V_{\underline{k}} e^{i\underline{k}\,\underline{R}_i}$ with $\underline{R}_i$ the position of impurity i. This form of the hybridization with $\underline{R}_i$ as a regular lattice vector, implies that the impurities are embedded in the lattice at

regular lattice sites.
Apart from the the local $U_i \equiv U$ term, no additional Coulomb matrix elements will be considered in the first place. Under these assumptions the TIAM Hamiltonian reads

$$\begin{aligned} H = &\sum_{\underline{k},\sigma} \epsilon_{\underline{k}}\ \hat{n}_{\underline{k}\sigma} + \epsilon^f \sum_{i,\sigma} \hat{n}^f_{i\sigma} + \sum_{\sigma} \left(t f^\dagger_{1,\sigma} f_{2\sigma} + h.c. \right) \\ &+ \sum_{i,\underline{k},\sigma} V_{\underline{k}} \left(e^{i\underline{k}\,\underline{R}_i} c^\dagger_{\underline{k},\sigma} f_{i\sigma} + h.c. \right) + U \sum_i \hat{n}^f_{i\uparrow} \hat{n}^f_{i\downarrow}. \end{aligned} \tag{3.1}$$

Although the TIAM-solver discussed in the previous chapter calculates its results in the f-basis defined in Equation (2.16) it is sometimes convenient to transform the ionic basis in even and odd states

$$f_{o\sigma} = \frac{1}{\sqrt{2}}(f_{1\sigma} - f_{2\sigma}) \qquad f^\dagger_{o\sigma} = \frac{1}{\sqrt{2}}(f^\dagger_{1\sigma} - f^\dagger_{2\sigma}) \tag{3.2}$$

$$f_{e\sigma} = \frac{1}{\sqrt{2}}(f_{1\sigma} + f_{2\sigma}) \qquad f^\dagger_{e\sigma} = \frac{1}{\sqrt{2}}(f^\dagger_{1\sigma} + f^\dagger_{2\sigma}) \tag{3.3}$$

and review results in that basis. The Hamiltonian (3.1) after this transformation reads

$$\begin{aligned} H \longrightarrow &\sum_{\underline{k},\sigma} \epsilon_{\underline{k}}\ \hat{n}_{\underline{k}\sigma} + \sum_{\nu=\{e,o\},\sigma} \epsilon^f_\nu f^\dagger_{\nu\sigma} f_{\nu\sigma} \\ &+ 2 \sum_{\underline{k},\sigma} |V_{\underline{k}}| e^{i\underline{k}\,\underline{R_0}} \left[\cos(\frac{1}{2}\underline{k}\ \underline{d}) \left(c^\dagger_{\underline{k}\sigma} f_{e\sigma} + h.c. \right) + \sin(\frac{1}{2}\underline{k}\ \underline{d}) \left(c^\dagger_{\underline{k}\sigma} f_{o\sigma} + h.c. \right) \right] \\ &+ \frac{1}{4} U \sum_{\nu=\{e,o\},\sigma} f^\dagger_{\nu,\sigma} f_{\nu,\sigma} f^\dagger_{\nu,-\sigma} f_{\nu,-\sigma} + \underbrace{\frac{1}{2} U}_{\tilde{V}} \sum_\sigma f^\dagger_{e,\sigma} f_{e,\sigma} f^\dagger_{o,-\sigma} f_{o,-\sigma} \\ &- \underbrace{\frac{1}{4} U}_{Y} \sum_\sigma \left(f^\dagger_{e\sigma} f^\dagger_{e-\sigma} f_{o\sigma} f_{o-\sigma} + f^\dagger_{e\sigma} f^\dagger_{o-\sigma} f_{o\sigma} f_{e-\sigma} \right), \end{aligned} \tag{3.4}$$

with $\epsilon^f_e = \epsilon^f + t$ and $\epsilon^f_o = \epsilon^f - t$. $\underline{d} = \underline{R}_2 - \underline{R}_1$ denotes the impurity distance and $\underline{R}_0 = \underline{R}_2 - \frac{\underline{d}}{2}$ the center coordinate of the two impurities.
This representation of the TIAM has the advantage that the hybridization of the even/odd impurity states with the host lattice separates in an orthogonal symmetric (even) and an antisymmetric (odd) channel. The diagonalization of the t hopping matrix element is a further favorable side effect of this transformation.

It will be shown in the next section, that for vanishing impurity distance $|\underline{d}| \longrightarrow 0$ only the even states couple to the host lattice, while the odd impurity site is completely decoupled. Unfortunately the local Coulomb interaction U in this representation mixes the even/odd impurity states via the nearest neighbor interaction $\tilde{V}$ and the double hopping Y terms defined in equation (3.4).

This chapter tries to give an overview of the physical properties of the TIAM. Due to the many adjustable parameters of the model and the possible shortcomings of the approximate

TIAM-solvers used, this is a rather delicate task. In order to gain a physical understanding of the numerical results from the TIAM-solvers each section in this chapter investigates a certain limit or a certain aspect of the TIAM. In section 3.3 the influence of RKKY processes is excluded in the calculations. Concerning these processes the impurities can be thought of as placed at an infinite distance $|\underline{d}| \longrightarrow \infty$. Without additional inter-impurity matrix elements the impurities are completely decoupled and one obtains two independent single-impurity models. In 3.3.1 this limit is used to compare numerical results from the SNCATI/ENCATI against those from the established SNCA/ENCA solvers for the SIAM. This comparison is undertaken in order to get more insight in the ability of the TIAM-approximations to describe the Kondo-effect.
In section 3.3.4 a direct-exchange coupling J is then switched on between the impurities, and in section 3.3.5 the TIAM is investigated with direct hopping t between the impurities. In these sections the Kondo-effect for each impurity competes with these direct-matrix elements. In many aspects this leads to similar results as in the following section 3.4, where the TIAM with RKKY-correlations is investigated for various impurity distances. There we concentrate on the influence of the RKKY-coupling alone, i.e. the two impurities are not coupled by direct inter-impurity matrix-elements.

Magnifications of the Figures presented in this chapter can be found in appendix C.1.

3.2 Resonant level solution of the TIAM

In order to elucidate the basic physics of the TIAM it is instructive to study the exactly solvable $U = 0$ resonant level version of the TIAM and compare the results with the corresponding ones from the SIAM.

Starting with the Hamiltonian (3.1) and setting $U = 0$ the one particle Greenfunction in the even/odd base can easily be calculated with e.g. the equations of motion method

$$zG_{A,B}(z) =< \{A,B\} > + G_{A,[H,B]}(z), \tag{3.5}$$

which leads to

$$G_{f_e,f_e^\dagger}(z) = \left[z - \epsilon_e^f - \Delta^e(z) - \xcancel{\frac{g^2(z)}{z - \epsilon_o^f - 2\Delta^o(z)}} \right]^{-1} \tag{3.6}$$

$$G_{f_o,f_o^\dagger}(z) = \left[z - \epsilon_o^f - \Delta^o(z) - \xcancel{\frac{g^2(z)}{z - \epsilon_e^f - 2\Delta^e(z)}} \right]^{-1} \tag{3.7}$$

with

$$\Delta^e(z) = \frac{2}{N} \sum_k \frac{|V_{\underline{k}}|^2 \cos(\frac{1}{2}\ \underline{k}\ \underline{d})^2}{z - \epsilon_{\underline{k}}} \ , \qquad \Delta^o(z) = \frac{2}{N} \sum_k \frac{|V_{\underline{k}}|^2 \sin(\frac{1}{2}\ \underline{k}\ \underline{d})^2}{z - \epsilon_{\underline{k}}}, \tag{3.8}$$

$$g(z) = \frac{2}{N} \sum_k \frac{V_{\underline{k}} \sin(\underline{k}\ \underline{d})}{z - \epsilon_{\underline{k}}}. \tag{3.9}$$

Here Δ^e, Δ^o are the hybridization functions for the even/odd channels of the underlying host DOS and the coupling of the even/odd states is described by the function $g(z)$. A

closer inspection of this function reveals that for an even hybridization $V_{\underline{k}} = |V_{\underline{k}}|\; g(z) \equiv 0$. This can be seen from the fact that the dispersion function $\epsilon_{\underline{k}}$ must reflect the symmetry of the underlying lattice structure which for all regular lattices incorporates a point inversion symmetry for each lattice site.
This implies that $\epsilon_{\underline{k}}$ is a symmetric function $\epsilon_{\underline{k}} = \epsilon_{-\underline{k}}$, so the $\underline{k}$ sum in combination with the antisymmetric sine function in the numerator of equation (3.9) all terms in the sum cancel exactly to zero.

The even/odd hybridization functions are related by

$$2\Delta(z) = \Delta^e(z) + \Delta^o(z) \tag{3.10}$$

with $\Delta(z) = \frac{1}{N}\sum_{\underline{k}} \frac{|V_{\underline{k}}|^2}{z-\epsilon_{\underline{k}}}$ the usual Anderson hybridization function of the SIAM.

In the case of large impurity distances $|\underline{d}|$, $\Delta^o(z)$ and $\Delta^e(z)$ both reduce to the SIAM hybridization function:

$$\Delta^o(z) \xrightarrow{d \gg 1} \Delta(z) \qquad , \qquad \Delta^e(z) \xrightarrow{d \gg 1} \Delta(z)\;, \tag{3.11}$$

which means that in this limit equation (3.6) and equation (3.7) become equal, constituting the solution of two uncoupled impurities.
In the opposite $\underline{d} = 0$ limit only the even impurity directly hybridizes with the host lattice

$$\Delta^o(z) \xrightarrow{d=0} 0 \qquad , \qquad \Delta^e(z) \xrightarrow{d=0} 2\Delta(z). \tag{3.12}$$

These results show, apart from also diagonalizing the optional direct hopping term t, the benefits of the odd and even decomposition of the local f-states. The TIAM effectively decouples into a two channel problem. For $|\underline{d}| = 0$ the odd impurity completely decouples from the host contrary to the uncoupled $|\underline{d}| \longrightarrow \infty$ limit where each channel - as expected - hybridizes with the hybridization function of the SIAM.

For small and intermediate distances the complexity of the problem is hidden in the energetic structure of the even/odd hybridization function, where for each $\underline{k}$ different spectral weight is shifted from one hybridization function to the other obeying relation (3.10).

Quantitatively this shift of spectral weight is shown in Figure 3.1, where the spectra of the hybridization functions are shown for a three dimensional simple cubic host lattice with $|V_k|^2 \equiv |V|^2 = 0.3$ and for impurity distances from $\underline{d} = 0$ to $\underline{d} = 20\underline{e}_i$ along one of euclidian the symmetry vectors of the lattice .
The even/odd hybridization functions roughly resemble the form of the SIAM hybridization function $\Delta(z)$ (which according to equation (3.11) is equal to the Δ^e function for $|\underline{d}| = 0$) but are modulated by oscillations with a characteristic wavelength roughly given by $\frac{d}{2}$. The large distance limit in equation (3.11) is already clearly visible for $\underline{d} = 6\underline{e}_i$.

The corresponding spectra of the one particle Greenfunctions obtained from the exact formulas (3.6) and (3.7) with $\epsilon^f_e = \epsilon^f_o = -1$ and $\Delta(0) = 0.3$ are shown in Figure 3.2.

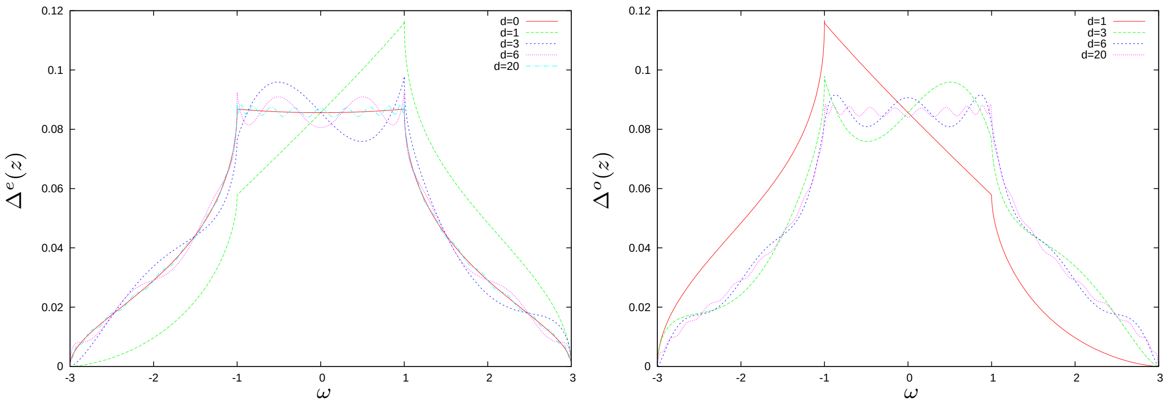

(a) (b)

Figure 3.1: Imaginary part of the hybridization functions $\Delta^e(z)$ (a), $\Delta^o(z)$ (b) for various impurity distances $\underline{d} = n\underline{e}_i$ along one of the euclidian symmetry axes $\underline{e}_i$ of the sc-lattice and $|V_{\underline{k}}|^2 \equiv |V|^2 = 0.3$.

The influence of the shifts and modulations of spectral weight in the hybridization functions become here visible in deviations of the resonant level position and the detailed shape of resonant level peak. Except for small distances i.e. for $d = 0, d = 1$ and $d = 2$ (not shown) case the differences seem to be rather small. Altogether in calculations with switched on Coulomb interactions these differences in the hybridization functions mediate the effective impurity-impurity interactions, and the findings here substantiate the evident physical expectation that these effective interactions are stronger for small distances.

For the SNCA/ENCA type approximations the $U = 0$ resonant-level regime represents a conceptual worst case scenario, as the included diagrams where chosen in order to describe properly the intermediate and large U case. For small U the crossing diagrams neglected become equally important as their non crossing counterparts, leading in some aspects to the failure of this approximations [Sch08]. This and the detailed arguments given in [Sch08] are also true for the SNCATI/ENCATI.

However, for the TIAM approximations the unphysical artefacts in the resonant level regime are of more interest than in the SIAM case. As already discussed in detail in chapter 2., the SNCATI/ENCATI treats processes involving the on site Coulomb interaction U on the same footing as processes involving the nearest impurity neighbor Coulomb interaction $\tilde{V}$. In cases where no $\tilde{V}$ is present, which is the generic case considered here, the approximation concerning $\tilde{V}$ is expected to behave much like the resonant-level $U = 0$ case for the SIAM approximations.
It is therefore worthwhile to inspect the resonant-level regime for the SNCATI/ENCATI as unphysical signatures seen here may also be visible in results calculated with non neglible U.

The ENCATI/SNCATI even/odd resonant level regime spectra in comparison with the exact solution are shown in Figure 3.3 for $d = 1$ with the same parameters as in Figure 3.2. The general shape of the approximated spectra is surprisingly close to the exact solution. Even the reminiscents of the van Hove singularities of the underlying host DOS are visible near $\omega = -1$.

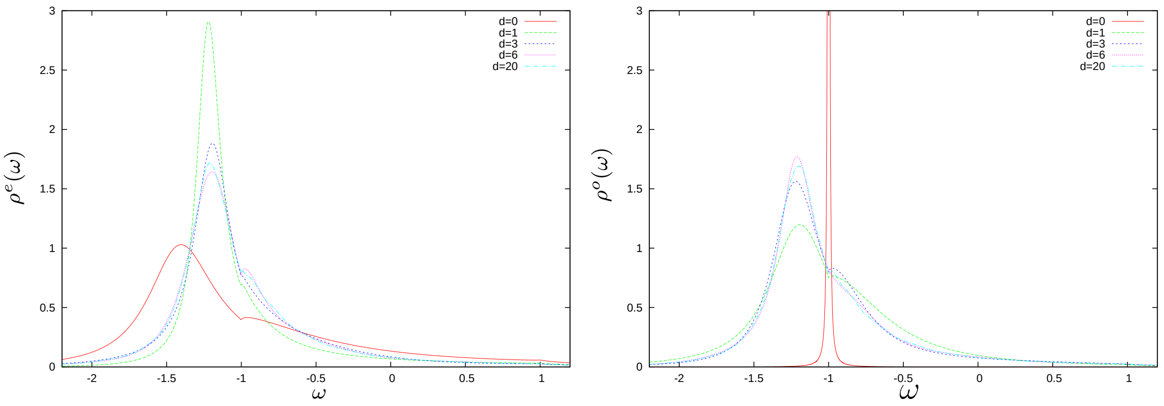

Figure 3.2: Spectra of the resonant level even/odd Greenfunctions $\rho^e(\omega) = -\frac{1}{\pi}Im(G_{f_e,f_e^\dagger}(\omega + i\delta))$ (left) and $\rho^o(\omega) = -\frac{1}{\pi}Im(G_{f_o,f_o^\dagger}(\omega + i\delta))$ (right) for various distances $|\underline{d}| \equiv d$ and $\epsilon_e^f = \epsilon_o^f = -1, \Delta(0) = 0.3$. The delta peak in the right picture for $d = 0$ is broadened by a small imaginary part.

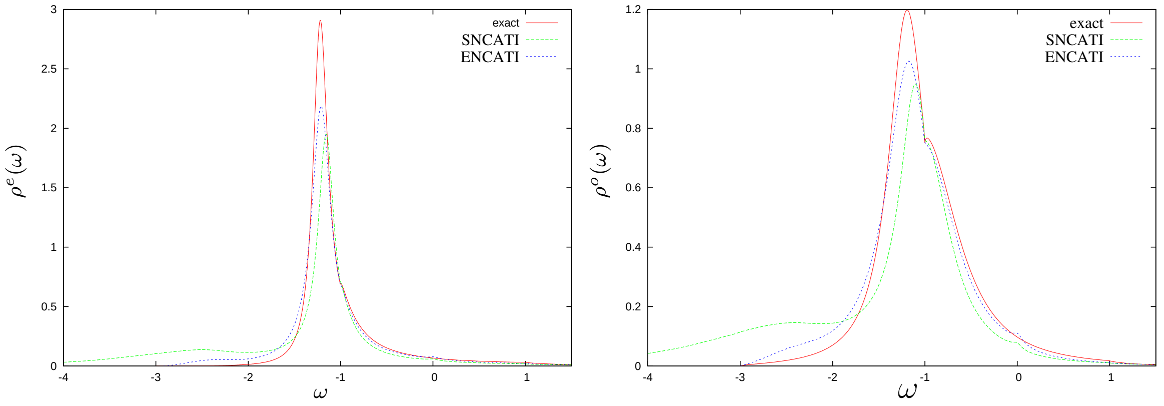

Figure 3.3: Spectra of the resonant level even (left) and odd (right) SNCATI/ENCATI Greenfunctions ρ^e, ρ^o for $|\underline{d}| = 1$. The other parameters are as in 3.2.

In the high energy region SNCATI and ENCATI have slightly less spectral weight than the exact solution and approximations both tend to develop the pathological NCA-spike discussed in [Gre83] at $\omega = 0$. By the virtue of the peak position in the spectra it seems that the ENCATI reproduces better the position of the renormalized ionic level position than the SNCATI. This type of behavior is also known from the SIAM resonant level solutions obtained from SNCA/ENCA [Sch08].

Unique to the TIAM approximations is that in comparison with the exact solution a large amount of spectral weight is shifted to lower energies. The form of this low energy tail indicates that this is not solely due to the structureless broadening tendencies of this approximations, but also due to the formation of a second unphysical peak near $\omega \approx -2.4$.
This is most noticeable in the SNCATI spectra. For ENCATI this peak is far more suppressed, but still clearly visible. In calculations - not shown here - with smaller Anderson-width this feature becomes more pronounced suggesting that its origin is due to the transition between states with relative sharp energies, which supports the interpretation of the forma-

tion of a peak in the low energy region.

The appearance of this peak is interesting because traces of it remain in all calculations with no direct nearest neighbor Coulomb interaction $\tilde{V}$, but with arbitrary values of the on-site Coulomb interaction U. This feature is directly related to the failure of the approximations to describe independent non coupled impurities. By choosing only a subclass of diagrams in the SNCATI/ENCATI approximation the eigenstates of the independent systems get mixed, with the result that unphysical transitions of this admixed states in the spectrum appear.
In case of the spectra depicted in Figure 3.3, the local ionic projection of the groundstate is expected to consist mainly of the ionic groundstate, which for $\epsilon^f < 0$ and $|\Delta| < |\epsilon^f|$ is the fully occupied 4 particle state ($E = 4\epsilon^f$), and some admixtures of the energetically neighbored three-particle states ($E = 3\epsilon^f$). Ionic states with lower occupation are energetically more separated from the ionic groundstate energy, which means their admixtures are expected to be small.
The spectrum, showing the transition energies to the adjacent particle sectors, should therefore show a main peak roughly situated at $\omega = \epsilon^f$ with about the width $\Delta\omega \approx \Delta$, but no spectral weight at $\omega = 3\epsilon^f$ as seen in the SNCATI/ENCATI calculations.

In Figure 3.4 the spectrum of the fully occupied propagator $-\frac{1}{\pi}Im(P_{22}(\omega + i\delta))$ is shown

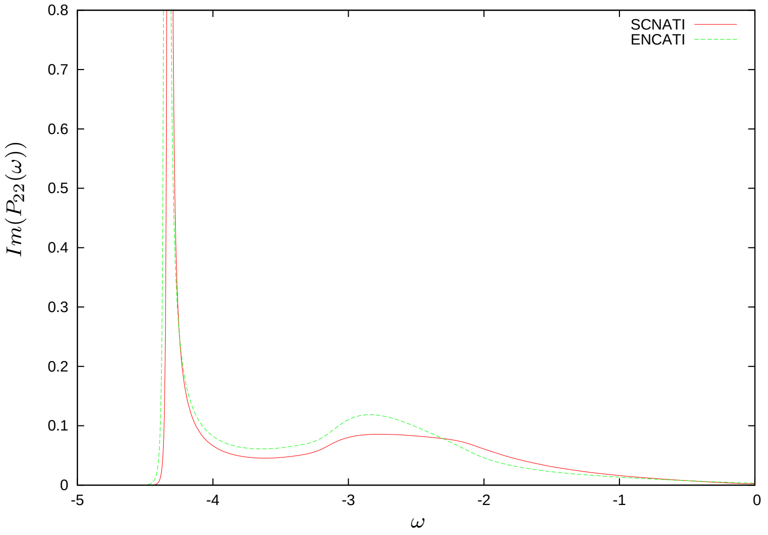

Figure 3.4: Spectrum of the doubly occupied ionic propagator $-\frac{1}{\pi}Im(P_{22}(\omega + i\delta))$ from SNCATI and ENCATI for $|\underline{d}| = 1$,$\epsilon^f = -1$ and $\Delta(0) = 0.3$ as in Figure 3.3. The peak at $\omega \approx -4.2$ exceeds the y-axis of the Figure and goes up to values of about 170.

from a SNCATI/ENCATI calculation with the same parameters as in Figure 3.3.
The spectrum shows - as expected - that the main spectral weight is concentrated in the peak near $\omega \approx 4\epsilon^f = -4$. In direct comparison the ENCATI peak is situated at a slightly lower energy. Further the propagator spectrum not only contains admixtures of the three-particle state at $\omega \approx -3\epsilon^f = -3$ but also non negligible spectral weight near the doubly occupied ionic state energies $\omega \approx 2\epsilon^f = -2$. This behavior is more pronounced for the SNCATI, while the ENCATI propagator spectral weight is more concentrated near the ionic

three-particle state energy, i.e. has less admixtures of the ionic two-particle states. As the one-particle Greenfunction is generated by convolutions of the ionic propagators, it is very likely that low energy tail in the Greenfunction can be traced back to this misbehavior of the ionic propagators.

3.3 TIAM without RKKY coupling

3.3.1 Uncoupled impurities

In case of large impurity distances $|\underline{d}|$ the inter-impurity hybridization function $\Delta_{\underline{d}}(z)$ becomes increasingly small and finally vanishes for infinite distances, leading to the decoupling of the two impurities. In that case the TIAM reduces to two independent SIAM's, and as was explained in section 2.5 it is a crucial point in the evaluation of any TIAM-solver how this limit is reproduced.
One has to keep in mind that the solution of the SIAM itself, due to the occurrence of infrared divergencies in perturbative expansions, is a highly nontrivial task which generally cannot be solved exactly. The various methods which attack this problem all have their assets and drawbacks and work reliable only in certain parameter regimes, or are called exact but fail to derive uniquely determined physical results from a discrete set of numerical exact data[Tro05]. It is therefore not reasonable to expect a TIAM-solver to be exact in the SIAM limit, the best achievable scenario is the reproduction of the corresponding SIAM-solver results.

It was shown in section 2.5 that both ENCATI and presumably more worse the SNCATI do not contain this limit exactly. The results and the comparison to SNCA/ENCA for the $U = 0$ resonant level regime in the previous section 3.2 already give a first impression of the possible extent of this failure in practical calculations. But for the resonant level limit the SNCA/ENCA are insufficient approximations, too. It is of much more interest to inspect the behavior of SNCATI/ENCATI in the low temperature large U regime, where SNCA and ENCA have proven to be reasonable approximations.

Apart from some exactly known relations a good benchmark for the SIAM is the comparison of TIAM-solver results against results from established SIAM-solvers. Due to their close relationship (see section 2.5), it is a reasonable procedure to compare ENCATI/SNCATI against their counterpart approximation for the SIAM, i.e. the SNCA/ENCA.
The ENCA/SNCA itself are very well studied, their assets and drawbacks against other SIAM-solvers and exact relations are known and will be not reviewed here. They can for example looked up in [Gre08] and the references therein.

In this work especially the behavior of the TIAM solver in the local moment regime $-\Delta < \epsilon_f \ll 0 \ll U$ is of interest. A good solver should there be able to produce a decent description of the Kondo-effect, i.e. the buildup of a low energy scale due to the screening of the impurity magnetic moment by itinerant host electrons.

Connected with the Kondo-effect is the occurrence of a common ionic threshold energy

E_g in the ionic propagators [Men88]

$$ImP_M(\omega - i\delta) \propto \frac{1}{(\omega - E_g)^{\alpha_m}} \tag{3.13}$$

with α_m the ionic threshold exponent [Noz69, Kur85c, Sch69]. The energy shift

$$\Delta E = E_g - \epsilon^f \tag{3.14}$$

with ϵ^f the energy of the unperturbed singly occupied ionic site, is a direct measure of the Kondo temperature, which for the SIAM in this regime is given by

$$[k_B]T_K = 2\pi a\sqrt{J}exp(-\frac{\pi}{J}) \text{ with } J = -\frac{2U\Delta}{\epsilon_f(\epsilon + U)} \tag{3.15}$$

and $a = min(U, W)$ where W denotes the bandwidth.

The ionic propagators obtained from the TIAM have the same algebraic structure as in equation (3.13), but since here two independent Kondo-effects take place the ionic threshold energy should be twice as small compared to the SIAM

$$E_g^{(TIAM)} = 2E_g^{(SIAM)}. \tag{3.16}$$

In order to make the energy shift due to the Kondo-effect from the TIAM directly comparable with the one from SIAM, it is defined as

$$\Delta E^{TIAM} = \frac{1}{2}(E_g^{TIAM} - 2\epsilon^f). \tag{3.17}$$

Figure 3.5 compares the threshold behavior of the different SIAM and TIAM approximations for $U = 3$ and $U = 6$. Shown are the spectra of the ionic propagators with one electron per impurity site. For the SIAM the ionic propagator spectrum is plotted relative to the unperturbed ionic energy level, i.e. $\frac{-1}{\pi}Im\left(P_\sigma(\omega + i\delta - \epsilon)\right)$ and for the TIAM in accord with equation 3.17, i.e. $\frac{-1}{\pi}Im\left(P_{\sigma\sigma';\sigma\sigma'}(\frac{1}{2}(\omega + i\delta - 2\epsilon))\right)$.
The peak positions thereby correspond directly to the energy lowering of the ground-state due to the Kondo-effect and are a measure of the Kondo temperature T_K.

The difference in the peak position is most distinct between SNCA and SNCATI, indicating that SNCATI has a much lower T_K than SNCA. The non-diagonal vertex correction terms in ENCATI seem to reduce the artificial inter-impurity correlations considerably and lead to an estimate of T_K which is in much closer accordance to the ENCA result. The artificial impurity-impurity correlations still lead to a weakening of the binding energy of the dynamic Kondo singlet and thereby to a lower T_K. In comparison the difference in T_K between SNCA/SNCATI and ENCA/ENCATI is larger than the difference between the SIAM- and the corresponding TIAM approximation, which is a good result concerning the quality of the TI-solvers.

It should be noted that the difference in the total spectral weight of TIAM propagators compared to the SIAM propagators is expected and no direct sign of weakness of these approximations. One has to recall, that the SIAM P_σ does not directly correspond to the

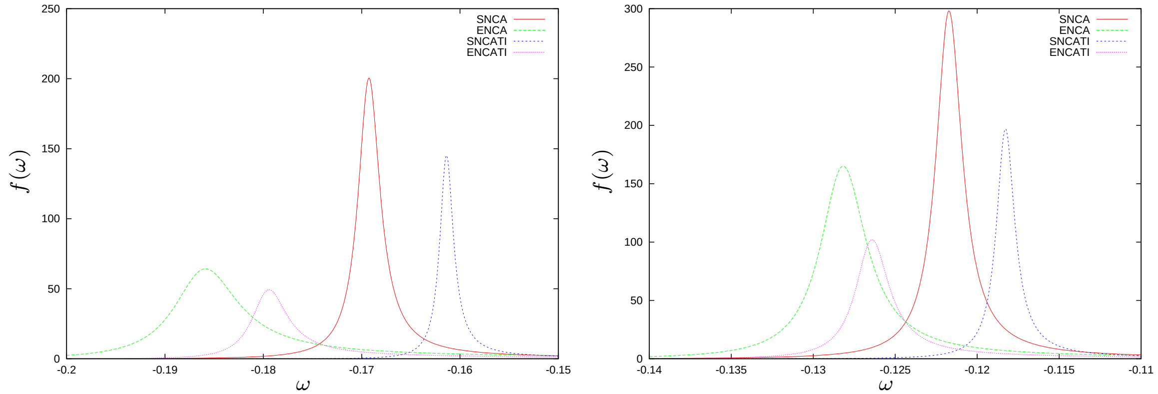

(a) $U = 3$

(b) $U = 6$

Figure 3.5: Comparison of the ionic threshold behavior of the TIAM and SIAM propagators for $U = 3$ and $U = 6$ with $\epsilon^f = -1.5$,$\beta = 100$ and $\Delta = 0.3$ for a 3 dimensional cubic lattice. For the SIAM the function $f(x)$ is defined as $f(x) = \frac{-1}{\pi} Im \left(P_\sigma(\omega + i\delta - \epsilon)\right)$, the ionic propagator spectrum for a singly occupied site. For the TIAM $f(x)$ is defined as $f(x) = \frac{-1}{\pi} Im \left(P_{\sigma\sigma';\sigma\sigma'}(\frac{1}{2}(\omega + i\delta - 2\epsilon))\right)$ the diagonal ionic propagator spectrum with one electron at each impurity. Note that only the peak positions of $f(x)$ are directly comparable (see text near equation (3.17), for a detailed explanation).

TIAM propagator $P_{\sigma\sigma';\sigma\sigma'}$. In $P_{\sigma\sigma';\sigma\sigma'}$ the occupation of impurity site two is fixed to a σ' electron, while the equivalent quantity P_σ deduced from the TIAM would implicitly contain an average over all possible occupations of the other impurity site.

P_σ and $P_{\sigma\sigma';\sigma\sigma'}$ are only comparable in the sense, that the real many-particle ground-state is predominantly build out of the ionic state with one electron per impurity site, and both these ionic propagators essentially describe the dynamics of the ground-state.

The close similarity in the shape of the SIAM and TIAM propagator visible in Figure 3.5 is therefore a rather encouraging feature for the quality of the TI-approximations.

In Figure 3.6 the resulting spectra for the same parameter set as in Figure 3.5 is shown. The spectra comply with the properties deduced from the ionic propagators.

In the low energy regime the Kondo-peak of the TI-approximations is less developed, the width and height of the ASR is about half the size of the peak in the corresponding SIAM approximation. For the half-filled $U = 3$ case the ENCATI has a higher Kondo-temperature than the SNCA, while for the asymmetric $U = 6$ case the Kondo-temperature of the ENCATI is on par with the one from the SNCA.

In summary, the quality of the ENCATI in the SIAM limit ranges between the ENCA and the SNCA, while the quality of the SNCATI in this limit is below the SNCA.

In the foregoing section 3.2 the calculations for $U = 0$ showed that the SNCATI tends to develop unphysical peak like structures in the high energy region. These unphysical flanks persist also for the $U \neq 0$ calculations and are especially pronounced for the particle-hole symmetric $U = 3$-case.

The flanks are not visible in the ENCATI, indicating that the leading order terms in the non-diagonal vertex corrections are sufficient to correct for this misbehavior. Unfortunately

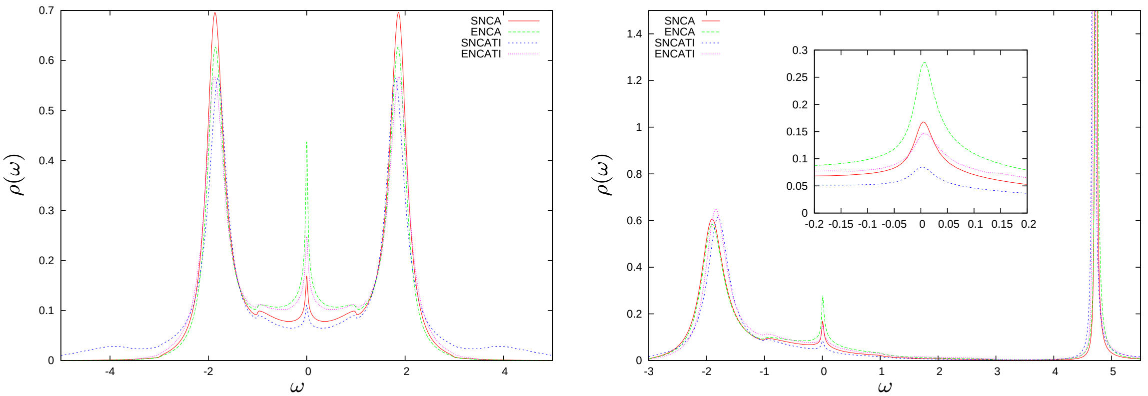

(a) $U = 3$ (b) $U = 6$

Figure 3.6: Corresponding spectra of the Greenfunctions $\rho(\omega) = -\frac{1}{\pi}Im(G(\omega))$ with the same parameters as in Figure 3.5. The inset shows the low-energy region around the Fermi level.

the ENCATI for many parameter sets has the tendency to overestimate these corrections, leading to a wrong sign of the imaginary part in the spectrum at these energies.

This is better seen in Figure 3.7, where the spectrum of the $\underline{\underline{\Sigma}}_U$ self-energy defined by

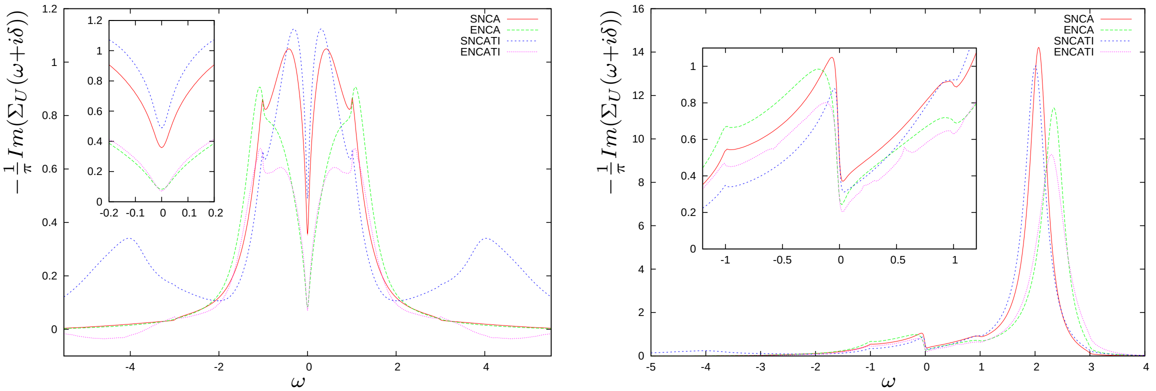

(a) $U = 3$ (b) $U = 6$

Figure 3.7: The imaginary part of the Σ_U self-energies deduced from the Greensfunctions shown in Figure 3.6. The inset shows the region around the Fermi level.

$$\underline{\underline{G}}(z) = \left[z - \underline{\underline{\epsilon}} - \underline{\underline{\Sigma}}_U(z) - \underline{\underline{\Delta}}(z)\right]^{-1} \qquad \text{or} \tag{3.18}$$

$$\underline{\underline{\Sigma}}_U(z) = \left(\underline{\underline{G}}(z)\right)^{-1} - z + \underline{\underline{\epsilon}} + \underline{\underline{\Delta}}(z) \tag{3.19}$$

is plotted. In the case considered here of two uncoupled impurities the matrix equation (3.19) for $\underline{\underline{\Sigma}}_U$ is diagonal and the TIAM Anderson-matrix-function

$$\underline{\underline{\Delta}}(z) = \begin{pmatrix} \Delta_0(z) & 0 \\ 0 & \Delta_0(z) \end{pmatrix}$$

on the diagonal contains the Anderson-width from the SIAM

$$\Delta(z) = \frac{1}{N} \sum_{\underline{k}} \frac{|V_{\underline{k}}|^2}{z - \epsilon_{\underline{k}}} = \Delta_0(z).$$

The SNCATI self-energy in the region around $|\omega| = 4$ shows a large scattering amplitude and the correction terms in the ENCATI self-energy lead to the described acausal behavior. In the $U = 6$ calculation this acausality is not present.
Whether this acausality stems from numerical errors or is a general unpleasant feature of the ENCATI approximation is not clear at the time of writing. A different numerical implementation of the ENCA for uncoupled impurities by Prof. Norbert Grewe shows similar acausalities, which makes a simple implementation error rather implausible.
On the other hand, due to the strongly peaked nature of the propagators and the two-dimensional vertex functions, it is always possible that the internal adaptive integration routines miss important contributions of the integrand. Much effort was spend by the author to rule out this possibility and as the shape and weight of these flanks persist even in calculations with largely increased numerical accuracy, it is more plausible that the acausality is an intrinsic feature of the ENCATI.

Nevertheless, the mid- and low-energy regions of the self-energy shows sensible physical behavior, which is in close accordance with the SNCA/ENCA self-energies. Both SNCATI and ENCATI show a quadratic minimum at the Fermi level, indicating the presence of a local Fermi-liquid phase due to the Kondo-effect[Hew93]. The ENCATI self-energy curve in the low energy region is very close to the ENCA result, which points to similar properties of the quasi-particles.
Larger differences are visible for the $U = 3$ calculation in the mid-energy region $|\omega| = 1-2$, corresponding to the ionic excitation energies $\Delta\epsilon = \pm 1.5$. The spectral weight of the ENCATI approximation is there strongly reduced. It seems that the same vertex correction terms, which correct the unphysical flanks of the SNCATI, also lead in the mid-energy region to a reduction of scattering events.
In the $U = 6$ calculation, where in the SNCATI the flanks are largely suppressed, the shape of SNCATI and ENCATI curves is much more similar to the ones from SNCA/ENCA. For ENCATI there is a small peak near $\omega = 0.5$ visible, which is unphysical but unfortunately also persists in calculations with higher numerical accuracy.

Figure 3.8 shows the magnetic excitation spectrum and the real part of the local magnetic susceptibility $\chi_{11}(z) = \langle\langle S_{z_1} S_{z_1} \rangle\rangle(z)$ for the different approximations and two different values of U. All curves show, that magnetic low-energy behavior is strongly influenced by the Kondo-effect. The spectra show in the real part at energies below the Kondo-temperature a strongly enhanced magnetic response, due to spin-flip excitations which are possible without destroying the Kondo screening cloud. For excitation energies below T_K the local Fermi-liquid is stable and the connected quasi-particles show in the real part Pauli-Paramagnetic behavior.

In comparison, the response for the two impurity approximations is a little weaker than for the corresponding SIAM theory. The magnetic excitation spectra depicted at the top of Figure 3.8 show a peak roughly situated at the Kondo-temperature.

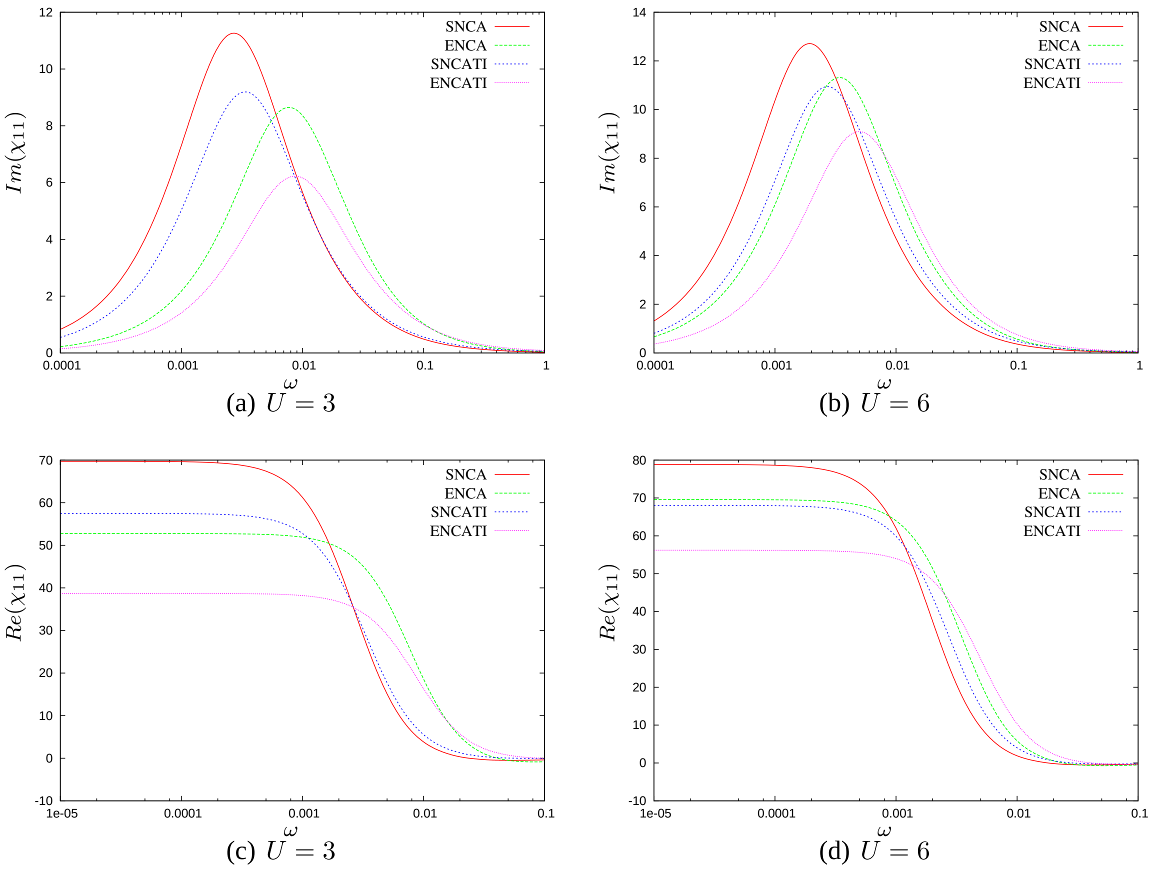

(a) $U = 3$ (b) $U = 6$

(c) $U = 3$ (d) $U = 6$

Figure 3.8: The real- and imaginary part of the one-site magnetic susceptibility for the different approximations and $U = 3$ and $U = 6$. The other parameters are the same is in Figure 3.5.

Surprisingly, the peak for SNCATI/ENCATI is situated at higher energies than for SNCA/ENCA. This is most notable in the $U = 6$ magnetic spectrum and is contrary to the finding so far, namely that the two-impurity approximations have a lower Kondo-temperature. The artificial correlations between the two impurity sites must therefore shift the magnetic response spectrum to higher energies in a way which does not imply a higher Kondo-temperature.

Unfortunately a further investigation of such a mechanism is hard to undertake. The artificial coupling between the two impurities cannot be measured by the calculation of non-local two-particle quantities like the non-local magnetic susceptibility $\chi_{12}(z) = \langle\langle S_{z_1} S_{z_2} \rangle\rangle(z)$. All non-local two-particle Greenfunctions contain at least one non-diagonal process, i.e. a non-diagonal band-propagation or a direct matrix element. These Greenfunctions are therefore exactly zero in the uncoupled limit.

On the other hand this is the correct limiting behavior for non-local two-particle quantities and the desired feature of a good TIAM-solver.

In Figure 3.9 a temperature scan for $\beta = 5{-}200$ with $\beta = \frac{1}{k_B T}$ is shown for the particle-hole symmetric $U = 3$ case. The changes in width and height of the ASR in SNCATI/ENCATI are very similar to the SNCA/ENCA. For nearly every temperature the ASR-peaks have about the same width, but for the two-impurity calculations the height is smaller by about a

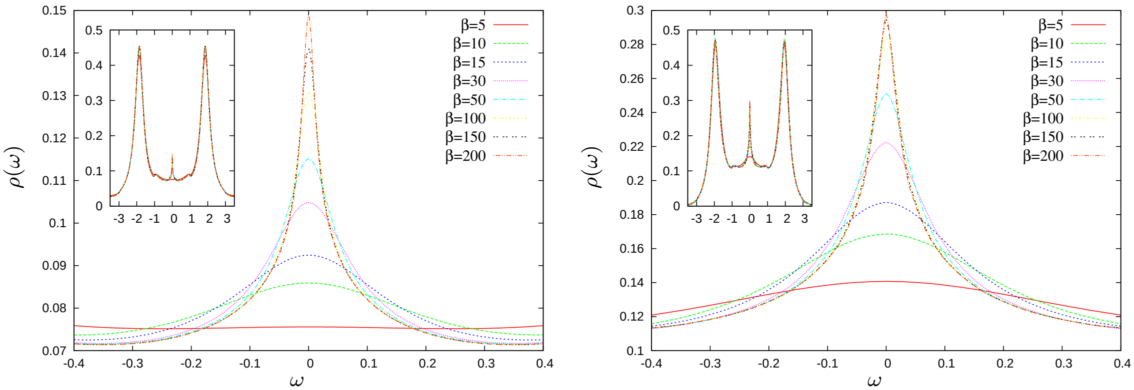

(a) SNCATI

(b) ENCATI

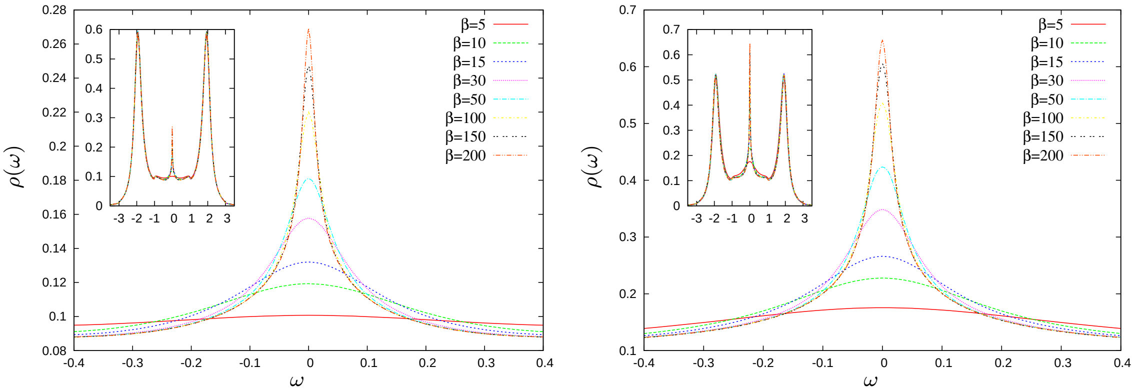

(c) SNCA

(d) ENCA

Figure 3.9: Temperature scan of the one-particle Greenfunction $\rho(\omega) = -\frac{1}{\pi} Im(G(\omega))$ for $U = 3$ calculated with (a) SNCATI, (b) ENCATI, (c) SNCA and (d) ENCA. The other parameters are the same as in Figure 3.5. The insets show magnifications of the region near the Fermi-energy.

factor two.

It seems that this reduction in the strength of the Kondo-effect by about a factor two is no coincidence. A plausible explanation for this fact could be, that within the two-impurity approximations the independent timelines of each impurity are condensed into one timeline. By incorporating only non-crossing diagrams in the self-energy in the SNCATI the number of allowed contributions for one impurity site is reduced. In about half the cases a process on one site is prevented to happen, as this - in combination with the process on the other impurity-site - would generate a crossing diagram.
This reasoning essentially also holds for the ENCATI, in which just the lowest order crossing diagrams are contained, i.e. a crossing diagram with electron lines starting and ending at the same impurity-site cannot be crossed by a further electron line starting and ending at the other impurity-site. Such processes would be contained in a two-impurity generalization of the FNCA, i.e. the incorporation of the ENCA-type vertex corrections up to infinite order.

3.3.2 Directly coupled impurities

In the Hamiltonian (2.1) the two impurities become coupled by two different mechanisms. On the one hand there is the hybridization $V_{\underline{k}i}$ between the impurities and band electrons which in the order $O(V^4)$ generates RKKY-like interactions between the impurities. These interactions depend strongly on the distance of the impurities and the details of the dispersion function of the host lattice electrons. In case of uncoupled impurities this hybridization for not too large coupling strengths $V_{\underline{k}\sigma}$ and $\epsilon^f \ll \epsilon_{fermi} \ll \epsilon^f + U$ also generates the Kondo-effect at low temperatures individually for each impurity.

Apart from the indirect coupling of the two impurities via the RKKY-like interactions generated by the hybridization term $V_{\underline{k}\sigma}$ of the impurity electrons with the c band electrons, the impurities can also be coupled by direct matrix elements for example by a direct hopping t or a direct exchange-coupling term J. The study of such a directly coupled system has the advantage that the correlations between the two sites mediated by these matrix elements can be adjusted independently from the hybridization strength $V_{\underline{k}i}$. In this section the influence of these direct couplings in absence of any RKKY-coupling is investigated. For the hybridization processes the impurities can be thought of as placed at an infinite distance, so that the RKKY-like interactions mediated via the band electrons vanish. The dynamics of the system is thereby solely governed by the competition between the local Kondo-effect and the impurity-impurity coupling through the direct matrix elements.
The focus in this section is especially on the inclusion of a hopping term t and an exchange-coupling term J. The J-term is of special interest because the RKKY-like interactions generate an effective energy dependent exchange coupling $J^{RKKY}(\omega)$ and a direct J can be seen as an approximation, helping to understand calculations which contain the full dynamics of this interaction. The study of the TIAM coupled by a direct hopping is especially interesting for the application of the TI-solver in the effective lattice theory presented in chapter 4. In this theory lattice sites are mapped to effective impurity sites and there at least the nearest neighbor sites are coupled by a direct hopping matrix element t.

It is also worth noting, that the setup described here can also be seen as the most simplest realization of a two-orbital single impurity model. Two equivalent s-shell orbitals are connected by local direct matrix elements and hybridize equally to the same host-DOS.

3.3.3 Ionic solution: V=0

By switching off the hybridization V the two-impurity model is reduced to the ionic model, i.e. two ions coupled by direct interactions. The Hamiltonian under consideration is

$$H = \sum_{i=\{1,2\},\sigma} \epsilon^f n_{i,\sigma} + t \sum_{\sigma} \left(f^\dagger_{1\sigma} f_{2\sigma} + f^\dagger_{2\sigma} f_{1\sigma} \right) + U \sum_i n_{i\uparrow} n_{i\downarrow} - J \underline{S}_1 \underline{S}_2. \tag{3.20}$$

The Fock-space of the two s-shells contains only up to four electrons and it is possible to solve the Eigenwertproblem of the Hamiltonmatrix analytically. For a proper discussion of calculations with hybridization, it is reasonable to review some exact results for the ionic system.
Of special interest is here the two-particle Hilbert-space. In the intermediate valence regime the ionic projection of the ground-state falls mainly in this Hilbert-space.

For the calculation of the low temperature one-particle excitation spectra the eigenstates of the neighboring one- and three-particle sectors are then also of interest, because according to the Lehmann formula for the one-particle spectrum

$$\rho_{\underline{k},\sigma}(\omega) = \frac{\hbar}{Z} \sum_{n,m} |\langle E_n | a_{\underline{k},\sigma} | E_m >^2 e^{-\beta E_n} \left(e^{-\beta\omega} + 1 \right) \delta(\omega - (E_n - E_m)), \tag{3.21}$$

only these sectors contribute. For low temperatures the contribution of the other sectors is suppressed by the exponential factors in equation (3.21).
For particle-hole symmetric systems the three-particle Hilbert-space can be exactly mapped onto the one-particle Hilbert-space. It is therefore sufficient to discuss only the one- and two-particle sector of the Fock-space.

The one particle Hilbert-space is spanned by the single-particle eigenstates of the two impurities $|\sigma, 0\rangle$; $|0, \sigma\rangle$. The two-particle interactions U and J have no effect in this sector. These states become mixed in the Hamilton-matrix by the hopping term t

$$\underline{\underline{H}}^{(1P)}_{\sigma} = \begin{pmatrix} \epsilon^f & t \\ t & \epsilon^f \end{pmatrix}. \tag{3.22}$$

The new eigenstates $|e\rangle, |o\rangle$ are the symmetric/antisymmetric linear-combinations of the single-particle impurity states

$$H^{(1P)}_{\sigma} |e\rangle = \left(\epsilon^f - t \right) \left[\frac{1}{\sqrt{2}} \left(|\sigma, 0\rangle - |0, \sigma\rangle \right) \right] \tag{3.23}$$

$$H^{(1P)}_{\sigma} |o\rangle = \left(\epsilon^f + t \right) \left[\frac{1}{\sqrt{2}} \left(|\sigma, 0\rangle + |0, \sigma\rangle \right) \right], \tag{3.24}$$

with the eigenenergies $E_o = \epsilon^f - t$ and $E_e = \epsilon^f + t$.

Far more interesting is the two-particle sector. There all matrix elements of the ionic Hamiltonian defined in equation (3.20) contribute to the Hamilton-matrix. As H commutes with the total Spin operator $[H, \underline{S}]$ with $\underline{S} = \underline{S}_1 + \underline{S}_2$, $\underline{S}$ is a good quantum number. $\underline{\underline{H}}^{(2P)}$ can therefore be decomposed into two uncoupled sub-blocks, with three different states in the (s=1) triplet block and three different states in the (s=0) singlet block. The three triplet states are

$$|s = 1, m = \sigma > \equiv |\sigma, \sigma\rangle \tag{3.25}$$

$$|s = 1, m = 0 > \equiv \frac{1}{\sqrt{2}} \left(|\uparrow, \downarrow\rangle + |\downarrow, \uparrow\rangle \right). \tag{3.26}$$

The triplet block of $\underline{\underline{H}}^{(2P)}$ is diagonal and the three eigenergies are degenerate

$$E_T = 2\epsilon^f - \frac{\hbar}{4} J \tag{3.27}$$

$$\underline{\underline{H}}^{(2P)}_{|s=1} = Diag\left(E_T \right). \tag{3.28}$$

The factor $\frac{\hbar^2}{4}$ in equation (3.27) from the exchange coupling term $\underline{S}_1 \underline{S}_2$ can be easily deduced from

$$S^2 |s = 1, m >= s(s+1)\hbar^2 |s = 1, m >= 2\hbar |s = 1, m >, \tag{3.29}$$

which is the same as

$$(\underbrace{\underline{S}_1^2+\underline{S}_2^2}_{\frac{3}{4}\hbar^2+\frac{3}{4}\hbar^2=\frac{3}{2}\hbar^2}+2\underline{S}_1\underline{S}_2)|s=1,m>=2\hbar|s=1,m> \tag{3.30}$$

and it follows

$$\underline{S}_1\underline{S}_2|s=1,m>=\frac{1}{4}\hbar^2|s=1,m> . \tag{3.31}$$

As expected, for ferromagnetic exchange coupling $J>0$ the energy is lowered for the triplet states.

The calculation of the eigenenergies of the three (s=0) singlet states

$$|S_1\rangle=|2,0\rangle\ ; \qquad |S_2\rangle=|0,2\rangle \tag{3.32}$$

$$|S_3\rangle=\frac{1}{\sqrt{2}}\left(|\uparrow,\downarrow\rangle-|\downarrow,\uparrow\rangle\right) \tag{3.33}$$

is a little more complicated, as the states become mixed by the hopping t. The singlet sub-block of $\underline{\underline{H}}^{(2P)}$ is

$$\underline{\underline{H}}^{(2P)}_{|s=0}=\begin{pmatrix} 2\epsilon^f+U & 0 & \sqrt{2}t \\ 0 & 2\epsilon^f+U & \sqrt{2}t \\ \sqrt{2}t & \sqrt{2}t & 2\epsilon^f+\frac{3}{4}\hbar^2\ J \end{pmatrix}. \tag{3.34}$$

The prefactor $\frac{3}{4}\hbar^2$ in the lower diagonal element of the singlet Hamiltonmatrix can be deduced by

$$S^2|S_3\rangle=(\underbrace{\underline{S}_1^2+\underline{S}_2^2}_{=\frac{3}{2}\hbar^2}+2\underline{S}_1\underline{S}_2)|S_3\rangle=s(s+1)\hbar^2|S_3\rangle=0|S_3\rangle \tag{3.35}$$

$$\underline{S}_1\underline{S}_2|S_3\rangle=-\frac{3}{4}\hbar^2|S_3\rangle. \tag{3.36}$$

The singlet eigenstates and eigenenergies are

$$H^{(2P)}_{|s=0}|E_0\rangle=E_0\left[\frac{1}{\sqrt{2}}\left(|S_2\rangle-|S_1\rangle\right)\right] \tag{3.37}$$

$$H^{(2P)}_{|s=0}|E_+\rangle=E_+\left[\frac{1}{N_+}\left(|S_3\rangle+a_+\left(|S_1\rangle+|S_2\rangle\right)\right)\right] \tag{3.38}$$

$$H^{(2P)}_{|s=0}|E_-\rangle=E_-\left[\frac{1}{N_-}\left(|S_3\rangle+a_-\left(|S_1\rangle+|S_2\rangle\right)\right)\right] \tag{3.39}$$

with

$$E_0=2\epsilon^f+U \tag{3.40}$$

$$E_\pm=2\epsilon^f+\frac{3\hbar}{8}J+\frac{1}{2}U\left(1\pm\sqrt{1+16\frac{t^2}{U^2}+\frac{9\hbar^2}{16}\frac{J^2}{U^2}-\frac{3\hbar}{2}\frac{J}{U}}\right) \tag{3.41}$$

$$a_\pm=\frac{t}{\frac{3\hbar}{8}J-\frac{1}{2}U\left(1\pm\sqrt{1+16\frac{t^2}{U^2}+\frac{9\hbar^2}{16}\frac{J^2}{U^2}-\frac{3\hbar}{2}\frac{J}{U}}\right)} \tag{3.42}$$

and the normalization factors $N_{\pm} = \sqrt{1 + 2a_{\pm}^2}$. If the largest energy scale is set by the local Coulomb interaction U, i.e. $U \gg t$ and $U \gg J$, the square-root in equation (3.41) and equation (3.42) can be expanded up to quadratic order, resulting in

$$E_+ = 2\epsilon^f + U + 4\frac{t^2}{U} \qquad E_- = 2\epsilon^f + \frac{3\hbar}{4}J - 4\frac{t^2}{U} \tag{3.43}$$

$$a_+ = \frac{\sqrt{2}t}{\frac{3\hbar}{4}J - U - 4\frac{t^2}{U}} \qquad a_- = \frac{U}{\sqrt{8}t}. \tag{3.44}$$

For $\epsilon^f < 0$ the energetically lowest lying states are $|E_-\rangle$, and the three degenerate triplet states with energy E_T. For anti-ferromagnetic exchange coupling, i. e. $J < 0$, or large t the groundstate is the $|E_-\rangle$-singlet. For $J > 0$ it depends on the strength of the hopping t if the singlet- or any linear-combination of the three degenerate triplet-states represent the ionic ground state. In the two-particle sector the direct hopping t acts as effective anti-ferromagnetic exchange coupling term $J^t = -4\frac{t^2}{U}$, leading to the effective exchange coupling $J^{eff} = J + J^t$ between the singlet and triplet states. So only if $J > |J^t|$ the groundstate is a triplet.

3.3.4 Direct exchange-coupling : J

The competition between the singlet and the triplet groundstate in the ionic-model, i.e between the anti-ferromagnetic and ferromagnetic tendencies, has very interesting consequences for the low energy properties of the full TIAM, i.e. with switched on hybridization term. The Kondo-effect for the SIAM originates from the screening of the impurity spin by the band electrons. The band electrons in the vicinity of the impurity build a dynamic singlet object with the impurity electron.
The spatial extent of this so called Kondo-cloud can be roughly estimated by $\zeta \propto \frac{v_F}{k_b T_K}$ with v_F the Fermi velocity and T_K the Kondo-temperature. Typical extents of the Kondo-cloud are of the order of $\zeta \approx 100 - 1000$ nearest neighbor site distances a [Bor09]. For not too large impurity distances these screening clouds overlap and mediate an effective coupling between the impurity electrons.

In the vicinity of the Kondo-regime, where the impurity electrons are well localized, this coupling consists mainly of RKKY-like interactions, i.e. only the impurity spins get coupled by an effective exchange interaction J. As a function of the distance J is typically an oscillating function, changing its sign from ferro- to anti-ferromagnetic values on the scale of a and its decay generally follows a $\frac{1}{|\underline{d}|^3}$ power-law behavior.
From the viewpoint of the ionic model with J interpreted as effective RKKY interaction, the degeneracy between the $|E_-\rangle$-singlet and the triplet states is lifted, and it depends on the distance of the impurities whether the ionic groundstate is a singlet or a triplet.

A strongly bound ionic singlet object on the other hand cannot coexist with the Kondo-effect. The electron spin at the impurity-sites is then already “screened” by the spin of the other impurity-site. The formation of the dynamic Kondo-singlet would imply the breakup of this ionic singlet. So the Kondo-effect is in competition with any anti-ferromagnetic coupling between the impurities. The calculation in the previous subsection 3.3.3 showed, that such an anti-ferromagnetic-coupling can also be caused by the direct hopping $J^t = -4\frac{t^2}{U}$. At least for the impurities situated at neighboring sites, it is sensible to include a direct hopping term in the model.

The situation is different for the triplet case. Here the two electrons build an object with spin one (the triplet) and a nonlocal Kondo-effect, the screening of the total spin of the combined two-impurity system, can take place. Even more, according to literature[San94, Jon87, Sim06] for ferromagnetic RKKY-interaction the Kondo-effect is believed to happen in two stages for such systems. At a first Kondo-temperature T_{K_1} the two impurity spin $s = 1$ is screened down to $s = \frac{1}{2}$ and at T_{K_2} a second Kondo-effect sets in, screening the remaining spin $s = \frac{1}{2}$ to $s = 0$. The two different temperature scales arise due to the different couplings to the band in the even/odd hybridization functions Δ^e, Δ^o defined in equation (3.8). The even and odd channel therefore have different exchange-couplings to the band J^e, J^o, which leads to the two different Kondo-temperatures $T_K(J^e)$ and $T_K(J^o)$. In the case considered here the impurities are coupled only by a direct exchange-coupling J and $\Delta^e = \Delta^o$ (see equation (3.11)) and a two-stage Kondo-effect for ferromagnetic J is not expected to take place.

A calculation of the spectral function of the TIAM for various ferromagnetic exchange couplings ($J > 0$) is shown in Figure 3.10. The spectra show only small differences in the high energy regions. No splittings occur and only small fractions of the spectral weight are redistributed in the that region. In direct comparison the ENCATI has more total spectral weight in the depicted region, but as explained in the previous section the SNCATI produces unphysical high energy flanks with relatively large spectral weight. For the calculation presented these flanks are situated near $|\omega| = 5$ which is beyond the range shown in Figure 3.10.

The changes due to the ferromagnetic exchange J mainly occur in the low energy regions, i.e. in the vicinity of the ASR. For small J the peak value of the ASR is reduced but maintains its overall width. If J comes in the region of the Kondo-temperature, i.e. is comparable to the half-width of the unperturbed ASR, a new feature emerges. In the flanks of the ASR gaps with small side-peaks are produced at $|\omega| = J$, while - in a much narrower region around the Fermi-edge - the ASR-peak sustains. With further increasing J the gap continues to grow and the side-peaks become smaller, while the width and height of the ASR does not change notably.

Qualitatively the ENCATI and the SNCATI show the same behavior. Due to the lower Kondo-temperature in the SNCATI the gap opens earlier and is a little more pronounced compared to the ENCATI. One has to remember that even in the unperturbed $J = 0$ case the SNCATI has far less spectral weight in the regions where the gap opens. It seems that the ordering mechanism leading to the gap is more effective with less scattering events or spectral weight in the background.

In order to eludicate the many-particle aspect of the side-peak formation Figure 3.11 shows the spectrum with $J = 0.05$ from Figure 3.10 for different temperatures in the vicinity of the Fermi-energy. The inset shows the uncoupled $J = 0$ spectrum with $\beta = 150$ for SNCATI and $\beta = 75$ for ENCATI.

The temperature range from $\beta = 5$ to $\beta \approx 40 - 80$ shows the formation of a single Kondo-peak. But in difference to the SIAM, because of $T_K < J$ this Kondo resonance is mainly

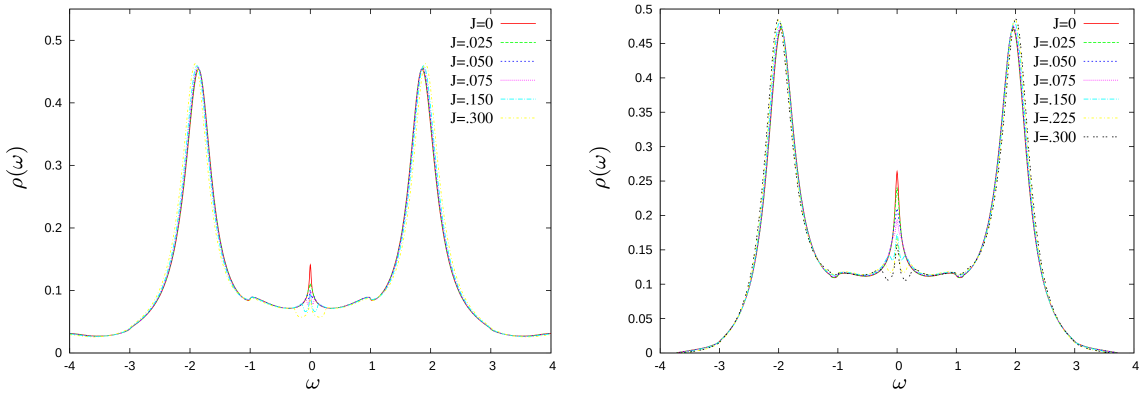

(a) SNCATI (b) ENCATI

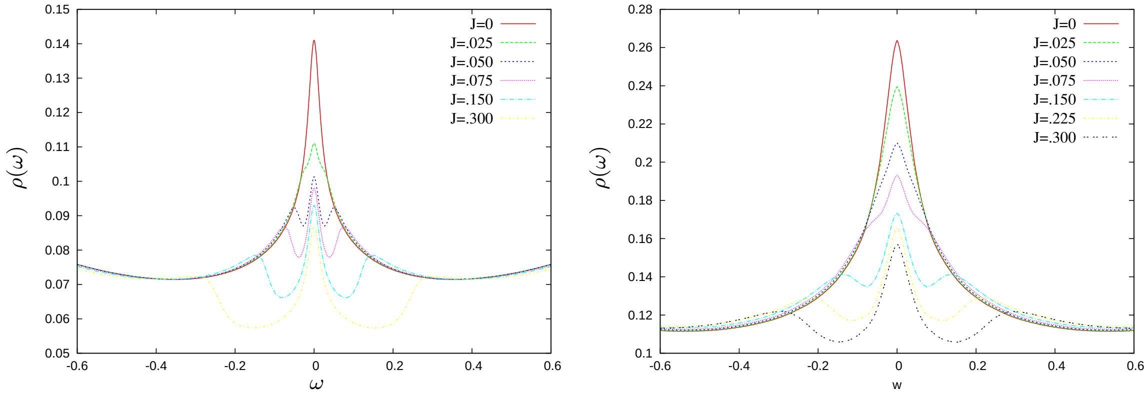

(c) SNCATI (d) ENCATI

Figure 3.10: Spectral functions for ferromagnetic $J > 0$ with $\epsilon^f = -1.5, U = 3, \Delta = 0.3$ for a 3D sc-lattice. The SNCATI spectrum (a),(c) was calculated for $\beta = 150$ and the ENCATI (b),(d) for $\beta = 75$. The two bottom pictures (c),(d) are magnifications of the region around the Fermi-energy. In both approximations a partial breakdown of ASR with increasing J becomes visible.

due to the screening of the Spin 1 ionic triplet states. This can be deduced from Figure 3.11(c) and Figure 3.11(d), which shows the expectation value of the ionic singlet $\langle n_S \rangle$ and triplet $\langle n_T \rangle$ occupation as function of β. The Kondo-screening cloud for the ferromagnetic TIAM is a nonlocal object involving both impurity sites. With decreasing temperature the ionic singlet state becomes de-populated in favor of the triplet states. For lower temperatures $\beta > 80$ $\langle n_S \rangle$ is stabilized and decreases not further. Correspondingly, the smaller side-peaks emerge in the spectra, which are separated from the main peak at $\omega = 0$ with about the energy of the ionic singlet/triplet splitting J.

The SNCATI/ENCATI results for the triplet ($S = 1$) Kondo-effect indicate that also for directly coupled impurities the Kondo-effect shows a two-staged behavior, due to the residual occupation of the ionic singlet. Below a second temperature scale singlet-triplet excitations with the energy J become visible in spectrum.

It is a nice feature of direct perturbation theory that expectation values of ionic occupations are accessible quantities, which can be calculated very easily. For example, the singlet

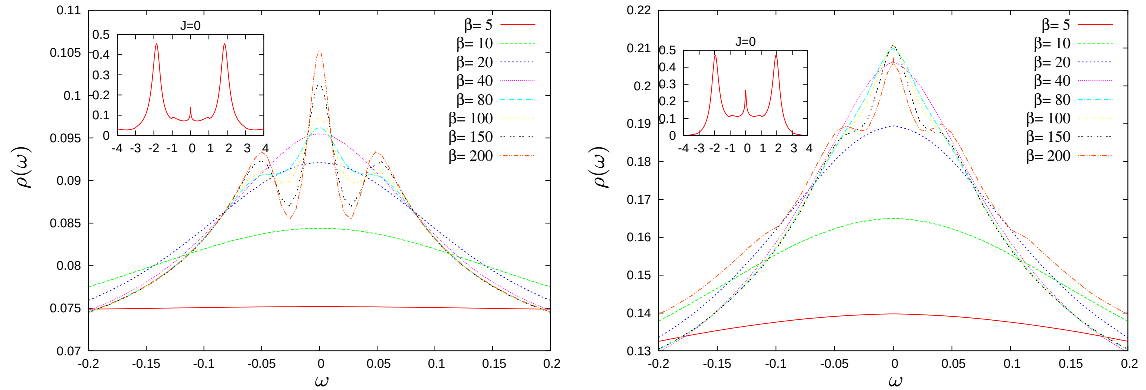

(a) SNCATI (b) ENCATI

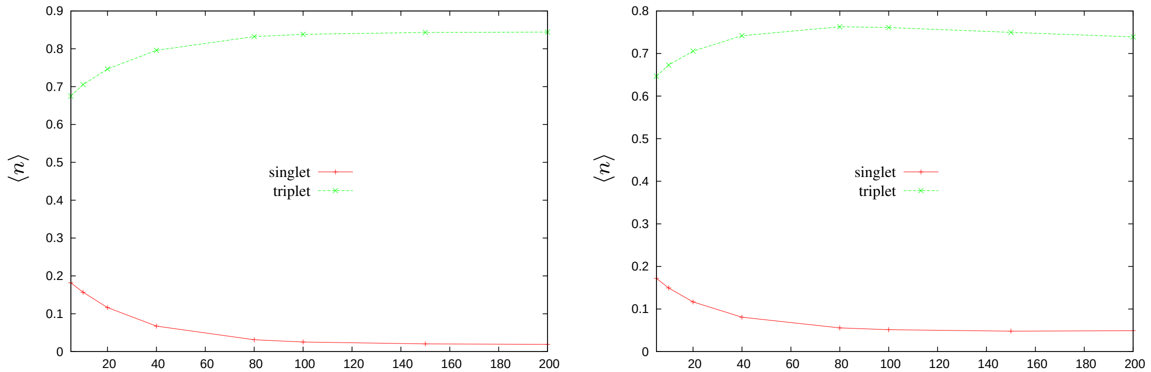

(c) SNCATI (d) ENCATI

Figure 3.11: Spectral functions near the Fermi-energy with ferromagnetic $J = 0.05$ for different temperatures. The other parameters are the same as in Figure 3.10. The inset shows for comparison an uncoupled spectrum, i.e. $J = 0$, with (a) $\beta = 150$ and (b) $\beta = 75$. The two bottom figures (c) and (d) show the expectation value of the ionic singlet/triplet occupation for these temperatures.

occupation value is given by

$$\langle n_S \rangle = -\frac{1}{Z} \sum_{\sigma} \oint \frac{dz}{2\pi i} e^{-\beta z} \left(P_{\sigma-\sigma;\sigma-\sigma}(z) - P_{\sigma-\sigma;-\sigma\sigma}(z) \right) \tag{3.45}$$

$$= \sum_{\sigma} \int d\omega \left(\zeta_{\sigma-\sigma;\sigma-\sigma}(\omega) - \zeta_{\sigma-\sigma;-\sigma\sigma}(\omega) \right), \tag{3.46}$$

with $\zeta_{M;M'}$ the ionic defect propagators defined in equation (2.50). The expectation value of the three triplet states can be calculated by

$$\langle n_T \rangle = \sum_{\sigma} \int d\omega \left(\zeta_{\sigma-\sigma;\sigma-\sigma;}(\omega) + \zeta_{\sigma-\sigma;-\sigma\sigma;}(\omega) + \zeta_{\sigma\sigma;\sigma\sigma}(\omega) \right). \tag{3.47}$$

The ionic expectation values for the singlet/triplet states from anti- to ferromagnetic values of the exchange coupling J are depicted in Figure 3.12. The other parameters are the same as in Figure 3.10, the temperature in both approximations is set to $\beta = 75$. For antiferromagnetic exchange coupling $J < 0$, it is the ionic singlet state which is predominantly occupied and the triplet state is depopulated. For $J = 0$ the singlet and triplet Eigenenergies

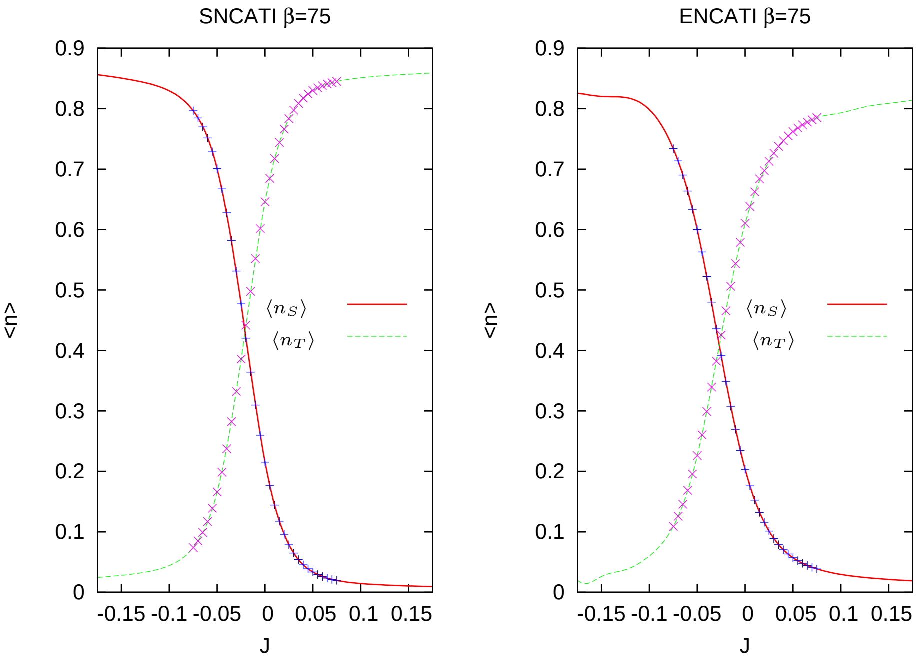

Figure 3.12: Ionic singlet ($\langle n_S \rangle$) and triplet ($\langle n_T \rangle$) occupation expectation values for anti- to ferromagnetic exchange J. The other parameters are the same as in 3.10.

are degenerate, and the states are evenly occupied. The opposite happens for ferromagnetic coupling $J > 0$, with the triplet as the predominantly occupied state. The crossing of the two regimes occurs exponentially on the scale of the temperature

$$\frac{\langle n_T \rangle}{\langle n_S \rangle} \propto e^{-\beta J}. \tag{3.48}$$

Note, that the combined occupation $\langle n_S \rangle + \langle n_T \rangle < \sum_\sigma \langle n_\sigma \rangle$, where for half filling $\sum_\sigma \langle n_\sigma \rangle = 1$. In Figure 3.12 $\langle n_S \rangle + \langle n_T \rangle \approx 0.85$, the missing 0.15 fall upon the occupation of the other ionic states, e.g. predominantly the singly occupied state.

Figure 3.13 shows for various anti-ferromagnetic exchange couplings $J < 0$ the spectral functions. Similar to the ferromagnetic spectra in Figure 3.10 the high energy features of the spectra change only slightly. The outer peaks gain a little more weight and are shifted with decreasing J. This is mainly due to the breakdown of the ASR and the opening of a gap in the low energy spectrum. The spectral weight of the gap is redistributed to the high energy peaks. The breakdown of the ASR indicates the strong presence of the ionic-singlet state. The impurity-spins screen each other gaining the energy $|J|$. For energies or temperatures below $|\omega| < |J|$ the energy is not sufficient to break up the ionic singlet state, which would be a necessary condition for the Kondo-effect to take place. The visible gaps in Figure 3.13 with about the width J show this breakdown of the ASR.

For small J, the effective anti-ferromagnetic Kondo-coupling in equation (2.35) between the impurity and the band-electrons is larger than the direct impurity-impurity coupling and the Kondo-effect is energetically more favorable than the buildup of the ionic singlet. The ASR is only weakened in that regime.

If the direct anti-ferromagnetic coupling out-weights the Kondo-coupling a gap of width J

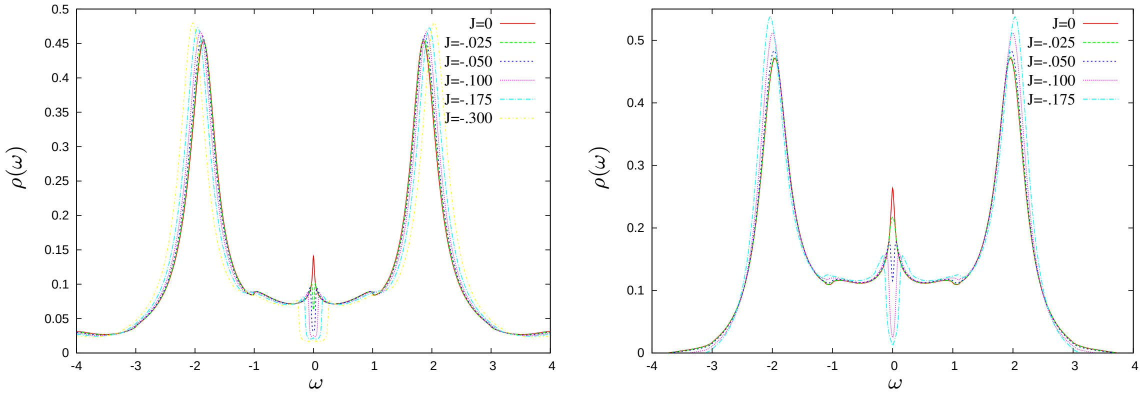

(a) SNCATI (b) ENCATI

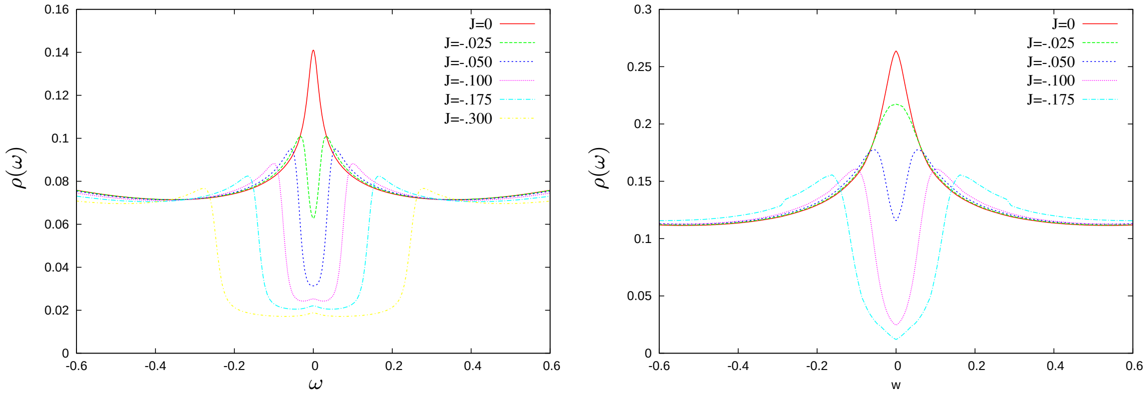

(c) SNCATI (d) ENCATI

Figure 3.13: Spectral functions for anti-ferromagnetic $J < 0$ with $\epsilon^f = -1.5$,$U = 3$,$\Delta = 0.3$ for a 3D sc-lattice. The SNCATI spectrum was calculated for $\beta = 150$ and the ENCATI for $\beta = 75$. The two bottom pictures (c),(d) are magnifications of the region around the Fermi-energy. In both approximations a a breakdown of the ASR with increasing J becomes visible.

opens. Interestingly even for relatively large J the borders of the gaps show an increased DOS, which follow in shape the form of the flanks of the uncoupled ASR.

Figure 3.14 shows the spectrum for fixed $J = -0.05$ for different temperatures. For decreasing temperatures the gap becomes more pronounced and the peaks at the borders of the gap become larger. The strong temperature dependence of the side-peaks support their interpretation as reminiscents of the ASR. Figure 3.15 shows in the top picture the nonlocal static magnetic susceptibility $\chi_{12}^{stat.} = Re\,(\langle\langle \underline{S}_1 \underline{S}_2 \rangle\rangle(0 + i\delta))$ versus J, and in the two bottom pictures the corresponding dynamic magnetic excitation spectra for the two approximations SNCATI and ENCATI.

Note that, like the non-diagonal one-particle two-impurity Greenfunction G_{12}, the nonlocal magnetic excitation spectrum of $\chi_{12}(z)$ has no definite imaginary part and the sign of the $\chi_{12}^{stat.}$ indicates ferromagnetic or anti-ferromagnetic coupling. In accordance with the findings in this section, for ferromagnetic $J > 0$ coupling there is a broad magnetic resonance corresponding to the Kondo-effect. The emergence of the three-speak structure in the FM-spectra in Figure 3.10 becomes visible in the magnetic spectra in the smaller excitation

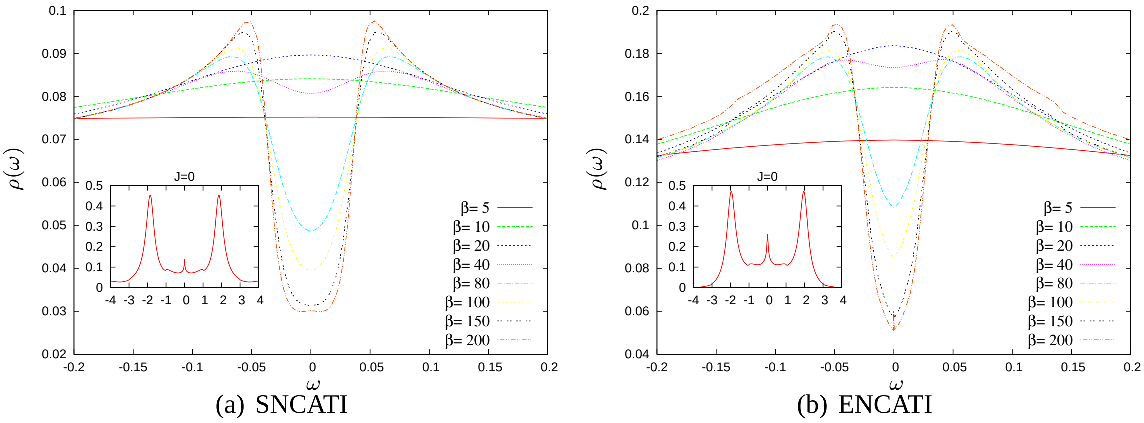

(a) SNCATI (b) ENCATI

Figure 3.14: Spectral functions near the Fermi-energy with anti-ferromagnetic $J = -0.05$ for different temperatures. The other parameters are the same as in Figure 3.13. The inset shows for comparison an uncoupled spectrum, i.e. $J = 0$, with (a) $\beta = 150$ and (b) $\beta = 75$.

peaks near the energy J. For AF-coupling only these excitation peaks survive and get narrower for larger anti-ferromagnetic exchange J. In accordance with magnetic spectra, the static susceptibility shows a FM-response for positive J and the AF-response for negative J. In comparison the ENCATI has much wider peaks and features as the SNCATI. This behavior is due to higher Kondo-temperature of the triplet $S = 1$ Kondo-effect in ENCATI. This becomes visible by the broad magnetic resonance peak near $\omega \approx 0.01$, which is at a higher energy and much larger then the corresponding SNCATI feature at $\omega \approx 0.003$. The ionic singlet-triplet excitations are thereby much more influenced by the Kondo-excitations, leading to broader structures in the spectra.

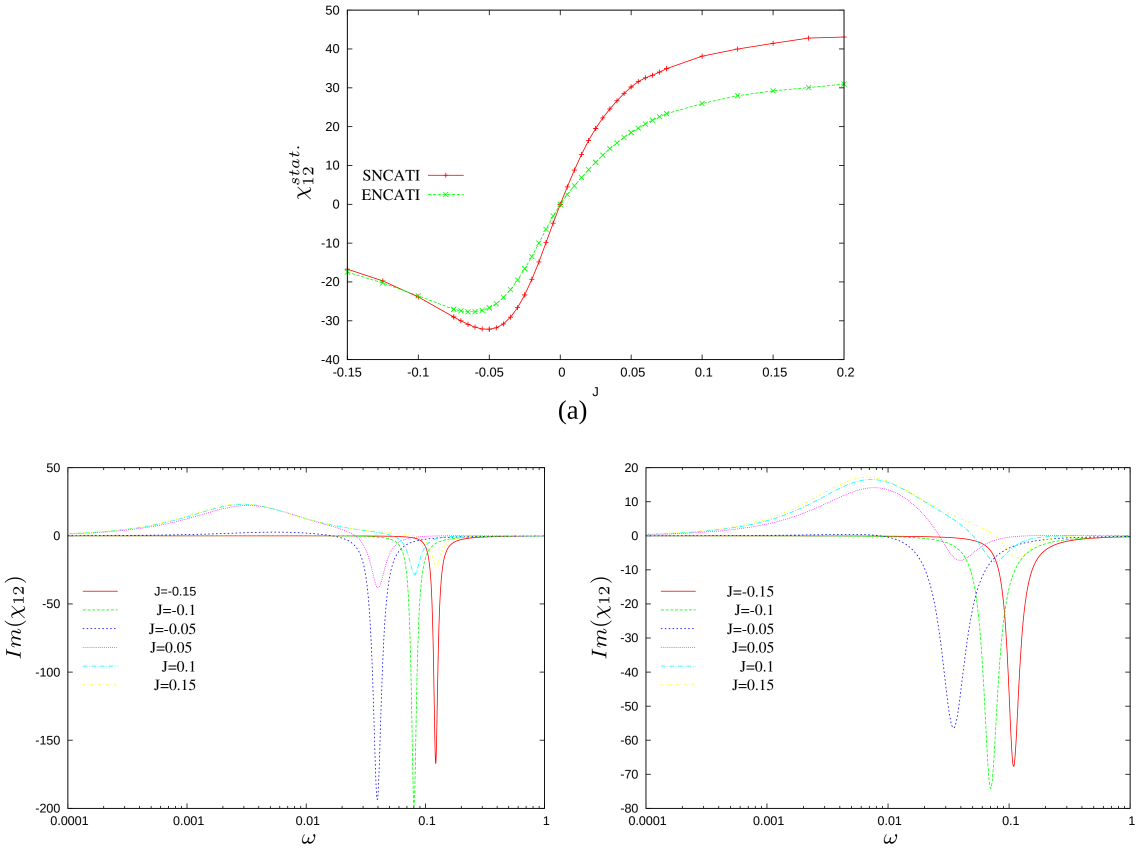

(a)

(b) SNCATI

(c) ENCATI

Figure 3.15: (a) shows the nonlocal static magnetic susceptibility $Re(\chi_{12}(0))$ vs. the exchange J, (b) and (c) the spectrum of the dynamic magnetic susceptibility $\chi_{12}(\omega) \equiv Im(\chi_{12}(\omega + i\delta))$ for SNCATI/ENCATI and different J. The inverse temperature is $\beta = 75$ and the other parameters are as in Figure 3.10.

3.3.5 Direct hopping t

The evaluation of the ionic solution of the TIAM in subsection 3.3.3 has shown, that a direct hopping t between the two impurities leads to an energy reduction of the lowest lying singlet state $|E_-\rangle$ defined in equation (3.39) of the order $\Delta E = 4\frac{t^2}{U}$. The degeneracy of this ionic singlet state with the ionic triplet states 3.25 is thereby lifted. Therefore the quantity $\frac{t^2}{U}$ can also be interpreted as effective anti-ferromagnetic exchange coupling term $J^t \equiv -4\frac{t^2}{U}$. In that sense, the situation is very similar to the TIAM with anti-ferromagnetic direct exchange coupling J, which was discussed in the last subsection 3.3.4.

But the hopping t also modifies the eigenstates of the adjacent ionic one- and three-particle sector, where t leads to a level splitting between the bonding and anti-bonding state with energy difference $\Delta E = 2t$ (see subsection 3.3.3). This certainly modifies the high energy features of the TIAM, but no simple guess can be made for the low energy features and the competition with the Kondo-effect. A minimal frame for the occurrence of a Kondo-effect in the TIAM is achieved for $U \longrightarrow \infty$, i.e. the case when SNCATI/ENCATI reduce to the NCATI and only the zero-, one- and the non-interacting part (i.e. one electron per site) of the two-particle sector in the ionic Fock-space participate in the dynamics of the model.
In this limit the Kondo-effect is essentially produced by subsequent particle-hole excitations from the two-impurity state with one electron at each site to the state with only one electron at one impurity site and back. The self-energy Diagram 3.16 depicts such a process.

For the TIAM with hopping, the ionic two-particle Eigenstates are the singlet- and the triplet-state and particle-hole excitations lead to intermediate bonding/antibonding one-particle states of the two impurities. One can therefore expect, that apart from the singlet-triplet splitting the direct hopping t also modifies the character of the Kondo-effect.

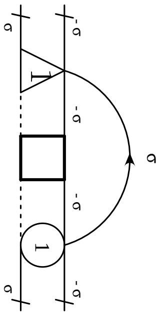

Figure 3.16: Generating self-energy of the Kondo-effect in the NCATI.

The results in this subsection will be presented in close analogy to the ones obtained with direct exchange coupling J in the preceding subsection 3.3.4. Therefore - unless differently stated - the model parameters are again $\epsilon^f = -1.5$, $U = 3$, $\beta = 75$ and $\Delta = 0.3$ for simple cubic lattice in three dimensions and the impurities not coupled by hybridizations to the band, i.e. situated at an infinite distance.

Figure 3.17 shows for different values of the hopping t the spectral functions for SNCATI and ENCATI. It becomes obvious that the direct hopping t also affects the high energy re-

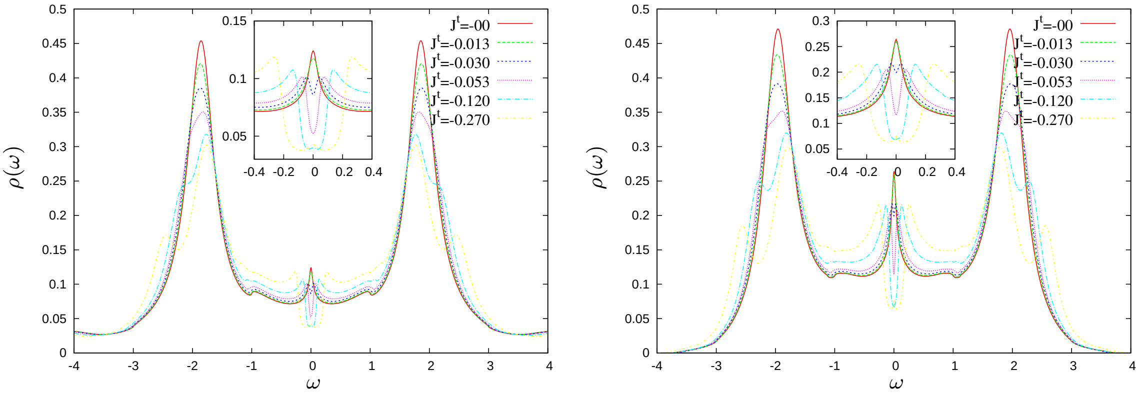

(a) SNCATI (b) ENCATI

Figure 3.17: Spectral functions for different t and $\epsilon^f = -1.5$, $U = 3$, $\beta = 75$ and $\Delta = 0.3$. The inset shows the region around the Fermi-edge. The J^t values correspond in the given order to $t = 0,\ 0.1,\ 0.15,\ 0.2,\ 0.3,\ 0.5$

gions in the spectrum. The high energy resonances split up, the larger peak moves towards lower energies and the smaller peak towards higher energies with inreasing t. The width of the gap between these two peaks increases linearly with t and is more pronounced for the ENCATI calculation.

This is at first a bit surprising as features in ENCA/ENCATI are generally more broadened compared to the SNCA/SNCATI. On the other hand, in the perturbative expansion undertaken in these approximations the hopping t is treated effectively as non-diagonal term. The ENCATI by inclusion of vertex corrections includes also a better treatment of the processes which involve t in combination with the hybridization V.

As mentioned already, from the viewpoint of the ionic solution of the TIAM the occurrence of a high energy gap is no surprise. The hopping lifts the degeneracy between the even/odd or bonding/anti-bonding linear combinations in the ionic one- and three-particle sector by the energy $\Delta E = 2t$. In the spectra this difference becomes visible in the transition energies between the ionic two-particle and the one- and three-particle sector. For the low energy region, the spectra show a behavior similar to the spectra with anti-ferromagnetic exchange $J < 0$ in subsection 3.3.4.

Beyond a critical hopping $t > t_{crit}$ a gap opens and the original Kondo-effect near $\omega = 0$ breaks down. Figure 3.18 shows the ionic singlet- and triplet-occupation expectation values $\langle n_s \rangle, \langle n_T \rangle$. For t below t_{crit} the singlet- and triplet-occupation values are stabilized by the Kondo-effect and a breakdown of the triplet occupation in favor of the singlet occurs for $t > t_{crit}$. For large t the singlet occupation drops again, while the triplet occupation decreases further. This is due the bonding state $|E_{-}\rangle$ from the ionic one-particle sector with $E_{=}\epsilon^f - t$, which for large t becomes energetically closer to the singlet state and gets more populated.

A more detailed inspection of the low-energy features of the spectra reveals drastic differences to the spectra with direct anti-ferromagnetic coupling depicted in Figure 3.13. For a better comparison in Figure 3.19 the spectra with direct exchange $J = -0.05$ and a hopping induced exchange coupling $J^t = -4\frac{t^2}{U} = -0.05$ are presented. The split-up of the high-

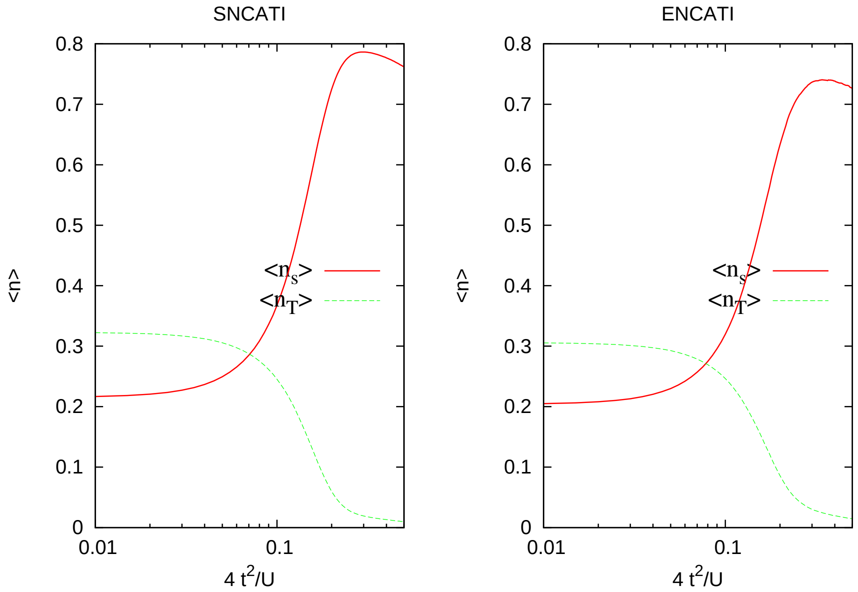

Figure 3.18: Ionic singlet-triplet expectation values $\langle n_s \rangle$, $\langle n_T \rangle$ for SNCATI and ENCATI.

energy peaks for the spectra with switched on hopping leads to more spectral weight in the central region. The gap is about the same size, but the peaks adjacent to the gap contain more spectral weight and are much wider. Additonally, in contrast to the spectra with direct J, the peaks do not follow the shape of the flanks of the original uncoupled $J = 0,\ t = 0$ Kondo-peak. The inspection of the gap-width W_{gap} as function of the hopping induced exchange coupling J^t undertaken in Figure 3.20 reveals, that only for large J^t the gap opens linearly with J^t. For small J^t beyond a critical value $J^t_{crit} \approx= 0.01$ the opening shows a squareroot behavior, i.e. $W_{gap} \propto t$ for small $t > t_{crit}$. An Ansatz for the gap function in the form $W_{gap}(t) = at^* + 4\frac{(t^*)^2}{U}$ also depicted in Figure 3.20 is in close agreement with the numerical data, where $t^* \equiv t - t_{crit}$ and a is a free fitting parameter accounting for the renormalized dispersion of the quasiparticles.

Both SNCATI and ENCATI show qualitatively the same behavior in the gap function. Connected to the higher Kondo-temperature of the ENCATI the critical hopping t_{crit} is a bit larger for this approximation.
The results, so far, at least for small t point to the strong influence of the ionic bonding/antibonding one-particle states for the low-energy features of the spectra. The question arises, whether in the linear regime of the gap function the Kondo-effect really breaks down. The strong presence of the side-peaks could also indicate the split-up of the Kondo-peak in a bonding and an antibonding Kondo-resonance. One also has to keep in mind, that in effective lattice theories, namely the DMFT, the quasiparticles formed by the lattice Kondo-effect are particles with a $\underline{k}$-dependent dispersion function $\epsilon^{QP}(\underline{k}) \neq const.$.
From that point of view the antibonding/bonding one-particle states in the TIAM can be associated with the $k = -\pi$ and $k = 0$ states in a lattice with two sites and effective media given by the Anderson-matrix $\underline{\underline{\Delta}}$. This picture coincides with the odd/even Greenfunctions $G(k = -\pi) \equiv$ and G_o $G(k = 0) \equiv G_e$ defined in the discussion of the TIAM resonant-level limit in section 3.2. In terms of the one-particle Greenfunctions for the ionic

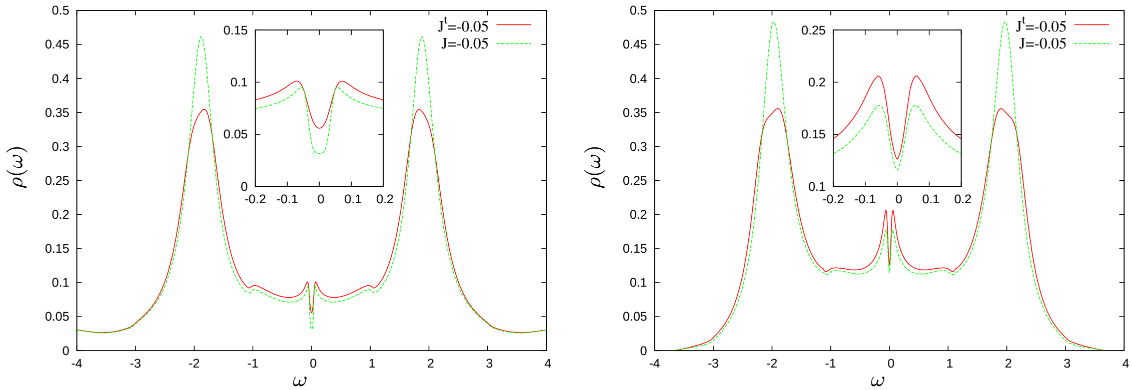

(a) SNCATI (b) ENCATI

Figure 3.19: Comparison of the spectral functions with direct exchange coupling $J = -0.05$ and hopping induced effective exchange coupling $J^t = -4\frac{t^2}{U} = -0.05$

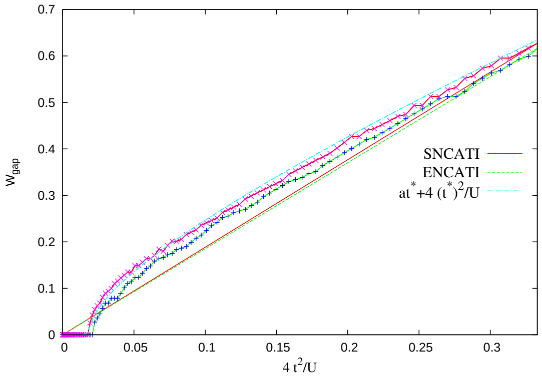

Figure 3.20: Width of the central gap over the hopping induced exchange coupling $4\frac{t^2}{U} = -J^t$ for SNCATI and ENCATI. The blue dash-dotted curve shows a fitting ansatz $W_{gap}(t^*) = at^* + 4\frac{(t^*)^2}{U}$ with $t^* \equiv t - t_{crit}$ and $a = 0.65$ a fitting parameter accounting for the renormalized effective hopping of the low-energy Quasiparticles .

f-operators $f^\dagger_{i,\sigma}$, $f^{i,\sigma}$ used so far, the odd/even one-particle Greenfunctions are given by

$$G_o(z) = \frac{1}{2}\left(G_{1,1}(z) + G_{2,2}(z) - G_{1,2}(z) - G_{2,1}(z)\right) = G_{1,1}(z) - G_{1,2}(z) \tag{3.49}$$

$$G_e(z) = \frac{1}{2}\left(G_{1,1}(z) + G_{2,2}(z) + G_{1,2}(z) + G_{2,1}(z)\right) = G_{1,1}(z) + G_{1,2}(z), \tag{3.50}$$

where for the last identity $G_{1,1} = G_{2,2}$ and $G_{1,2} = G_{2,1}$, i.e. identical impurities, are assumed. The result of the even/odd transformed spectra with $J^t = -0.05$ from Figure 3.19 is shown in Figure 3.21. The odd spectrum shows only the $\omega < 0$ side-peak, while the upper $\omega > 0$ peak is strongly suppressed. The even spectrum has the opposite configuration with a large $\omega > 0$ side-peak and a suppressed $\omega < 0$ peak. This finding is in accordance with the interpretation of the odd-states as the the bonding band-states and the even-states as the anti-bonding band-states. It should further be noted, that the even/odd spectra for the TIAM with direct J, which are not presented here, do not show this kind of behavior. For direct J the even spectrum is equal to the odd spectrum. Another indicator for the presence of

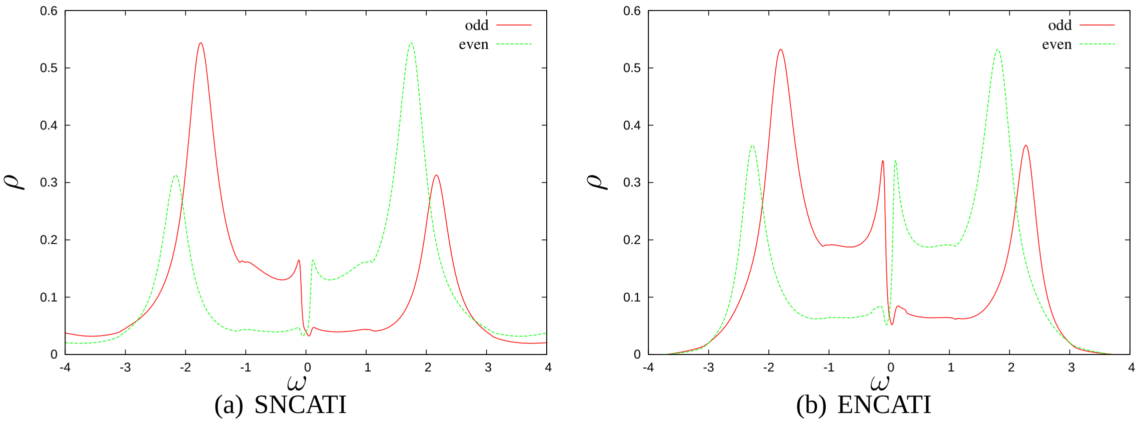

(a) SNCATI (b) ENCATI

Figure 3.21: Spectra of the even/odd impurity Greenfunctions with $J^t = -0.05$, i.e $t = 0.273$, for SNCATI (a) and ENCATI (b).

an odd/even Kondo-effect can be deduced from the on-site magnetic susceptibility $\chi_{11}(z)$ shown in Figure 3.22.

There the excitation spectrum of the local magnetic susceptibility is plotted versus J^t

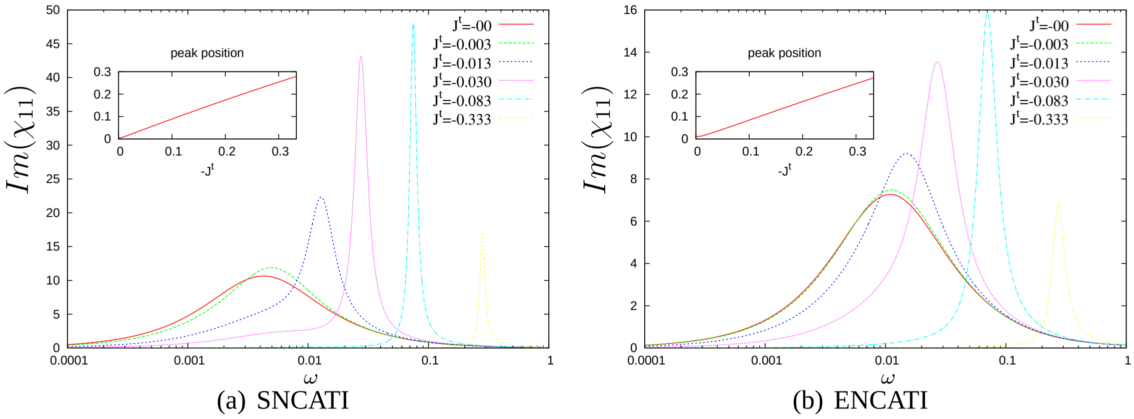

(a) SNCATI (b) ENCATI

Figure 3.22: Magnetic excitation spectrum for the on-site magnetic susceptibility $\chi_{11}(z)$ for different hoppings t. The inset shows the position of the excitation peak versus the effective hopping induced exchange coupling $J^t = -4\frac{t^2}{U}$, except for very small J^t, the curve shows a perfect linear behavior with gradient one.

on a logarithmic scale. For $J^t = 0$ a low lying resonance due to the spin-flip scattering events of the Kondo-effect is visible. For switched on effective exchange coupling the main peak moves on the scale of J^t to higher energies, while for not too large J^t some spectral weight sustains at the excitation energy of the Kondo-effect. Gradually, for increasing $|J^t|$ this spectral weight vanishes and only the peak at J^t sustains.

In the insets of Figure 3.22 the position of the main peak as function of $-J^t$ is depicted. It shows for both approximations a perfect linear dependence of the magnetic resonance with the hopping induced exchange coupling J^t. This behavior confirms that for the magnetic properties no term linear in the hopping t contributes. This is another indicator, that the linear t^*-term in the gap function $W_{gap}(t^*)$ originates from the level repulsion of the ionic one-particle states.

In summary the low energy features of the TIAM with hopping t are essentially determined on the one hand by the anti-ferromagnetic singlet-triplet splitting of the ionic two-particle sector which is of the order $\propto t^2$ and on the other hand by the level repulsion of the quasiparticles, which is an effect linear in t. The strong presence of the side-peaks for small t indicates, that the Kondo-effect is not destroyed by this repulsion. The Kondo-effect only changes its character to a minimalistic version of a lattice Kondo-effect with two k-modes $(-\pi, 0)$ for the effective quasiparticles.

3.4 TIAM with RKKY coupling

In the preceeding section 3.3 the TIAM was investigated for the impurities at an infinite distance, i.e. switched off RKKY interaction . The impurities were coupled only by direct couplings t and J in the ionic Hamiltonian. In this section the direct couplings are not under consideration, instead the restriction of infinite impurity distances will be dropped and the competition of the Kondo-effect and the RKKY-like interactions both induced by the same hybridization term V will be investigated.

A simple picture for the effective coupling of impurity-spins in the Kondo-Regime via the conduction electrons for the TIAM is achieved by a two stage transformation process of the TIAM Hamiltonian defined in equation 3.1. In the first step - the so called Schrieffer-Wolff transformation - the degrees of freedom of the impurity electron is reduced to the effective spin dynamics between the impurity spin $\underline{S}_i$ and the band-electron spin $\underline{s}_i$ at the impurity site i, resulting in the two-impurity Kondo-Hamiltonian

$$H_{2K} = \sum_{\underline{k},\sigma} \epsilon_{\underline{k}} c^{\dagger}_{\underline{k},\sigma} c_{\underline{k},\sigma} + J\left(\underline{S}_1 \underline{s}_1 + \underline{S}_2 \underline{s}_2\right) \tag{3.51}$$

$$\tag{3.52}$$

with the effective exchange coupling

$$J = V^2 \sum_{\underline{k}} \left(\frac{\theta(\epsilon_{\underline{k}} - \mu)}{\epsilon_{\underline{k}} - \epsilon^f} + \frac{\theta(\mu - \epsilon_{\underline{k}})}{\epsilon^f + U - \epsilon_{\underline{k}}} \right), \tag{3.53}$$

where the hybridization is assumed to be $\underline{k}$-independent $V \equiv V_{\underline{k}}$.
By means of a further canonical transformation the dynamics of the impurity-spin can be completely decoupled from the spin of the conduction electrons and one obtains the so called RKKY-Hamiltonian

$$H_{RKKY} = \sum_{\underline{k},\sigma} \epsilon_{\underline{k}} c^{\dagger}_{\underline{k},\sigma} c_{\underline{k},\sigma} + I(\underline{R}_1 - \underline{R}_2)\ \underline{S}_1 \underline{S}_2, \tag{3.54}$$

where $I(\underline{R}_1 - \underline{R}_2)$ is the RKKY-coupling function

$$I(\underline{R}_1 - \underline{R}_2) = J^2 \sum_{\underline{k},\underline{q}} \cos\left((\underline{k} - \underline{q})(\underline{R}_1 - \underline{R}_2)\right) \frac{f(\epsilon_{\underline{k}}) - f(\epsilon_{\underline{q}})}{\epsilon_{\underline{q}} - \epsilon_{\underline{q}}}. \tag{3.55}$$

For free-electrons with $\epsilon_{\underline{k}} = \frac{k^2}{2m}$ Equation (3.55) can be evaluated analytically and one obtains the famous RKKY-coupling formula

$$I(d) = -J^2 \left(\frac{k_F\ a}{2}\right)^6 \frac{\sin(2\ k_F\ d) + 2\ k_F\ d\ \cos(2k_F\ d)}{(2\ k_F\ d)^4} \tag{3.56}$$

with the typical $\frac{1}{d^3}$ decay for large impurity distances $d = |\underline{R}_1 - \underline{R}_2|$. A more detailed derivation of Equation (3.54) and (3.56) can be found in [Faz99].

Naturally H_{RKKY} contains only a very crude sketch of the rich dynamics of the TIAM and also of the two-impurity Kondo-model. The band-electrons are completely decoupled from the impurities, the model is trivially solvable. On the other hand the coupling function $I(d)$ sets a scale for the strength and decay of the AF-FM impurity-impurity correlations in the TIAM. Functions of the distance deviating from the characteristics of $I(d)$ signalize the existence of many-particle effects modifying the simple RKKY-picture.

For the TIAM the RKKY-interactions come into play by the Anderson hybridization function $\underline{\underline{\Delta}}(z)$, which for finite distances becomes a matrix of real functions with off-diagonal elements

$$\underline{\underline{\Delta}}(z) = \begin{pmatrix} \Delta_0(z) & \Delta_{\underline{d}}(z) \\ \Delta_{-\underline{d}}(z) & \Delta_0(z) \end{pmatrix}, \tag{3.57}$$

where $\underline{d} = \underline{R}_1 - \underline{R}_2$ denotes the distance vector of the two impurities and $\Delta_0(z)$ is the SIAM hybridization function. The off diagonal hybridization function is given by

$$\Delta_{\underline{d}}(\omega) = -\frac{1}{N} Im \left(\sum_{\underline{k}} \frac{e^{i\underline{k}\,(\underline{R}_1 - \underline{R}_2)}}{\omega + i\delta - \epsilon_{\underline{k}}} \right) = -\frac{1}{N} Im \left(\sum_{\underline{k}} \frac{cos\,(\underline{k}\ \underline{d})}{\omega + i\delta - \epsilon_{\underline{k}}} \right), \tag{3.58}$$

where for the last equality a symmetric dispersion $\epsilon_{\underline{k}} = \epsilon_{-\underline{k}}$ was assumed, i.e. $\Delta_{\underline{d}}$=$\Delta_{-\underline{d}}$. The function $\Delta_{\underline{d}}$ is depicted in Figure 3.23 for various distances.

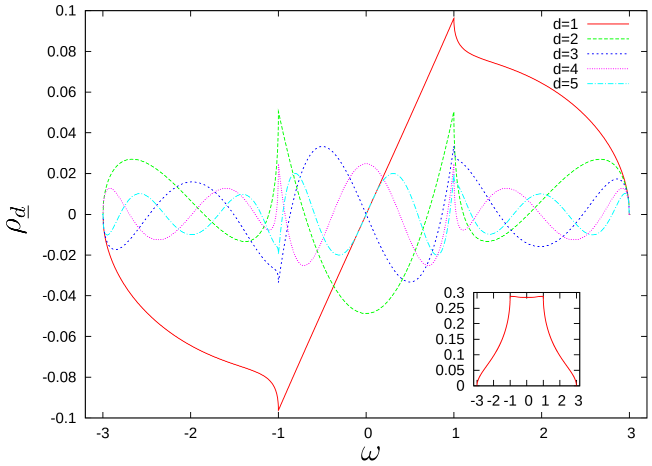

Figure 3.23: The off-diagonal hybridization function $\Delta_{\underline{d}}$ for different distances in $(1, 0, 0)$-direction in a three dimensional simple cubic lattice and $|V_{\underline{k}}|^2 = 1$. The inset on the lower right shows the spectrum of the diagonal hybridization function $\Delta(z)$.

With increasing distance $\Delta_{\underline{d}}$ becomes highly oscillatory with vanishing amplitude. For even distances $\underline{d} = 2n\ \underline{e}_i$ the function is symmetric around the origin and antisymmetric for odd distances $\underline{d} = (2n + 1)\ \underline{e}_i$.

The analytic structure of $\Delta_{\underline{d}}$ in Equation (3.58) implies

$$\int d\omega \Delta_{\underline{d}}(\omega) = \pi \delta_{\underline{d},\underline{0}} \qquad \text{and} \tag{3.59}$$

$$|\Delta_{\underline{d}}(\omega)| \leq \Delta_0(\omega) \quad \forall\, \omega. \tag{3.60}$$

These are very useful relations for the use of the TIAM in the effective lattice-theory presented in the next chapter. There Δ_0 and $\Delta_{\underline{d}}$ are determined self-consistently, and Equation 3.59 and 3.60 are very handy consistency checks for the validity of numerical calculations.

According to the Doniach picture [Don71] depicted in Figure 3.24 the effective anti-ferromagnetic exchange coupling $J \propto V^2$ (see Equation (3.53)) between the impurity-spin and the band-electron-spin sets two different low-temperature scales.

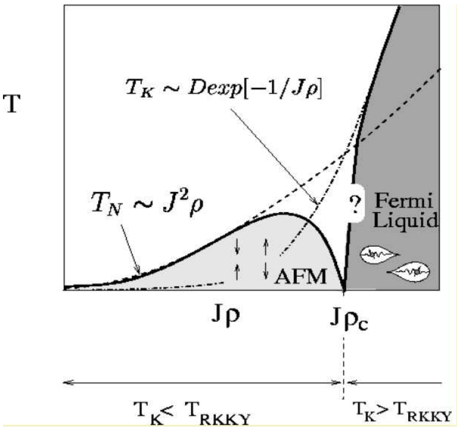

Figure 3.24: Classical Doniach picture for the two different scales emerging from the effective anti-ferromagnetic coupling J between impurity-spin and band-electron-spin. (1) the Kondo-scale $T_K \propto e^{-\rho/J}$, connected to a local Fermi-liquid phase (2) RKKY-scale $T_{RKKY} \propto J^2$, connected to an anti-ferromagnetically ordered phase.

The Kondo-scale, connected to the buildup of a local Fermi-liquid phase, depends exponentially $T_K \propto e^{-\rho/J}$ on the exchange, while the RKKY-scale - according to Doniach - for the setup of magnetically ordered phases depends only quadratically on J, i.e $T_{RKKY} \propto J^2 \propto V^4$ according to Equation (3.53) and Equation (3.55).

Left out in the discussion of the Doniach picture is that terms quadratic in V, like $|V_{\underline{k}}|^2 e^{i\underline{k}(\underline{R}_1-\underline{R}_2)}$ can be seen as effective hopping amplitudes t_{eff} between the two impurities.
The discussion of the TIAM with direct hopping in the preceding section (3.3.5) showed that a direct hopping also leads to an even/odd Kondo-effect. By virtue of t_{eff}, one can expect this even/odd Kondo-effect also to be present if the impurities are coupled only indirectly by hybridization to the band.

In the following discussion an isotropic hybridization matrix element, i.e $V \equiv V_{\underline{k}}$, is assumed and the strength of the coupling to the band will be specified by V^2. Unless differently stated as host DOS a three-dimensional cubic lattice with bandwidth $W = 6$ is used. Furthermore only ENCATI calculations will be presented.

In Figure 3.25 the spectral functions for distance $|\underline{d}| = \infty$, $\underline{d} = 1\underline{e}_i$ and $\underline{d} = 2\underline{e}_i$ are shown for different hybridization strengths V^2. Figure 3.25(c) for the uncoupled $|\underline{d}| = \infty$ spectrum is shown for reference, where the strongest dependence on V^2 is the broadening of the peaks at the ionic excitation energies and the increase of the Kondo-scale with V^2.

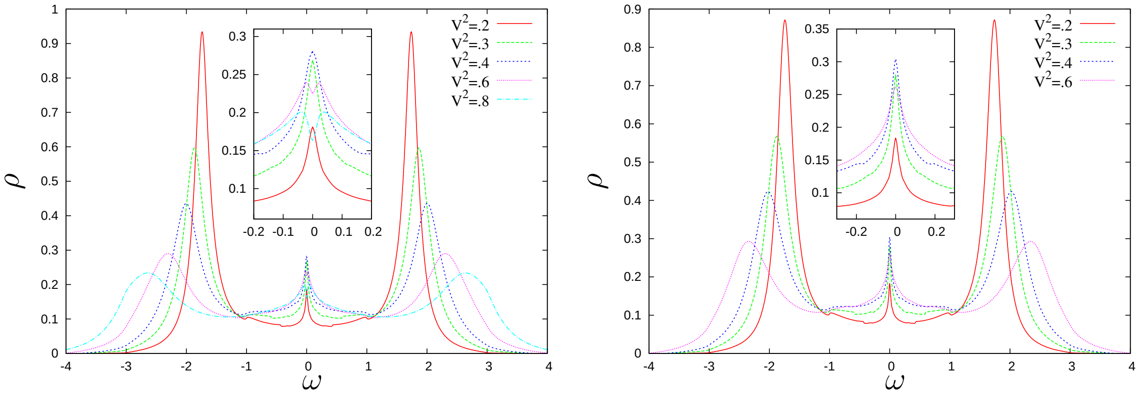

(a) $\underline{d} = 1\ \underline{e}_i$

(b) $\underline{d} = 2\ \underline{e}_i$

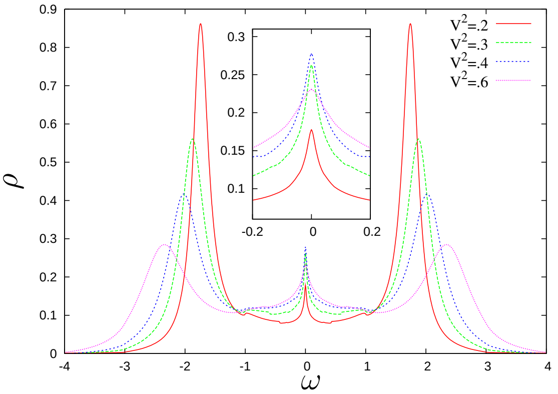

(c) $|\underline{d}| = \infty$

Figure 3.25: Spectral functions from an ENCATI calculation for different hybridizations V^2 and impurity distances (a) $\underline{d} = 1\underline{e}_i$ (b) $\underline{d} = 2\underline{e}_i$ (c) $|\underline{d}| = \infty$. The inset shows the region near the Fermi-level. In all case the other parameters are $\epsilon^f = -1.5$, $U = 3$ and $\beta = 150$.

These effects are visible in the spectra for all distances shown. The differences, which originate due to the varying distance of the impurities are small. They are essentially only visible in the insets, depicting magnifications of the spectra near the Fermi-edge.

For small hybridizations $V^2 \approx 0.2$ no differences compared to the uncoupled $|\underline{d} = \infty|$ spectra are visible. The ASR has about the same height and width. The spectra start to differ for moderate hybridizations at $V \approx 0.4$. For distance $\underline{d} = 1\underline{e}_i$ the ASR is getting broader and a gap opens up for $V^2 = 0.6$. This gap becomes wider with further increasing V^2, reducing the total spectral weight of the remaining ASR.
The behavior of the $\underline{d} = 1\underline{e}_i$ spectra is in contrast to the $\underline{d} = 2\underline{e}_i$ spectra. There the width of the ASR-peak is smaller, but - compared to the uncoupled case - reaches higher peak values.

The different characteristic behavior of the $\underline{d} = 1\underline{e}_i$ and $\underline{d} = 2\underline{e}_i$ ASR-peaks could be an indicator for a different sign in the effective magnetic exchange coupling J mediated by the band-electrons. For $\underline{d} = 2\underline{e}_i$ it seems, that the coupling is ferro-magnetic. The spectra calculated in subsection 3.14 with direct exchange coupling $J > 0$ also showed a taller ASR-peak. Absent in the $\underline{d} = 2\underline{e}_i$ spectra is the emergence of side-gaps in the ASR, which appeared in the calculations with direct J. On the other hand these side-gaps started to show

up only for large J, and the small changes in the ASR of the $\underline{d} = 2\underline{e}_i$ spectra indicate a relatively small effective ferro-magnetic J. It is also the question in how far the effective $\propto V^2$ hopping term t_{eff} alters the spectrum for effective ferromagnetic couplings[1].
The appearance of a gap for the $\underline{d} = 1\underline{e}_i$ spectra clearly points towards an effective anti-ferromagnetic coupling or a strong effective hopping t_{eff} and the connected even/odd Kondo-effect.

More insight in the influence of the effective hopping t_{eff} can be gained by the observation of the even/odd spectral functions. The even/odd spectral functions for the same parameter set as in Figure 3.25 are shown in Figure 3.26.

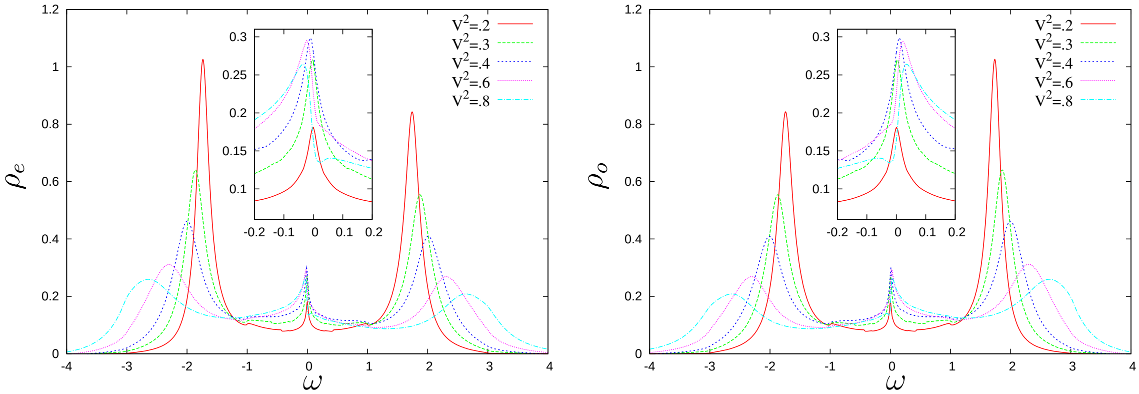

(a) $\underline{d} = 1\ \underline{e}_i$, even (b) $\underline{d} = 1\ \underline{e}_i$, odd

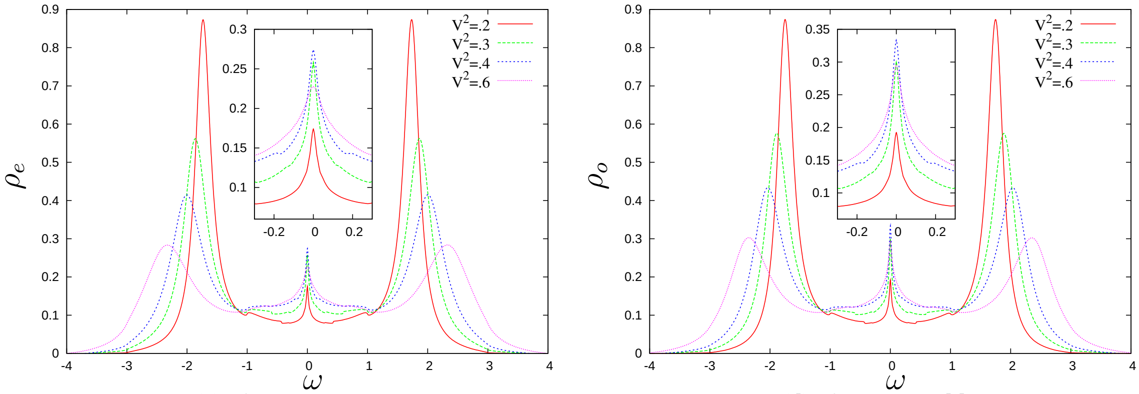

(c) $\underline{d} = 2\ \underline{e}_i$, even (d) $\underline{d} = 2\ \underline{e}_i$, odd

Figure 3.26: Even/odd ENCATI spectral function representation for $\underline{d} = 1\underline{e}_i$ and $\underline{d} = 2\underline{e}_i$ according to Equation (3.2) for the same parameters as the spectra shown in figure (3.25)

The results are very interesting. For small hybridization the effects of the hopping are only visible in the asymmetry of the peak heights at the outer ionic excitation peaks, but no differences are visible at the ASR-peak. For $V^2 = 0.4$ the ASR becomes slightly asymmetric and develops a sharp flank towards $\omega = 0$ for hybridizations $V^2 > 0.4$, while the asymmetry of the outer ionic-peaks remains at about the same relative size. Furthermore the maximum of the ASR-peak is increasingly shifted towards lower energies for the odd spectra and to-

---

[1] The direct hopping term t investigated in section 3.3.5, only led to an effective anti-ferromagnetic coupling $J = -4\frac{t^2}{U}$

wards higher energies for the even spectra. Concerning the ASR the $|\underline{d}| = 1$ spectra are very similar to the spectrum shown in figure 3.21 calculated with a direct t. Even the small dip at the bottom of the sharp flank of the ASR is visible for large V^2.

The even/odd spectra for distance $|\underline{d}| = 2$ show a completely different behavior. The spectra remain particle-hole symmetric and no differences are visible between the even and the odd spectra near the ionic excitation energies. An ASR-peak is visible in both the even and the odd spectra, they only differ slightly in width and height. The even ASR-peak's for various V^2 depicted in Figure 3.26(c) are broader and have a smaller peak-height then the odd-peaks depicted in Figure 3.26(d). This is visible not only for large but also for small hybridizations, e.g. the odd-peak for $V^2 = 0.2$ is a little larger then the even-peak. But in contrast to the distance $\underline{d} = 1\underline{e}_i$ the position of the ASR-peak is not shifted.

The physical interpretation of the $\underline{d} = 1\underline{e}_i$ and $\underline{d} = 2\underline{e}_i$ results is not completely obvious in the effective picture presented here. It seems that the picture of the hybridization V only as source of a scalar effective hopping t_{eff} and/or exchange J term concerning the impurity-impurity interactions is too simple. On the one hand the closer similarity of the spectra with direct hopping to the calculations with $\underline{d} = 1\underline{e}_i$, than to the spectra with direct AF-exchange J, indicates the predominant presence of an effective hopping term for this distance. On the other hand the results for $|\underline{d}| = 2$, with only small differences in the even/odd spectra, are more in accord with the interpretation of V^2 predominantly mediating an effective ferromagnetic exchange coupling J.

The impurity-impurity magnetic spin susceptibility $\chi_{1\,2}(\omega)$ for the two distances is depicted in Figure 3.27. The two top Figures show the real part and the spectrum of $\chi_{1\,2}$ for distance $\underline{d} = 1\underline{e}_i$. The corresponding Figures for $\underline{d} = 2\underline{e}_i$ are presented at the bottom.

The susceptibility confirms the conjecture that the impurity-impurity coupling for $\underline{d} = 1\underline{e}_i$ is essentially anti-ferromagnetic. The static magnetic susceptibility, i.e. the real part of $\chi_{1\,2}$ at $\omega = 0$, has negative sign. In the spectra with $V^2 > 0.2$ a one-peak structure is visible, with the position of maximum increasing with the hybridization strength V^2. The position of the peak maximum can interpreted as the effective exchange strength J. The excitation energy of the maximum as function of the hybridization V^4 is presented in the inset of Figure 3.27(b). The inset reveals, for not too small hybridizations, a linear increase of the effective exchange J with V^4.[2]

The static magnetic susceptibility for $\underline{d} = 2\underline{e}_i$ switches it sign from negative (AFM) to positive (FM) values between $V^2 = 0.2$ and $V^2 = 0.3$. This is connected to a second peak in the magnetic spectrum near $\omega = 0.001$. This second peak at about the same energy - but with opposite sign - is also visible in the $\underline{d} = 1\underline{e}_i$ spectrum for $V^2 = 0.2$. This peak is probably a fingerprint of the magnetic excitations situated at the same energy in the $\chi_{1\,1}$-susceptibility related to the single-impurity Kondo-effect, which leaves it traces in the $\chi_{1\,2}(\omega)$-spectrum.
For small hybridizations the differences in the one-particle spectra are relatively small compared to the uncoupled spectra depicted in Figure (3.25(c)). Larger differences become

---

[2] The V^4 fitting, is afflicted with some reservations by the author. For the calculated data, a sensible linear fit of J could also be undertaken with V^2.

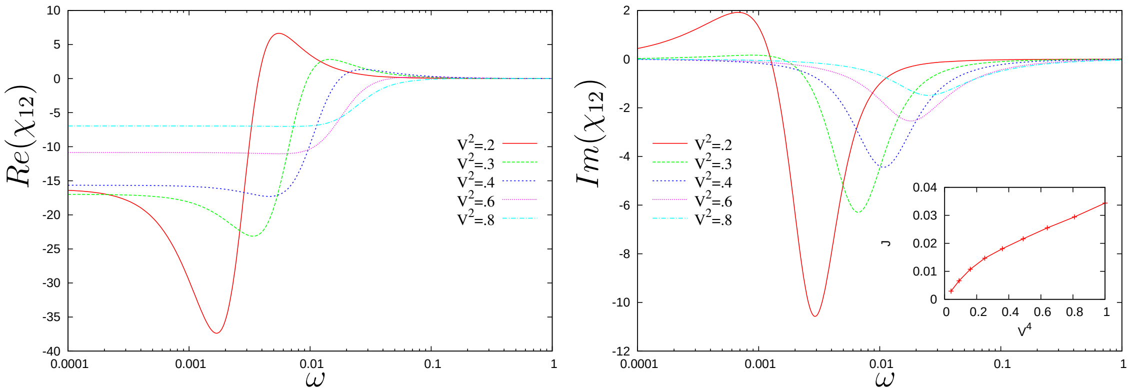

(a) $\underline{d} = 1\ \underline{e}_i$ (b) $\underline{d} = 1\ \underline{e}_i$

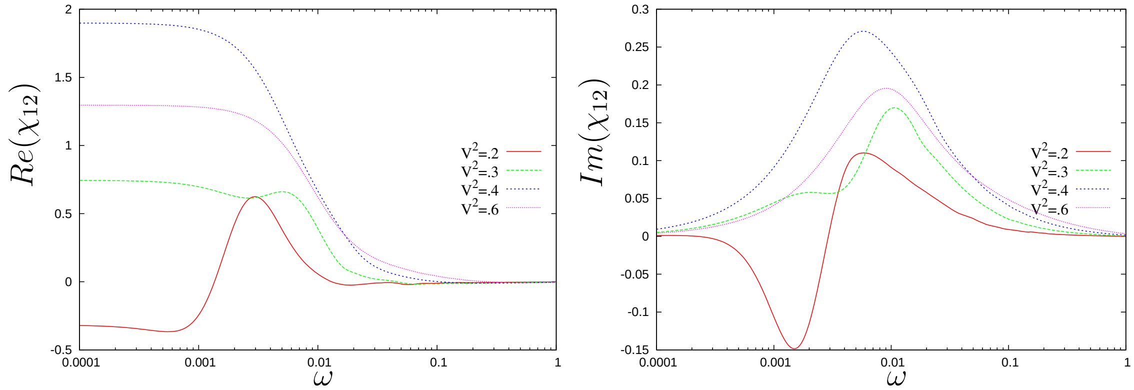

(c) $\underline{d} = 2\ \underline{e}_i$ (d) $\underline{d} = 2\ \underline{e}_i$

Figure 3.27: ENCATI magnetic spectrum (right) and real part (left) of the $\underline{S}_1\ \underline{S}_2$ susceptibility $\chi_{1\,2}(\omega)$ for $\underline{d} = 1\underline{e}_i$ and $\underline{d} = 2\underline{e}_i$ and various hybridizations. The parameters are the same as in figure (3.25). The Inset in (b) shows the position of the minimum of the peak in the spectrum as function of V^2.

notable at about $V^2 = 0.3$, which is about the hybridization strength where the second peak in the magnetic spectra vanishes and the linear $J \propto V^4$ regime for $|\underline{d}| = 1$ sets in and a unique positive peak in the $\underline{d} = 2\underline{e}_i$ magnetic spectrum appears.
For larger hybridizations the magnetic spectrum for $\underline{d} = 2\underline{e}_i$ shows no linear increase in the peak position with increasing V^2 as in the spectra with unit distance. The peaks itself have opposite sign and are at lower energies for $V^2 > 0.3$ than for the corresponding $\underline{d} = 1\underline{e}_i$ spectra.
The one-particle and magnetic spectra for $|\underline{d}| = 2$ clearly indicate ferromagnetic coupling between the impurities and the presence of a two-impurity Kondo-effect screening the ionic triplet-state.

The investigation of the effective impurity-impurity couplings can be easily extended to larger distances. In the Figures 3.28(a)-3.28(c) the hybridization is fixed to $V^2 = 0.54$ and a magnification of the one-particle spectrum in the vincinity of the fermi-edge is shown for distances $\underline{d} = 1\underline{e}_i$ up to $\underline{d} = 19\ \underline{e}_i$ along the symmetry axes of the sc-lattice, i.e. $\underline{e}_x, \underline{e}_y, \underline{e}_z$. In each Figure the ASR of the uncoupled $|\underline{d}| = \infty$ spectrum is depicted for reference.

Except for distance $\underline{d} = 1\underline{e}_i$the ASR is larger or has at least the same height as for $\underline{d} = \infty$.

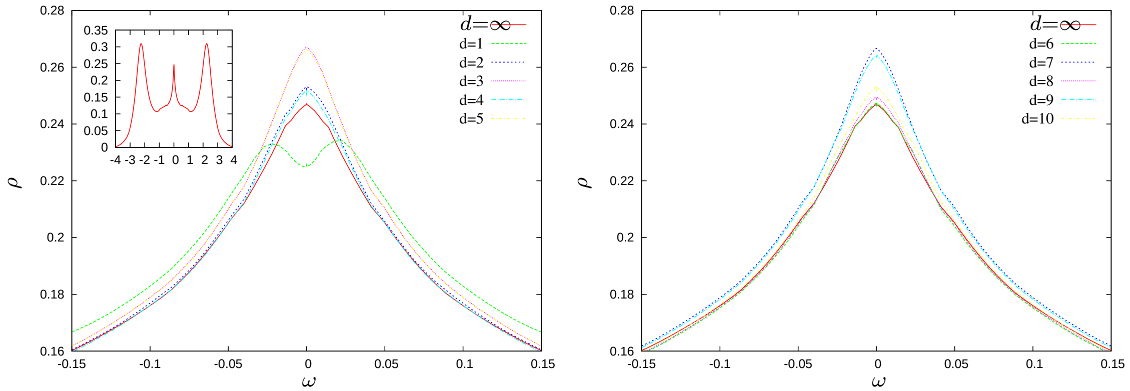

(a) $\underline{d} = 1\underline{e}_i - 5\ \underline{e}_i$ (b) $\underline{d} = 6\underline{e}_i - 10\ \underline{e}_i$

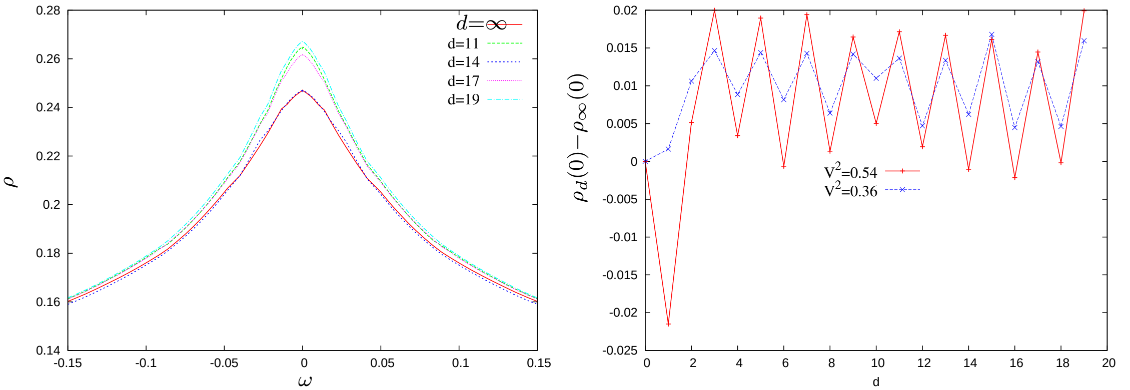

(c) $\underline{d} = 11\underline{e}_i - 19\ \underline{e}_i$ (d)

Figure 3.28: (a)-(c) One-particle ENCATI spectra in the vicinity of the fermi-edge for distances $|\underline{d}|$=1-19 along the $(1,0)^T$ direction in a three dimensional sc-lattice with $V^2 = 0.54$. The other parameters are the same as in figure (3.25). (a) The inset shows the full spectrum for $|\underline{d}| = \infty$ as reference. (d) The deviations of the maximum of the ASR relative to the uncoupled $|\underline{d}| = \infty$ ASR-maximum as function of the impurity distance for $V^2 = 0.54$ and $V^2 = 0.36$.

Apart from the $\underline{d} = 1\ \underline{e}_i$ case the peaks for odd-distances are magnified and broader than the uncoupled reference peak. Interestingly this magnifictation decreases only slightly for larger distances. The peak-heights for even distances are much closer to the uncoupled peak and the differences become smaller for large distances.

The oscillating behavior of the ASR can be seen more clearly in Figure 3.28(d). There the deviations of the ASR-heights relative to uncoupled ASR is shown as function of the distance for $V^2 = 0.54$ and $V^2 = 0.36$. For weaker hybridization ($V^2 = 0.36$) the differences between the maxima and minima are smaller, but in the average the ASR shows about the same mean increase in the height as for $V^2 = 0.54$. It also decreases very slowly with increasing distance.

A possible explanation for this mean increase of spectral weight in the ASR is, that the nondiagonal hybridization function $\Delta_{\underline{d}}$ not only mediates the impurity-impurity correlations, but also acts as additional hybridization channel for the impurities. If for example the Coulomb-interaction U would be absent on the impurity sites no impurity-impurity correlations would exist, but the impurity electrons site still could gain kinetic energy by indirect hopping processes to the other impurity-site and back. This leads to an increased broadening of the resonances in the spectrum, which is in effect the same as a larger diagonal hybdrization function $\Delta_0(\omega)$, i.e. greater V^2, for uncoupled impurities.

One question remaining is whether the oscillatory behavior of the ASR peak-values can be seen as an indicator for the sign and the strength of the AFM-FM RKKY-coupling. In that case one expects - relative to the mean-value - a lower ASR for anti-ferromagnetic RKKY-coupling and a higher ASR for ferromagnetic RKKY-coupling. Opposing to this picture is that the amplitudes of the oscillations decrease very slowly with distance and do not show the typical $\frac{1}{d^3}$ power-law behavior of the RKKY-interaction. The preceeding discussion of the TIAM for distance $|\underline{d}| = 1$ already showed the strong influence of the additional hybridization channel on the one-particle properties, which cannot be explained by just an effective AFM-FM impurity-impurity coupling mediated by this channel.

Figure 3.29 shows the spectrum of the magnetic susceptibility $\chi_{1\ 2}$ for different distances

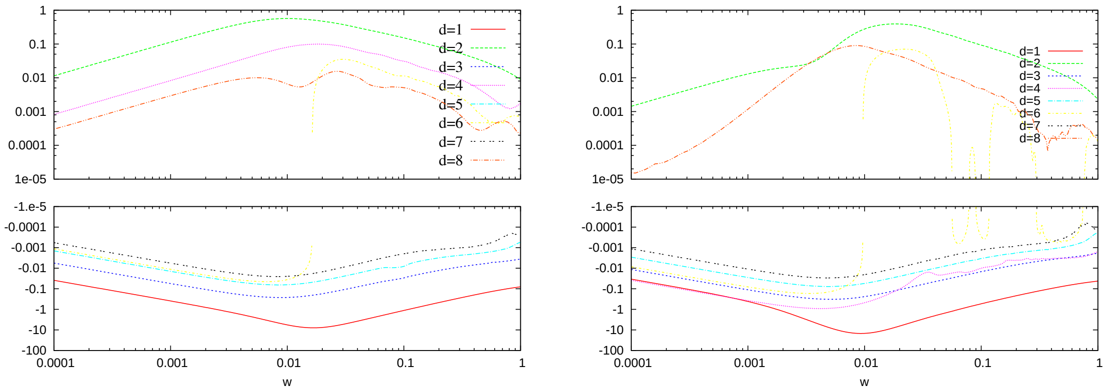

(a) $Im(\chi_{1\ 2})$, $V^2 = 0.54$

(b) $Im(\chi_{1\ 2}), V^2 = 0.36$

Figure 3.29: ENCATI double-logarithmic magnetic spectrum of the $\chi_{1\ 2}$-susceptibility for (a) $V^2 = 0.54$, (b) $V^2 = 0.36$ and impurity distances from $\underline{d} = 1\ \underline{e}_i - 8\ \underline{e}_i$. The top figures have a positive logarithmic y-scale for the bottom figures the scale is negative.

and two different hybridizations. All spectra - except for distance $\underline{d} = 6\ \underline{e}_i$ -[3] show essentially a one peak structure, and a decrease of the peak height with increasing distance is clearly visible in the double-logarithmic plot. For $V^2 = 0.54$, depicted in Figure 3.29(a), the peak oscillates from negative to positive values. For even distances the peak is positive, indicating ferromagnetic coupling and negative for odd distances, indicating anti-ferromagnetic coupling.

---

[3] For both hybridizations the $\underline{d} = 6\ \underline{e}_i$ spectrum shows no simple peak structure. The spectrum changes it sign roughly at the energie, where the peak of the other spectra is situated. Additionally the oscillating behavior at high energies in the spectrum for $V^2 = 0.36$ look more like numerical artefacts. It seems that for this distance no distinct ferromagnetic or anti-ferromagnetic impurity-impurity coupling can be identified. It is in accord with this finding that the corresponding one-particle spectrum, depicted in Figure 3.25, is very close to the uncoupled spectrum i.e. $|\underline{d}| = \infty$.

The $V^2 = 0.36$ spectra, depicted in Figure 3.29(b), show in principle the same oscillating behavior, but here - contrary to the $V^2 = 0.54$ calculation - the coupling for $\underline{d} = 4\ \underline{e}_i$ is anti-ferromagnetic. This type of behavior is also present in the $V^2 = 0.54$ calculations for larger distances. Inspect for example Figure 3.30(b), where the peak-height is depicted as function of the impurity-impurity distance $d\ \underline{e}_i$. At the even distances $\underline{d} = 12\ \underline{e}_i$ and $\underline{d} = 18\ \underline{e}_i$ the coupling is anti-ferromagnetic, while the corresponding $V^2 = 0.36$ spectra show ferromagnetic coupling.

The different characteristics of the impurity-impurity coupling for different hybridization strengths V^2 is beyond the scope of the simple RKKY-formula in Equation (3.55). There the sign of the effective exchange coupling is solely determined by the distance, the hybridization V^2 affects only the coupling strength $I(\underline{d}) \propto V^4$. The magnetic spectra calculated here indicate that the sign of the effective exchange is not only a function of $\underline{d}$ but also of the hybridization strength V^2.

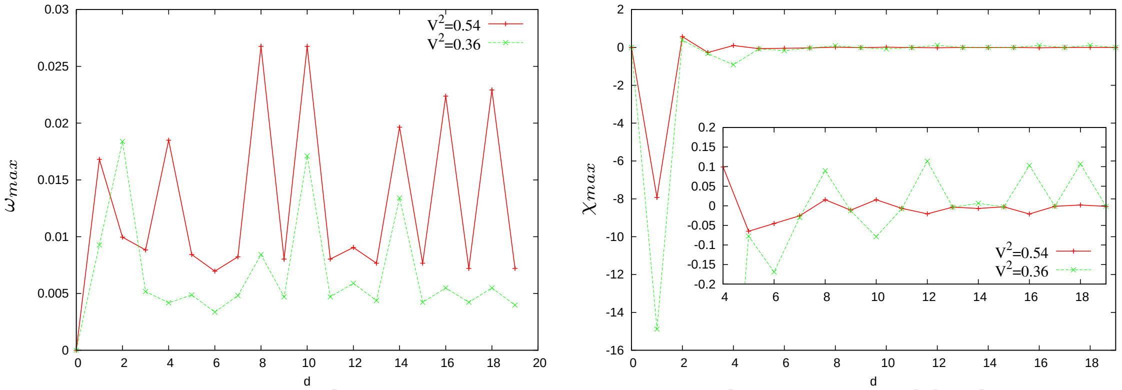

(a) resonance-peak energy (b) resonance-peak height

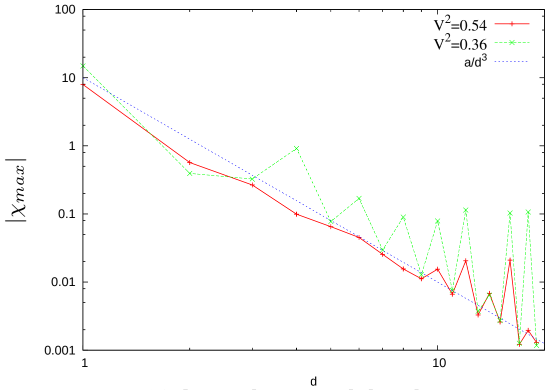

(c) logarithmic peak height

Figure 3.30: Peak heights and positions deduced from the magnetic spectra shown in Figure 3.29 as function of the impurity-impurity distance $\underline{d} = d\underline{e}_i$. (a) excitation energy ω_{max} at the peak maximum, i.e. $|Im(\chi_{1\,2}(\omega_{max}))| = \max(|Im(\chi_{1\,2}(\omega)|))$. (b) height of the resonance: $\chi_{max} \equiv Im(\chi_{\underline{S}_1\underline{S}_2}(\omega_{max}))$. The inset show a magnifictation of the resonance amplitudes in the range $\underline{d} = 4\underline{e}_i$ to $\underline{d} = 19\underline{e}_i$ (c) double logarithmic plot of the absolute value of the resonance amplitudes: $log(|\chi_{max}|)$ compared to a RKKY like $\frac{a}{d^3}$ decay, where a is a fitting constant.

Nevertheless, the double logarithmic plot of the absolute resonance peak heights as function of the distance depicted in Figure 3.30(c) shows a typical RKKY-like $\frac{1}{|\underline{d}|^3}$ decay of the resonance amplitude. It is also in accord with the RKKY-formula in Equation (3.56) that the mean decay is independent of the hybridization strength, i.e. is equal for $V^2 = 0.54$ and $V^2 = 0.36$.

At first sight it is a bit surprising, that the magnetic excitation amplitudes are larger for the smaller hybridization $V^2 = 0.36$. The height of the resonance is no measure of the effective exchange coupling J. Only the sign of the peak-values indicates the prefactor of the effective exchange. The total spectral weight under the peak is a measure, in how far the physics of the TIAM is influenced by the effective impurity-impurity coupling J. A measure of the absolute value of the effective exchange $|J|$ is the excitation energy ω_{max} at the resonance. One has to remember that the resonance in the magnetic excitation spectrum of the TIAM with direct J is situated at $\omega_{max} = |J|$, see e.g. Figure 3.15.
As function of the distance ω_{max} is depicted in Figure 3.30(a). As expected, the excitation energies ω_{max} are higher for the stronger hybridization and are smaller for the weaker hybridization $V^2 = 0.36$.

In summary, the effective J is larger for stronger hybridizations but the resonance peaks in the magnetic spectra are more suppressed for smaller hybridizations. For effective antiferromagnetic coupling this behavior complies with the Doniach picture depicted in Figure 3.24, in which the influence of the RKKY interactions is expected to be larger for smaller V^2. On the other hand for the distances with effective ferromagnetic impurity-impurity exchange this behavior cannot be explained with the Doniach picture, as the competition with the Kondo-effect is absent. The discussion of the low-energy one-particle properties showed that the oscillations in the height of the ASR are not necessarily connected to the FM-AFM oscillations in the impurity-impurity coupling. The additional non-diagonal hybridization channel also modifies the single impurity properties, even if correlation effects with the other impurity site are suppressed. The one-particle spectra for large $|\underline{d}| > 2$ distances indicate, that these modifications are very strong.
In effect, a consistent combined interpretation of the two- and one-particle properties of the TIAM is hard to undertake and is certainly more complex than the simple picture of just an effective exchange coupling connecting impurities at finite distances.

So far, the impurities where placed along one of three equal symmetry axes of the three dimensional sc-lattice, which are the Euclidian unit-vectors $\underline{e}_x, \underline{e}_y, \underline{e}_z$. This restriction will now be dropped.
Numerically this is very easy, as in the TIAM-solver the impurity distance only enters in the off-diagonal hybridization function $\Delta_{\underline{d}}$. The numerical calculation of $\Delta_{\underline{d}}$ for arbitary distance vectors $\underline{d}$ is a bit more complicated, since the $\underline{k}$-summation in Equation (3.58) cannot be reduced to one-dimensional numerical integrations. Instead a real three dimensional $\underline{k}$-integration needs to be done. For the sake of simplicity the two impurities are placed only at arbitary places in the (x,y)-plane. The other parameters are the same as for the calculations along the symmetry axis.

In Figure 3.31 the two-dimensional color-encoded analogue of Figure 3.28(d) is depicted. The peak-value of the ASR relative to the uncoupled value is shown. The inset in black/white

encodation shows whether the ASR peak in the coupled TIAM is smaller/larger than the uncoupled value. Comparison of the insets for the two hybridizations reveals very similiar deviations from the uncoupled ASR peak values.
For both hybridizations the peak is reduced at nearest neighbour sites and for $x \geq 3$ along the line $\underline{d} = (x, 1)^T$ (and the line $\underline{d} = (1, x)^T$ by symmetry). Additionally two spots with reduced ASR's appear along the $(1, 1)^T$ diagonal direction. Between these spots regions with greatly increased ASR's appear, which maintain their size even for large distances. Take for example the distance $\underline{d} = (10, 9)^T$, which shows for both hybridizations a very large increase of the ASR.

The monochrome inset for $V^2 = 0.54$ in Figure 3.31(a) shows some distances with reduced ASR (e.g. $\underline{d} = (2, 2)^T$), which are not reduced in the corresponding Figure 3.31(b) for $V^2 = 0.36$. A closer inspection of these spots in Figure 3.31(b) reveals, that there the ASR peaks are very close to the uncoupled value and at these distances no ASR's with largely increased peak-value appear. In that sense the ASR's for both hybridizations show the same tendencies with the distance. In total, the differences to the uncoupled ASR are larger for the $V^2 = 0.54$ spectra, which is most probably due to the greater Kondo-temperature magnifying the effects of the additional non-diagonal hybridization channel in the ASR.

The strength of the ferromagnetic/anti-ferromagnetic impurity-impurity coupling deduced from the maximum resonance amplitude of the $\chi_{1\,2}$ excitation spectrum is depicted in Figure 3.32. The color-encoded tiles show the absolute value of the amplitude $\max(|Im(\chi_{1\,2}(\omega))|)$ on a logarithmic scale. The signum of the amplitudes can be read of from the black/white encoded inset, where black squares indicate negative (anti-ferromagnetic) and white squares positive (ferromagnetic) peak-values.
The tiles depicted in blue indicate regions of very small impurity-impurity coupling. These regions are situated along the $(1, x)^T, (x, 1)^T$ line for $x \geq 3$ and the two spots adjactent to the $(1, 1)^T$ diagonal line, at the distances $\underline{d} = (5, 5)^T$ and $\underline{d} = (8, 8)^T$. Comparison with Figure 3.31 reveals that these are exactly the spots, where in the one-particle spectra the ASR-peaks are reduced or at least the difference to the uncoupled ASR is very small. The results from the magnetic spectra support the interpretation, that for these regions destructive interference of the non-diagonal hybridization processes occur. The two impurities are effectively decoupled for these distances. As the brighter colors indicate larger couplings, one can clearly see that the mean coupling strength is larger for the smaller hybridization $V^2 = 0.36$. This conjecture, already seen from the coupling strengths along a symmetry line depicted in Figure 3.30(b), stays also true for arbitrary distance vectors. Especially the region nearby the origin shows stronger coupling values to a greater spatial extend than the couplings for $V^2 = 0.54$. In both plots the regions of relative large coupling are situated along the $(1, 0)^T, (0, 1)^T$ lines and along the diagonal line, separated by the discussed spots of neglible coupling in between.

Concerning the signum of the impurity-impurity coupling the insets show a very interesting structure. For not too far distances the inset for $V^2 = 0.54$ shows a perfect chessboard structure, i.e. the change from ferromagnetic to anti-ferromagnetic coupling for nearest neighbour distances. For short distances this structure is less visible for $V^2 = 0.36$, instead the chessboard structure is visible for large distances. In total there are more distances with anti-ferromagnetic coupling, more for $V^2 = 0.36$ and less for $V^2 = 0.54$. A close inspection of the occuring distances with ferromagnetic coupling (white squares) shows, that these distances follow the chessboard-rule. The chessboard-rule is broken for distances with anti-ferromagnetic coupling, forming closed anti-ferromagnetic regions.

In summary, the calculations of the TIAM with impurities situated at arbitrary positions in the (x,y)-plane showed that it is not only the scalar distance $|\underline{d}|$, which determines the strength and the sign of the impurity-impurity coupling. The geometry of the host lattice, manifested in the energetic structure of the Anderson hybridization matrix $\underline{\underline{\Delta}}(\omega)$, plays a vital role.
The allowed hopping processes connected with for each distance different phase-factors in the host lattice lead to interference effects suppressing or enforcing the impurity-impurity coupling-strength. Thereby for certain distances the impurity-impurity coupling can be relatively strong, even if the impuritites are separated by a large distance. One can expect these interference effects to become more pronounced, if the hybridization function is a non-uniform $\underline{k}$-dependent function $V \longrightarrow V_{\underline{k},i}$. As this is the case for the use of the TIAM in effective lattice theories, such interference effects might be of great physical relevance beyond the scope of TIAM. Furthermore the calculated data in the (x, y)-plane confirms the finding, that the sign of the exchange coupling depends critically on the hybridization strength V^2 and not only on the distance-vector $\underline{d}$.

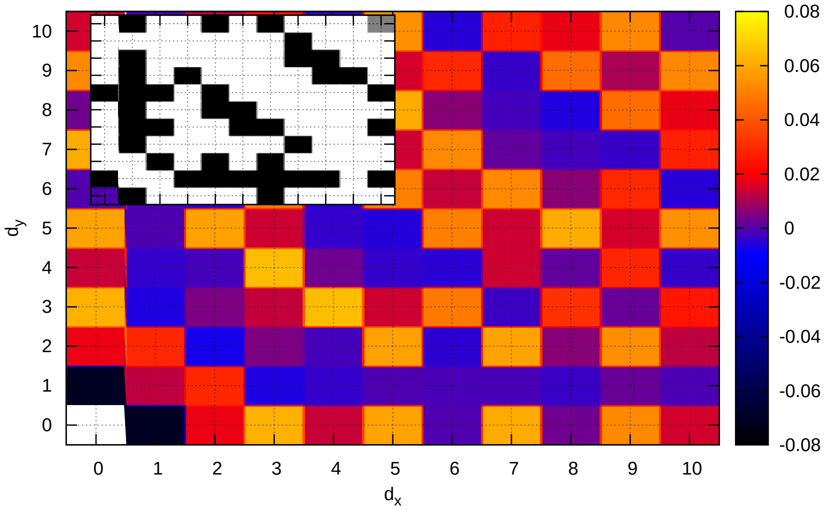

(a) $\rho_{\underline{d}}(0) - \rho_\infty(0), V^2 = 0.54$

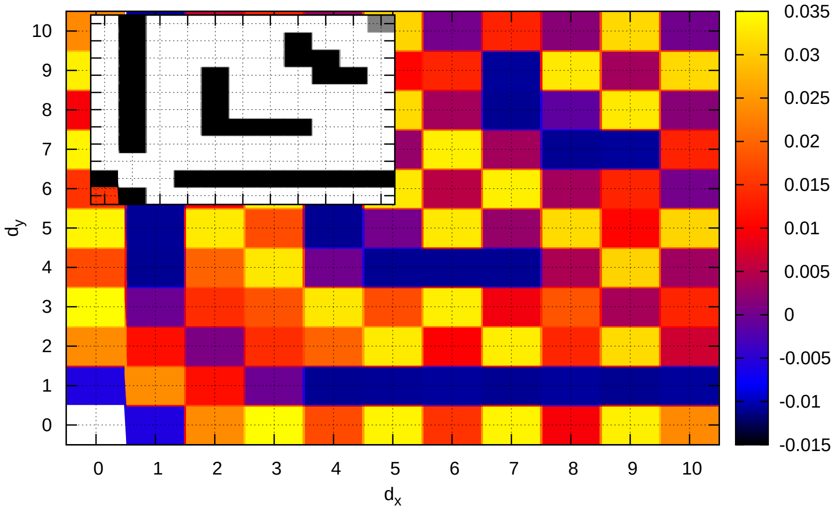

(b) $\rho_{\underline{d}}(0) - \rho_\infty(0), V^2 = 0.36$

Figure 3.31: Color-encoded height of the ASR relative to the height of the uncoupled $\underline{d} = \infty$ ASR: $\rho_{\underline{d}}(0) - \rho_\infty(0)$. The impurities are placed in the ($\underline{e}_x$,$\underline{e}_y$)-plane. In the inset at the top left corner black squares indicate a smaller ASR $\rho_{\underline{d}}(0) < \rho_\infty(0)$ and white squares a larger ASR $\rho_{\underline{d}}(0) > \rho_\infty(0)$. The parameters are $\epsilon^f = -1.5$, $U = 3$, $\beta = 150$ with the hybridization (a) $V^2 = 0.54$ and (b) $V^2 = 0.36$.

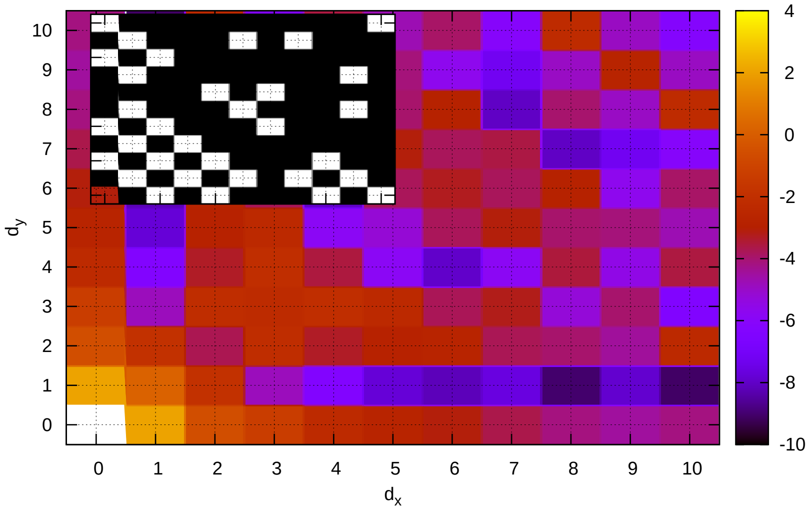

(a) $V^2 = 0.54$

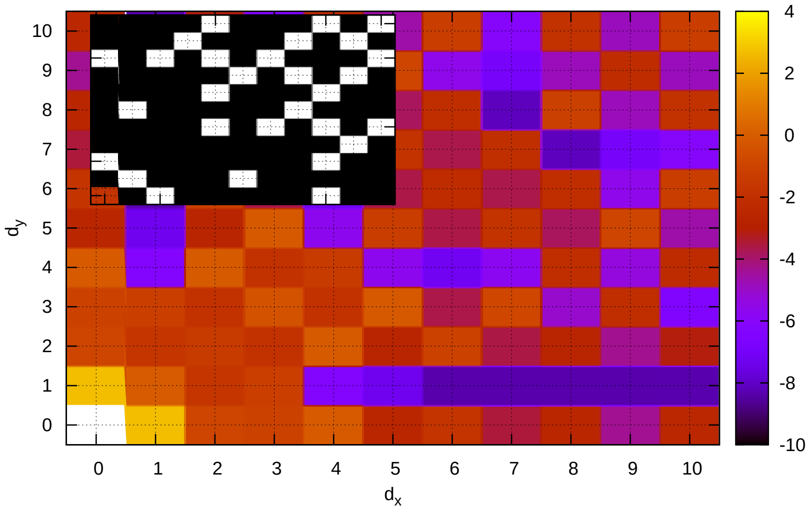

(b) $V^2 = 0.36$

Figure 3.32: Color-encoded logarithmic plot of the maximum resonance amplitude: $\max(|Im(\chi_{1\,2}(\omega))|)$ for (a) $V^2 = 0.54$ and (b) $V^2 = 0.36$. The monochrome inset at the top left corner depicts the sign of the coupling, with black squares for anti-ferromagnetic and white squares for ferromagnetic coupling. The parameter set is the same as in Figure 3.31.

4 DMFT and nonlocal extensions

4.1 Introduction

In this chapter extended mean field schemes for the solution of lattice problems are introduced and discussed. The methods aim at systems where the strength of the electron-electron interaction is comparable or even larger than the kinetic energy of the electrons. It is therefore disadvantageous to start a perturbation scheme from the non-interacting limit.
Far more favorable are approaches where the solution is constructed from parts which contain the relevant part of the strong interactions in a non perturbative manner. Extented mean field schemes fall in this class of approaches. Here the degrees of freedom are subdivided in two parts. One part has usually very few degrees of freedom and is solved exactly or with methods which go beyond the mean field scope of restoring the picture of independent particles via the introduction of effective one particle parameters. The other part is then treated as generalized dynamical mean field for the first part and has in turn to be determined self-consistently from the solution of the first part.
Standard textbook examples for mean field theories usually reduce the mean field to a quantity describable by a single complex or non-complex number. The usually large set of degrees of freedom of the second part of the system is thereby reduced to only one parameter. This limits the complexity of the effective model and allows for a solution.
The Ising model with nearest neighbor spin interaction

$$H = \sum_i hS_i - \sum_{<i,j>} J_{i,j} S_i S_j \tag{4.1}$$

is a simple example, where the effective Hamiltonian H_{eff} for one site i reduces to

$$H_{eff} = \sum_i (h + h_{MF}) S_i \qquad \text{with} \qquad h_{MF} = \sum_{o \neq i} J_{o,i} \langle S_o \rangle \tag{4.2}$$

the mean field for a site. From that point of view it is very natural to obtain better approximations by increasing the number of explicitly and exactly treated local sites in the effective model. In turn, however, thereby the degrees of freedom of the corresponding mean field and the effective model increases, it is usually very rapidly beyond the scope of any appropriate solution with theoretical methods.

Applied to strongly correlated lattices these ideas lead to extended mean field theories which reduce the complexity of the full lattice problem to the dynamics of one lattice site or one cluster of lattice sites in a self-consistent way. The dynamics of the surrounding lattice is then mimiced by an energy dependent mean field. The problem is therefore reduced to the self-consistent solution of an effective impurity model where the mean field parameters are encoded in the hybridization matrix elements of the impurity electrons with the host and in

the energetical structure of the host states.
The simplest realization of this scheme reduces the local cluster to one site and maps the whole lattice problem onto an effective single impurity model; it is in the literature commonly referred to as Dynamic Mean Field Theory or short DMFT [Geo96, A.G04, Bul06]. Prior to the DMFT an equivalent self consistent scheme with focus on the Periodic Anderson Model (PAM) termed XNCA was developed from Kuramoto [Kur85a]. He made explicit use of direct perturbation theory [Kei70, Kei71a, Gre81, Kei84], as impurity solver in the scheme and did not present it as an interchangeable building block like the later work on the DMFT.

The DMFT approximation is often characterized as the exact solution for the self-energy in the limit $d \longrightarrow \infty$ [Met89, MH89, Met91, Bra89] with d the dimension of the lattice or coordination number. In this limit the spatial correlations in the system become irrelevant which can be formally characterized by a $\underline{k}$-independent self-energy in the one-particle lattice Greenfunction

$$G_\sigma(\underline{k}, z) = \frac{1}{z - \epsilon_{\underline{k},\sigma} - \Sigma_\sigma(\underline{k}, z)} \overset{DMFT}{\longrightarrow} G_\sigma^{DMFT}(\underline{k}, z) = \frac{1}{z - \epsilon_{\underline{k},\sigma} - \Sigma_\sigma(z)} \;, \tag{4.3}$$

where the $\underline{k}$-dependency in G^{DMFT} is solely determined by the dispersion function $\epsilon_{\underline{k},\sigma}$.
Despite its successes [Kot04], for example in the description of the correlation driven Mott metal-insulator transition in Materials like $NiS_{2-x}Se_x$ [Mat98] or Vanadium- ($X_xV_{2-x}O_3$) [Mai00b] and Titanium-(($X_{1-x}Ti_xO_3$)) [Mai07] Oxide compounds the theory is critically flawed by the fact that it does not incorporate the dynamic effects of inter-site correlations. Such dynamic effects are however crucial for the correct description of many correlated fermion problems. Among these are the formation of Luttinger Liquids in low dimensional systems [And97] and pseudogap behavior due to strong anti-ferromagnetic spin fluctuations in the one particle spectrum of High-Tc materials [Din96]. It generally fails to describe nonlocal order parameters such as the superconducting order parameter in High-Tc superconductors with d-wave symmetry [Tsu00] or to describe the behavior towards a classical or quantum critical point where long range spatial fluctuations of the order parameter occur. Another related wide field, which must be addressed with methods incorporating spatial fluctuations is the interplay and competition of the lattice Kondo effect and the RKKY interaction in Heavy Fermion compounds[Gre91],[Geg08]. There the coherent buildup of a local Fermi liquid phase near the Fermi edge through the lattice at the so called coherence temperature T^* is essentially captured by the DMFT approximation [Gre05]. But on the other hand DMFT completely fails to properly include RKKY type interactions which couple dynamically local moments and thereby favors a magnetically ordered ground state. The RKKY interaction is a rather slowly decaying function of the distance ($J^{RKKY} \propto \frac{1}{|\underline{r}^3|}$), which is inherently non-local in nature.

In [Gre96] and in [Gre05] Grewe develops the “Lokale Theorie” which is a perturbation expansion of a lattice Hamiltonian $H = H_0 + T$ in T, where T contains transfer processes and nonlocal interactions around the limit of purely local parts H_0 containing the correlated local contributions of the constituent ionic shells. In case of the Hubbard model (Equation 4.4) one may think of H_0 as the part containing the isolated s-shells with the local Coulomb interaction U and T the part describing the hopping between these shells.
Due to the interactions in H_0 the Wick-Theorem is absent and the excluded volume problem

is solved by the use of cumulants. Within this approach the “lokal vollständige Näherung” is constructed which is equivalent to the DMFT, if H_0 is defined as the part containing isolated lattice sites. But due to its construction as a lattice theory from a local point of view, short range correlations can be simply included by increasing the spatial extend of the objects contained exactly in H_0.
For the Hubbard model this could for example mean to include clusters of adjacent sites with the nearest neighbor sites connected via the hopping t in H_0 and T now describing the hybridization between the clusters defined in H_0. In the literature this approximation is termed Cellular DMFT or short CDMFT[Kot01].

In the last 10 years several cluster extensions of the DMFT have been proposed with namely the CDMFT and the dynamical cluster approximation (DCA) [Het98, Jar01a] as the de facto standard methods in this area. Both will be inspected more closely later on. A good overview on this topic can be found in [Mai05] and the references therein.
Apart from the different details of these cluster algorithms, they all share the same severe limitation. All cluster approaches reduce the full lattice problem to an effective cluster-impurity problem, spatial correlations beyond the size of the cluster are simply cut off.

Physical phenomena originating from long wavelength-fluctuations, such as the aforementioned critical phase-transitions can therefore not be captured by cluster methods. Due to the exponential increasing complexity of solving large cluster impurity models it is impossible for practical numerical reasons to significantly increase the cutoff wavelength to more than a few neighboring sites. Methods trying to overcome this limitation try therefore to formulate analytical more or less systematic corrections to the DMFT limit. Among the most recent developments is the Dynamical Vertex Approximation (DΓA)[Tos07] which calculates $\underline{k}$-dependent contributions to the self energy from the two-particle vertex. In this approximation the vertex is constructed with the use of Bethe-Salpeter equations from the local irreducible two particle vertex which is obtained from the impurity solver. Similar approximations are described in [Sle06] and [Kus06].

A more systematic way to include diagrammatic corrections to the DMFT follow the local strong coupling ansatz given in the “Lokale Theorie” [Gre96] and [Met91] later also in [Sta04], where corrections can be identified and formulated with the use of cumulant vertices. But practical calculations have so far - to the authors knowledge - not originated directly from this ansatz. Most recently the so called Dual Fermion Approach (DF) has been introduced [Rub08, Bre08] as systematic extension to the DMFT or the DMFT cluster extensions [Haf08]. This formalism is formulated with the use of path integral methods and includes nonlocal correlations by the self-consistent calculation of non-local diagrams with effective n-particle vertices. At the time of writing this scheme in its simplest realization has been applied to the one- and two-dimensional Hubbard model and showed only minor corrections to the cluster DMFT-approaches.

In this work a different self-consistent approach capable of dealing with short and long-ranged correlations at the same time is proposed and presented.
The basic idea is to reduce the lattice problem to N_p different effective two impurity models with N_p the number of all distinct pairs of lattice sites of different separation. The results of the N_p two impurity problems are then used to calculate an approximation for

the $\underline{k}$-dependent lattice self energy which then can be used to construct new effective media for the N_p effective two impurity problems until consistency is reached. A similar idea was already proposed in [Sch95, Geo96] but only executed for nearest neighbor sites in the Falicov-Kimbal model with a very restricted impurity solver at hand. For more complicated models, e.g. the Hubbard model, it was dropped due to severe causality problems. The scheme proposed here is in many respects essential different.

4.2 Theory

The theory to be developed in this chapter aims at the calculation of the one particle lattice Greenfunction $G_{\underline{k},\sigma}(z)$. Unless explicitly stated spin degeneracy is assumed and the spin index σ is dropped in the following formulas, i.e. $G_{\underline{k},\sigma}(z) \longrightarrow G_{\underline{k}}(z)$. Additionally, even if theory present is applicable to general lattice models the focus here - for the sake of simplicity - is on application to the Hubbard model

$$H = \epsilon \sum_{i,\sigma} c^{\dagger}_{i,\sigma} c_{i,\sigma} \; + t \sum_{<i,j>,\sigma} \left(c^{\dagger}_{i,\sigma} c_{j,\sigma} + c^{\dagger}_{j,\sigma} c_{i,\sigma} \right) + U \sum_{i} c^{\dagger}_{i,\uparrow} c_{i,\uparrow} c^{\dagger}_{i,\downarrow} c_{i,\downarrow} \tag{4.4}$$

on a cubic lattice in d dimensions, with nearest neighbor hopping t and simple s shells as lattice sites with the local Coulomb interaction U. Simplifications and specialties arising from the restriction to this model will be commented when they appear.

Formally, the one particle Greenfunctions of a lattice model can be expressed in terms of an irreducible self energy $\underline{\underline{\Sigma}}_{\underline{k}}(z)$

$$\underline{\underline{G}}_{\underline{k}}(z) = \left[z - \underline{\underline{\epsilon}} - \underline{\underline{\Sigma}}_{\underline{k}}(z) - \underline{\underline{t}}_{\underline{k}} \right]^{-1} \;, \tag{4.5}$$

where the matrix representation takes the orbital structure of the lattice site into account, $\underline{\underline{\epsilon}}$ the energies of the non interacting atomic limit of a site, $\underline{\underline{t}}_{\underline{k}}$ describes the hybridization processes between the sites and $\underline{\underline{\Sigma}}_{\underline{k}}(z)$ contains all corrections arising due to the interactions term. For the single band Hubbard model in equation (4.4) equation (4.5) reduces to its scalar version

$$G_{\underline{k}}(z) = \left[z - \epsilon - \Sigma_{\underline{k}}(z) - t_{\underline{k}} \right]^{-1} . \tag{4.6}$$

For the sc-lattice with nearest neighbor hopping the hybridization term is given as

$$t_{\underline{k}} = -2td \sum_{i=1}^{d} cos(k_i a_i) \tag{4.7}$$

with a_i the nearest neighbor distance along the i-axis which is in the following uniformly set to unity $a_i = 1$ and d the dimension of the lattice.
Following the local viewpoint i.e. the evolvement of equation (4.6) from the strong coupling or ionic limit of the model it is sensible to introduce a new quantity $g_{\underline{k}}$ and restate the equation as

$$G_{\underline{k}}(z) = \left[g^{-1}_{\underline{k}}(z) - t_{\underline{k}} \right]^{-1} . \tag{4.8}$$

Comparison with equation (4.6) reveals

$$g_{\underline{k}}^{-1}(z) = z - \epsilon - \Sigma_{\underline{k}}(z). \tag{4.9}$$

Alternatively, by using the unperturbed ionic Greenfunction $G^{(0)}$, one may write

$$g_{\underline{k}}^{-1}(z) = (G^{(0)}(z))^{-1} - \tilde{\Sigma}_{\underline{k}}(z) \ . \tag{4.10}$$

In this picture the irreducible self energy $\tilde{\Sigma}_{\underline{k}}$ now contains only the dynamic correction terms in U relative to the strong coupling limit contained in $G^{(0)}$. As such the self-energy $\tilde{\Sigma}_{\underline{k}}$ in the leading order is not only proportional to U but also to the hybridization matrix element t

$$\Sigma_{\underline{k}}(z) \xrightarrow{U=0} 0 \qquad , \qquad \Sigma_{\underline{k}}(z) \xrightarrow{t=0} \left(G^{(0)}(z)\right)^{-1} - (z+\epsilon) \tag{4.11}$$

$$\tilde{\Sigma}_{\underline{k}}(z) \xrightarrow{U=0} 0 \qquad , \qquad \tilde{\Sigma}_{\underline{k}}(z) \xrightarrow{t=0} 0 \ . \tag{4.12}$$

For the Hubbard model above defined $G^{(0)}(z)$ is easily calculated [Gre96] to be

$$G^{(0)}(z) = \frac{\zeta^1}{z-\epsilon} + \frac{\zeta^2}{z-\epsilon-U} \tag{4.13}$$

with temperature dependent occupation factors

$$\zeta^1 = \frac{1}{Z^{(0)}}\left(e^{-\beta\,0} + e^{-\beta\,\epsilon}\right) = \frac{1+e^{-\beta\,\epsilon}}{Z^{(0)}} \tag{4.14}$$

$$\zeta_2 = \frac{1}{Z^{(0)}}\left(e^{-\beta\epsilon} + e^{-\beta(2\epsilon+U)}\right) \tag{4.15}$$

$$\tag{4.16}$$

and the local partition function

$$Z^{(0)} = 1 + 2e^{-\beta\epsilon} + e^{-\beta(2\epsilon+U)} \ . \tag{4.17}$$

Calculation are within the grand canonical ensemble with the chemical potential and the ionic vacuum at energy zero. The relation $\zeta^1 + \zeta^2 = 1$ is obviously fulfilled for the local spectral weights distributing a particle between the two excitation energies corresponding to transitions from the unoccupied to the singly occupied ($\Delta E = \epsilon$) and from the single to the doubly occupied state ($\Delta E = \epsilon + U$).

The form of equation (4.8) interpreted as Dyson equation reveals the meaning of the quantity $g_{\underline{k}}(z)$ as irreducible effective propagator of an ionic shell. Figure 4.1 shows the diagrammatic representation of 4.8 as free propagation through the lattice. In the afore

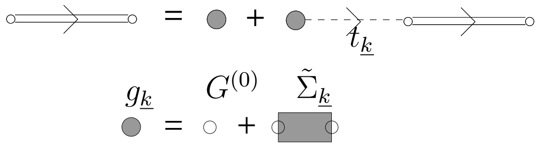

Figure 4.1: Diagrammatic representation of equation 4.8

mentioned expansion around the atomic limit undertaken in [Gre96] and [Gre05] diagram rules for the systematic expansion of $\tilde{\Sigma}_{\underline{k}}(z)$ are formulated. This undertaking will not be followed in this work. The reader interested in more details on this topic is advised to consult the above given references. Nevertheless it is worth noting that already in its simplest form, i.e. $\tilde{\Sigma}_{\underline{k}}(z) = 0$, the Hubbard I approximation[Hub63] is reproduced for the special case of the Hubbard model. Figure 4.2 shows the calculated spectra for this approximation

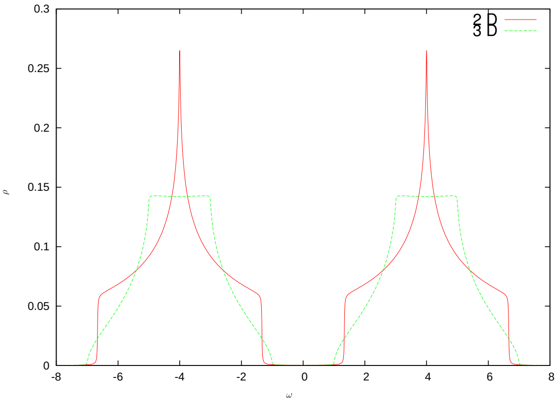

Figure 4.2: Hubbard I approximation for the two and three-dimensional sc-lattice with $\epsilon = -4$,$U = 8$ and bandwidth $W = 6$ for both dimensions, with characteristic Van-Hove singularities.

for the two and three-dimensional sc-lattice with the typical lower and upper Hubbard bands separated by a gap with a width $\propto U$. Even in its simplest form this approximation goes far beyond the scope of the Density Functional Theory (DFT) or any other effective one-particle theory by reproducing the leading effect of the Mott transition.

In the following it is very useful to continue with the real space representation of equation (4.8). Therefore the geometric series representation of equation (4.8)

$$G_{\underline{k}} = \sum_{n=0}^{\infty} g_{\underline{k}} \left(t_{\underline{k}} g_{\underline{k}}\right)^n = g_{\underline{k}} + g_{\underline{k}} t_{\underline{k}} g_{\underline{k}} + g_{\underline{k}} t_{\underline{k}} g_{\underline{k}} t_{\underline{k}} g_{\underline{k}} + \dots \tag{4.18}$$

is used and Fourier transformed $G_{\underline{a}} = \frac{1}{N} \sum_{\underline{k}} G_{\underline{k}} e^{-i\underline{k}\underline{a}}$ term by term

$$\begin{aligned} G_{\underline{a}} &= g_{\underline{a}} + \sum_{\underline{a}^{(1)},\underline{h}^{(1)}} g_{\underline{a}-\underline{a}^{(1)}-\underline{h}^{(1)}}\ t_{\underline{h}^{(1)}}\ g_{\underline{a}^{(1)}} + \sum_{\substack{\underline{a}^{(1)},\underline{a}^{(2)},\\ \underline{h}^{(1)},\underline{h}^{(2)}}} g_{\underline{a}-\underline{a}^{(1)}-\underline{h}^{(1)}-\underline{h}^{(2)}-\underline{a}^{(2)}}\ t_{\underline{h}^{(1)}}\ g_{\underline{a}^{(1)}} t_{\underline{h}^{(2)}}\ g_{\underline{a}^{(2)}} + \dots \\ &= g_{\underline{a}} + \sum_{n=1}^{\infty} \sum_{\substack{\underline{a}^{(1)},\dots,\underline{a}^{(n)}\\ \underline{h}^{(1)},\dots,\underline{h}^{(n)}}} \left(g_{\underline{a}-\sum\limits_{i=1}^{n}\underline{a}^{(i)}-\sum\limits_{i=1}^{n}\underline{h}^{(i)}} \prod_{i=1}^{n} t_{\underline{h}^{(i)}} g_{\underline{a}^{(i)}} \right) . \end{aligned} \tag{4.19}$$

The energy dependence of the above used quantities is omitted from now on for brevity. The sums over $\underline{a}^{(i)}, \underline{h}^{(i)}$ need to be taken over all lattice vectors. For the Hubbard model on a sc-lattice with nearest hopping the hopping matrix elements reduce with unity nearest neighbor distance to

$$t_{\underline{h}} = \frac{1}{N} \sum_{\underline{k}} t_{\underline{k}} e^{-i\underline{k}\,\underline{h}} = \delta_{|\underline{h}|,1}. \tag{4.20}$$

With equation 4.19 at hand the T matrix is defined as

$$T_{\underline{a}} = t_{\underline{a}} + \sum_{n=1}^{\infty} \sum_{\substack{\underline{a}^{(1)},\ldots,\underline{a}^{(n)} \\ \underline{h}^{(1)},\ldots,\underline{h}^{(n)}}} \left(t_{\underline{a} - \sum_{i=1}^{n} \underline{a}^{(i)} - \sum_{i=1}^{n} \underline{h}^{(i)}} \prod_{i=1}^{n} g_{\underline{a}^{(i)}} t_{\underline{h}^{(i)}} \right) \tag{4.21}$$

yielding to

$$G_{\underline{a}} = g_{\underline{a}} + \sum_{\underline{a}^{(1)},\underline{a}^{(2)}} g_{\underline{a}-\underline{a}^{(1)}} T_{\underline{a}^{(1)}-\underline{a}^{(2)}} g_{\underline{a}^{(2)}} \ . \tag{4.22}$$

The above equation (4.22) constitutes the starting point for the approximations introduced in the next sections. It will be further transformed and effective theories derived from it.

4.3 DMFT

The DMFT approximation arises if the self energy in $\tilde{\Sigma}_{\underline{k}}$ in $g_{\underline{k}}$ is assumed to be $\underline{k}$ independent

$$\tilde{\Sigma}_k \xrightarrow{DMFT} \tilde{\Sigma}, \tag{4.23}$$

and as a consequence the irreducible Greenfunction becomes local in space

$$\frac{1}{N} \sum_{\underline{k}} g_k e^{-i\underline{k}\underline{a}} \xrightarrow{DMFT} \frac{1}{N} \sum_{\underline{k}} g_0 e^{-i\underline{k}\underline{a}} = g_0 \delta_{\underline{a},\underline{0}} \ . \tag{4.24}$$

For the local lattice Greenfunction with $\underline{a} = 0$ equation (4.22) simplifies to

$$G_0 = g_0 + g_0 T_0 g_o \ . \tag{4.25}$$

So far no rule or scheme has been specified how to calculate the above used quantities G_o, g_0, T_0. What helps now is insight that the above defined lattice equation 4.25 and the setup with the purely local quantity g_0 is closely related to the physics of a single impurity problem. The dynamics of an impurity electron is determined by the local Coulomb interaction on the impurity and subsequent free propagation processes of impurity electrons through the host of non-interacting band electrons and back to the impurity. Due to the non-interacting nature of the band electrons, electrons can get correlated with other electrons solely on the impurity site. In this sense the band propagation processes are free propagations.

In terms of a Dyson equation the one-particle impurity Greenfunction can generally be be stated as

$$\begin{aligned} G^{(imp)} &= g^{(imp)} + g^{(imp)} \tilde{T}^{(imp)} g^{(imp)} + g^{(imp)} \tilde{T}^{(imp)} g^{(imp)} \tilde{T}^{(imp)} g^{(imp)} + \ldots \\ &= g^{(imp)} + g^{(imp)} \tilde{T}^{(imp)} G^{(imp)} \\ &= \left[\left(g^{(imp)} \right)^{-1} - \tilde{T}^{(imp)} \right]^{-1} \end{aligned} \tag{4.26}$$

with $\tilde{T}^{(imp)}$ the irreducible T-matrix describing the hybridization and free propagation through the host and $g^{(imp)}$ is the local irreducible impurity propagator. In the standard terminology of the SIAM this is usually written as

$$G^{(imp)}(z) = \left[z - \epsilon^f - \Sigma^{imp}(z) - \frac{1}{N} \sum_{\underline{k}} \frac{V_{\underline{k}}^2}{z - \epsilon_{\underline{k}}} \right]^{-1} . \tag{4.27}$$

In this notation the irreducible impurity propagator can be identified with

$$g^{(imp)}(z) \equiv \left[z - \epsilon^f - \Sigma^{imp}(z) \right]^{-1} \tag{4.28}$$

and the irreducible T-matrix is the Anderson hybridization-function Δ

$$\tilde{T}^{(imp)}(z) \equiv \Delta(z) = \frac{1}{N} \sum_{\underline{k}} \frac{V_{\underline{k}}^2}{z - \epsilon_{\underline{k}}} . \tag{4.29}$$

The propagation processes in the lattice T matrix T_0 contains loops, which can be characterized as free propagations. These are all processes in which the propagating electron does not meet any other electron during the propagation. In the impurity problem electrons get correlated with other electrons solely on the impurity site. Intermediate visits of the impurity site are therefore excluded in the impurity T-matrix $\tilde{T}^{(imp)}$. For the local lattice T-matrix the same can be achieved by the introduction of the irreducible lattice T-matrix $\tilde{T}_0$ via the Dyson equation

$$\begin{aligned} T_0 &= \tilde{T}_0 + \tilde{T}_0 g_0 \tilde{T}_0 + \tilde{T}_0 g_0 \tilde{T}_0 g_0 \tilde{T}_0 + \dots \\ &= \left[\tilde{T}_0^{-1} - g_0 \right]^{-1} \end{aligned} \tag{4.30}$$

or equivalently

$$\tilde{T}_0 = \left[T_0^{-1} + g_0 \right]^{-1} . \tag{4.31}$$

$\tilde{T}_0$ is now irreducible in the sense that intermediate visits of site 0 are excluded. According to Equation (4.25) the lattice Greenfunction expressed with $\tilde{T}_0$ has then the same analytic structure

$$G_0 = \left[g_0^{-1} - \tilde{T}_0 \right]^{-1} \tag{4.32}$$

as the impurity Greenfunction $G^{(imp)}$.

But at this point the approximation is still not sufficiently characterized to see more than a formal similarity in equations (4.30) and (4.26). The loops in $\tilde{T}_0$ still contains processes where the propagating electron meets electrons at other lattice sites and thereby correlates the dynamics of these sites.

Within DMFT these processes are approximated by effective free propagations !

The interaction of the propagating electron on any other site than site 0 is contained only on the mean field level. The lattice T-matrix $\tilde{T}_0$ thereby becomes a quantity which needs to be self-consistently determined and contains only effective free propagations.

This further assumption allows for the mapping of lattice quantities with otherwise unrelated impurity quantities. The approximation of effective free loops in $\tilde{T}_0$ can be justified from the viewpoint of the DMFT as exact theory in the limit of infinite dimensions [Met89],[MH89]. It can be shown, with the hopping matrix element t rescaled by a factor $\frac{1}{\sqrt{d}}$, that two loops starting at the same site i and meeting at an other site j lead to a contribution of order $1/\sqrt{d^{|i-j|}}$ with $|i-j|$ the Manhattan distance between the two sites. Thereby these contributions vanish in the $d \longrightarrow \infty$ limit.
Stated differently, two random walks starting at the same site never meet in a lattice with infinite dimensions.

With this further approximation the impurity Greenfunction as functional $G^{(imp)}[\tilde{T}_0]$ of the irreducible T matrix of the lattice describes the same physical processes as the lattice Greenfunction G_0. Therefore the lattice problem is mapped onto an effective impurity problem.
Even more, in a self-consistency cycle yet to be defined the solution of the impurity model can be used to determine the lattice quantity $\tilde{T}_0$ and thereby the full lattice Greenfunction $G_{\underline{k}}$. The procedure is presented in the box below.

0. Start with an initial guess of the irreducible T matrix $\tilde{T}^{(imp)}$.
   Here the spectrum of a broadened Hubbard I Greenfunction usually serves as a good starting point. For numerical reasons it is always advantageous to make broadening wide enough so that spectral weight is shifted in areas where structures are expected to evolve during the iteration procedure.
1. Use this irreducible T-matrix to calculate an effective impurity Greenfunction G^{imp}, with an impurity solver of your choice.
2. With G^{imp} and $\tilde{T}^{(imp)}$ at hand calculate via

   $$g^{(imp)} = \left[\left(G^{(imp)}\right)^{-1} + \tilde{T}^{(imp)}\right]^{-1} \tag{4.33}$$

   the effective irreducible impurity propagator.
3. Approximate the irreducible lattice propagator g_0 by the one from the impurity problem

   $$g^{(imp)} \longrightarrow g_0 \tag{4.34}$$

   and calculate

   $$G_0 = \frac{1}{N}\sum_{\underline{k}} \left[g^{(imp)} - t_{\underline{k}}\right]^{-1} \tag{4.35}$$

   an approximation for the local lattice Greenfunction.
4. Use G_0 from step 3 and calculate the irreducible lattice T matrix

   $$\tilde{T}_0 = g_0^{-1} - \left(G^{(0)}\right)^{-1} \tag{4.36}$$

5. If $\tilde{T}_0 = \tilde{T}^{(imp)}$ then convergency is reached, and T_0 and g_0 constitute the correct approximated lattice quantities.
   Otherwise set

   $$\tilde{T}_0 \longrightarrow \tilde{T}^{(imp)} \tag{4.37}$$

   and continue with step 1 until convergence is reached.

In [Pru01] it is shown that the above defined DMFT-cycle leads to physical solutions, i.e. that no poles in the upper half-plane of the Greenfunction appear as long as the SIAM solver preserves the correct analytical structure of the solution.
Unfortunately the direct perturbation theory methods used in this work in certain parameter regimes fail to preserve the correct analytic structure. The well known NCA pathology[Gre83, Gre08] for low temperatures is as an example for this.

4.4 Basic cluster scheme: CDMFT

Within the systematics of an $(1/d)$ expansion the leading order corrections to the $(d = \infty)$ DMFT limit arise from the incorporation of the correlations introduced by the presence of nearest neighbor sites. These short range correlations are accessible by the use of cluster schemes. The one emerging straightforward from the DMFT equations of the preceeding section is termed Cellular DMFT (CDMFT) in the literature [Kot01].
As a matter of fact the CDMFT is equivalent to the multi-orbital DMFT scheme already presented in [Gre96]. A cluster of N_c sites has the same structure and complexity as one site with N_c orbitals when the orbitals are coupled by the same matrix elements as the corresponding cluster. So the only thing that changes is that one starts with the matrix generalization of equation (4.8)

$$\underline{\underline{G}}_{\underline{k}'} = \left[\underline{\underline{g}}^{-1}_{\underline{k}'} - \underline{\underline{t}}_{\underline{k}'}\right]^{-1} \tag{4.38}$$

and all equations in the DMFT scheme from the previous section need only be replaced by their matrix equivalents.
It is important to notice that equation 4.38 effectively increases the volume of the unit cell by a factor N_C and therefore $\underline{k}$ dependent lattice quantities are to be considered in a reduced Brillouin zone. In equation 4.38 this is indicated by the primed crystal momentum $\underline{k}'$.
One of the major drawbacks of the CDMFT scheme is that translational invariance is broken. The correlations between two sites in the same cluster are treated differently than the - in principle - equivalent correlation between two sites separated by the same lattice vector but sitting in different clusters.
The CDMFT scheme will in the following be exemplified for the 1D-Hubbard model. As the focus of this work lies on the correlations describable by effective two impurity models a cluster of size $N_c = 2$ is chosen. For the 1D-Hubbard model this results in two different possible setups, building the lattice out of two site clusters. The situation is shown in Figure 4.3 where the two possible different cluster setups are shown.

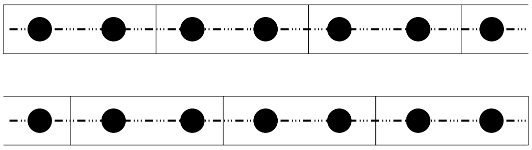

Figure 4.3: Two different cluster configurations for the 1D Hubbard model, with cluster size $N_c = 2$. The first setup is shifted relative to the second one by one lattice site.

The breaking of the transitional invariance of the CDMFT originates in these different but

equivalent initial cluster setups. CDMFT keeps spatial intra-cluster correlations and omits inter-cluster correlations. It depends on the specific and arbitrary cluster setup if a nearest neighbor pair lies in the same or in two adjacent clusters.
For the two site cluster with the sites named a and b the effective irreducible lattice site propagator is a 2x2 matrix

$$\begin{aligned}\underline{\underline{g}}_{\underline{k}'} &= \begin{pmatrix} g_{a,a} & g_{a,b} \\ g_{b,a} & g_{b,b} \end{pmatrix}_{\underline{k}'} \\ &= \begin{pmatrix} g_0 & g_1 \\ g_{-1} & g_0 \end{pmatrix}_{\underline{k}'} \quad .\end{aligned} \tag{4.39}$$

The transfer matrix element between the clusters couples a sites with b sites, so Equation (4.38) takes the form

$$\underline{\underline{G}}_{k'} = \left[\underline{\underline{g}}_{k'}^{-1} - \begin{pmatrix} 0 & t_{k'} \\ t_{k'} & 0 \end{pmatrix} \right]^{-1} \tag{4.40}$$

with $t_{k'} = 2tcos(k')$ and k' defined in the reduced Brillouin zone $[-\frac{\pi}{2}, \frac{\pi}{2})$. In analogy to the single site DMFT setup $\underline{\underline{g}}_{k'}$ is now assumed to be k' independent

$$\underline{\underline{g}}_{k'} \longrightarrow \underline{\underline{g}}_{0} \quad . \tag{4.41}$$

In direct analogy to Equation (4.32) one ends up with a matrix equation for the local lattice Greenfunction G_0

$$\underline{\underline{G}}_0 = \left[\underline{\underline{g}}_0^{-1} - \underline{\underline{\tilde{T}}}_0 \right]^{-1} \quad . \tag{4.42}$$

With the same line of reasoning as in the DMFT the quantities in lattice equation (4.42) can then be mapped to an effective two-impurity model $\underline{\underline{G}}_0 \equiv \underline{\underline{G}}^{(2imp)} \left[\underline{\underline{\tilde{T}}}_0 \right]$. The presentation of the self-consistency cycle, which is completely analogous to the one in the DMFT (see section 4.3), will be omitted here.
Instead, anticipating the scheme which will be presented in the next section it is helpful to inspect the mapping on the two-impurity model in some more detail. From the viewpoint of the local two impurities in the cluster there exist three different kind of irreducible processes:

(i) An impurity electron can hybridize and then, completely unaware of the other impurity, propagate freely through the host lattice back to its starting point.

(ii) The electron hybridizes and freely propagates to the other impurity where it gets correlated with the electrons at that site.

(iii) The impurities can be coupled by direct matrix elements. This can be a simple single particle transfer term or an interaction term.

The propagations in (i) correspond to the diagonal part of $\underline{\underline{\tilde{T}}}_0$ and the free propagation described in (ii) to the off-diagonal part of $\underline{\underline{\tilde{T}}}_0$. The processes contained in (iii) are direct couplings and are contained in the non-diagonal parts of the unperturbed ionic two-impurity Greenfunction $\underline{\underline{G}}^{(0)}$.

The full local impurity dynamic consists of all possible combinations of (i), (ii) and (iii) together with the diagonal terms in $\underline{\underline{G}}^{(0)}$. The Dyson equation (4.42) condenses the above made remarks in mathematical form. As mentioned the CDMFT does not respect translational invariance; within this approach one tries to fix this, after convergence of the self-consistency cycle is reached, by imposing the relation

$$g_{i,j} = \frac{1}{N_c} \sum_{\mu,\nu} \left(\underline{\underline{g}}_0 \right)_{\mu,\nu} \delta_{\underline{R}_\nu - \underline{R}_\mu, \underline{R}_i - \underline{R}_j} \tag{4.43}$$

to the irreducible Greenfunction, The $\underline{R}_x$ are lattice vectors of the original, not coarse grained lattice and N_c is the number of sites in the cluster. In momentum space this translates into taking only the $\underline{Q} = 0$ contribution of the effective local propagator

$$g_{\underline{k},\underline{k}'} = \frac{1}{N_c} \sum_{\underline{Q}} \sum_{\mu,\nu} e^{-i\underline{k}\underline{R}_\mu} \left(\underline{\underline{g}}_0 \right)_{\mu,\nu} e^{i\underline{k}'\underline{R}_\nu} \, \delta_{\underline{k}-\underline{k}'-\underline{Q},0} \tag{4.44}$$

i.e.

$$g_{\underline{k}} \equiv g_{\underline{k},\underline{k}} \frac{1}{N_c} \sum_{\mu,\nu} e^{i\underline{k}\,\left(\underline{R}_\mu - \underline{R}_\nu\right)} \left(\underline{\underline{g}}_0 \right)_{\mu,\nu} \; . \tag{4.45}$$

With equation (4.45) the scalar version of equation (4.38) in the full Brillouin zone is regained. It is important to notice that $g_{\underline{k}}$ does not enter the CDMFT iteration cycle and therefore is not a self-consistent lattice quantity. Nevertheless it is shown in [Kot01] that the CDMFT is derivable from a Baym-Kadanoff functional Φ and is thermodynamically consistent. In other words, observables calculated from the lattice Greenfunction $G_{\underline{k}}$ agree with those calculated as derivates from the grand potential Ω.

4.5 Beyond the cluster approximations: DMFT2S

The previously defined cluster schemes map the lattice problem onto an effective cluster impurity problem, and it is evident that they cannot capture spatial correlations beyond the extent of this cluster. Reliable solutions of larger cluster impurity models are numerically very costly, and practical applications are limited to very small clusters with only some sites in it. Applied to a lattice model in the regime under consideration, one should therefore always critically check whether the essential physics is captured by short range correlations and that results are not strongly affected by finite size effects. Furthermore the question of how translational invariance of lattice quantities is implemented in these schemes is very subtle and leads e.g. to different scaling behaviors of the implemented cluster size towards the exact solution, which is an infinitely large cluster [Bir02].

In the mapping to an effective N-impurity model these cluster schemes place the N effective impurities on nearest neighbor sites. This specific geometrical placements restricts the contained spatial correlations to the size of the cluster. The basic idea of the DMFT2S approximation, introduced in this section, is to consider effective two-impurity clusters of all different impurity separations at the same time. Thereby short and long range correlations can be incorporated in this approximation scheme.

The DMFT mapping onto an effective single impurity problem, from that perspective is a scheme which includes exactly all those processes where electrons can get correlated at one site. All other correlations are included only approximately in the energy dependent irreducible T-matrix $\tilde{T}_0$. For a thorough derivation of the DMFT scheme from this viewpoint the reader is advised to consult [Gre05]. The here proposed extension of the DMFT can be characterized by the number of explictly correlated sites. That means the irreducible propagator (4.9) can be written as

$$g_{\underline{k}}^{-1} = (G^{(0)})^{-1} - \tilde{\Sigma}^{(1S)} - \tilde{\Sigma}_{\underline{k}}^{(2S)} - \tilde{\Sigma}_{\underline{k}}^{(3S)} - \dots \ . \tag{4.46}$$

The $\underline{k}$-independent first contribution $\tilde{\Sigma}^{(1S)}$ to the self-energy coincides with the DMFT self-energy

$$\tilde{\Sigma}^{(1S)} \equiv \tilde{\Sigma}^{(DMFT)} \ . \tag{4.47}$$

The next term $\tilde{\Sigma}_{\underline{k}}^{(2S)}$ in this expansion contains all spatial correlations between two sites and as such the first $\underline{k}$-dependent corrections to the DMFT.
In focus of this thesis is the calculation of $\tilde{\Sigma}_{\underline{k}}^{(2S)}$ exemplified for the Hubbard model. In the following this approximation will be termed DMFT2S, with the suffix 2S indicating that the DMFT is extended by the processes contained in $\tilde{\Sigma}_{\underline{k}}^{(2S)}$. The basic tool is a solver for a two-impurity problem, which captures the correlations between two sites with arbitrary distance. For the Hubbard model the relevant effective impurity model is the Two Impurity Anderson Model (TIAM), and the solvers at hand are generalizations of SNCA and ENCA approximations to the two impurity case, the SNCATI and ENCATI. Both methods were thoroughly introduced in chapters 2 and 3.

4.5.1 Introductory remarks on the DMFT2S presentation

The following derivation of the DMFT2S scheme is structurized in subsections, where different aspects of the simultaneous mapping of effective two-impurity models for various impurity distances to the lattice problem are discussed and finally a self consistent calculation scheme is presented. Due to the complexity of the problem it is reasonable to start the presentation of the DMFT2S with some introductory remarks on the proceedings.
The basic question for the formulation of an effective lattice theory, which reduces the complexity of the lattice problem onto one or more effective two-impurity problems, concerns the identification of an effective two-impurity quantity, which can be mapped onto the corresponding lattice quantity.

In subsection 4.5.2 the translational invariance of lattice quantities in contrast to two-impurity quantities is investigated. Already for one definite two-impurity cluster the argumentation in this subsection leads to only one possible mapping candidate.

This candidate, later to be defined as the irreducible two-impurity propagator $\underline{\underline{g}}^{(2imp),\underline{d}}$, is discussed in detail in subsection 4.5.3. There the embedding procedure of $\underline{\underline{g}}^{(2imp),\underline{d}}$ to the lattice for only one two-impurity separation $\underline{d}$ is presented.

Subsection 4.5.4 deals with the synchronous mapping of effective two-impurity models for different separation vectors $\underline{d}$ onto the lattice, i.e. how a multitude of different irreducible two impurity propagators $\underline{\underline{g}}^{(2imp),\underline{d}_i}$ can be used to approximate the same lattice problem. Furthermore it is explained in detail how three- or more site correlations are approximated within DMFT2S.

The presentation of the DMFT2S concludes with subsection 4.5.5, where a self-consistent calculation scheme of this approximation is introduced.

4.5.2 Translational invariance

In this section the structural differences of the Equations for real-space lattice Greenfunctions $G_{\underline{0}}$, $G_{\underline{d}}$ to the corresponding Equations two-impurity Greenfunction with impurity distance $\underline{d}$ is eludicated. In order to keep the line of reasoning simple for the presentation of the DMFT2S scheme, it is helpful for the start to assume a one-dimensional lattice, i.e $R_i = \underline{R}_i$, and that relative to any particular site R_0 only correlations between the two sites with distance |d| exist. For the one-dimensional lattice it follows that only g_0, g_d and g_{-d} need to be considered for the real space representation of irreducible lattice propagator defined in Equation (4.9). These restrictions will be dropped at an appropriate point in the proceeding.

With only g_0 and $g_{\pm d}$ the exact T matrix relation for the real space lattice Greenfunctions G_0 and $G_{\pm d}$ defined in Equation (4.22) simplifies to

$$\begin{aligned} G_0 =& g_0 + g_0 T_0 g_0 + g_d T_0 g_{-d} + g_{-d} T_0 g_d + g_0 T_d g_{-d} + g_0 T_{-d} g_d + g_{-d} T_d g_0 \\ &+ g_d T_{-d} g_0 + g_{-d} T_{2d} g_{-d} + g_d T_{-2d} g_d \\ =& g_0 + g_0 T_0 g_0 + g_d T_0 g_{-d} + \; g_d T_{-d} g_0 + \; g_0 T_d g_{-d} + \; L_0^{(d)} \end{aligned} \tag{4.48}$$

with

$$L_0^{(d)} = g_{-d} T_{2d} g_{-d} + \; g_d T_{-2d} g_d + \; g_{-d} T_0 g_d + \; g_{-d} T_d g_0 + \; g_0 T_{-d} g_d \; . \tag{4.49}$$

Here the quantity $L_0^{(d)}$ is introduced for the comparison with the corresponding Equation for the two-impurity Greenfunction undertaken later on. Similarly it follows for G_d

$$\begin{aligned} G_d =& g_d + g_0 T_d g_0 + g_d T_d g_{-d} + g_{-d} T_d g_d + g_0 T_{2d} g_{-d} + g_0 T_0 g_d + g_d T_{-d} g_d \\ &+ g_d T_0 g_0 + g_{-d} T_{2d} g_0 + g_{-d} T_{3d} g_{-d} \\ =& g_d + g_0 T_d g_0 + g_0 T_0 g_d + g_d T_d g_{-d} + g_d T_{-d} g_d + \; L_d \end{aligned} \tag{4.50}$$

with

$$L_d = g_{-d} T_d g_d + g_d T_0 g_0 + g_{-d} T_{2d} g_0 + g_0 T_{2d} g_{-d} + g_{-d} T_{3d} g_{-d} \; . \tag{4.51}$$

G_{-d} and L_{-d} can be simply obtained by interchanging $g_d \leftrightarrow g_{-d}$ and $T_x \leftrightarrow T_{-x}$ in Equations (4.50) and (4.51).

By introducing the matrix notation

$$\underline{\underline{G}}^{(d)} = \begin{pmatrix} G_{R_0,R_0} & G_{R_0,R_d} \\ G_{R_d,R_0} & G_{R_d,R_d} \end{pmatrix} = \begin{pmatrix} G_0 & G_d \\ G_{-d} & G_0 \end{pmatrix} \quad \text{with} \quad R_d - R_0 = d, \tag{4.52}$$

where translational invariance $G_{R_0,R_d} = G_{R_d-R_0}$ is assumed and $\underline{\underline{g}}^{(d)}, \underline{\underline{T}}^{(d)}, \underline{\underline{L}}^{(d)}$ accordingly defined, one obtains the matrix equation

$$\underline{\underline{G}}^{(d)} = \underline{\underline{g}}^{(d)} + \underline{\underline{g}}^{(d)}\,\underline{\underline{T}}^{(d)}\,\underline{\underline{g}}^{(d)} + \underline{\underline{L}}^{(d)} \tag{4.53}$$

for the three lattice Greenfunctions involving the sites R_0, R_d.

Equation (4.53) splits the contributions to the three lattice Greenfunctions into two parts. The first two terms on the right hand side of the equation explicitly connect only the two picked sites R_0 and R_d. $\underline{\underline{L}}^{(d)}$ contains terms which explicitly connects these sites R_0 and/or R_d with site R_{-d} (see Figure 4.4). It will be shown in the following that these $\underline{\underline{L}}^{(d)}$ are manifestations of the translational invariance of the lattice Greenfunctions and are structurally absent in the corresponding two-impurity Greenfunctions.

For an effective two-impurity model with the impurity sites at 0 and $\underline{d}$ structurally similar equations can be defined for the two-impurity Greenfunction. With the definition

$$\underline{\underline{G}}^{(2imp),d} = \begin{pmatrix} G_0^{(2imp),d} & G_d^{(2imp)} \\ G_{-d}^{(2imp)} & G_0^{(2imp),d} \end{pmatrix} \tag{4.54}$$

of the two-impurity Greenfunction matrix for impurities separated by the distance d, the two-impurity equation can be written as

$$\underline{\underline{G}}^{(2imp),d} = \underline{\underline{g}}^{(2imp),d} + \underline{\underline{g}}^{(2imp),d}\underline{\underline{T}}^{(2imp),d}\underline{\underline{g}}^{(2imp),d} \tag{4.55}$$

or written out in components

$$\begin{aligned} G_0^{(2imp),d} =& g_0^{(2imp),d} + g_0^{(2imp),d} T_0^{(2imp),d} g_0^{(2imp),d} + g_d^{(2imp)} T_0^{(2imp),d} g_{-d}^{(2imp)} \\ &+ g_0^{(2imp),d} T_{-d}^{(2imp),d} g_d^{(2imp)} \end{aligned} \tag{4.56}$$

$$\begin{aligned} G_d^{(2imp),d} =& g_d^{(2imp)} + g_0^{(2imp),d} T_d^{(2imp)} g_0^{(2imp),d} + g_d^{(2imp)} T_d^{(2imp)} g_{-d}^{(2imp)} \\ &+ g_d^{(2imp)} T_0^{(2imp),d} g_0^{(2imp),d} \,, \end{aligned} \tag{4.57}$$

where the reducible two-impurity T matrix $\underline{\underline{T}}^{(2imp),d}$ and the irreducible two-impurity propagator $\underline{\underline{g}}^{(2imp),d}$ were introduced.

Comparison of the structure of equation (4.48) with (4.56) and equation (4.50) with (4.57) reveals that, unlike in the equivalent DMFT equations where only g_0 and T_0 need to be considered, the lattice Greenfunctions in the projected approximation have the additional terms $L_0^{(d)}$ and L_d.

These terms stem from the translational invariance of the lattice quantities g_d,g_{-d} and T_x and the correlations induced by this.

A diagrammatic sketch of the terms contained in $L_0^{(d)}$ for $d = 1$ is depicted in Figure (4.4). In the first two contributions the sites R_{-1} and R_1 are connected by a T matrix which tides over site R_0, Thereby the two diagrams involve the presence of 3 sites which for obvious reasons is not contained in a two impurity model. The three diagrams below correlate site R_0 with site R_{-1} which is also beyond the scope of an effective two-impurity model if

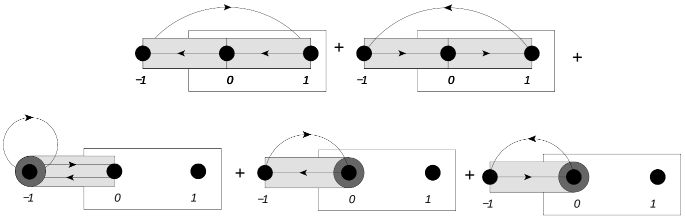

Figure 4.4: Diagrammatic sketch of the terms in $L_0^{(d)}$ from equation (4.48) with $d = 1$. All diagrams correlate sites which do not belong to the two picked sites R_0 and R_1. The two picked sites are indicated by the unfilled box. The two diagrams which involve the T-matrix for distance $|d| = 2$ are shown on the top and the other 3 terms which involve only two neighboring sites are shown below. The arced arrow represents the T-matrix, the filled box with the arrow in it g_1 or g_{-1} and the darker filled blob g_0.

the two-impurity sites are chosen to be R_0 and R_1 as indicated by the unfilled box in the diagrams. As sites R_0 and R_1 are correlated in the two impurity model the correct incorporation of the three bottom diagrams would therefore also correlate more than two sites. The situation is similar for the terms contained in L_1 and L_{-1}. So by the virtue of the terms in $\underline{\underline{L}}^{(d)}$ it is evident that the translational invariance of the lattice Greenfunction cannot be mapped on the Greenfunction of a two-impurity model. This is the reason why the CDMFT-scheme presented in section 4.4 violates translational invariance.

Even more, the $\underline{\underline{L}}^{(d)}$ contains two site correlations between $\underline{R}_0$ and $\underline{R}_{-d}$, e.g. in the last three terms of $L_0^{(d)}$, which are not contained in $\underline{\underline{G}}^{(2imp),d}$. On the other hand it is the aim of the DMFT2S approximation to incorporate these two-site correlations. By the virtue of the additional $\underline{\underline{L}}^{(d)}$-term in $\underline{\underline{G}}^{(d)}$ it is evident that an effective two-impurity Greenfunction $\underline{\underline{G}}^{(2imp),d}$ cannot be mapped to the corresponding lattice Greenfunction in the projected lattice approximation.

4.5.3 Mapping for one two-impurity separation

The discussion in the preceeding subsection showed that - unlike in the DMFT - within the DMFT2S no effective irreducible T-matrix $\underline{\underline{\tilde{T}}}^{(d)}$ can be identified, so that the lattice Greenfunction would coincide with the corresponding impurity Greenfunction as functional of an effective irreducible T-matrix

$$\underline{\underline{G}}^{(d)} \neq \underline{\underline{G}}^{(2imp),d}[\underline{\underline{\tilde{T}}}^{(d)}] \tag{4.58}$$

with

$$\begin{aligned} \underline{\underline{G}}^{(2imp),d}[\underline{\underline{\tilde{T}}}^{(d)}] &= \underline{\underline{g}}^{(2imp),d} + \underline{\underline{g}}^{(2imp),d}\underline{\underline{\tilde{T}}}^{(d)}\underline{\underline{g}}^{(2imp),d} \qquad (4.59) \\ &\quad + \underline{\underline{g}}^{(2imp),d}\underline{\underline{\tilde{T}}}^{(d)}\underline{\underline{g}}^{(2imp),d}\underline{\underline{\tilde{T}}}^{(d)}\underline{\underline{g}}^{(2imp),d} + \dots \\ &= \left[\left(\underline{\underline{g}}^{(2imp),d}\right)^{-1} - \underline{\underline{\tilde{T}}}^{(d)}\right]^{-1} . \qquad (4.60) \end{aligned}$$

In other words the two-impurity Greenfunction contains only the correlations between two explicit sites, while the lattice Greenfunction contains the correlations between each pair of sites with that distance.

A more promising candidate for the mapping of a lattice quantity to an effective two-impurity quantity is the irreducible lattice propagator $\underline{\underline{g}}^{(d)}$. The diagonal part g_0 contains the irreducible purely local contributions which -in contrast to the DMFT g_0 - incorporate the $\underline{k}$-independent correlated contributions of all sites with distance $|d|$. In the off-diagonal part $g_{\pm d}$ only two sites with distance d are explictly correlated.

It will be explained in the following, that the two-impurity propagator $\underline{\underline{g}}^{(2imp),d}$ has a slightly different meaning. Therefore, a direct mapping in the form $\underline{\underline{g}}^{(2imp),d} = \underline{\underline{g}}^{(d)}$ to an effective impurity model cannot be undertaken.
First of all, for sites which are directly connected by a hopping matrix element, e.g. nearest neighbor sites, $\underline{\underline{g}}^{(2imp),d}$ is still reducible towards the direct hopping processes t between the two impurity sites (see Figure 4.5).
The irreducible lattice propagators g_0 and g_d are irreducible with respect to all hopping processes t. The reducible inter-impurity hopping processes can be excluded from $\underline{\underline{g}}^{(2imp),1}$ with the help of a further Dyson-equation

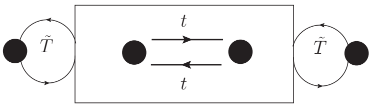

Figure 4.5: In the TIAM solution for $\underline{\underline{g}}^{(2imp),1}$; the nearest neighbor impurity-sites in the box are still connected by reducible direct hopping processes t. $\underline{\underline{g}}^{(2imp),1}$ is only irreducible with respect to the propagations involving the uncorrelated outer sites, which are described by the irreducible T-matrix $\underline{\underline{\tilde{T}}}^{(1)}$

$$
\begin{aligned}
\underline{\underline{g}}^{(2imp),d} =& \underline{\underline{\tilde{g}}}^{(2imp),d} + \underline{\underline{\tilde{g}}}^{(2imp),d} \, \underline{\underline{t}}^{(d)} \, \underline{\underline{g}}^{(2imp),d} && (4.61) \\
\underline{\underline{\tilde{g}}}^{(2imp),d} =& \left[\left(\underline{\underline{g}}^{(2imp),d} \right)^{-1} + \underline{\underline{t}}^{(d)} \right]^{-1} , && (4.62)
\end{aligned}
$$

where for the Hubbard model with nearest neighbor hopping $\underline{\underline{t}}^{(d)}$ is given by

$$
\underline{\underline{t}}^{(d)} = t \begin{pmatrix} 0 & \delta_{|d|,1} \\ \delta_{|d|,1} & 0 \end{pmatrix} . \tag{4.63}
$$

The two-impurity propagator $\underline{\underline{\tilde{g}}}^{(2imp),d}$ introduced is now irreducible with respect to all hopping processes.

In terms of $\underline{\underline{\tilde{g}}}^{(2imp),d}$ the two-impurity Greenfunction is given by

$$
\begin{aligned}
\underline{\underline{\tilde{G}}}^{(2imp),d} =& \underline{\underline{\tilde{g}}}^{(2imp),d} + \underline{\underline{\tilde{g}}}^{(2imp),d} \left(\underline{\underline{t}}^{(d)} + \underline{\underline{\tilde{T}}}^{(d)} \right) \underline{\underline{\tilde{g}}}^{(2imp),d} + \dots && (4.64) \\
=& \left[\left(\underline{\underline{\tilde{g}}}^{(2imp),d} \right)^{-1} - \underline{\underline{t}}^{(d)} - \underline{\underline{\tilde{T}}}^{(d)} \right]^{-1} && (4.65)
\end{aligned}
$$

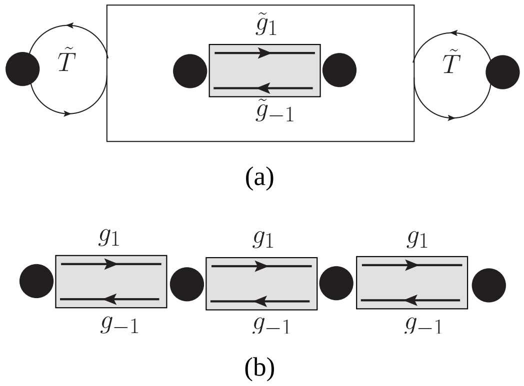

Figure 4.6: (a) 4-site lattice from the viewpoint of the TIAM, only two sites are connected by $\tilde{g}_{\pm 1} \equiv \tilde{g}^{(2imp)}_{\pm 1}$. (b) For the irreducible lattice propagator all nearest neighbor sites are connected by $g_{\pm 1}$.

and thus appears in the following explicit expression for the irreducible propagator:

$$\tilde{\underline{\underline{g}}}^{(2imp),d} = \left[\left(\underline{\underline{G}}^{(2imp),d} \right)^{-1} + \underline{\underline{t}}^{(d)} + \underline{\underline{\tilde{T}}}^{(d)} \right]^{-1} . \tag{4.66}$$

For the mapping of the two-impurity model to the lattice $\tilde{\underline{\underline{g}}}^{(2imp),d}$ is from now on the quantity under consideration.

Unfortunately the processes in $\tilde{\underline{\underline{g}}}^{(2imp),d}$ still differ qualitatively from those in $\underline{\underline{g}}^{(d)}$. These differences will in the following be inspected in detail.

The difference is connected to the missing translational invariance of the spatial correlations included in an effective two-impurity model and is closely related to the observations undertaken in subsection 4.5.2. An example is depicted in Figure 4.6. There the configuration for a lattice with four sites is shown. Figure 4.6(a) shows the lattice setup from the viewpoint of a two-impurity solver for nearest neighbor impurities ($d = 1$). The two central sites represent the two impurities, the irreducible propagator connects only the impurity sites, while the outer sites to the left and right are not reached by the off-diagonal parts of $\tilde{\underline{\underline{g}}}^{(2imp),1}$. Processes to these sites can in the TIAM only be implemented by the irreducible T-matrix $\underline{\underline{\tilde{T}}}^{(1)}$. The desired situation for a translationally invariant irreducible lattice propagator is shown in Figure 4.6(b). Here all nearest neighbor sites are connected by the off-diagonal irreducible lattice propagators $\underline{\underline{g}}^{(1)}$. The two-impurity extension to the DMFT proposed so far [Sch95, Geo96] neglects the different roles of the irreducible impurity propagator $\tilde{\underline{\underline{g}}}^{(2imp),d}$ and the irreducible band propagator $\underline{\underline{g}}^{(d)}$. Apart from some differences in the formulation of the problem, there the mapping of the lattice problem to an effective two-impurity problem is in essence undertaken by

$$\underline{\underline{g}}^{(d)} \longleftrightarrow \tilde{\underline{\underline{g}}}^{(2imp),d} . \tag{4.67}$$

The causality violations for the lattice Greenfunction reported by the authors[1] of these works originate from this kind of mapping.

Equation (4.67) formulates an identity between two irreducible quantities, but the irreducibility of $\underline{\underline{\tilde{g}}}^{(2imp),d}$ is a different irreducibility than the one of $\underline{\underline{g}}^{(d)}$. $\underline{\underline{\tilde{g}}}^{(2imp),d}$ is irreducible with respect to a random walk between the impurities, expressed by the two-impurity Dyson-equation (4.64). Among others, the irreducible two-impurity T-matrix $\underline{\underline{\tilde{T}}}^{(d)}$ contains processes with intermediate visits of sites at distance $\pm d$, which are not part of the two-impurity cluster and are effectively non-interacting. In the random walk, generated by the two-impurity Dyson-equation, these intermediate visits are subsequently generated. Due to the irreducibility of $\underline{\underline{\tilde{g}}}^{(2imp),d}$ with respect to this random walk $\underline{\underline{\tilde{g}}}^{(2imp),d}$ inhibits the correct number of counterterms for processes which cannot be described by a random walk. In these counterterms all sites, except the two impurity sites, are treated as effectively non-interacting. Among them are the counterterms for the sites at distance $\pm d$, which do not belong to the impurity cluster.
Simply stated, $\underline{\underline{\tilde{g}}}^{(2imp),d}$ is only irreducible with respect to a random walk through a lattice with exactly two sites at distance d with local Coulomb-interaction U. The irreducibility of the corresponding lattice propagator $\underline{\underline{g}}^{(d)}$ within the two-site approximation is a different one. The translational invariance of lattice quantities imposes that $\underline{\underline{g}}^{(d)}$ must be irreducible with respect to a random walk through the lattice, where all equivalent placements of two-impurity clusters with distance d are treated in the same fashion. A mapping in the form $\underline{\underline{g}}^{(d)} \longleftrightarrow \underline{\underline{\tilde{g}}}^{(2imp),d}$ mixes two different kinds of irreducibilities and lead in a self-consistent approximation to an acausal behavior of physical quantities. A related but more formal way to understand the causality violation imposed by the mapping in equation (4.67) can be deduced from the $\underline{k}$-dependent lattice Dyson-equation (4.8) for the lattice Greenfunction $G_{\underline{k}}$. A definite imaginary part of the lattice Greenfunction

$$Im(G_{\underline{k}}) < 0 \tag{4.68}$$

implies necessarily the condition

$$Im(g_{\underline{k}}) = Im\left(\sum_{\underline{d}} g_{\underline{d}} e^{i\underline{k}\,\underline{d}}\right) < 0 \qquad \forall \underline{k}. \tag{4.69}$$

If only the site $\underline{d} = 0$ and the spatial correlations to sites with $|\underline{d}| = d$ in the n-dimensional sc-lattice are considered this condition reduces to

$$Im\left(g_{\underline{k}}\right) = Im(g_0) + 2Im(g_d) \sum_{k_i=1}^{n} \cos(k_i d_i) \ < 0 \qquad \forall \underline{k}, \tag{4.70}$$

where $g_{\underline{d}} = g_d$ is assumed. As $\underline{k}$ is arbitrary for this consideration, the maximum contribution of the g_d term is given by $k_i = 0$ or $k_i = \frac{\pi}{d_i}$, i.e.

$$Im(g_0) \pm 2nIm(g_d) < 0 \tag{4.71}$$

---

[1] These violations were never explicitly published, some vague comments concerning this issue can be found in [Mai05]

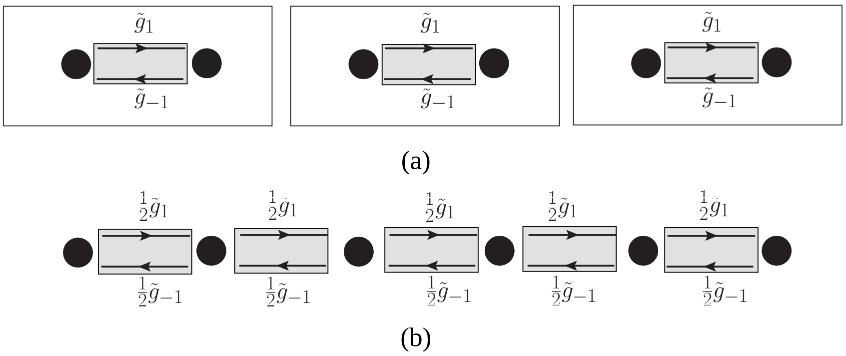

Figure 4.7: (a) lattice out of two-impurity clusters connected by the irreducible impurity propagator $\tilde{g}_{\pm1} \equiv \tilde{g}_{\pm1}^{(2imp)}$ (b) mapping of the averaged irreducible effective two-impurity propagator to the irreducible lattice propagator $g_{\pm1} = \frac{1}{2}\tilde{g}_{\pm1}^{(2imp)}$ (compare Figure 4.6(b)). All lattice sites are equally connected.

with n the dimension of the lattice. Using $\tilde{g}_d^{(2imp)}$ for g_d as proposed in Equation (4.67) the relation (4.71) can only be fulfilled, if $Im(\tilde{g}_d^{(2imp)})$ decays at least like $\frac{1}{2n}$ in the effective two-impurity model.
Practical calculations for $d = 1$ show, that the condition (4.71) for dimension $n = 1$ is already violated. For low temperatures $\tilde{g}_0^{(2imp),1}$ and $\tilde{g}_1^{(2imp)}$ have about the same order of magnitude. Only the less restrictive condition

$$-Im\left(\tilde{g}_0^{(2imp),1}\right) > |Im\left(\tilde{g}_1^{(2imp)}\right)| \tag{4.72}$$

can be deduced from the definite imaginary part of the even/odd two-impurity Greenfunction (see Equations (3.49) and (3.50)).

The causality can be preserved if the missing translational invariance of the irreducible impurity propagators $\tilde{g}_{\pm1}^{(2imp)}$ is taken seriously, i.e. equivalent effective two-impurity placements need to be treated in the same way for a correct mapping to the irreducible lattice propagator.

This can be achieved, by representing the lattice in the form of two-impurity clusters (see Figure 4.7(a)) and average the irreducible impurity propagators between all lattice sites with the same distance. The resulting configuration, for a setup of impurity clusters with nearest neighbor impurity sites depicted in Figure 4.7(b), is translationally invariant. The proposed mapping of an effective irreducible two-impurity propagator to the lattice propagator is therefore

$$g_0 = \frac{1}{2}\left(\tilde{g}_0^{(2imp),d} + \tilde{g}_0^{(2imp),-d}\right) = \tilde{g}_0^{(2imp),d}\,, \tag{4.73}$$

$$g_{\pm d} = \frac{1}{2}\tilde{g}_{\pm d}^{(2imp)} = \frac{1}{2}\tilde{g}_d^{(2imp)}, \tag{4.74}$$

where the identity $\underline{\underline{\tilde{g}}}^{(2imp),d} = \underline{\underline{\tilde{g}}}^{(2imp),-d}$ was used.

For the mapping procedure described above it is not necessary to consider two-impurity clusters in a one-dimensional lattice only. The generalization to a n-dimensional lattice is easy. The distance between two impurities is then characterized by a distance-vector $\underline{d} = \underline{R}_d - \underline{R}_0$, and for a given distance vector $\underline{d}$ there exist more symmetry-related two-impurity placements, i.e. the crystal surrounding looks the same for these pair placements. Necessarily, for these symmetry-related distance-vectors $\underline{d}'$ the condition $\underline{\underline{\tilde{g}}}^{(2imp),\underline{d}} = \underline{\underline{\tilde{g}}}^{(2imp),\underline{d}'}$ is fulfilled. For the Hubbard model on a sc-lattice and a given distance-vector $\underline{d} = (d_x, d_y, d_z)^T$ the set of symmetry related distance-vectors $\mathcal{S}(\underline{d})$ can be obtained from the transformations

$$d_i \longrightarrow -d_i \tag{4.75}$$

$$d_i \longleftrightarrow d_j. \tag{4.76}$$

As example, for the nearest neighbor distance-vector $\underline{d}_1 = (1,0,0)^T$ the vectors in the same symmetry group are

$$\mathcal{S}(\underline{d}_1) = \{\pm \begin{pmatrix} 1 \\ 0 \\ 0 \end{pmatrix}, \pm \begin{pmatrix} 0 \\ 1 \\ 0 \end{pmatrix}, \pm \begin{pmatrix} 0 \\ 0 \\ 1 \end{pmatrix}\}, \tag{4.77}$$

which are all nearest neighbor sites in the three-dimensional sc-lattice. The mapping of the irreducible impurity propagator to the irreducible lattice propagator for one representative distance vector $\underline{d}$ is therefore

$$\begin{aligned} g_0 =& \frac{1}{N_{\underline{d}}} \sum_{\underline{d}' \in \mathcal{S}(\underline{d})} \tilde{g}_0^{(2imp),\underline{d}'} = \frac{1}{N_{\underline{d}}} \sum_{i=1}^{N_{\underline{d}}} \tilde{g}_0^{(2imp),\underline{d}} \\ =& \tilde{g}_0^{(2imp),\underline{d}} \end{aligned} \tag{4.78}$$

$$g_{\underline{d}'} = \begin{cases} \frac{1}{N_{\underline{d}}} \tilde{g}_{\underline{d}}^{(2imp)} & \forall\ \underline{d}' \in \mathcal{S}(\underline{d}) \\ 0 & \text{otherwise} \end{cases} \tag{4.79}$$

where $N_{\underline{d}}$ is the number of elements in $\mathcal{S}(\underline{d})$, e.g. $N_{\underline{d}_1} = 2n$ in the n-dimensional sc-lattice.

The $\underline{k}$-dependent irreducible lattice propagator, from which the lattice Greenfunction $G_{\underline{k}}$ can be deduced via equation (4.8), is then given by Fourier-transformation

$$g_{\underline{k}} = \tilde{g}_0^{(2imp),\underline{d}} + \frac{1}{N_{\underline{d}}} \tilde{g}_{\underline{d}}^{(2imp)} \sum_{\underline{d}' \in \mathcal{S}(\underline{d})} e^{i\underline{k}\,\underline{d}'} \tag{4.80}$$

$$= \tilde{g}_0^{(2imp),\underline{d}} + \frac{1}{N_{\underline{d}}} \tilde{g}_{\underline{d}}^{(2imp)} \sum_{\underline{d}' \in \mathcal{S}(\underline{d})} \cos(\underline{k}\ \underline{d}'). \tag{4.81}$$

4.5.4 Mapping for more than one impurity separation

Up to this point in the presentation the DMFT2S includes only spatial correlations between sites which lie in the symmetry group $\mathcal{S}(\underline{d})$ of one representative distance-vector $\underline{d}$. Physically such an approximation is most interesting for $\underline{d} = \underline{d}_1$, as the strongest spatial correlations are expected for nearest neighbor sites. However, the targeted aim of the DMFT2S is to include also spatial correlation with further distance-vectors, e.g. $\underline{d}_2 = (2,0,0)^T$ and/or $\underline{d}_{1,1} = (1,1,0)^T$ as representative distance-vectors. The inclusion of further spatial correlations can only be achieved by the mapping of additional effective TIAM's (one for each representative distance vector) to the lattice problem.

Unfortunately, there is no unique way to do this. Therefore, after a short characterization of the problem, two different possible approaches will presented. The first approach will then be dropped as candidate for the DMFTS2S for physical reasons, while the second approach constitutes the mapping scheme of the DMFT2S.
In order to keep the line of reason simple, the problem will be discussed for the representative distance-vectors $\underline{d}_1$ and $\underline{d}_2$.

The solution of the two-impurity problem for these distances yields the irreducible impurity propagators

$$\underline{\underline{\tilde{g}}}^{(2imp),\underline{d}_1} = \begin{pmatrix} \tilde{g}_0^{(2imp),\underline{d}_1} & \tilde{g}_{\underline{d}_1}^{(2imp)} \\ \tilde{g}_{-\underline{d}_1}^{(2imp)} & \tilde{g}_0^{(2imp),\underline{d}_1} \end{pmatrix} \qquad \text{and} \tag{4.82}$$

$$\underline{\underline{\tilde{g}}}^{(2imp),\underline{d}_2} = \begin{pmatrix} \tilde{g}_0^{(2imp),\underline{d}_2} & \tilde{g}_{\underline{d}_2}^{(2imp)} \\ \tilde{g}_{-\underline{d}_2}^{(2imp)} & \tilde{g}_0^{(2imp),\underline{d}_2} \end{pmatrix} . \tag{4.83}$$

The diagonal entries of these matrices already show the problem for the mapping of these quantities to the lattice propagator. Both $\tilde{g}_0^{(2imp),\underline{d}_1}$ and $\tilde{g}_0^{(2imp),\underline{d}_2}$ are local quantities and both have to be mapped to the one local irreducible lattice propagator g_0. Even if it would be possible to map the off-diagonal impurity propagators via an equation like (4.79) to the corresponding effective lattice propagators, the mapping procedure to the local irreducible lattice propagator g_0 remains unclear.

One has to keep in mind, that $\underline{\underline{\tilde{g}}}^{(2imp),\underline{d}_1}$ and $\underline{\underline{\tilde{g}}}^{(2imp),\underline{d}_2}$ are only irreducible with respect to the random walk expressed by the corresponding two-impurity Dyson-equation for that distance (see discussion below Equation (4.67)). The diagonal and off diagonal entries in $\underline{\underline{\tilde{g}}}^{(2imp),\underline{d}}$ are thereby delicately connected and the mapping of $\tilde{g}_0^{(2imp),\underline{d}_1}$ and $\tilde{g}_0^{(2imp),\underline{d}_2}$ to one g_0 needs to maintain this connection to $\tilde{g}_{\underline{d}_1}^{(2imp)}$ and $\tilde{g}_{\underline{d}_2}^{(2imp)}$ simultaneously. For the distance-vectors $\mathcal{S}(\underline{d})$ represented by $\underline{d}$ the balance between the diagonal and off-diagonal irreducible propagator is preserved through the mapping formula in Equations (4.78) and (4.79) by averaging the effective irreducible two-impurity propagators.

One possible approach to additionally include the spatial correlations from the distance vectors in the set $\mathcal{S}(\underline{d}_2)$ can be achieved by extending the averaging procedure for these further distance-vectors. With this idea the combined mapping procedure for the representative distance-vectors $\underline{d}_1$ and $\underline{d}_2$ is given by

$$g_0 = \frac{1}{N_{\underline{d}_1} + N_{\underline{d}_2}} \left(N_{\underline{d}_1}\, \tilde{g}_0^{(2imp),\underline{d}_1} + N_{\underline{d}_2}\, \tilde{g}_0^{(2imp),\underline{d}_2} \right) \tag{4.84}$$

$$g_{\underline{d}'} = \frac{1}{N_{\underline{d}_1} + N_{\underline{d}_2}} \begin{cases} \tilde{g}_{\underline{d}_1}^{(2imp)} & \forall\ \underline{d}' \in \mathcal{S}(\underline{d}_1) \\ \tilde{g}_{\underline{d}_2}^{(2imp)} & \forall\ \underline{d}' \in \mathcal{S}(\underline{d}_2) \\ 0 & \text{otherwise} \end{cases} . \tag{4.85}$$

Extensions of this scheme for the inclusion of further distance-vectors are straightforward. As any solution of the TIAM fulfills the condition

$$-Im(\tilde{g}_0^{(2imp),\underline{d}}) > |Im(\tilde{g}_{\underline{d}}^{(2imp)}|), \tag{4.86}$$

this mapping guarantees a causal lattice Greenfunction (see argumentation near equation (4.69)).

On the other hand this mapping scheme is not very physical. Spatial correlations become weaker the more distances are included. The strongest spatial correlations are expected for short distances. For large distances the effective non-diagonal irreducible two-impurity propagator is expected to vanish

$$\tilde{g}_{\underline{d}}^{(2imp)} \overset{|\underline{d}|\gg 1}{\longrightarrow} 0, \tag{4.87}$$

and the effective diagonal irreducible two-impurity propagator to limit in the effective SIAM or DMFT $(1S)$ propagator

$$\tilde{g}_{\underline{0}}^{(2imp),\underline{d}} \overset{|\underline{d}|\gg 1}{\longrightarrow} g_{\underline{0}}^{(1S)}. \tag{4.88}$$

The uniform averaging factor makes the contribution from each distance equally important. By including all distance-vectors only the large distances - with no spatial correlations - would effectively contribute, due to their greater number. The scheme would reduce the lattice problem to the DMFT approximation.

The mapping scheme of the DMFT2S approximation, to be presented now, preserves the spatial correlations if further representative distance-vectors are included. Unfortunately the author has no rigorous proof that this mapping scheme preserves the causality of the lattice Greenfunction. Nevertheless, the numerical calculations undertaken so far are very encouraging and show no signs of acausal behavior. The basic idea is to calculate an effective single-impurity propagator $g_{\underline{0}}^{(1S)}$, which contains no spatial correlations, and use this quantity to extract solely the spatial correlations via

$$\Delta\tilde{g}_0^{(2imp),\underline{d}} = \tilde{g}_0^{(2imp),\underline{d}} - g_{\underline{0}}^{(1S)} \tag{4.89}$$

from the effective irreducible local two-impurity propagator $\tilde{g}_0^{(2imp),\underline{d}}$. The irreducible local lattice propagator is then written as

$$\begin{aligned} g_0^{(2S)} =& g_0^{(1S)} + \frac{1}{N_{\underline{d}_1}} \sum_{\underline{d}'\in\mathcal{S}(\underline{d}_1)} \Delta\tilde{g}_0^{(2imp),\underline{d}'} + \frac{1}{N_{\underline{d}_2}} \sum_{\underline{d}'\in\mathcal{S}(\underline{d}_2)} \Delta\tilde{g}_0^{(2imp),\underline{d}'} + \ldots \\ =& g_0^{(1S)} + \Delta\tilde{g}_0^{(2imp),\underline{d}_1} + \Delta\tilde{g}_0^{(2imp),\underline{d}_2} + \ldots, \end{aligned} \tag{4.90}$$

i.e. as the single-impurity result with no spatial correlations and correction terms accounting for these correlations. The mapping of the off-diagonal irreducible two-impurity propagator remains in the form given by equation (4.79) but is extended to further representative distance vectors

$$g_{\underline{d}'}^{(2S)} = \begin{cases} \frac{1}{N_{\underline{d}_1}} \tilde{g}_{\underline{d}_1}^{(2imp)} & \text{for } \underline{d}' \in \mathcal{S}(\underline{d}_1) \\ \frac{1}{N_{\underline{d}_2}} \tilde{g}_{\underline{d}_2}^{(2imp)} & \text{for } \underline{d}' \in \mathcal{S}(\underline{d}_2) \\ \vdots & . \end{cases} \tag{4.91}$$

Equation (4.90) and equation (4.91) constitute the DMFT2S mapping scheme of the lattice problem to N effective two-impurity models, i.e. for each representative distance-vector $\underline{d}$ an effective two-impurity model !

In the following this mapping scheme will be investigated in more detail using the example of two representative distance-vectors $\underline{d}_1$ and $\underline{d}_2$, e.g. the nearest neighbor distances and the next nearest neighbor distances along one axis. The exact local irreducible lattice propagator g_0, which includes the spatial correlations between the sites represented by the distance-vector $\underline{d}_1$ and $\underline{d}_2$, contains in its internal loops three different kind of processes:

(i) loops which never involve the sites described by the representative distance-vectors $\underline{d}_1$ and $\underline{d}_2$.

(ii) loops which either involve visits on sites represented by $\underline{d}_1$ or by $\underline{d}_2$.

(iii) loops which involve visits on both sites represented by $\underline{d}_1$ and by $\underline{d}_2$.

The correlations induced by the loops in (i) are completely locally based and free of further correlations and therefore are also contained in the (1S)-approximation. The loops in (ii) correlate the sites only with one chosen representative distance-vector and should therefore be contained in the DMFT2S approximation.
The loops in (iii) correlate sites from both representative distance-vectors, and need therefore in the DMFT2S to be treated in an approximative way.

The contributions to the local irreducible lattice propagator within the DMFT2S approximation can therefore be subdivided as

$$g_0^{(2S)} = g_0^{(/1,/2)} + g_0^{(1,/2)} + g_0^{(/1,2)} + \hat{P}^{(2S)} g_0^{(1,2)}, \tag{4.92}$$

where $g_0^{(/1,/2)}$ corresponds to the processes described in (i), $g_0^{(1,/2)}$ and $g_0^{(/1,2)}$ to those in (ii) and $g_0^{(1,2)}$ with the processes in (iii). The operator $\hat{P}^{(2S)}$ dissolves spatial correlations which involve sites to more than one distance-vector, i.e. three site correlations, to two-site correlations. The specific way the operator does this shall be left unspecified at this moment. The local irreducible lattice propagator $g_0^{(1S)}$ from the mapping of the lattice problem to an effective SIAM contains in this sense the following contributions

$$g_0^{(1S)} = g_0^{(/1,/2)} + \tilde{g}_0^{(1,/2)} + \tilde{g}_0^{(/1,2)} + \tilde{g}_0^{(1,2)}. \tag{4.93}$$

A tilde on the different g_0's indicate that visits to the sites characterized by the representative distance-vectors $\underline{d}_1$ and $\underline{d}_2$ are contained only by effective free propagations in the internal loops and therefore contain no spatial correlations to these sites.

The processes contained in the effective irreducible local two impurity propagator $\tilde{g}_0^{(2imp),\underline{d}_1}$ are the following

$$\tilde{g}_0^{(2imp),\underline{d}_1} = g_0^{(/1,/2)} + \tilde{g}_0^{(/1,2)} + g_0^{(1,/2)} + \hat{P}_1 g_0^{(1,2)} \ , \tag{4.94}$$

where the operator $\hat{P}_1$ dissolves all spatial correlations apart from those with the sites represented by the distance-vector $\underline{d}_1$. A more detailed inspection of the properties of the

operators $\hat{P}_x$ and $\hat{P}^{2S}$ will be undertaken later-on.
The term $\tilde{g}_0^{(/1,2)}$ in equation (4.94) has no counterpart in $g_0^{(2S)}$, as here internal loops visit sites of the representative distance-vector $\underline{d}_2$ but no spatial correlations are induced for this distance-vector. Within the two-impurity solution for $\underline{d}_1$, these visiting processes are included only on the level of a single impurity approximation and are as such also included in $g_0^{(1S)}$ (see equation (4.93)). The correct DMFT2S contribution $g_0^{(/1,2)}$ is contained in the effective irreducible two-impurity propagator for the representative distance-vector $\underline{d}_2$

$$\tilde{g}_0^{(2imp),\underline{d}_2} = g_0^{(/1,/2)} + g_0^{(/1,2)} + \tilde{g}_0^{(1,/2)} + \hat{P}_2 g_0^{(1,2)} \ . \tag{4.95}$$

On the other hand $\tilde{g}_0^{(2imp),\underline{d}_2}$ contains the spatially uncorrelated contribution $\tilde{g}_0^{(1,/2)}$, but is included correctly in $\tilde{g}_0^{(2imp),\underline{d}_1}$. For a better overview, all contributions to the different local irreducible propagators are summarized below

$$g_0^{(2S)} = g_0^{(/1,/2)} + g_0^{(1,/2)} + g_0^{(/1,2)} + \hat{P}^{(2S)} g_0^{(1,2)} \tag{4.96}$$

$$\tilde{g}_0^{(2imp),\underline{d}_1} = g_0^{(/1,/2)} + \tilde{g}_0^{(/1,2)} + g_0^{(1,/2)} + \hat{P}_1 g_0^{(1,2)} \tag{4.97}$$

$$\tilde{g}_0^{(2imp),\underline{d}_2} = g_0^{(/1,/2)} + \tilde{g}_0^{(1,/2)} + g_0^{(/1,2)} + \hat{P}_2 g_0^{(1,2)} \tag{4.98}$$

$$g_0^{(1S)} = g_0^{(/1,/2)} + \tilde{g}_0^{(1,/2)} + \tilde{g}_0^{(/1,2)} + \tilde{g}_0^{(1,2)} . \tag{4.99}$$

A tilde on the different g_0's on the right hand side indicate that visits of the sites represented by the distance-vectors $\underline{d}_1$ and/or $\underline{d}_2$ are contained only as free propagations in the internal loops and therefore are treated uncorrelated. Now a quantity p_0 is introduced by the linear combination

$$\begin{aligned} p_0 &= g_0^{(1S)} + \Delta\tilde{g}_0^{(2imp),\underline{d}_1} + \Delta\tilde{g}_0^{(2imp),\underline{d}_2} \\ &= g_0^{(1S)} + \left(\tilde{g}_0^{(2imp),\underline{d}_1} - g_0^{(1S)}\right) + \left(\tilde{g}_0^{(2imp),\underline{d}_2} - g_0^{(1S)}\right) \\ &= \tilde{g}_0^{(2imp),\underline{d}_1} + \tilde{g}_0^{(2imp),\underline{d}_2} - g_0^{(1S)} \end{aligned} \tag{4.100}$$

by inserting equations (4.97), (4.98) and (4.99) one obtains

$$p_0 = g_0^{(/1,/2)} + g_0^{(1,/2)} + g_0^{(/1,2)} + \left(\hat{P}_1 + \hat{P}_2\right) g_0^{(1,2)} - \tilde{g}_0^{(1,2)} \ . \tag{4.101}$$

It will now be argued that p_0 can be identified with $g_0^{(2S)}$, i.e.

$$g_0^{(2S)} = p_0 \ , \tag{4.102}$$

or more explicitly by comparison with equation (4.96)

$$\hat{P}^{(2S)} g_0^{(1,2)} = \hat{P}_1 g_0^{(1,2)} + \hat{P}_2 g_0^{(1,2)} - \tilde{g}_0^{(1,2)} . \tag{4.103}$$

So far, the DMFT2S was only defined by the demand that it should contain two-site correlations. But this left completely unspecified how three- or more site correlations between sites with different representative distance-vectors should be approximated. In principle, there is no unique way to do this. For the three-site correlations contained in $g_0^{(1,2)}$ there would, for example, be the possibility to retain only the spatial correlations with the representative distance-vector $\underline{d}_1$, or with $\underline{d}_2$ or any linear combination of these cases. Even the case of considering no spatial correlations at all and approximate $g_0^{(1,2)}$ by the corresponding $g_0^{(1S)}$ term $\tilde{g}_0^{(1,2)}$ is a valid approximation in this spirit.

Therefore equation (4.103) can be seen as a defining equation, determining in which way these correlations are included in the DMFT2S. It is important to notice that through equation (4.103) no overcounting of terms occur. This is evident as each term on the right hand side of equation (4.103) is a valid approximation of $g_0^{(1,2)}$ on its own and the total spectral weight is preserved by the form of the linear combination.

4.5.5 DMFT2S scheme

With the mapping of the effective irreducible lattice propagator to effective irreducible two-impurity propagators in Equation (4.90) and (4.91) the decisive step is taken for the DMFT2S approximation. The irreducible lattice propagator $\underline{\underline{g}}$ can now be calculated from effective single- and two-impurity quantities, if the correct effective irreducible T-matrices $\underline{\underline{\tilde{T}}}^{(\underline{d})}$ for the different TIAM's and the SIAM T-matrix $\tilde{T}^{(SIAM)}$ are known. Unfortunately this is not the case. This knowledge would imply that the lattice problem is already solved. The whole mapping procedure of the lattice problem to effective two-impurity problems was undertaken in order to allow for an iterative self-consistent solution.
The last missing link to such a solution is the connection between the quantities entering the single- and the two-impurity solver, i.e. between the effective irreducible impurity T-matrices and the lattice T-matrix. The connection of these quantities will be introduced in the following. Thereafter a self-consistent calculation scheme for the DMFT2S approximation will be presented.

The irreducible T-matrix $\tilde{T}^{(SIAM)}$ for the effective SIAM is connected to the DMFT2S lattice T-matrix via the Dyson-equation

$$\begin{aligned} T_0^{(2S)} &= \tilde{T}^{(SIAM)} + \tilde{T}^{(SIAM)} g_0^{(2S)} \tilde{T}^{(SIAM)} + \tilde{T}^{(SIAM)} g_0^{(2S)} \tilde{T}^{(SIAM)} g_0^{(2S)} \tilde{T}^{(SIAM)} + \dots \\ &= \tilde{T}^{(SIAM)} + \tilde{T}^{(SIAM)} g_0^{(2S)} T_0^{(2S)}, \end{aligned} \tag{4.104}$$

which yields

$$\tilde{T}^{(SIAM)} = \left[\left(T_0^{(2S)} \right)^{-1} + g_0^{(2S)} \right]^{-1} . \tag{4.105}$$

The connection of the lattice T-matrix to the irreducible two-impurity T-matrix $\underline{\underline{\tilde{T}}}^{(\underline{d})}$ is given by

$$\begin{aligned} \underline{\underline{T}}^{(\underline{d})} = &\left(\underline{\underline{t}}^{(\underline{d})} + \underline{\underline{\tilde{T}}}^{(\underline{d})} \right) + \left(\underline{\underline{t}}^{(\underline{d})} + \underline{\underline{\tilde{T}}}^{(\underline{d})} \right) \underline{\underline{\tilde{g}}}^{(2imp),\underline{d}} \left(\underline{\underline{t}}^{(\underline{d})} + \underline{\underline{\tilde{T}}}^{(\underline{d})} \right) \\ &+ \left(\underline{\underline{t}}^{(\underline{d})} + \underline{\underline{\tilde{T}}}^{(\underline{d})} \right) \underline{\underline{\tilde{g}}}^{(2imp),\underline{d}} \left(\underline{\underline{t}}^{(\underline{d})} + \underline{\underline{\tilde{T}}}^{(\underline{d})} \right) \underline{\underline{\tilde{g}}}^{(2imp),\underline{d}} \left(\underline{\underline{t}}^{(\underline{d})} + \underline{\underline{\tilde{T}}}^{(\underline{d})} \right) + \dots \\ = &\left(\underline{\underline{t}}^{(\underline{d})} + \underline{\underline{\tilde{T}}}^{(\underline{d})} \right) + \left(\underline{\underline{t}}^{(\underline{d})} + \underline{\underline{\tilde{T}}}^{(\underline{d})} \right) \underline{\underline{\tilde{g}}}^{(2imp),\underline{d}} \underline{\underline{T}}^{(\underline{d})}, \end{aligned} \tag{4.106}$$

and can be resolved to

$$\underline{\underline{\tilde{T}}}^{(\underline{d})} = \left[\left(\underline{\underline{T}}^{(\underline{d})}\right)^{-1} + \underline{\underline{g}}^{(2imp),\underline{d}}\right]^{-1} - \underline{\underline{t}}^{(\underline{d})} \quad \text{with} \quad \underline{\underline{T}}^{(\underline{d})} = \begin{pmatrix} T_0^{(2S)} & T_{\underline{d}}^{(2S)} \\ T_{-\underline{d}}^{(2S)} & T_0^{(2S)} \end{pmatrix}, \tag{4.107}$$

where $\underline{\underline{t}}^{(\underline{d})}$ is the direct hopping matrix element for sites with distance $\underline{d}$. For the Hubbard model with nearest neighbor hopping it is given by

$$\underline{\underline{t}}^{(\underline{d})} = t \begin{pmatrix} 0 & \delta_{|\underline{d}|,1} \\ \delta_{|\underline{d}|,1} & 0 \end{pmatrix}. \tag{4.108}$$

The Dyson-equation (4.104) for the irreducible SIAM T-matrix excludes intermediate visits of a single chosen site in the lattice T-matrix, while the Dyson-equation (4.106) for the irreducible TIAM T-matrix excludes intermediate visits of two chosen sites with distance $\underline{d}$ in the lattice T-matrix. In the TIAM direct hopping processes $\underline{\underline{t}}^{(\underline{d})}$ between impurity sites are contained as direct matrix element in the Hamiltonian (see e.g equation (3.1)). Theses processes are not included in $\underline{\underline{\tilde{T}}}^{(\underline{d})}$, which is assured by the explicit $\underline{\underline{t}}^{(\underline{d})}$-term in equation (4.107).

The lattice T-matrix in real-space can be obtained via Fourier-transformation

$$T_{\underline{d}}^{(2S)} = \frac{1}{N} \sum_{\underline{k}} T_{\underline{k}}^{(2S)} e^{i\underline{k}\,\underline{d}} \tag{4.109}$$

from the $\underline{k}$-resolved lattice T-matrix

$$T_{\underline{k}}^{(2S)} = \frac{t_{\underline{k}}}{1 - g_{\underline{k}}^{(2S)} t_{\underline{k}}}, \tag{4.110}$$

where $g_{\underline{k}}^{(2S)}$ can be calculated from the Fourier-transform of the irreducible effective two-impurity propagators (see Equations (4.90) and (4.91))

$$\begin{aligned} g_{\underline{k}}^{(2S)} &= \sum_{\underline{d}} g_{\underline{d}}^{(2S)} e^{i\underline{k}\,\underline{d}} \\ &= g_0^{(2S)} + g_{\underline{d}_1}^{(2S)} \sum_{\underline{d}' \in \mathcal{S}(\underline{d}_1)} e^{i\underline{k}\,\underline{d}'} + g_{\underline{d}_2}^{(2S)} \sum_{\underline{d}' \in \mathcal{S}(\underline{d}_2)} e^{i\underline{k}\,\underline{d}'} + \ldots\ . \end{aligned} \tag{4.111}$$

With the mapping of the lattice problem onto a set of effective two-impurity problems and the connection of the lattice T-matrix to the different irreducible two-impurity T-matrices at hand, it is now possible to define a self-consistent calculation scheme for the solution of the lattice problem within the DMFT2S approximation. The calculation scheme is as follows:

0. Pick a set of N representative distance vectors $\mathcal{R} = \{\underline{d}_1, \ldots \underline{d}_N\}$ and determine the symmetry-related distance-vectors $\mathcal{S}(\underline{d}_i)$ for these vectors.

1. Start with an initial guess for the irreducible T-matrices $\underline{\underline{\tilde{T}}}^{(\underline{d}_i)}$ and the irreducible single-impurity T-matrix $\tilde{T}^{(SIAM)}$.
   Note: If in $\mathcal{R}$ a distance-vector is included, which is connected by a direct hopping term in the lattice, e.g. the nearest neighbor distance-vector, only an initial guess of $\tilde{T}^{(SIAM)}$ is necessary.

2. Solve

$$\begin{aligned} &G^{(2imp),\underline{d}_i}\left[\underline{\underline{\tilde{T}}}^{(\underline{d}_i)}\right] \quad \forall\ \underline{d}_i\ \in \mathcal{R}\ \ ; \\ &G^{(SIAM)}\left[\tilde{T}^{(SIAM)}\right] \end{aligned}$$

with help of an appropriate impurity- and two-impurity solver and calculate the irreducible impurity propagators

$$\begin{aligned} \underline{\underline{\tilde{g}}}^{(2imp),\underline{d}_i} &= \left[\left(\underline{\underline{G}}^{(2imp),\underline{d}_i}\right)^{-1} + \underline{\underline{t}}^{(\underline{d}_i)} + \underline{\underline{\tilde{T}}}^{(\underline{d}_i)}\right]^{-1} \qquad \forall\ \underline{d}_i \in \mathcal{R} \\ g_0^{(1S)} &= \left(G^{(SIAM)}\right)^{-1} + \tilde{T}^{(SIAM)} \end{aligned}$$

3. Map the irreducible impurity propagators onto the lattice propagators:

$$\begin{aligned} g_0^{(2S)} &= g_0^{(1S)} + \sum_i \left(g_0^{(2imp),\underline{d}_i} - g_0^{(1S)}\right) \\ g_{\underline{d}'}^{(2S)} &= \frac{1}{N_{\underline{d}_i}} g_{\underline{d}_i}^{(2imp)} \qquad \forall\ \underline{d}' \in \mathcal{S}(\underline{d}_i). \end{aligned}$$

4. Use the $\underline{k}$-dependent lattice T-matrix

$$\begin{aligned} T_{\underline{k}}^{(2S)} &= \frac{t_{\underline{k}}}{1 - t_{\underline{k}} g_{\underline{k}}^{(2S)}} \qquad \text{with} \\ g_{\underline{k}}^{(2S)} &= g_0^{(2S)} + \sum_i g_{\underline{d}_i}^{(2S)} \sum_{\underline{d}' \in \mathcal{S}(\underline{d}_i)} e^{i\underline{k}\,\underline{d}'} \end{aligned}$$

to calculate the real-space T-matrices for the vectors in $\mathcal{R}$ and $\underline{d} = 0$.

$$T_{\underline{d}_i}^{(2S)} = \frac{1}{N} \sum_{\underline{k}} T_{\underline{k}}^{(2S)} e^{-i\underline{k}\,\underline{d}_i} \qquad \forall\ \underline{d}_i \in \mathcal{R} \cup \{\underline{0}\}.$$

5. Calculate the irreducible T-matrices

$$\begin{aligned} \underline{\underline{\tilde{T}}}^{(\underline{d}_i)} &= \left[\left(\underline{\underline{T}}^{(\underline{d}_i)}\right)^{-1} + \underline{\underline{\tilde{g}}}^{(2imp),\underline{d}_i}\right]^{-1} - \underline{\underline{t}}^{(\underline{d}_i)} \qquad \forall\ \underline{d}_i \in \mathcal{R} \\ \tilde{T}^{(SIAM)} &= \left[\left(T_0^{(2S)}\right)^{-1} + g_0^{(2S)}\right]^{-1} \end{aligned}$$

and proceed with step 2, until convergence is reached with the irreducible T-matrices from the previous iteration.

5 DMFT2S results

5.1 Introduction

In this chapter the numerical application of the DMFT2S scheme to spectral properties of the two-dimensional Hubbard model defined in Equation (4.4) is presented. It is not the aim of this chapter to give a full and detailed coverage of this model with the DMFT2S. The main focus is to give the reader an impression of the potential of the DMFT2S approximation and to survey what can be done with this approximation.

The 2D-Hubbard model is of great interest in condensed matter physics, in particular since it is believed to capture the physics of the super-conducting planes in high-temperature superconductors [And97, Zha88, Aim07].

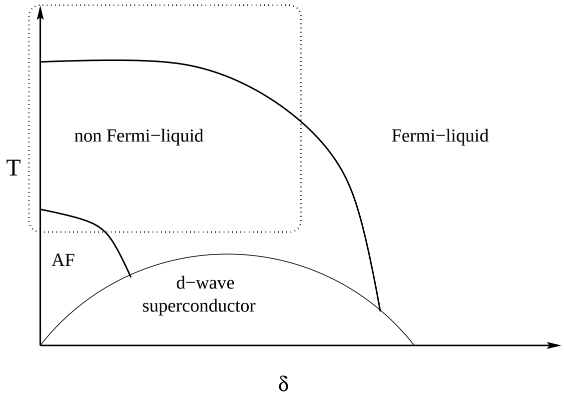

Figure 5.1: Schematic phase diagram of the 2D Hubbard model for $\frac{W}{U} \approx 1$ with respect to the Temperature T and $\delta = |1 - \sum_\sigma \langle n_\sigma \rangle|$ the occupation relative to half filling, i.e. $\epsilon = -\frac{U}{2}$. The dotted box indicates the regime investigated with the DMFT2S.

One of the most remarkable features of High-T_c superconductors in the normal state above T_c is the suppression of the density of states at the Fermi-energy in underdoped samples. Angular resolved photoemission experiments [FR98] show that in the $\underline{k}$-resolved spectral function this so called pseudogap has a d-wave anisotropy, i.e. the same symmetry as the superconducting order parameter in these materials. The presence of a pseudogap is nowadays commonly seen as possible precursor to the superconducting phase.

At half filling the groundstate of the 2D-Hubbard model is known to be an anti-ferromagnetic insulator [Hir85, Whi89], and the spectrum is therefore gapped at the Fermi-energy. On the other hand the Mermin-Wagner theorem prohibits a phase transition for $T > 0$ in two-dimensions. For finite temperatures, deducible from a continuity argument [Vil97], the appearance of a gap is still expected due to strong anti-ferromagnetic correlations. Naturally

real materials are three dimensional and e.g. the superconducting electrons in the high T_c cuprates are only to a high degree confined in the two-dimensional cuprate planes. Residual couplings between the cuprate planes through the interlayer material still exist and can stabilize a phase transition at finite temperatures.
For strong couplings $U \gg W$, with W the bandwidth, the origin of this gap is very well understood. Due to strong correlations a charge gap of order U develops in the spectrum. The spins are coupled by the effective exchange interaction $J = 4\frac{t^2}{U}$ and determine the low energy physics. In these so called Mott-insulators the anti-ferromagnetic order at $T = 0$ is a result of the Mott-transition at finite temperatures.
The situation is less clear for $U \ll W$. There two different scenarios are generally discussed. In the weak-coupling scenario a spin-density wave is formed at $T = 0$, due to the nesting of the Fermi surface, which leads to a doubling of the unit cell and a gap in the spectrum. The gap at finite temperatures is then directly connected to this so called Slater-mechanism [Sla51] at $T = 0$. This scenario is in direct contrast to an argument pointed out by Anderson [And97], in which the system is always in the strong-coupling regime and a Mott gap is present for all $U > 0$.

The half-filled and doped 2D-Hubbard model has been investigated with various methods. Due to the presence of strong anti-ferromagnetic correlations it is an appropriate playground for the validation of the DMFT2S approximation. Figure 5.1 shows a schematic phase diagram of the 2D-Hubbard model, where the dotted box indicates the regimes investigated with the DMFT2S approximation.
For the half-filled 2D-Hubbard model the DMFT approximation shows a Mott-transition only for large U. But even in the large U regime, due to the formation of a quasiparticle peak at the Fermi-energy, the system remains metallic. It is therefore not a Mott-insulator in a strict sense. Only the lower and upper Hubbard bands are separated by a gap of the order U. In approximations which include spatial correlations, like the CDMFT or the DCA, the quasiparticle peak collapses and the system becomes an insulator in this regime [Hus01, Jar01b, Sca06]. Furthermore these approximations tend to produce a pseudogap also at small and intermediate values of U. In this regime no separation of the Hubbard bands is visible in the DMFT and the spectrum shows there no sign of a gap.

Due to the limitations of the SNCATI/ENCATI two-impurity solvers concerning the weak coupling limit (see section 3.2) only results for large $U > W$ or intermediate $U \approx W$ are presented in this thesis. Additionally, only results for temperatures $k_b T > \frac{1}{60} W$ can be presented.
For lower temperatures the DMFT2S with SNCATI/ENCATI as two-impurity solver becomes numerically unstable. These instabilities are connected to insufficiencies of the two-impurity solvers used and not due to the DMFT2S scheme itself. The DMFT2S scheme for the 2D-Hubbard model produces very sharp peaks at low temperatures in the irreducible T-matrix $\underline{\underline{\tilde{T}}}^{(d_1)}$ for nearest neighbor distances[1]. This quantity enters the two-impurity solver and is, after solution of the two-impurity problem, added to the inverse of the effective two-

---

[1] T-matrices for greater distances, i.e. for sites not connected by a direct hopping, are less critical.

impurity Greenfunction $\underline{\underline{\tilde{G}}}^{(2imp),\underline{d}_i}$ in order to obtain the irreducible two-impurity propagator

$$\underline{\underline{\tilde{g}}}^{(2imp),\underline{d}_i} = \left[\left(\underline{\underline{G}}^{(2imp),\underline{d}_i} \right)^{-1} + \underline{\underline{t}}^{(\underline{d}_i)} + \underline{\underline{\tilde{T}}}^{(\underline{d}_i)} \right]^{-1} \tag{5.1}$$

in the DMFT2S scheme. The crucial step is restated in Equation (5.1). In case of an exact two-impurity solver this step leads to a well defined physical irreducible two-impurity propagator, i.e. $\underline{\underline{\tilde{g}}}^{(2imp),\underline{d}_i}$ is a causal quantity with a definite imaginary part of the diagonal propagator and the correct relation $|Im(\tilde{g}_0^{(2imp),\underline{d}_i})| > |Im(\tilde{g}_{\underline{d}_i}^{(2imp)})|$ (see section 4.5) between the diagonal and off-diagonal propagator. These conditions are not necessarily fulfilled for the SNCATI/ENCATI as solvers due to their approximative nature. It turns out, that the sharp peaks for low temperatures in $\underline{\underline{\tilde{T}}}^{(\underline{d}_1)}$ have not the correct counterpart in $\left(\underline{\underline{\tilde{G}}}^{(2imp),\underline{d}_1} \right)^{-1}$, and $\underline{\underline{\tilde{g}}}^{(2imp),\underline{d}_1}$ becomes acausal for some energies.
As these acausilities in $\underline{\underline{\tilde{g}}}^{(2imp),\underline{d}_1}$ do not occur at the Fermi-energy but at the borders of the pseudogap, this misbehavior is not necessarily connected to the well known NCA-pathology [Gre83]. On the other hand, the discussion of the TIAM coupled by a direct hopping matrix element t in section 3.3.5 showed the presence of an even-odd Kondo-effect with a gap at the Fermi-energy. It is therefore possible that via the direct hopping the NCA-pathology is shifted towards higher energies. Another possible more numerical reason for the failure of the SNCATI/ENCATI solver for low temperatures is connected to the Van-Hove singularities in the free DOS of the two-dimensional sc-lattice, which effectively enters the DMFT2S scheme for the 2D-Hubbard model via the Fourier transformation in Equation (4.110) for the lattice T-matrix. For low temperatures the Van-Hove singularities produce very sharp features in the irreducible two-impurity T-matrices $\underline{\underline{\tilde{T}}}^{(\underline{d}_i)}$, which in the numerical implementation of the two-impurity solvers are possibly not handled with sufficient numerical accuracy.

However, the temperatures numerical reachable are still within the range of the DMFT lattice coherence temperature T^*. Correlation effects should still be resolvable with the SNCATI/ENCATI as two-impurity solver for the DMFT2S.

In order to specify the different possible pair separations included in a DMFT2S calculation the notation DMFT2S(x) is introduced, where x is the maximum distance of site separations within the Manhattan metric

$$||\underline{d}||^0 \equiv |d|_x + |d|_y, \tag{5.2}$$

i.e. DMFT2S(x) is defined to include pair correlations between sites with a distance-vector $\underline{d}$ fulfilling the condition

$$||\underline{d}||^0 \leq x. \tag{5.3}$$

Physically interpreted, for lattices with only nearest neighbor hopping, the Manhattan metric counts the minimal number of direct hopping processes t necessary to connect two sites and is a more natural distance concept than the usual Euclidian metric on a lattice.

Practically, for DMFT2S(1) only one nearest neighbor effective two-impurity cluster needs to be calculated, e.g. $\underline{d} = (1,0)^T$. All other nearest neighbor site distance-vectors, i.e. $(-1,0)^T$ and $(0,\pm 1)$, are related by symmetry and contribute in the DMFT2S via the averaging procedure in the mapping Equation (4.79). For DMFT2S(2) three not symmetry related pair separations $(1,0)^T$,$(1,1)^T$, $(2,0)^T$ exist, i.e. three two-impurity problems must be solved in each iteration of the DMFT2S(2) scheme. For DMFT2S(3) already six effective two-impurity problems per iteration need to be considered and for DMFT2S(4) the number increases to nine different effective two-impurity problems.

Magnifications of the figures presented here can be found in appendix C.2.

5.2 2D-Hubbard model at half filling

It was already mentioned in the introduction of this section, that on physical grounds one expects a gap at the Fermi-energy for the spectrum of the half filled 2D-Hubbard at low temperatures. In Figure 5.2 DMFT2S spectra for various temperatures are presented with the SNCATI as two-impurity solver. For comparison, Figure 5.2(a) depicts the corresponding DMFT spectra calculated with the SNCATI used as single-impurity solver (see section 3.3.1). The same calculations but with the ENCATI used as solver are presented in Figure 5.3.

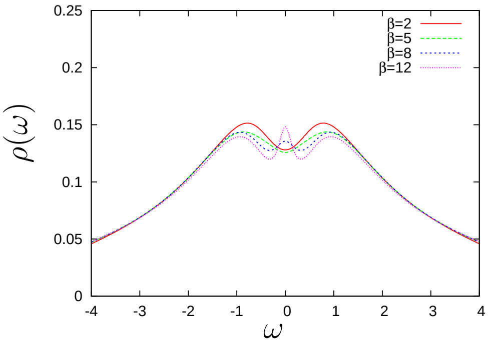

(a) DMFT/SNCATI

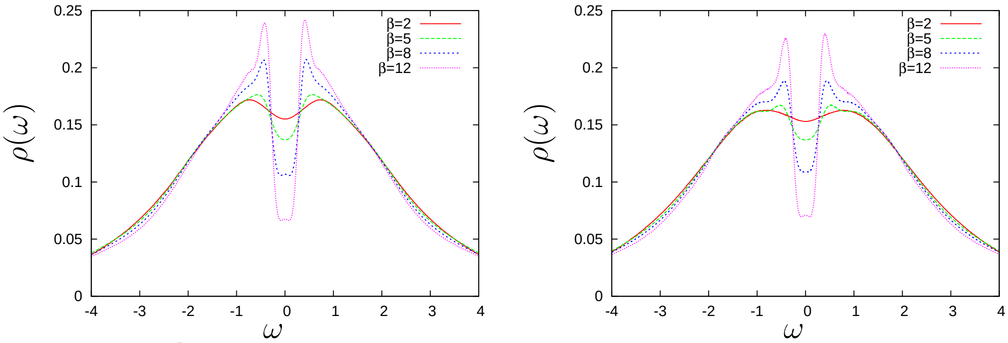

(b) DMFT2S(1) (c) DMFT2S(2)

Figure 5.2: Comparison of the spectral function for various inverse temperatures β for different lattice approximations with the SNCATI as solver: (a) the DMFT with the SNCATI used as single impurity solver, (b) the DMFT2S(1), (c) the DMFT2S(2). The parameters in all calculations are $t = 0.5, U = 2$ and $\epsilon = -1 = -\frac{U}{2}$

The DMFT spectra in Figures 5.2(a) and 5.3(a) show with decreasing temperature the familiar formation of a quasiparticle resonance at the Fermi-energy, i.e. the lattice Kondo-effect. The higher Kondo-temperature of the ENCATI also implies a higher coherence temperature T^* for the lattice Kondo-effect leading to larger quasiparticle peaks compared to the SNCATI. Similar to the findings from two-impurity calculations with fixed medium the SNCATI produces in the self-consistent DMFT scheme high-energy flanks containing much spectral weight. The DMFT spectra with the ENCATI used as single-impurity solver do not show these flanks. The ENCATI spectra are more compact. This finding is no surprise, since it has been shown in chapter 3.3.1 that to a large degree the vertex corrections contained in

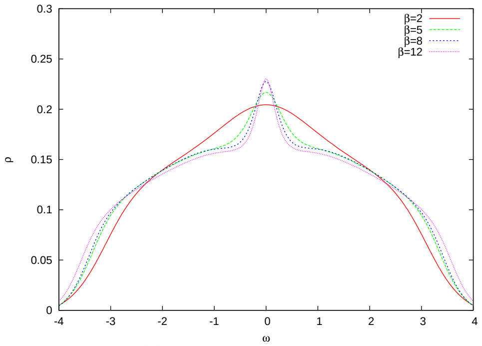

(a) DMFT/ENCATI

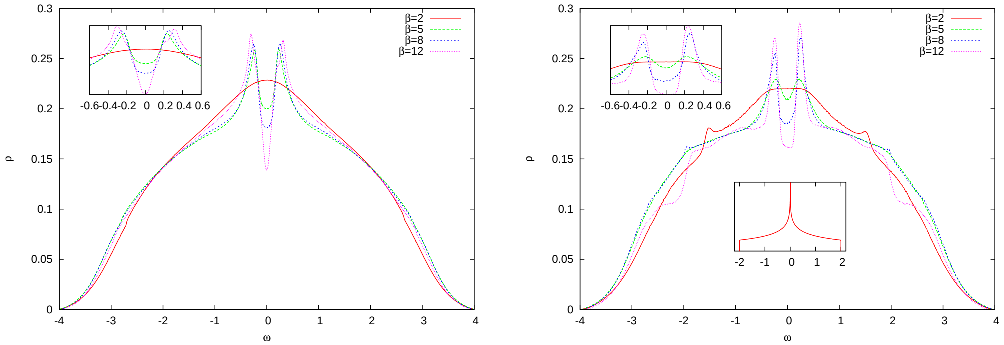

(b) DMFT2S(1) (c) DMFT2S(2)

Figure 5.3: Comparison of the spectral function for various inverse temperatures β for different lattice approximations with the ENCATI as solver: (a) the DMFT with the ENCATI used as single impurity solver, (b) the DMFT2S(1), (c) the DMFT2S(2), the top left inset shows a magnification of the energy interval at the Fermi-energy, the inset at the bottom the free DOS of the sc-lattice. The parameters in all calculations are $t = 0.5$, $U = 2$ and $\epsilon = -1 = -\frac{U}{2}$. Asymmetries in the spectra violating the particle-hole symmetry have numerical reasons.

ENCATI suffice to correct for these flanks. So in a self-consistent lattice approximation with the ENCATI as solver more compact spectra are expected.

The differences due to the DMFT corrections in the DMFT2S are qualitatively different from the corrections in DMFT spectra due to the use of different impurity-solvers. The inclusion of nearest neighbor pair correlations in DMFT2S(1) leads to a collapse of the quasiparticle peak at $\omega = 0$ and the connected Fermi-liquid phase. A gap appears at the Fermi-energy. The inclusion of further pair correlations in DMFT2S(2), i.e. all pair correlations between sites separated by a maximum of two direct hoppings t, leads to no further suppression of spectral weight in the gap compared to the DMFT2S(1). For DMFT2S(1) and DMFT2S(2) with SNCATI the gap becomes very steep for lower temperatures. It seems that in extrapolation to the $T = 0$ limit the remaining spectral weight at $\omega = 0$ could disappear completely. This would be in complete accordance with the known groundstate of the 2D-Hubbard model and a recent two-site DCA cluster calculation with NRG as impurity solver for $T = 0$ by Pruschke [Pru05], showing the complete suppression of spectral weight at the Fermi-energy. In the calculations with ENCATI as solver this tendency for $T = 0$ is less clear, the gap is narrower and not so sharp as for the SNCATI calculations.

Both ENCATI and SNCATI produce large and narrow side-peaks adjacent to the gap at the Fermi-energy. The $\underline{k}$-resolved origin of these sidepeaks will be inspected more closely later on. The appearance of these sidepeaks in the spectrum is in accord with numerical DCA/QMC results in literature [Hus01, Jar01b]. In these calculations relative large cluster sizes $N_c \geq 16$ are necessary in order to clearly resolve the gap and the sidepeaks. The nearest neighbor correlations contained in DMFT2S(1) suffice for the formation of these features. The inclusion of further spatial correlations in the DMFT2S(2) calculated with the SNCATI as two-impurity solver leads only to small modifications in the spectrum. The shape and depth of the gap has the same form as in the DMFT2S(1) spectra, only the sidepeaks are a bit smaller and narrower. The changes in the spectrum are larger for the DMFT2S(2) with the ENCATI as two-impurity solver shown in Figure 5.3(c). Here remainders of the Van-Hove singularities from the free two-dimensional sc-DOS near the energies $\omega = \pm 2$ become visible.
It should be noted, that the slightly asymmetric heights of the sidepeaks, e.g. clearly visible in the DMFT2S(2)/ENCATI spectrum for $\beta = 12$, are a numerical artefact. The earlier described insufficiencies of the SNCATI/ENCATI solvers at low temperatures arise at the energies of these sidepeaks. The asymmetries seen here are numerical precursors towards the numerical instability of the DMFT2S scheme with SNCATI/ENCATI as solver for lower temperatures. The differences in the spectrum due to the inclusion of further pair correlations in the various levels of the DMFT2S approximation with SNCATI and ENCATI as two-impurity solver are depicted in Figure 5.4.

The different DMFT2S(i) spectra with the SNCATI as two-impurity solver presented in

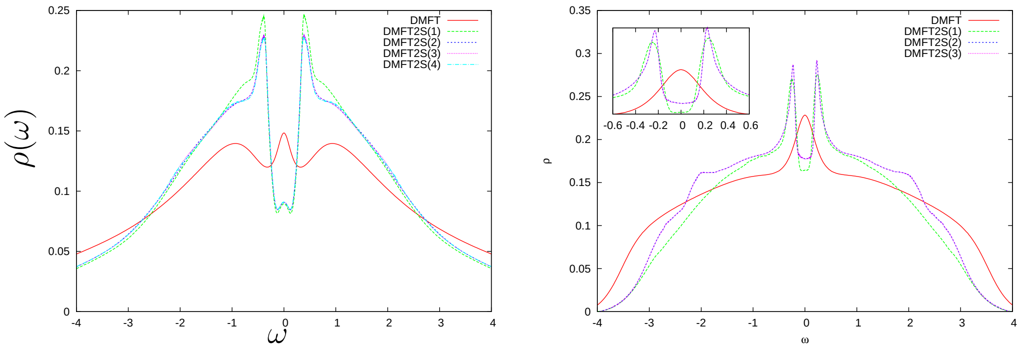

(a) DMFT2S/SNCATI (b) DMFT2S/ENCATI

Figure 5.4: Comparison of the spectral function for the different levels of the DMFT2S(i) approximation. The included pair correlations range from between nearest neighbor sites in DMFT2S(1) up to all pair correlations between sites reachable by four elementary hoppings t in DMFT2S(4). (a) shows the DMFT2S spectra and the DMFT spectrum calculated with the SNCATI as two-impurity solver, in (b) the corresponding calculation with the ENCATI as two-impurity solver is shown. The top left inset shows a magnification of the energy interval at the Fermi-energy The parameters are $\epsilon = -1, U = 2$ and $\beta = 10$. Asymmetries in the spectra violating the particle-hole symmetry have numerical reasons.

Figure 5.4(a) show only slight modifications, if further pair correlations are included in the scheme. The most notable effect is between the DMFT2S(1) and the DMFT2S(2) approximation, where the inclusion of next-nearest and the next-next-nearest neighbor pair correlations leads to a reduction of the width and the height of the sidepeaks. The inclusion of further pair correlations in DMFT2S(3) and DMFT2S(4) leads to no additional modifications in the spectrum. The gap at the Fermi-energy has for all levels of the DMFT2S approximation the same form. Furthermore in the gap a small additional dip is visible, which looks like an artefact of the lattice Kondo-effect from the DMFT approximation. The dip at the Fermi-energy is not visible in the corresponding DMFT2S spectra with ENCATI as two-impurity solver presented in Figure 5.4(b). Here the depth of the gap and the height of the sidepeaks increases with the inclusion of further pair correlations. Maybe the most notable effect with the ENCATI as two-impurity solver is the appearance of kinks at $\omega \approx \pm 2$ for the DMFT2S approximations beyond the level of the DMFT2S(1).

The emergence of the sidepeaks adjacent to the gap at $\omega = 0$ in all shown DMFT2S approximations signals the appearance of two new solutions in the quasiparticle equation for quasiparticles energies $\omega_{\underline{k}}$

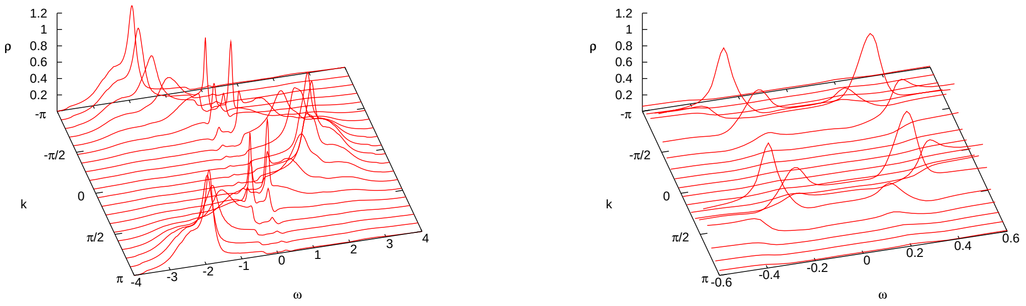

(a) (b)

Figure 5.5: $\underline{k}$-resolved spectrum of the DMFT2(2)/ENCATI along the $[1,1]$-direction for $\epsilon = -1, U = 2$ and $\beta = 10$. (a) shows the full energy interval, (b) magnification of the energy interval in vicinity of the Fermi-energy.

$$\mathrm{Re}\left[\omega - \epsilon - t_{\underline{k}} - \Sigma(\omega, \underline{k})\right] = 0 \tag{5.4}$$

for the same $\underline{k}$. In a $\underline{k}$-resolved spectrum, these two new quasiparticle solutions should be visible as narrow excitations at the borders of the gap at $\omega = 0$. The $\underline{k}$-resolved spectrum along the $[1,1]$ direction from an DMFT2S(2)/ENCATI calculation is depicted in Figure 5.5. The top picture shows the whole energy interval with excitations along the typical cosine dispersion-function $t_{\underline{k}}$ of the sc-lattice. Near the gap at the Fermi-energy relative two relative sharp excitations appear in the band near $k = \pm\frac{\pi}{2}$. A magnification of this region is shown in Figure 5.5(b). The height of these two peaks near $k = \pm\frac{\pi}{2}$ is not evenly distributed, but changes rapidly in a short k-interval from a large peak at $\omega < 0$ and a small peak at $\omega > 0$ to a small peak at $\omega < 0$ and a large peak at $\omega > 0$. The occurance of these splittings at k-values near $k = \pm\frac{\pi}{2}$ are an indicator for the presence of strong nearest neighbour correlations leading to these features.

In the discussion of the TIAM with the impurities coupled by a direct hopping t in chapter

3.3.5, similiar features appeared. There processes linear in t lead to a splitting $\propto t$ of the Kondo-resonance. Additionally, for large t the effective AF-exchange coupling $J^t = -4\frac{t^2}{U}$ leads to the binding of the impurity electrons into a two-impurity singlet state and a connected gap of the order J^t in the quasiparticle resonance. In the regime considered here for the 2D-Hubbard model the hopping t and the effective exchange contribution J^t between nearest neighbor sites have the same magnitude $|t| = |J^t|$. Both lead to strong correlations between nearest neighbour pairs. Via the self consistent treatment in the DMFT2S approximation the nearest neighbor correlations calculated with an effective TIAM contribute to the lattice problem in a lattice coherent fashion. The opening of a quasiparticle two-band structure near the Fermi-energy in a narrow k-interval in the vincinity of $k = \pm\frac{\pi}{2}$ are lattice coherent manifestations of the strong nearest neighbour correlations found in the TIAM for large t.

But not only the low energy features of the $\underline{k}$-resolved spectrum show interesting results. At high energies near the band-edges at $\omega = \pm 2$ in the vicinity of $k = \pm\pi$ and $k = 0$ in $[1, 1]$-direction sharp peaks are visible in Figure 5.5(a). In the $\underline{k}$-summed spectra in Figure 5.4(b) these peaks appear as kinks closely resembling the kinks in the free DOS of the 2D sc-lattice. These kinks emerge only in the DMFT2S(i)/ENCATI approximation with $i \geq 2$, i.e. their origin could be due to pair correlations between pairs with distance $|\underline{d}| > 1$.

5.3 Doped 2D-Hubbard model

The existence of a pseudogap, i.e. a large suppression of spectral weight at small excitation-energies of underdoped high-temperature superconductors, is nowadays an accepted experimental fact [Tim99]. Theorists have responded with a multitude of scenarios for the pseudogap [Ran97, Eme87, Zha97, And97]. But at present there is no common consensus on the real physical origin of the pseudogap. For the doped 2D-Hubbard model with intermediate and strong on-site Coulomb repulsion $U \geq W$ is is suppossed that the origin of the pseudogap is due to the influence of strong short range AF-correlations [Sta03]. Numerical investigations based on model calculations are highly desirable in order to clarify this issue.

Figure 5.6 depicts spectra for various U and fixed $\epsilon = -1$ and $\beta = 10$ calculated with

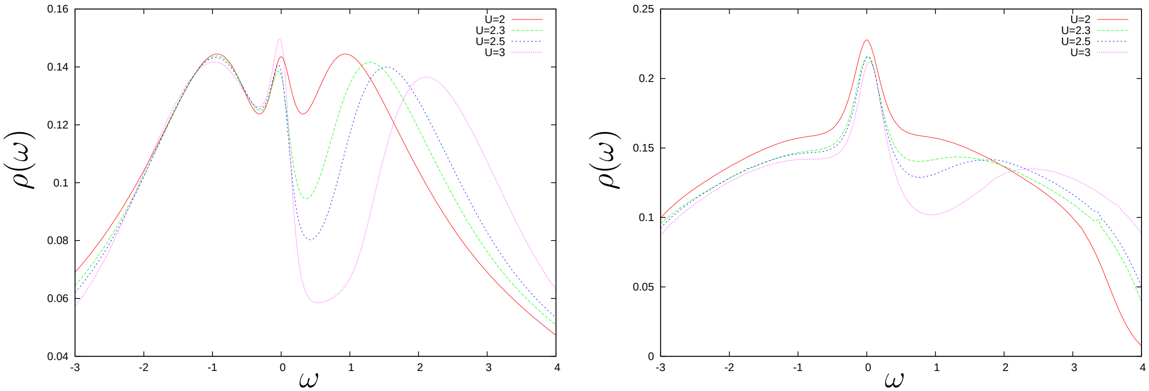

(a) DMFT/SNCATI (b) DMFT/ENCATI

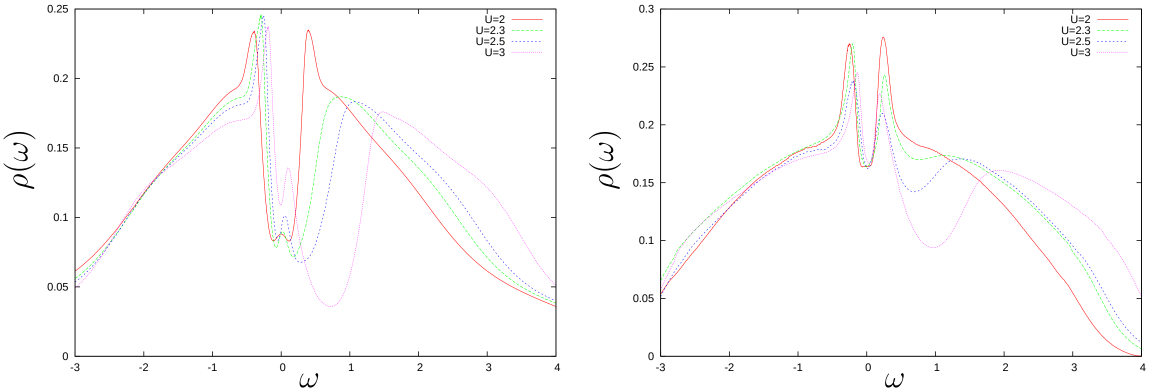

(c) DMFT2S(1)/SNCATI (d) DMFT2S(1)/ENCATI

Figure 5.6: Comparison of the spectral function for various U and $\epsilon = -1$ and inverse temperatures $\beta = 10$ for different lattice approximations. (a) the DMFT with the SNCATI used as single impurity solver, (b) the DMFT with the ENCATI used as single impurity solver, (c) the DMFT2S(1) with SNCATI, (d) the DMFT2S(1) with ENCATI.

the DMFT and the DMFT2S(1) with the SNCATI and the ENCATI as solver. The DMFT spectra for both solvers show the opening of a gap $\propto U$ and the quasiparticle resonance near the Fermi-energy. The separation of the lower and upper Hubbard band is for the DMFT/SNCATI already visible at halffilling (U=2). For greater U this leads to a much more pronounced gap than in the corresponding DMFT/ENCATI spectra. The higher Kondo-temperature of the ENCATI implies in the effective impurity problem a stronger effective hybridization to the band. This leads not only to a higher quasiparticle peak but also to broader features in the high-energy regions of the spectra. Higher values of U are therefore necessary for a Mott-transition within the DMFT/ENCATI.

The inclusion of nearest neighbor correlations in the DMFT2S(1) leads to large modifications compared to the DMFT results. At half filling a gap appears at the Fermi-energy, and adjacent to the gap two sidepeaks are visible (see section 5.2). These features at half filling are visible in the DMFT2S(1) spectra for both two-impurity solvers. But the behavior of the DMFT2S(1)/SNCATI differs significantly from the DMFT2S(1)/ENCATI away from half filling. In the DMFT2S(1)/SNCATI spectra for $U > 2$ it seems that the sidepeak at $\omega > 0$ abruptly collapses and instead a new smaller peak starts to grow near the Fermi-energy and opens a pseudogap at $\omega = 0$. The large sidepeak at $\omega < 0$ changes only slightly during the formation of the pseudogap.
The DMFT2S(1)/ENCATI shows a different behavior with increasing U. There the sidepeak at $\omega > 0$ does not collapse, it gets only somewhat smaller but develops continuously from the sidepeak at half filling. In effect in both approximations a pseudogap at the Fermi-energy remains. The pseudogap can, due to the sidepeak at $\omega > 0$, be clearly distinguished from the opening of the Mott gap with U, which also exists in the DMFT approximation. In comparison, the small dip-like pseudogap of the DMFT2S(1)/SCNATI spectrum has a closer resemblance to the spectra, which can be found in literature, calculated with DCA/QMC [Hus01] and DCA/NCA [Mai00a] for 4-site clusters. This resemblance could be expected for the DCA/NCA literature result, as the SNCATI for $U \longrightarrow \infty$ limits in the NCA. But at least for the DCA result with the “exact” QMC solver this is a surprising result. The ENCATI proved in chapter 3.3.1 to be a much better two-impurity solver than the SNCATI. The DMFT2S(1)/ECNATI calculations have therefore a much higher qualtity than the corresponding calculation with the SNCATI as solver. However, one should not be mistaken to compare apples with oranges, the DCA includes short range correlations in a different fashion than the DMFT2S(1). Differences in the spectra are therefore expected and not necessarily connected to the used impurity solver.

Figure 5.7 shows a comparison of the spectra obtained from the different levels i of the DMFTS(i) approxmation with the SNCATI and ENCATI used as two-impurity solvers. Similar to the findings for the DMFT2S(i)/SNCATI for the half filled 2D Hubbard model in Figure 5.4(a) the changes in the spectrum, due to the inclusion of longer ranged pair correlations, are only small. At least between the DMFT2S(2)/SNCATI and the DMFT2S(3)/SNCATI no differences are visible. Compared to the DMFT2S(1)/SNCATI spectrum the flank adjacent to the sidepeak at $\omega < 0$ becomes more pronounced and slight traces of the Van-Hove singularities appear at $\omega = -2$ and $\omega = 3$. Only very small differences are visible in the size and shape of the pseudogap at the Fermi-energy. The corresponding calculation with the ENCATI as two-impurity solver depicted in Figure 5.7(b) shows greater differences in the spectrum between the DMFT2S(1)/ENCATI and the DMFT2S(2)/ENCATI approximation. In DMFT2S(2)/ENCATI the asymmetry between the heights of the sidepeaks vanishes and the pseudogap is less pronounced. Concerning this feature no differences are visible between the DMFT2S(2)/ENCATI and the DMFT2S(3)/ENCATI approximation. Like the corresponding calculation for half filling in Figure 5.4(b) strong traces of the Van-Hove singularities at $\omega = -2$ and $\omega = 3$ become visible due to the inclusion of next-nearest and

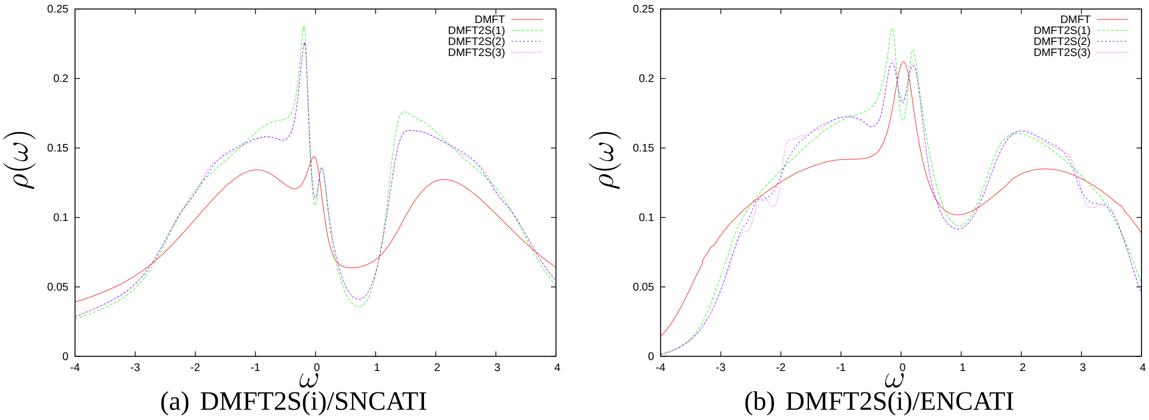

(a) DMFT2S(i)/SNCATI (b) DMFT2S(i)/ENCATI

Figure 5.7: Comparison of the spectrum for the different level i of th DMFT2S(i) approximation with $\epsilon = -1$, $U = 3$ and $\beta = 10$ with the SNCATI and ENCATI as solver. (a) the DMFTS(i)/SNCATI, (b) the DMFTS(i)/ENCATI.

next-next-nearest neighbor pair correlations in the DMFT2S(2). The wave-like features at $\omega = -2$ from the DMFT2S(3)/ENCATI calculation has numerical reasons and points towards a not fully converged solution.

In summary, the 2D-Hubbard model evaluated for spectral properties with the DMFT2S shows the dominant influence of nearest neighbor correlations in form of a pseudogap at the Fermi-energy. Only slight modifications in spectra occur due to the inclusion of longer ranged pair correlations. The spatial correlations are mainly driven by the direct hopping t and the connected effective magnetic exchange coupling $J^t = -4\frac{t^2}{U}$ between nearest neighbor sites. The scale set by $J^t \approx 0.5$, in the regimes considered, exceeds by far the DMFT lattice coherence temperature $T^* \approx 0.1$, which is the energy scale for the formation of quasi-particles and the connected Fermi-liquid phase at the Fermi-energy. For the 2D-Hubbard model it is therefore no surprise, that the inclusion of nearest neighbor correlations lead to strong corrections of the DMFT approximation.

6 Summary and outlook

In this thesis new approximations, which allow for the description of spatial correlations in strongly correlated electron systems, were introduced and investigated for the two-impurity Anderson model (TIAM) and the 2D-Hubbard model.

In chapter 2 a diagrammatic approach, to be used for the self-consistent solution of the TIAM was presented. This approach is formulated within the framework of direct perturbation theory for single impurity systems; it extends the toolbox of treatments for two-impurity systems. From this approach two new self-consistent approximations, i.e the SNCATI and the ENCATI, were derived and numerically implemented; they can be seen as generalizations of the existing simple non-crossing approximation (SNCA) and the extended non-crossing approximation (ENCA) for the single impurity Anderson model (SIAM) to the TIAM. The conceptual differences which arise in the diagrammatics of these approximations, due to the incorporation of inter-impurity band propagations and direct matrix elements between the two-impurities, were explained in detail, and useful hints allowing for a successful implementation were given in the presentation.

In the following chapter a detailed inspection of one-particle spectra and magnetic susceptibility of the TIAM with these new two-impurity solvers was undertaken. The question this chapter tried to answer was, in how far the different possible coupling mechanisms between two impurities are able to alter the dynamics of single-impurity systems.
The presentation started from the limit of two uncoupled impurities, where especially the ENCATI proved to be also a good approximation for the dynamic properties of independent impurities. The Kondo-scale estimated by the ENCATI was shown to be somewhat lower than in the ENCA approximation but higher than in the SCNA estimate. In the following sections of this chapter the competition or the cooperation of the single-impurity Kondo-effect with direct couplings and the indirect RKKY-interactions between the impurities was investigated. The calculations for a strong direct AF-exchange coupling J between the impurities showed a collapse of the Kondo-effect in favor of a two-impurity singlet (S=0). For a direct FM-exchange coupling the Kondo-cloud changed its character into a nonlocal object screening the two-impurity triplet (S=1) spin, and some remaining influence of the suppressed two-impurity singlet (S=0) became visible as singlet-triplet excitation in the quasiparticle resonance. The calculations with direct hopping t showed the emergence of an even-odd Kondo-effect, which in the following was interpreted as the most simple example for the band formation of quasiparticles with a non-constant dispersion function $\epsilon_{\underline{k}}$.
No simple physical pictures could be derived from the calculations of the spectrum and the magnetic susceptibilities, which included RKKY-interactions for various distances. It turned out, that the effective RKKY-coupling J^{RKKY} changes from anti- to ferromagnetic values not only as function of the impurity distance-vector $\underline{d}$ but also of the hybridization strength V. Furthermore, the numerical results showed strong evidence that band propagation processes between the impurities not only mediate the RKKY exchange-coupling

$J^{RKKY} \propto V^4$ but also a dynamic hopping $\propto V^2$. At least for some distances of the two sites the spectra showed an even-odd Kondo-effect, which indicated the presence of an effective hopping term between the impurities. Neither of these results can be explained with the usual picture of the RKKY-interaction alone or with the competition of this interaction with the Kondo-effect. Effective pictures like e.g. the Doniach picture thus seem to be oversimplifications. The results in this thesis showed that the full incorporation of the dynamic character of the RKKY-interaction can lead to qualitative different behavior than suggested in these pictures.

A second main aspect of this thesis was the introduction of a new effective lattice theory - the DMFT2S -, which also allows for the inclusion of long range spatial correlations. The dynamical mean-field theory 2-sites (DMFT2S) extends the in the known DMFT approximation, which maps the lattice problem onto an effective single-impurity problem and contains only local correlations, to the simultaneous inclusion of pair site correlations with the pair sites at arbitrary distance. In the self-consistent scheme developed the lattice problem is mapped onto a multitude of effective two-impurity models, i.e. for each different separation of two lattice sites one effective two-impurity model. In chapter 4.5 of this thesis the DMFT2S approximation was thoroughly introduced, and a self-consistent calculation scheme was presented. In the following chapter a numerical evaluation of the DMFT2S scheme with the ENCATI and the SNCATI approximations as two-impurity solvers was presented for spectral properties of the 2D-Hubbard model. The pseudogap behavior at the Fermi-energy, which is believed to stem from strong AF-correlations, could be reproduced in the half filled and the doped regime of this model. The calculated results were compared with literature results from e.g. the dynamical cluster approximation (DCA) and showed qualitative agreement with these approximations.

Concerning the future prospects certainly the DMFT2S approximation can be applied and further validated for numerous questions and models in the field of strongly-correlated electrons not considered in this thesis. The ability of this approximation to pick a set of site separations explicitly, for pair correlations to be included, opens the possibility to investigate the influence of long range correlations along certain directions. Furthermore, it should also be possible to reduce the numerical effort for the inclusion of long range pair correlations by an adaptive algorithm. The idea is to approximate the pair correlations between the sites separated by large distance vectors through the pair correlations for similar distance vectors. A simple implementation could be to lay a nonuniform mesh over the lattice sites. Close to the origin each cell of the mesh contains one lattice site and for larger distances the cells become larger, i.e. more lattice sites are contained. The pair correlations between the site at the origin and the sites in a cell could then be approximated by only one representative site in each cell. In this way the short range pair correlations could be exactly included and the weaker long range pair correlations would be approximated by some representative distance vectors.

A Self-energy equations

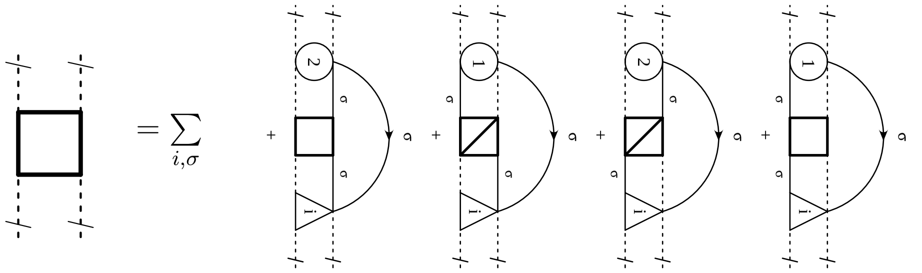

(A.1)

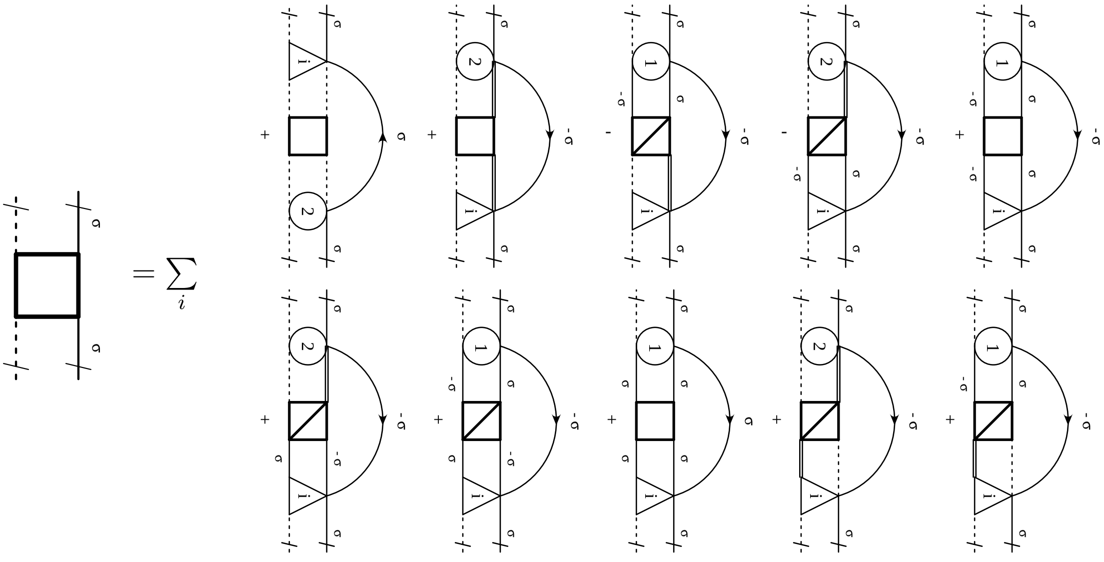

(A.2)

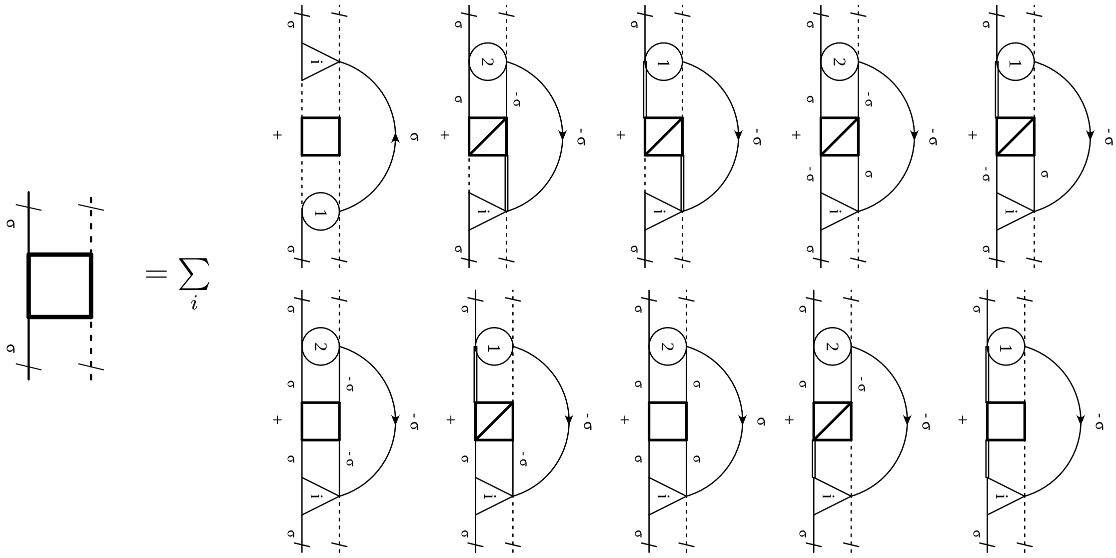

(A.3)

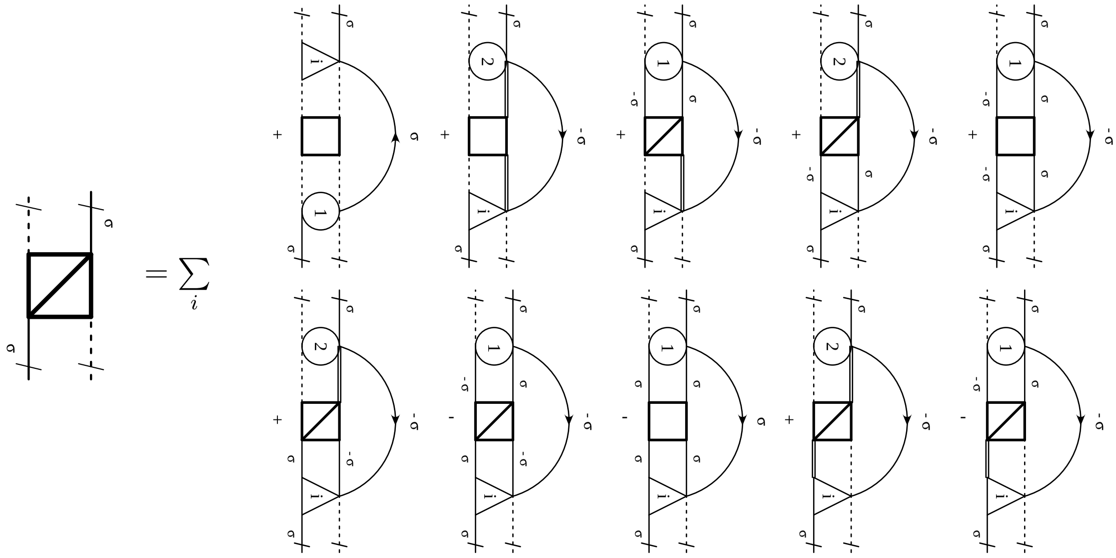

(A.4)

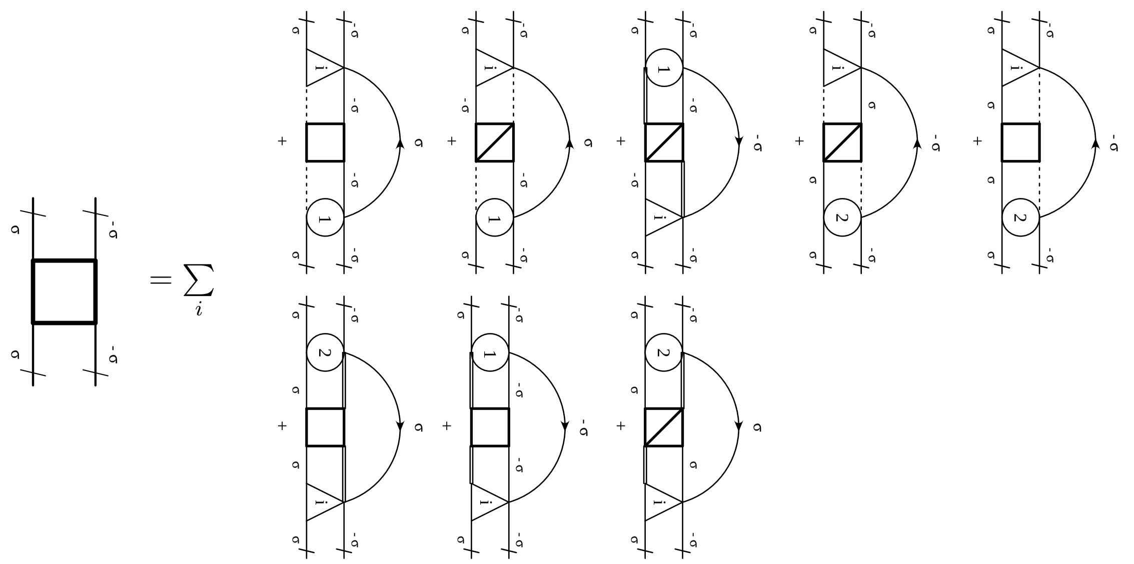

(A.5)

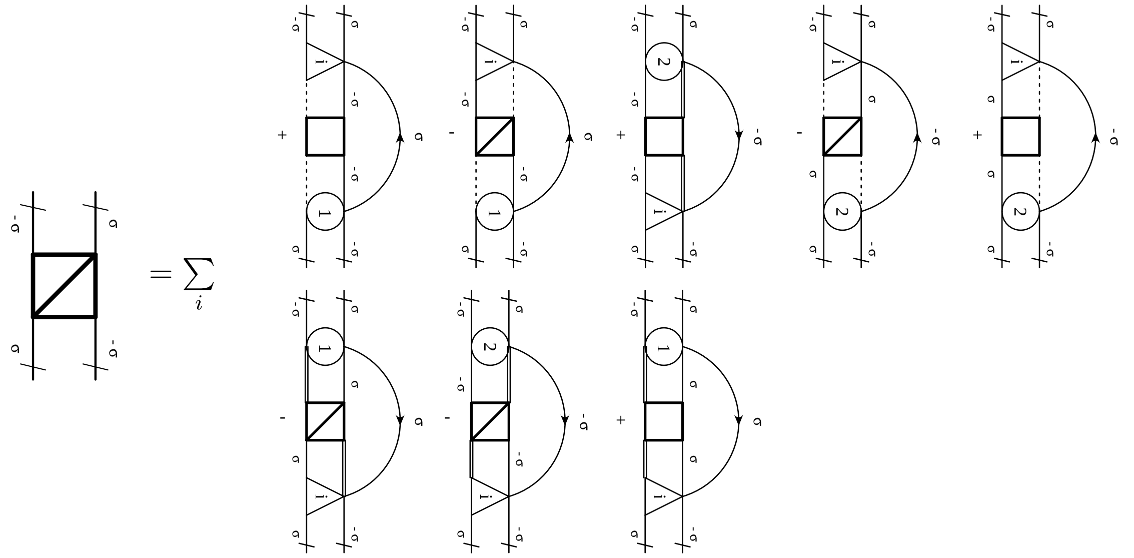

(A.6)

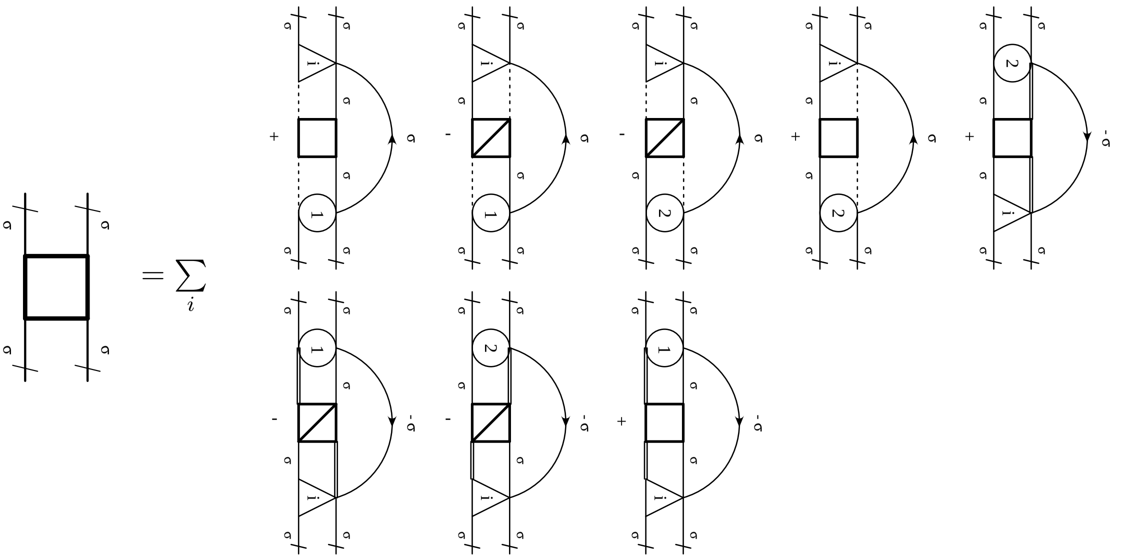

(A.7)

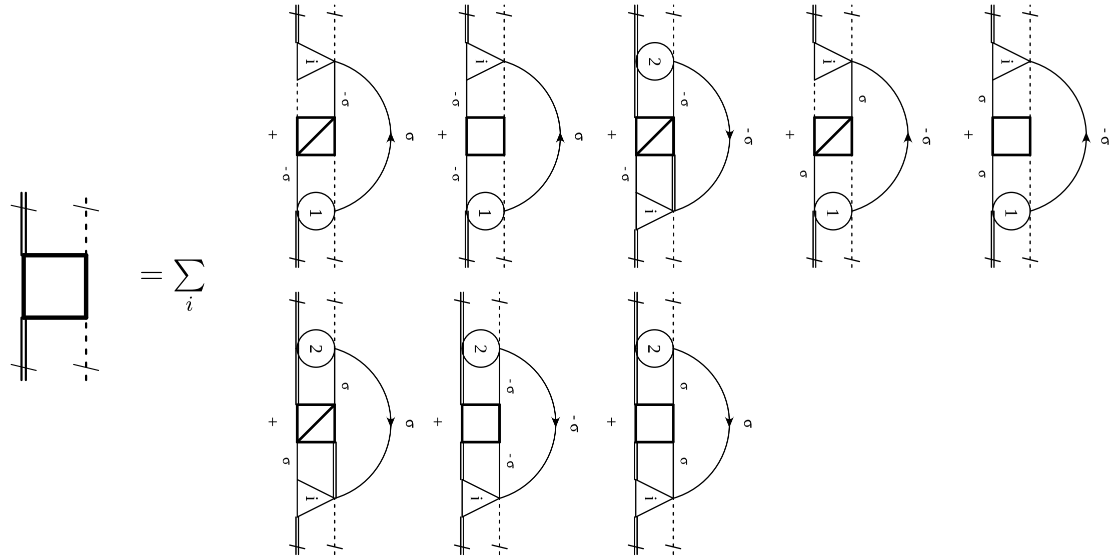

(A.8)

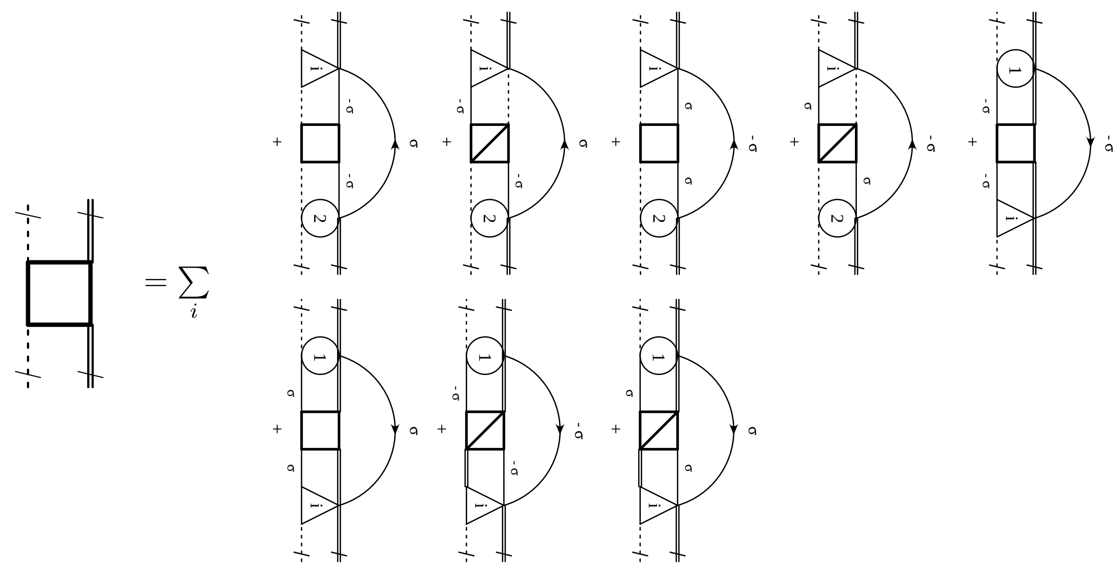

(A.9)

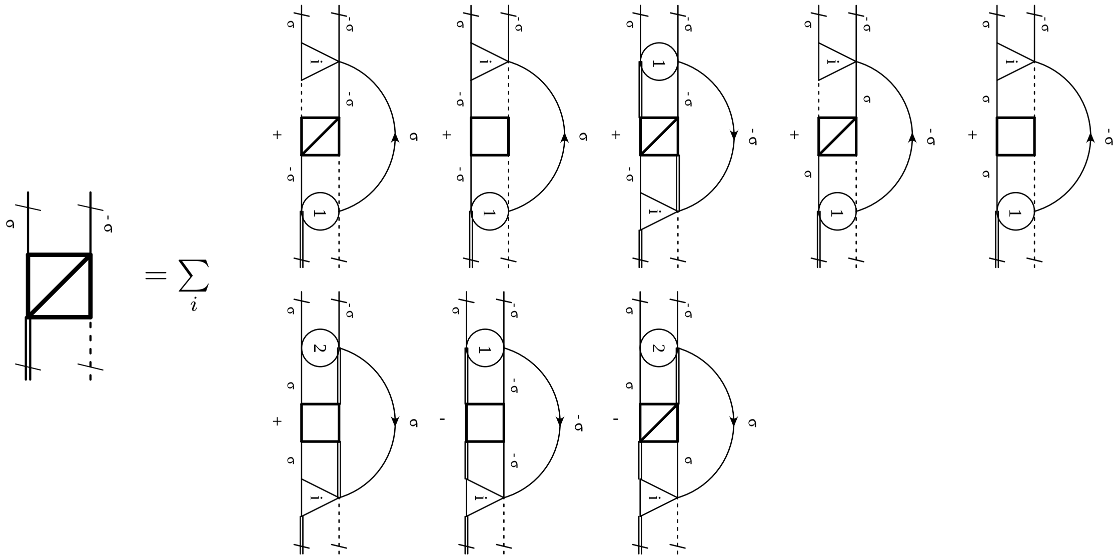

(A.10)

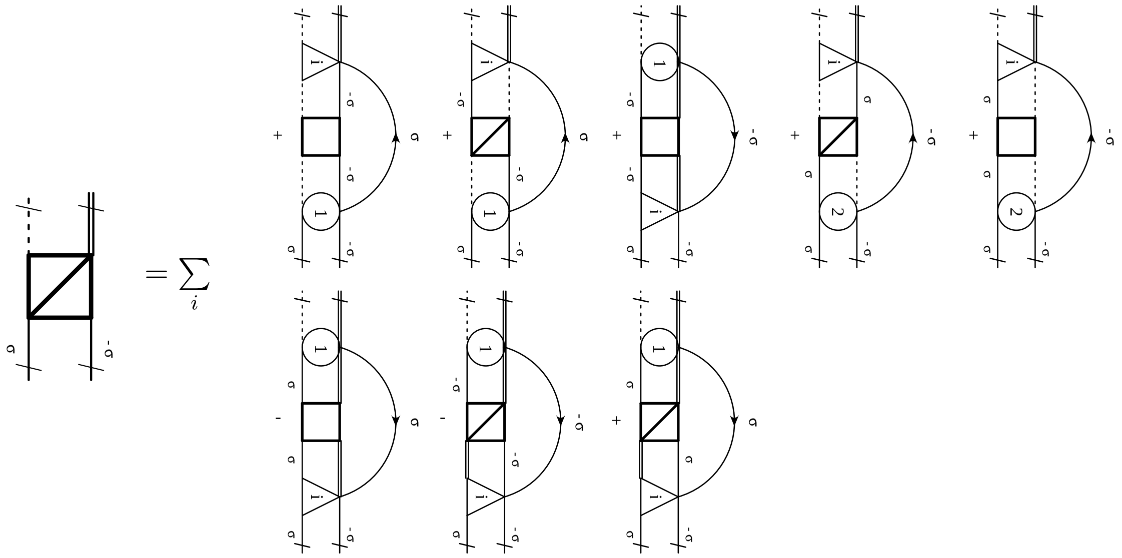

(A.11)

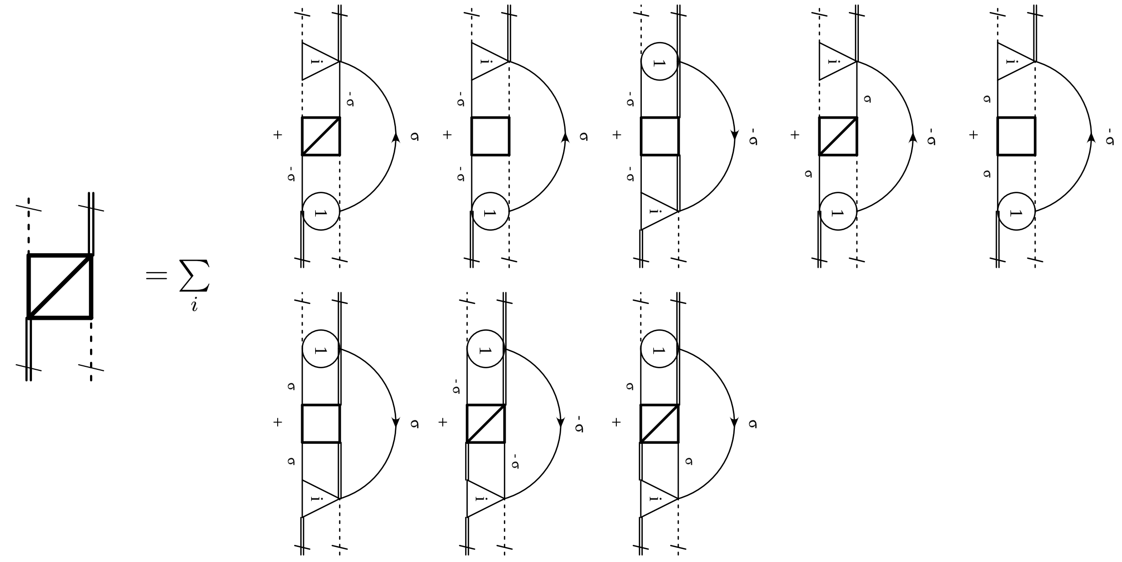

(A.12)

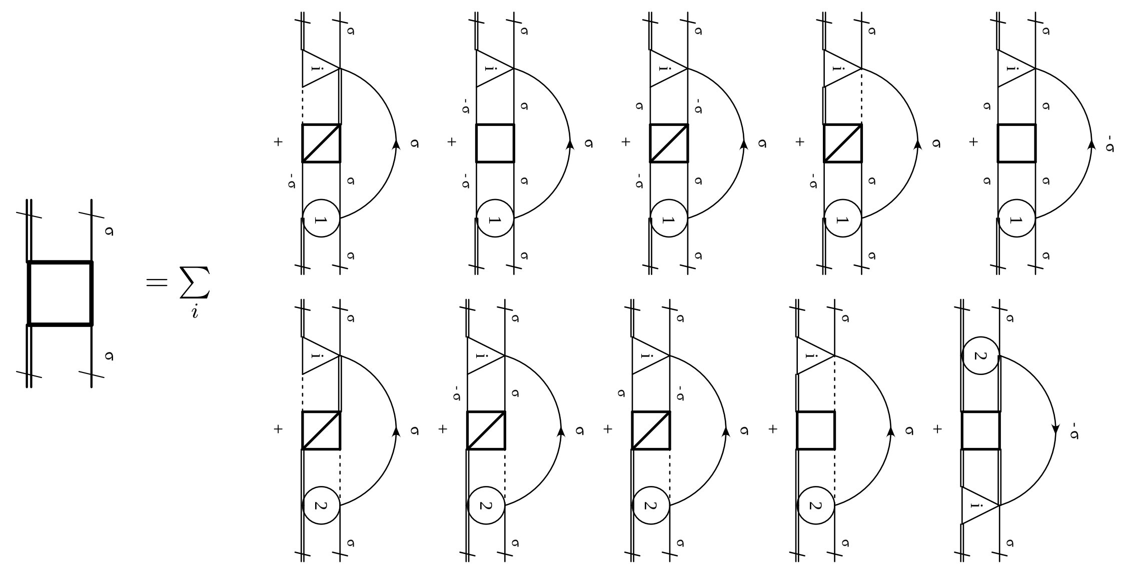

(A.13)

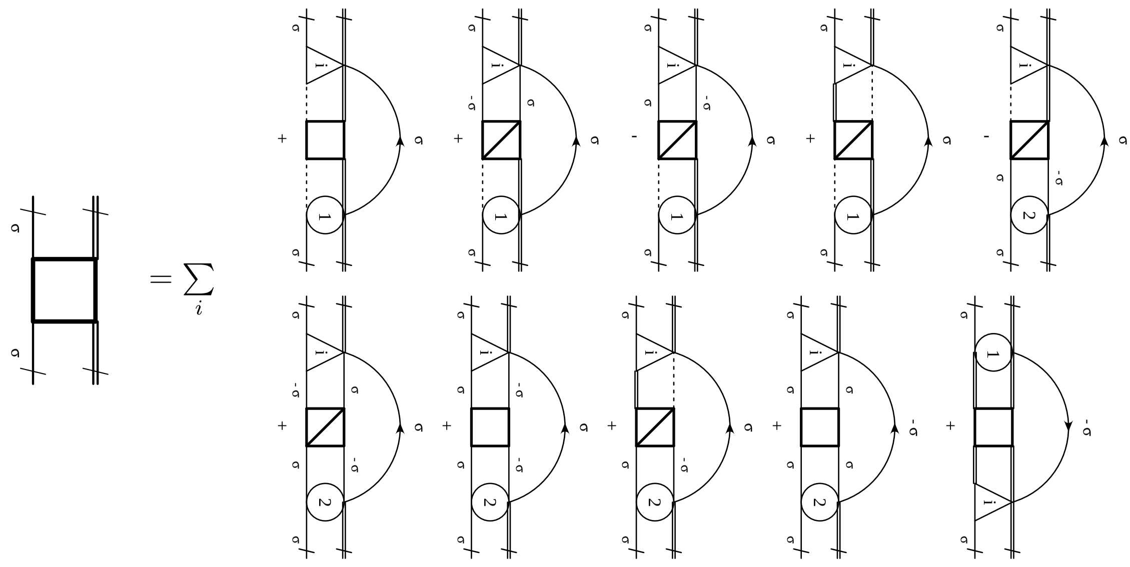

(A.14)

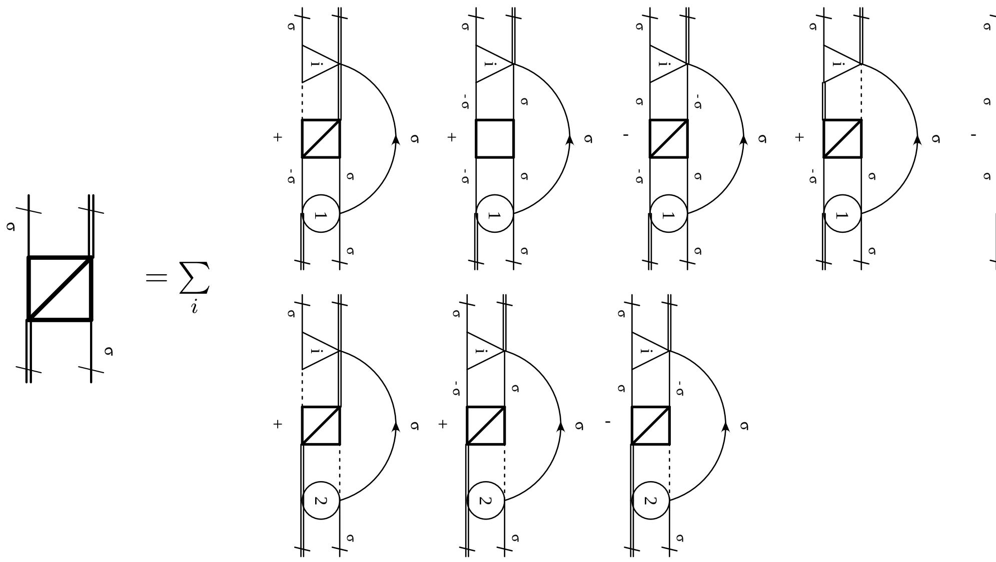

(A.15)

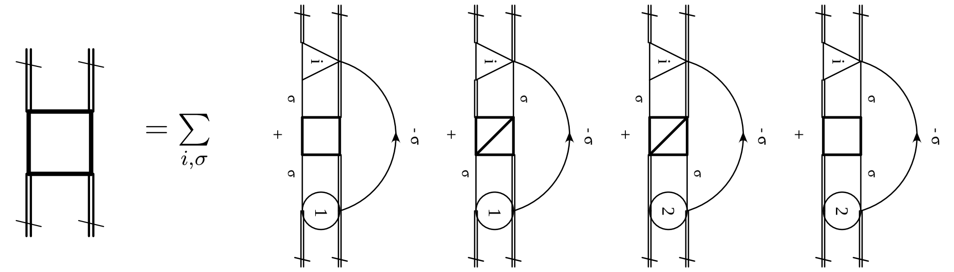

(A.16)

B ENCATI vertex equations

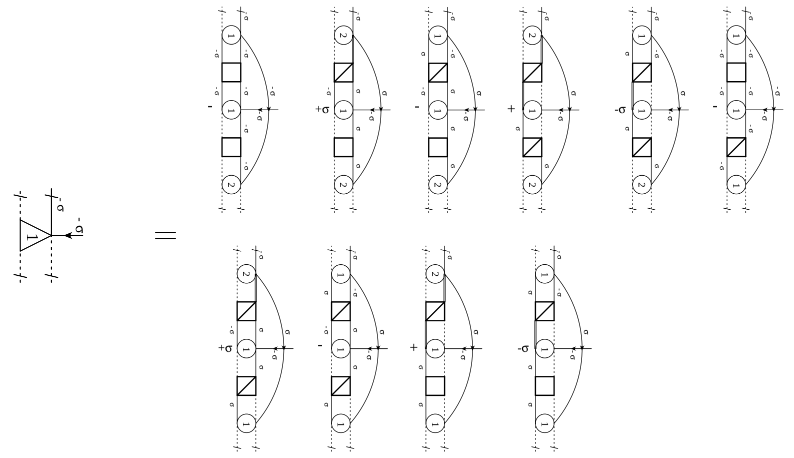

(B.1)

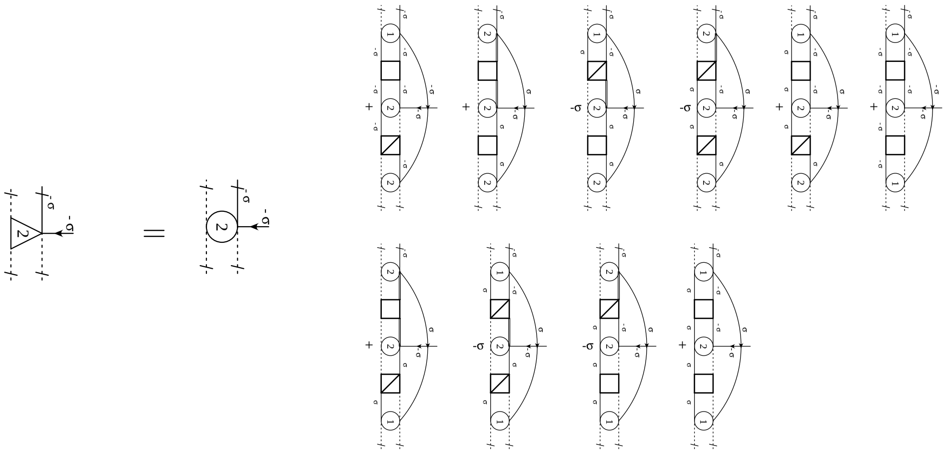

(B.2)

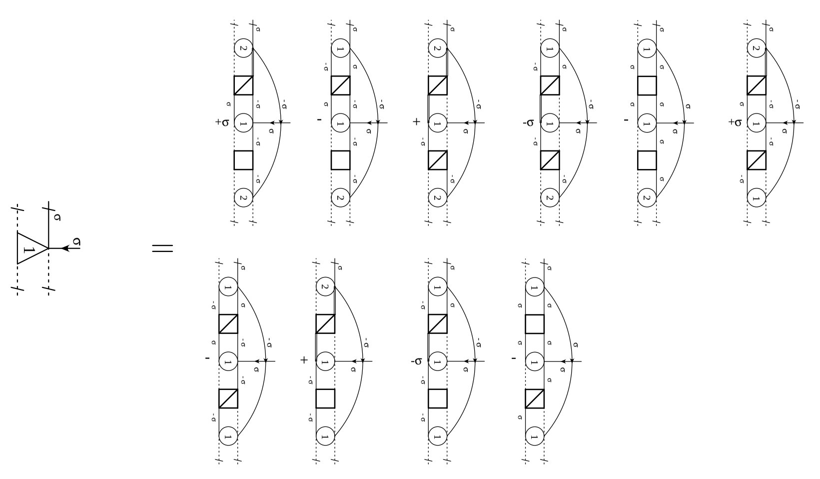

(B.3)

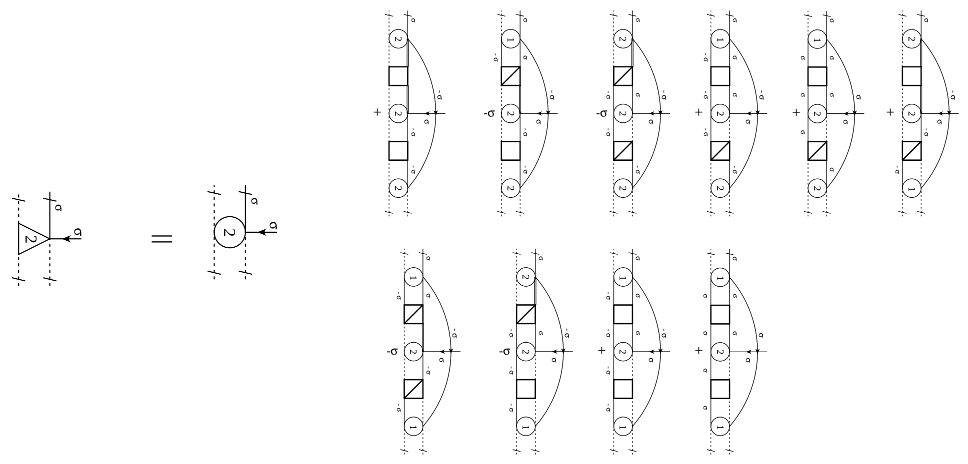

(B.4)

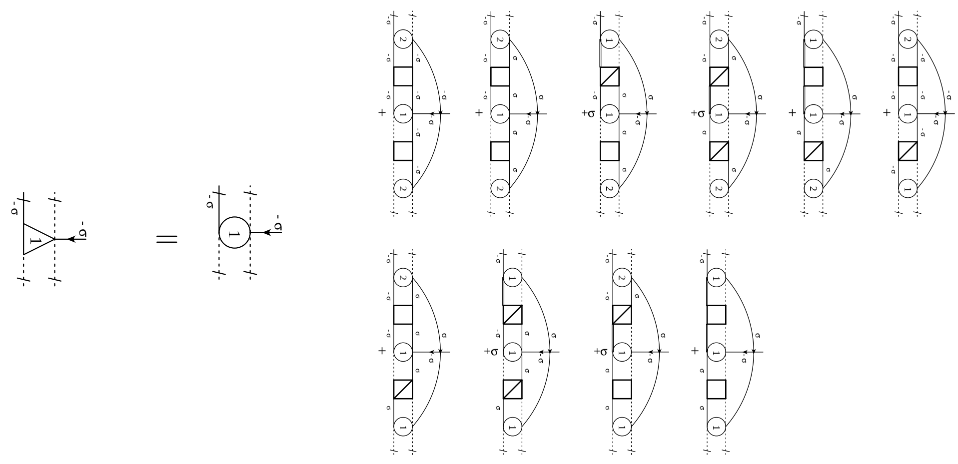

(B.5)

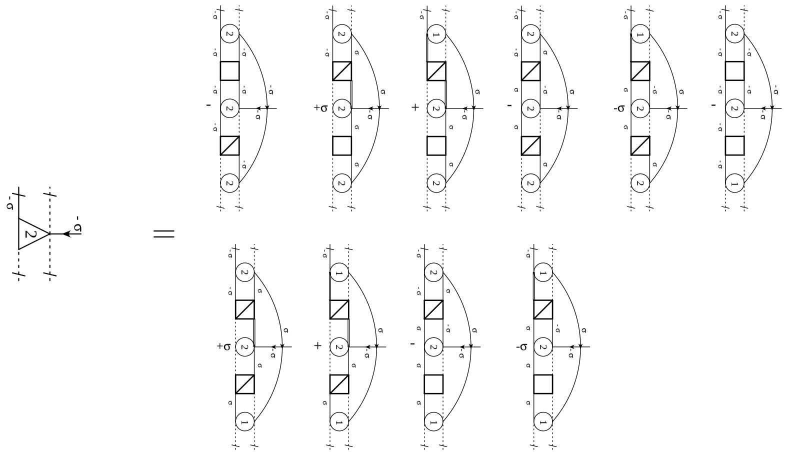

(B.6)

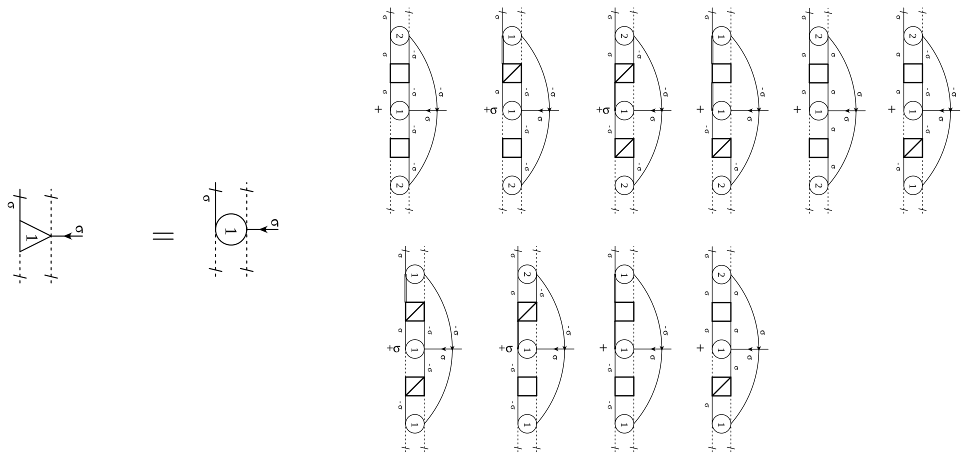

(B.7)

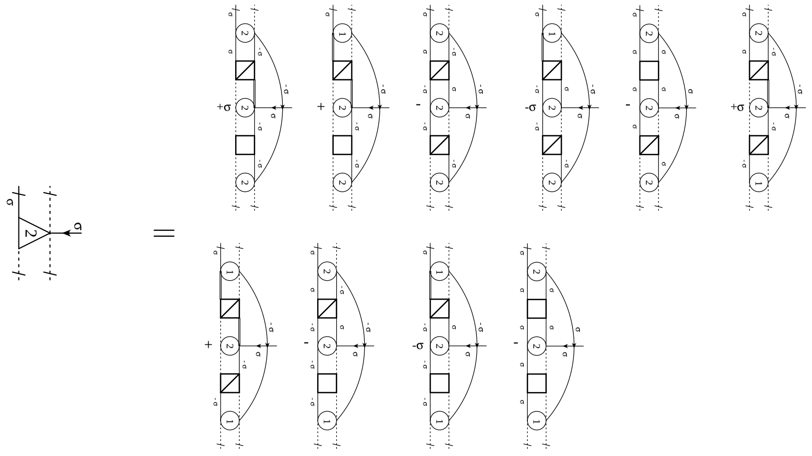

(B.8)

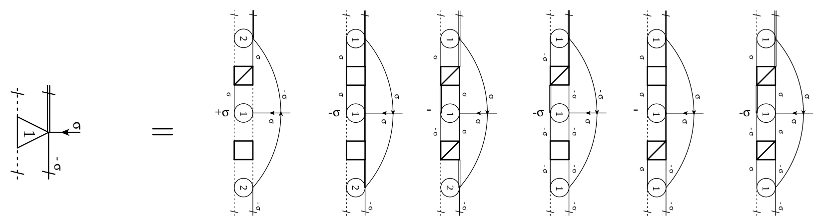

(B.9)

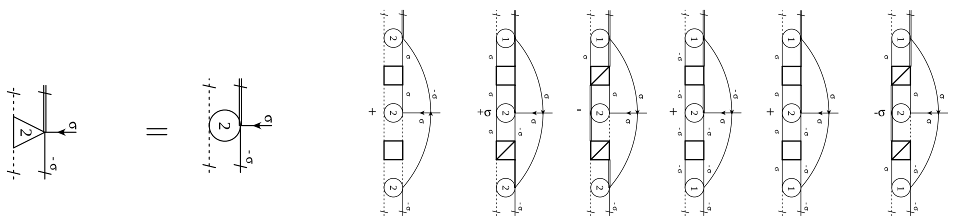

(B.10)

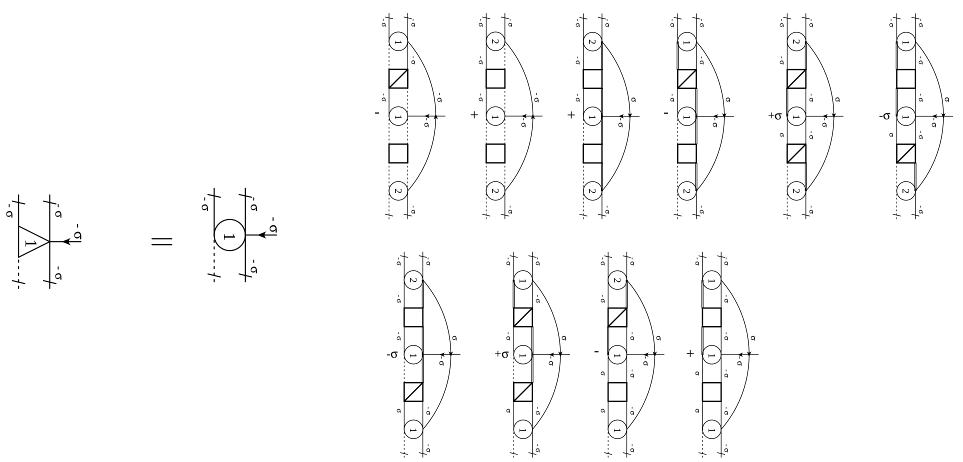

(B.11)

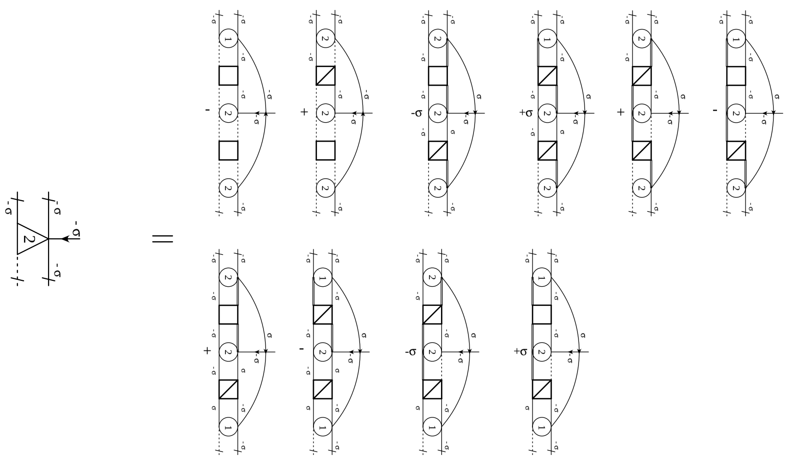

(B.12)

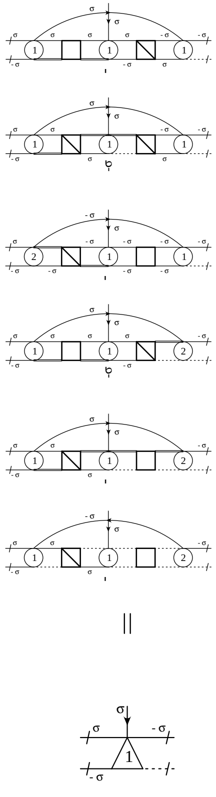

(B.13)

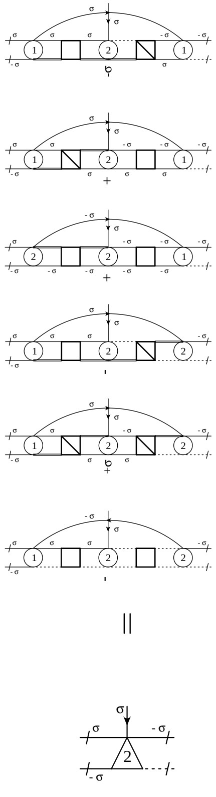

(B.14)

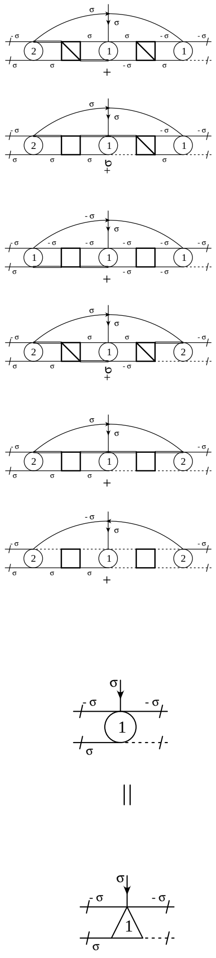

(B.15)

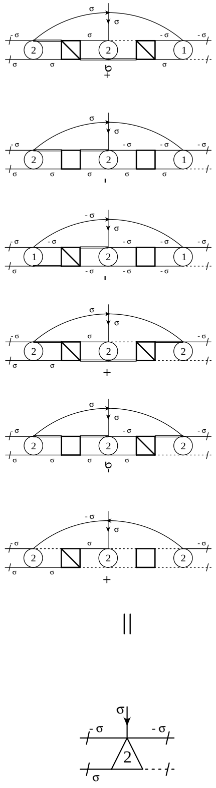

(B.16)

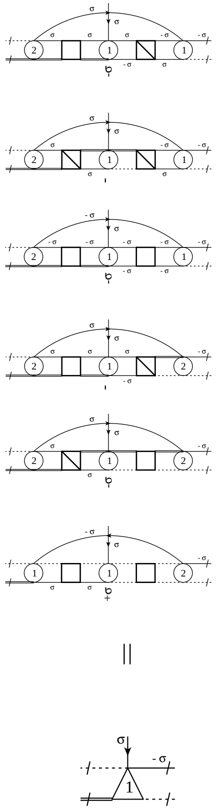

(B.17)

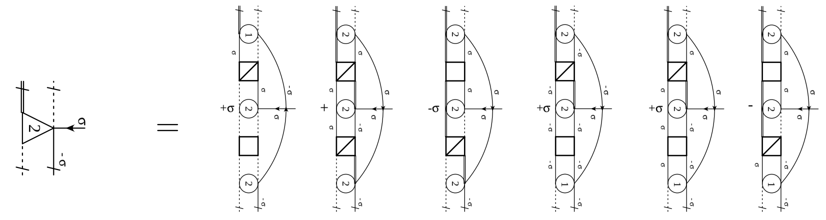

(B.18)

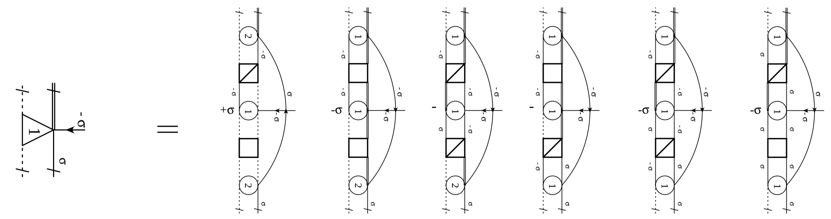

(B.19)

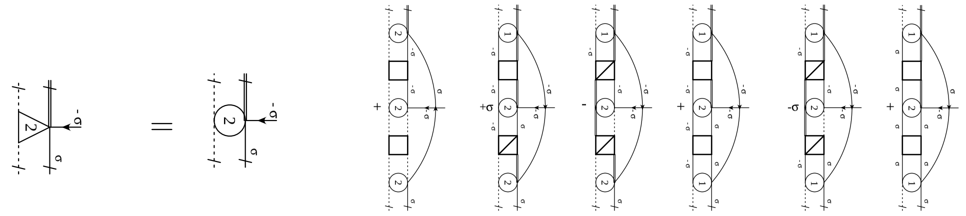

(B.20)

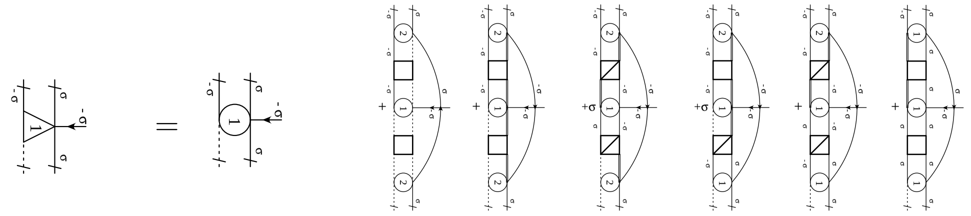

(B.21)

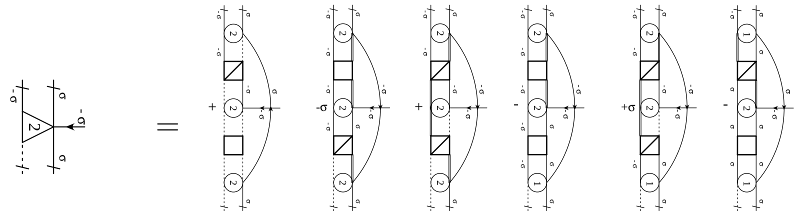

(B.22)

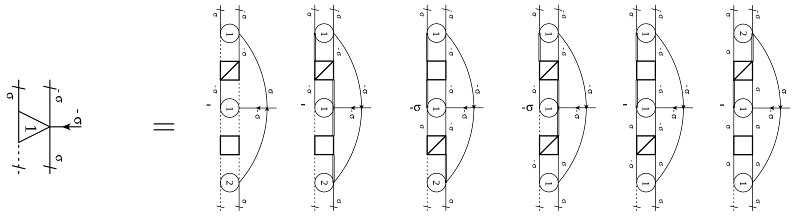

(B.23)

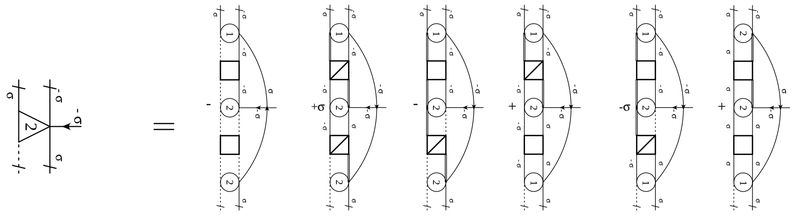

(B.24)

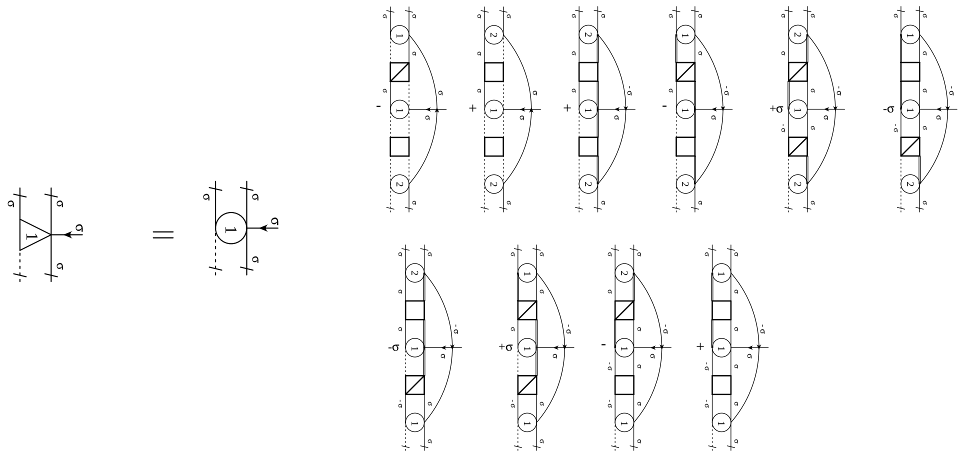

(B.25)

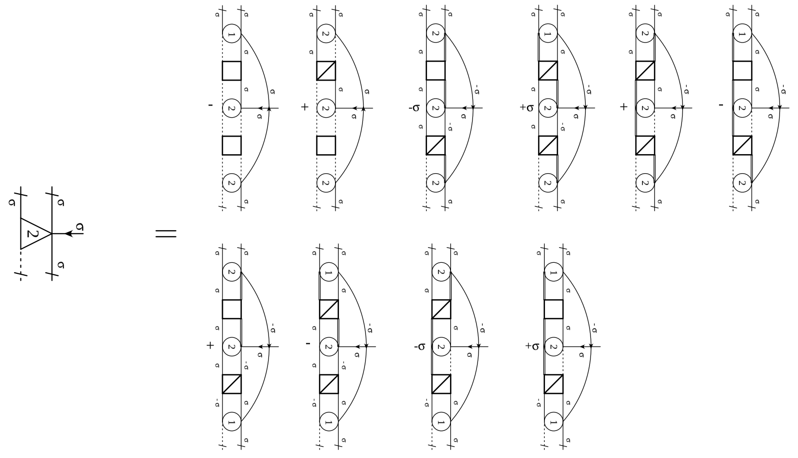

(B.26)

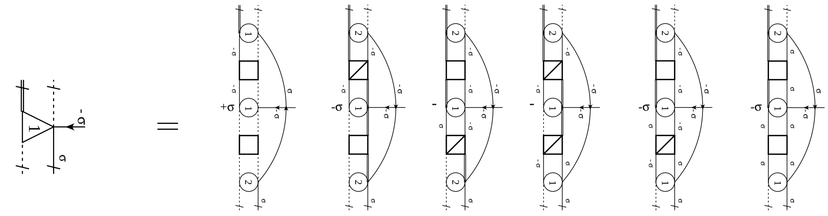

(B.27)

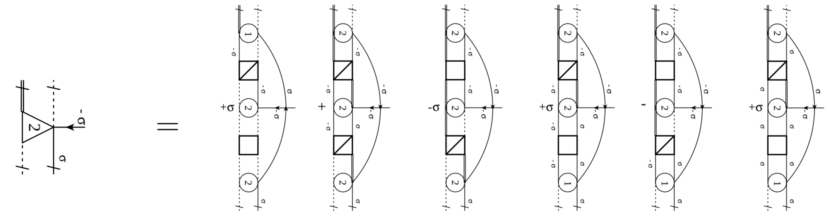

(B.28)

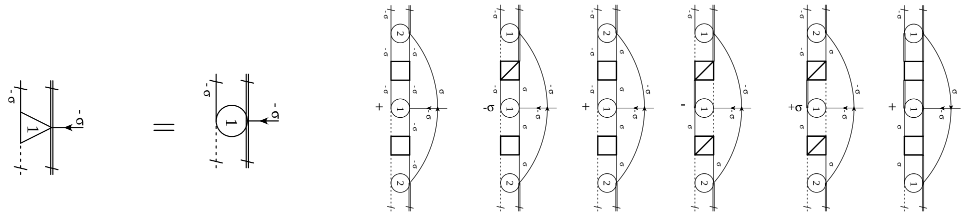

(B.29)

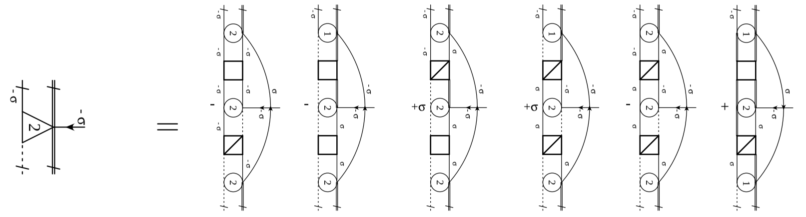

(B.30)

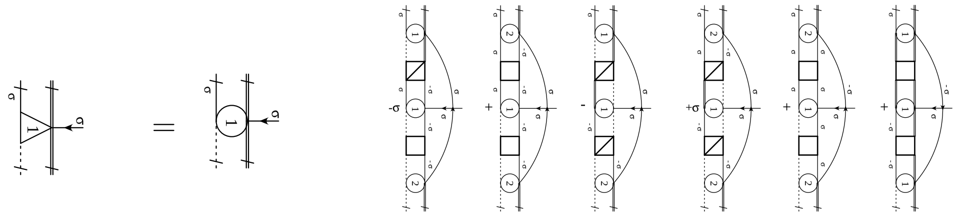

(B.31)

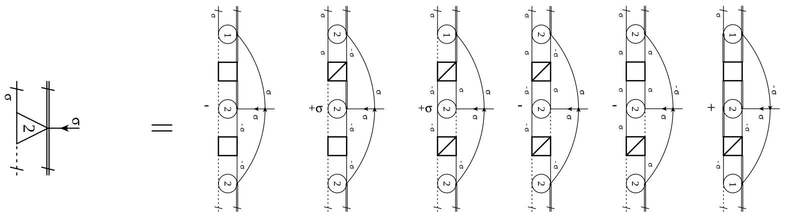

(B.32)

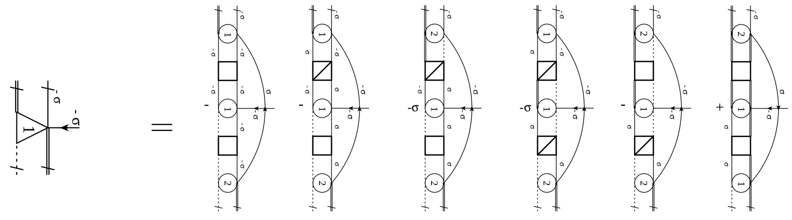

(B.33)

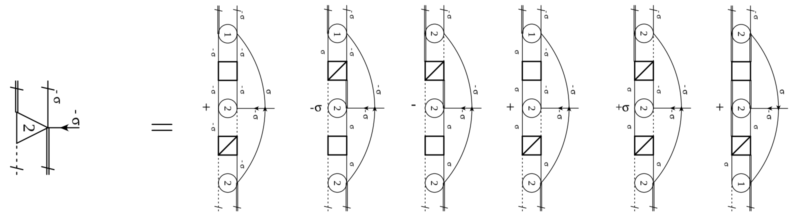

(B.34)

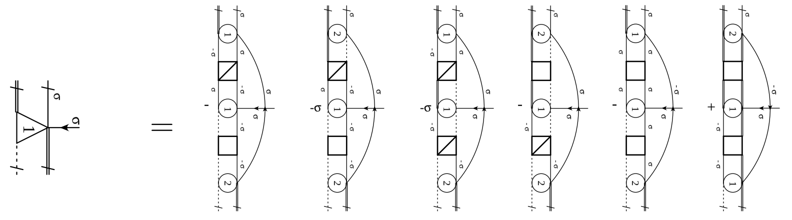

(B.35)

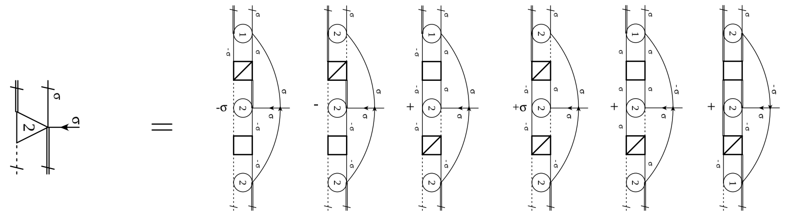

(B.36)

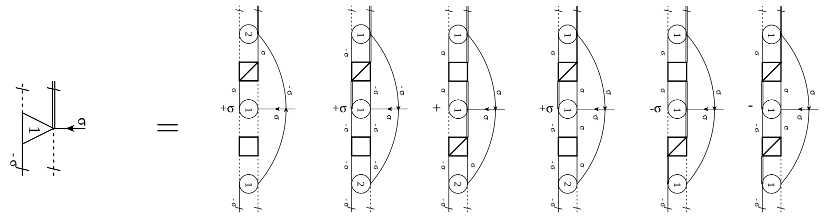

(B.37)

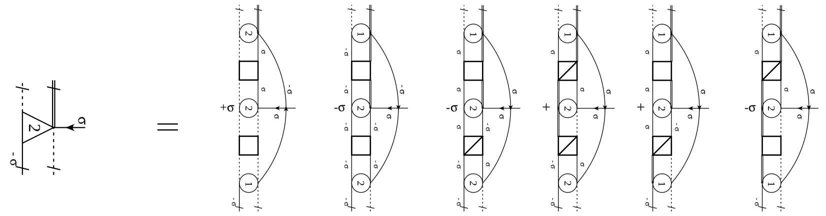

(B.38)

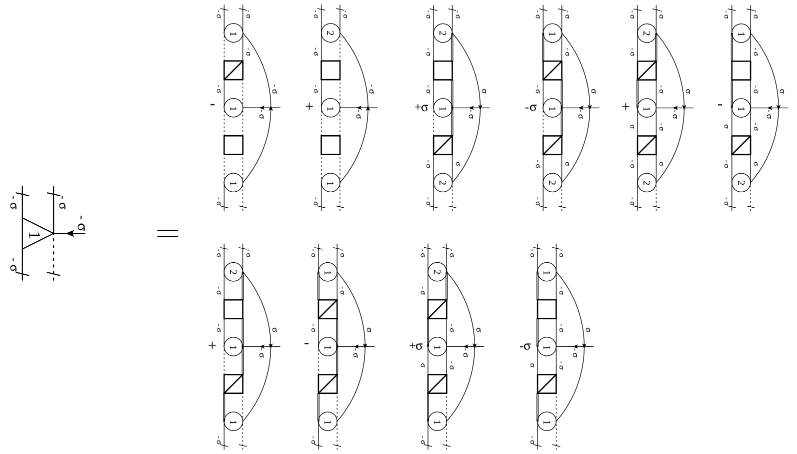

(B.39)

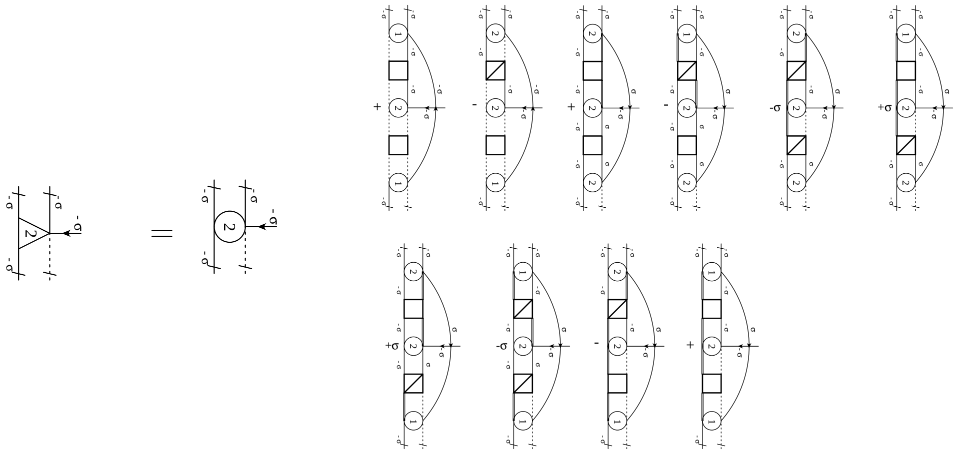

(B.40)

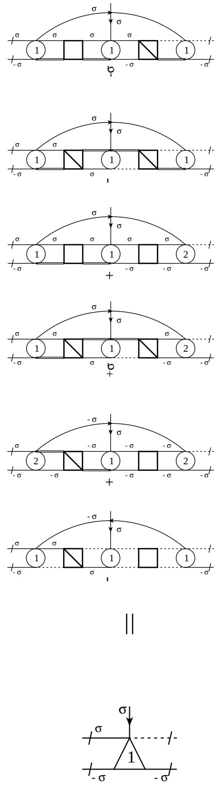

(B.41)

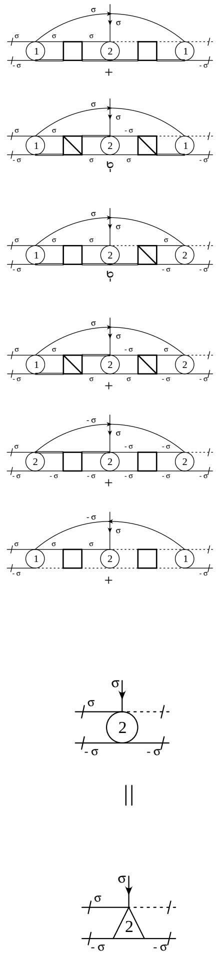

(B.42)

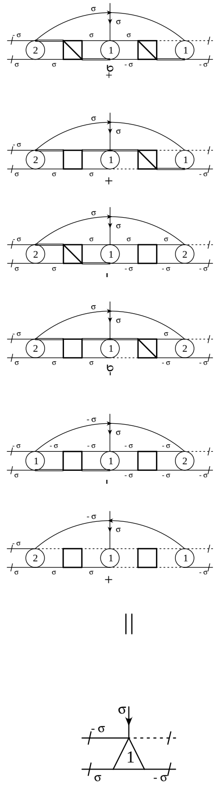

(B.43)

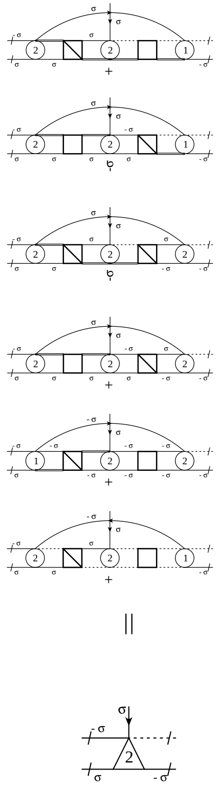

(B.44)

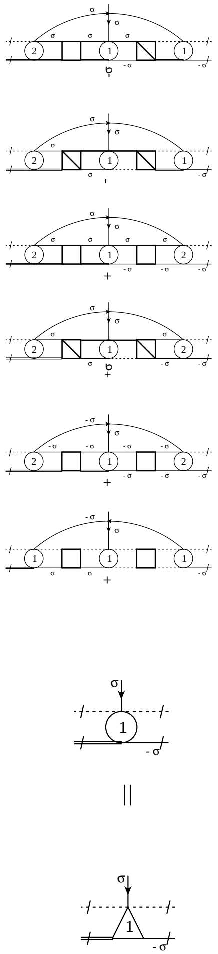

(B.45)

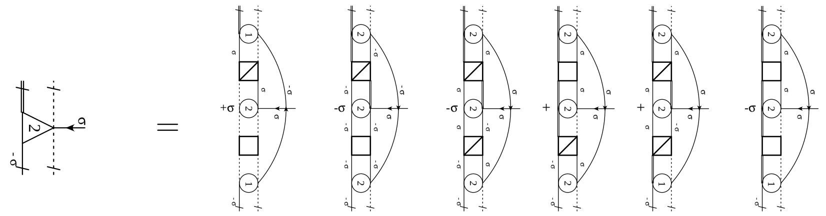

(B.46)

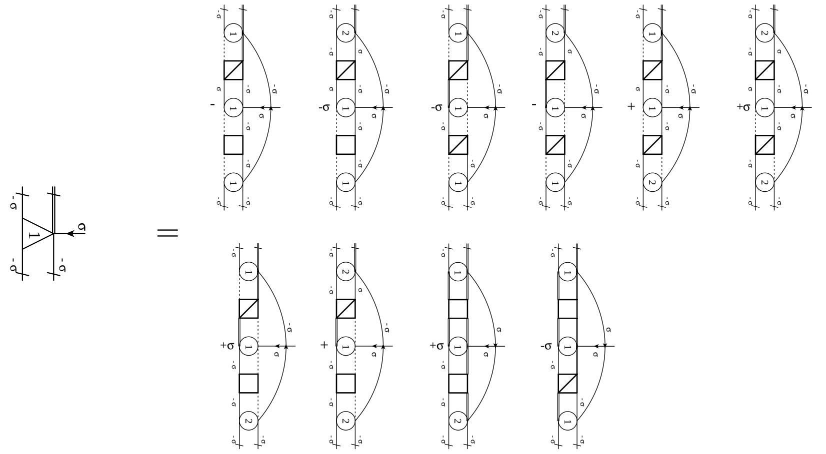

(B.47)

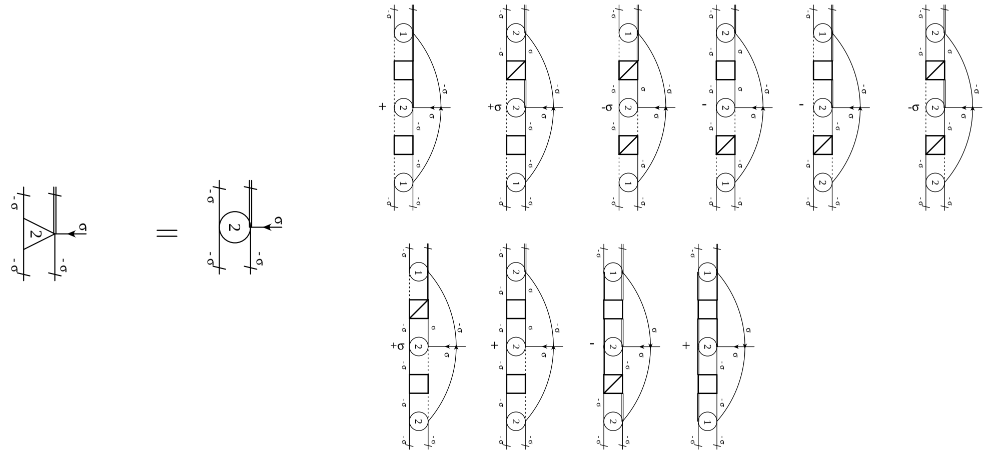

(B.48)

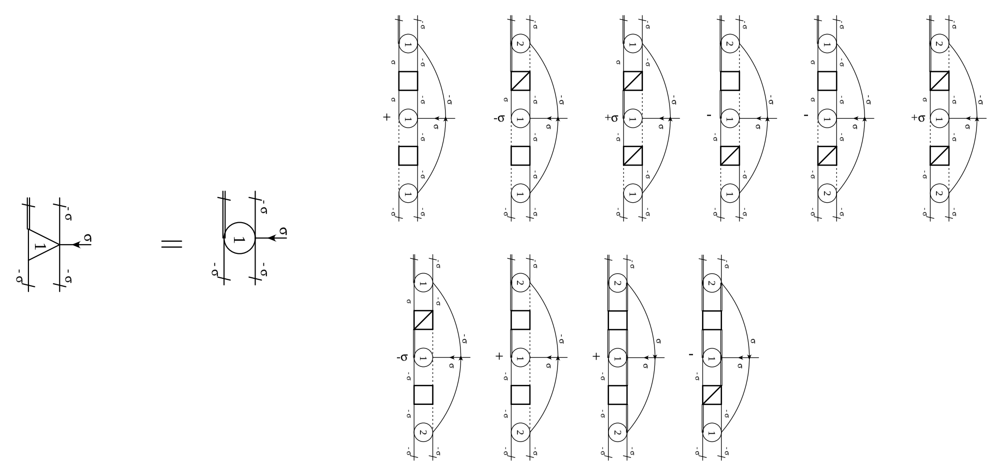

(B.49)

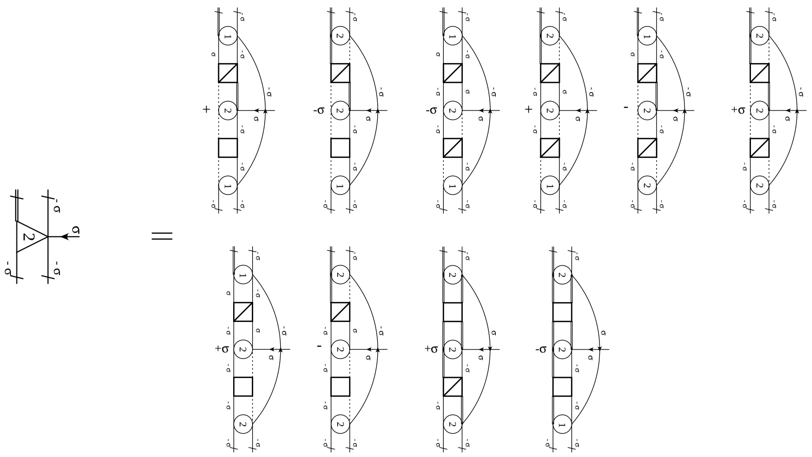

(B.50)

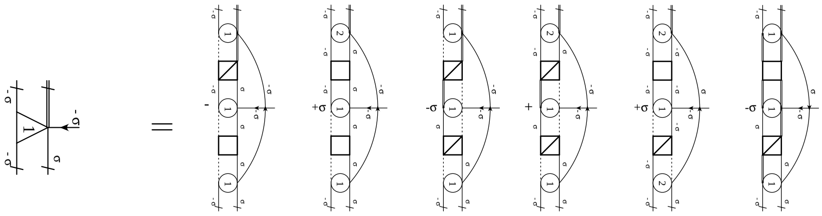

(B.51)

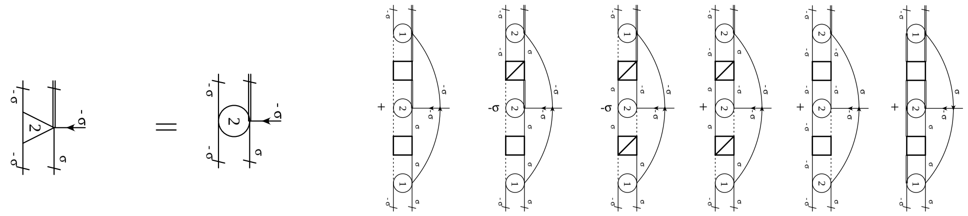

(B.52)

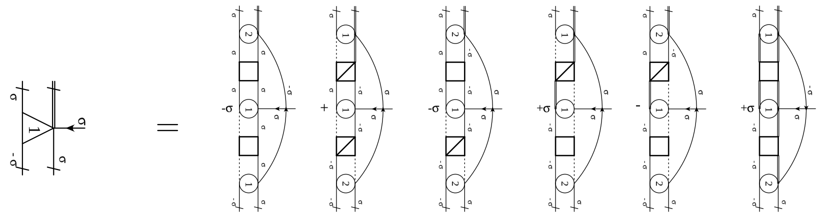

(B.53)

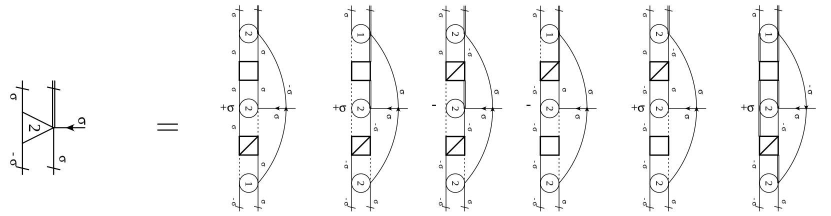

(B.54)

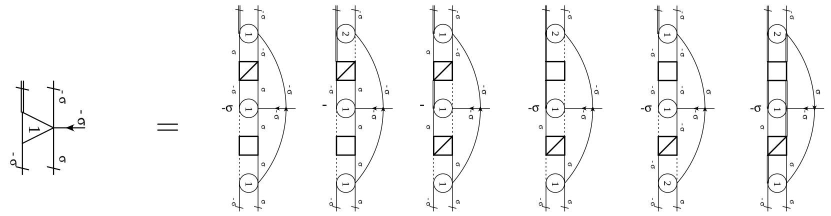

(B.55)

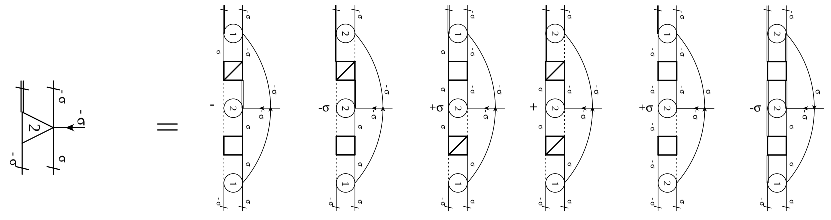

(B.56)

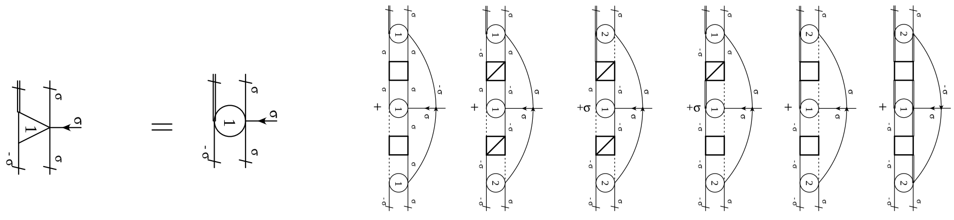

(B.57)

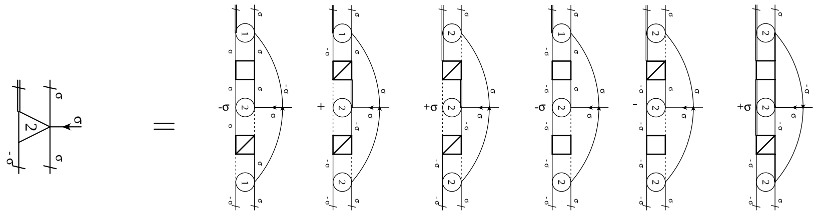

(B.58)

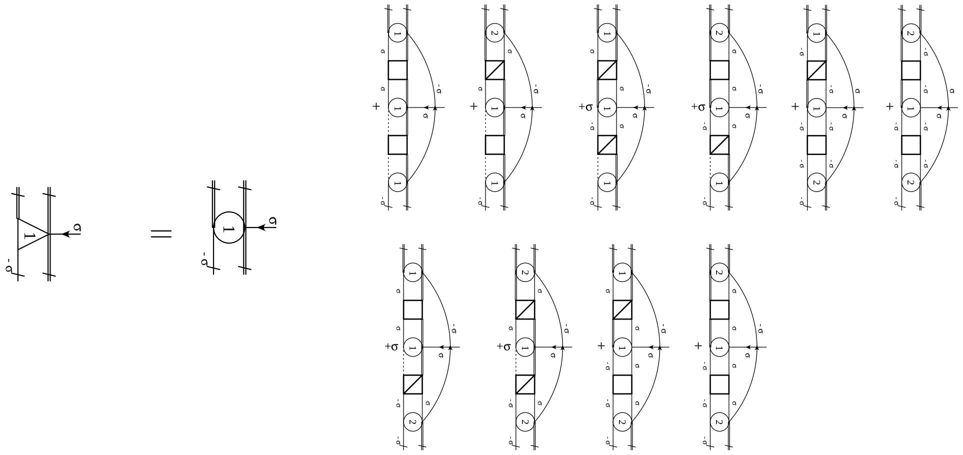

(B.59)

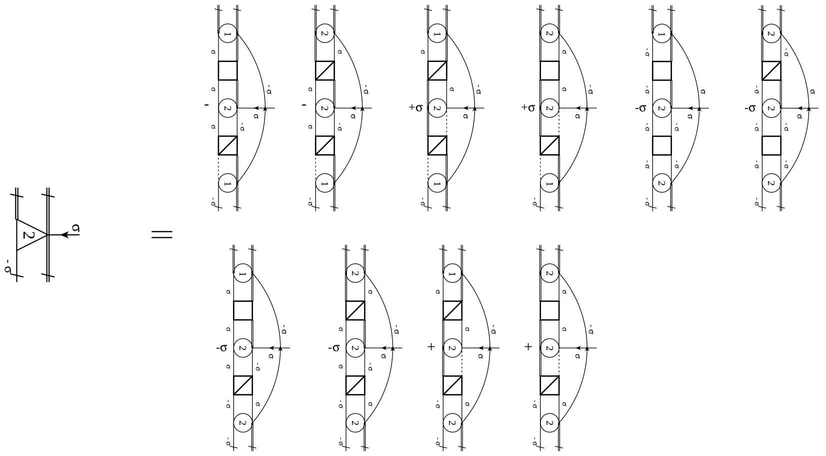

(B.60)

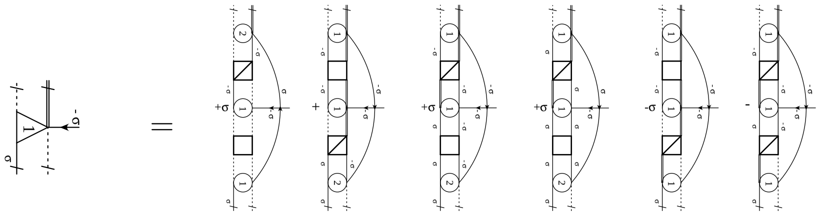

(B.61)

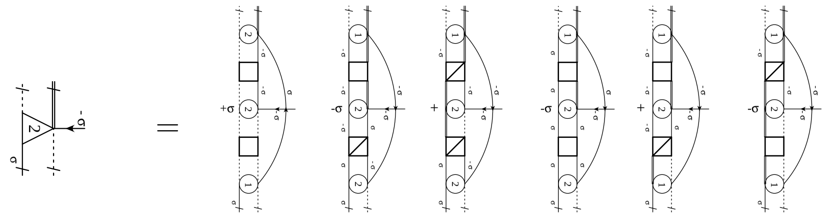

(B.62)

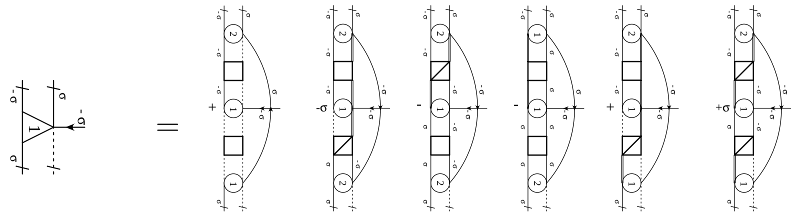

(B.63)

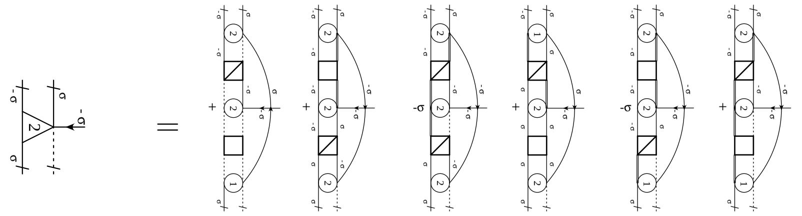

(B.64)

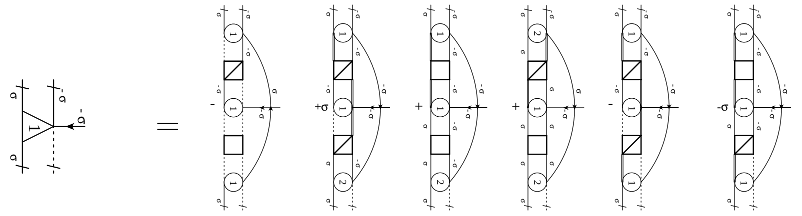

(B.65)

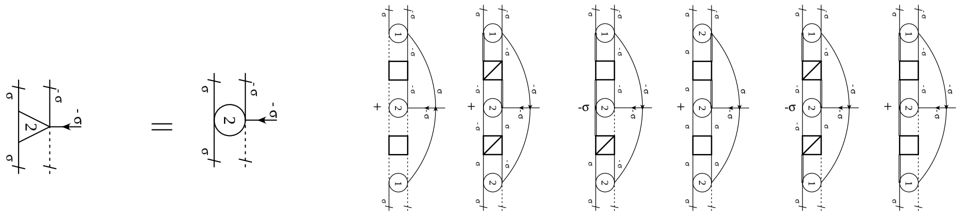

(B.66)

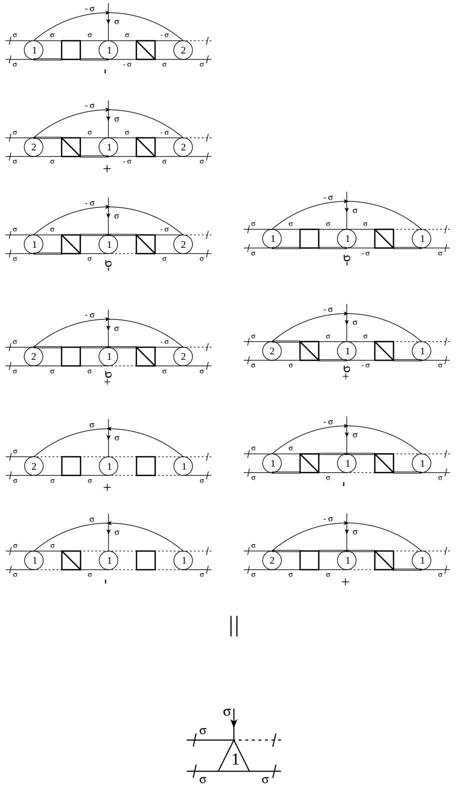

(B.67)

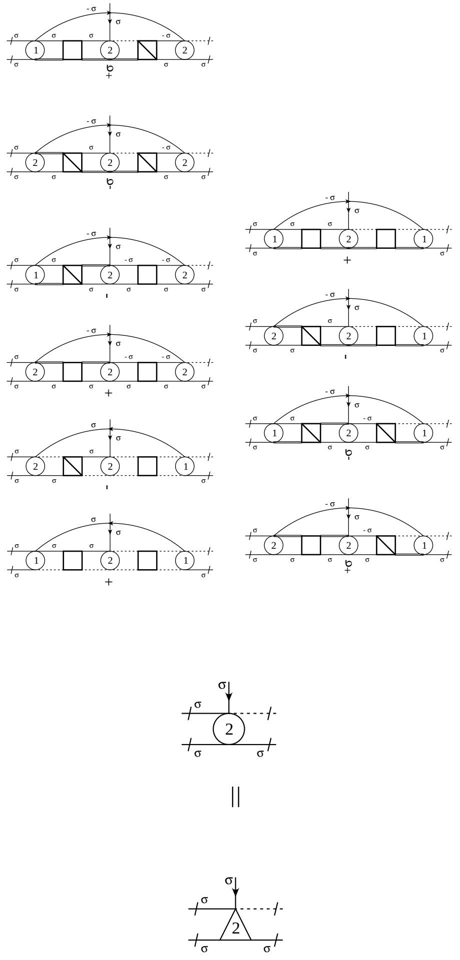

(B.68)

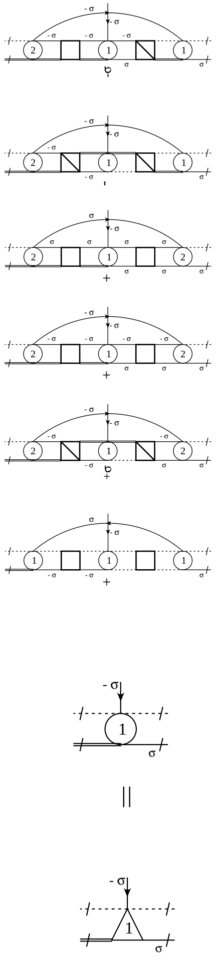

(B.69)

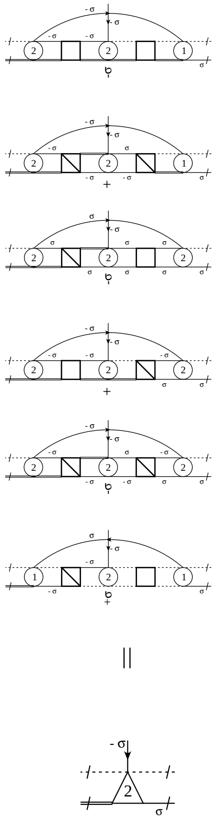

(B.70)

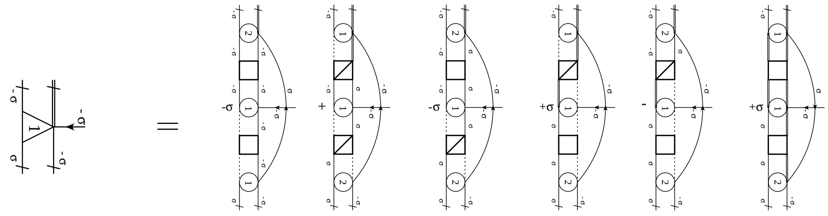

(B.71)

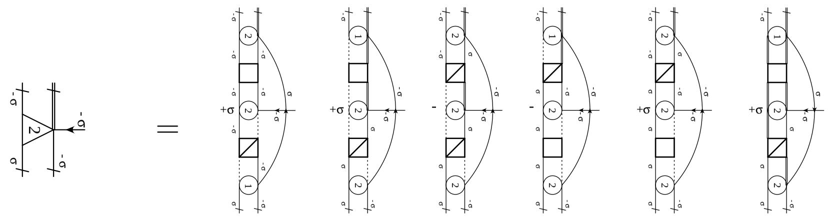

(B.72)

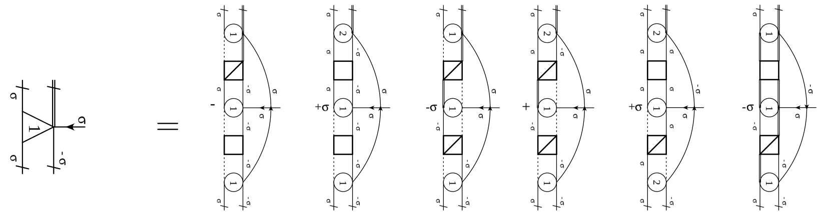

(B.73)

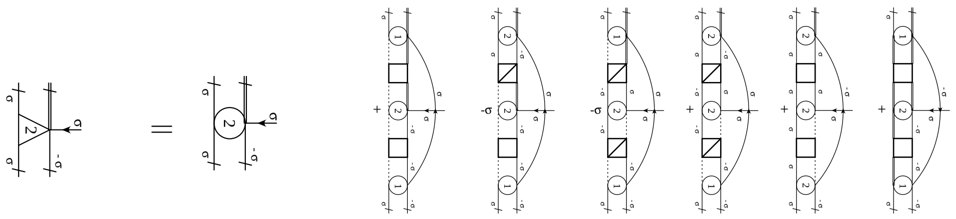

(B.74)

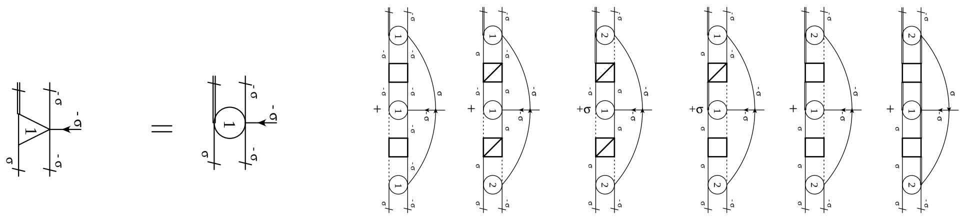

(B.75)

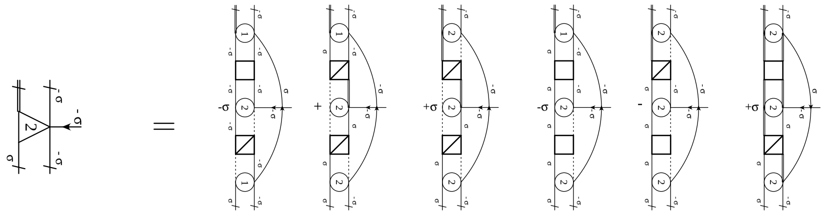

(B.76)

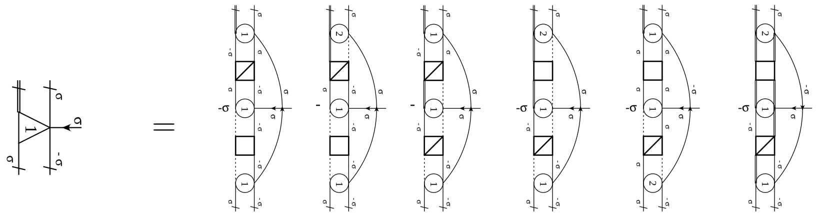

(B.77)

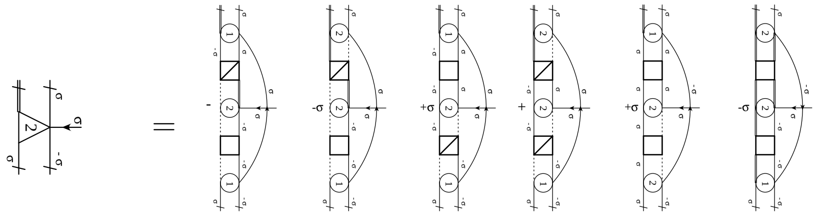

(B.78)

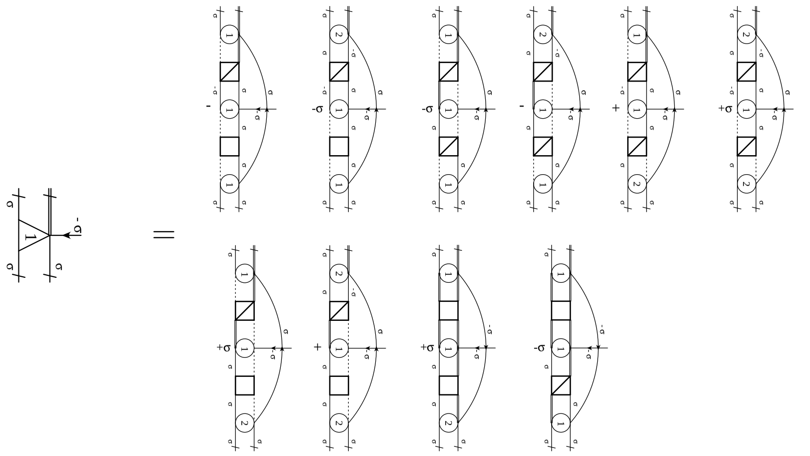

(B.79)

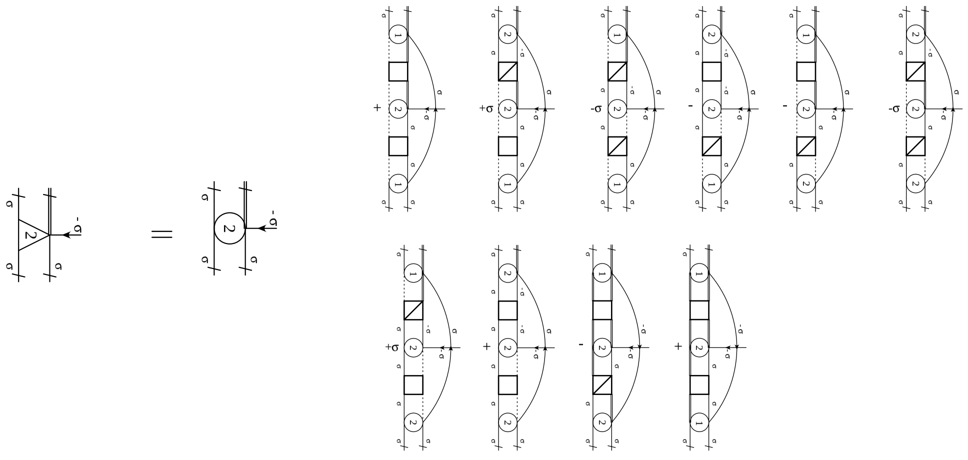

(B.80)

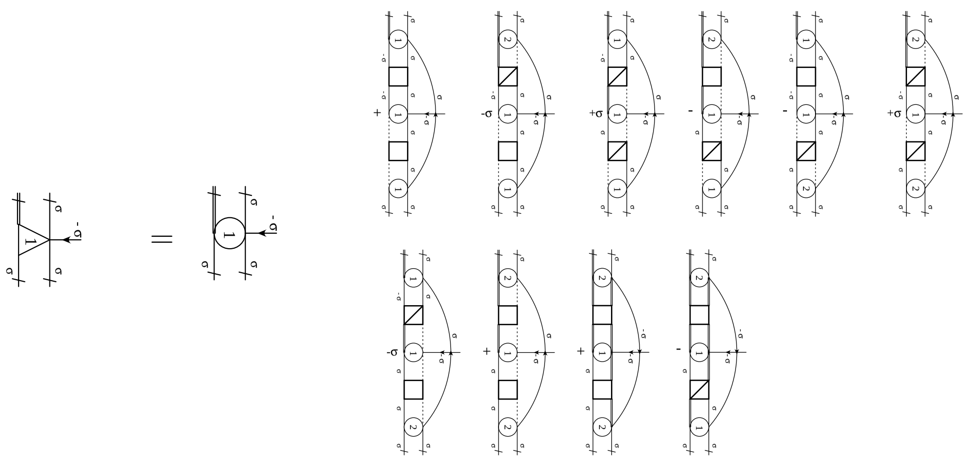

(B.81)

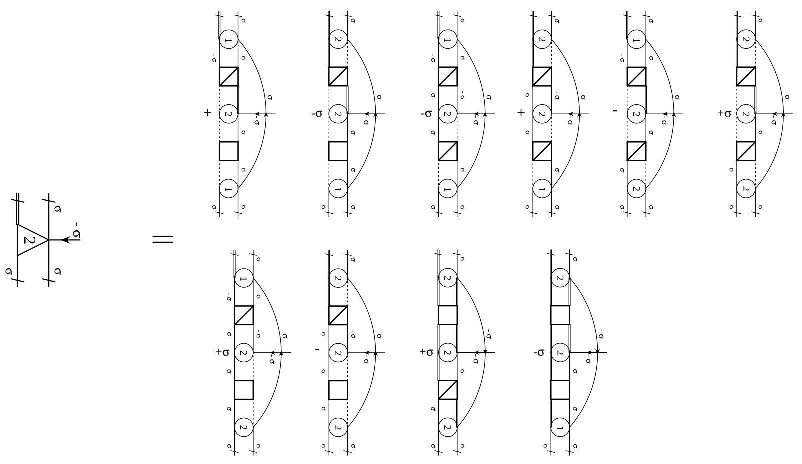

(B.82)

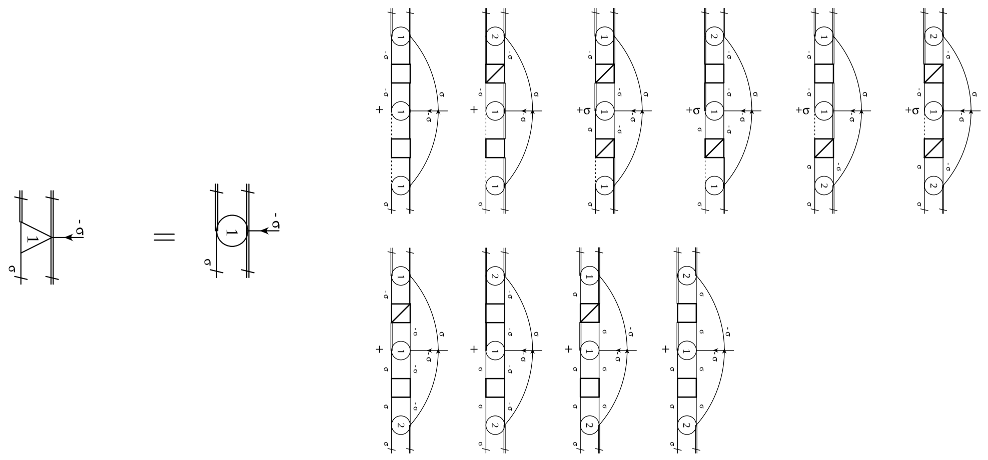

(B.83)

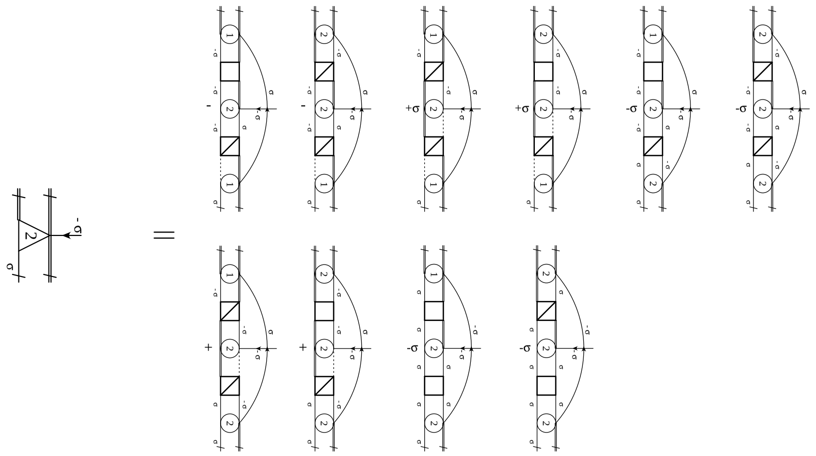

(B.84)

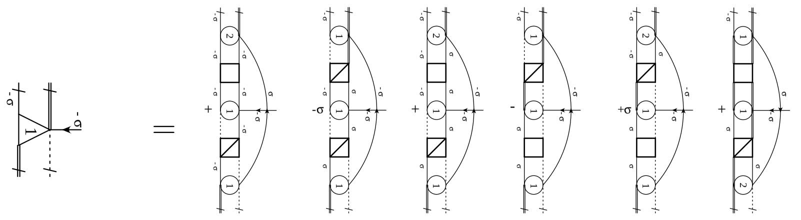

(B.85)

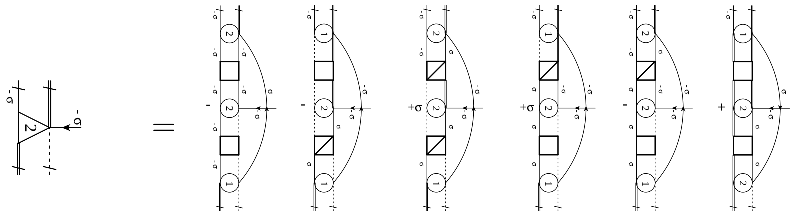

(B.86)

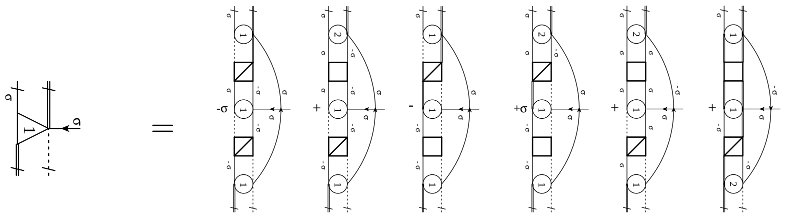

(B.87)

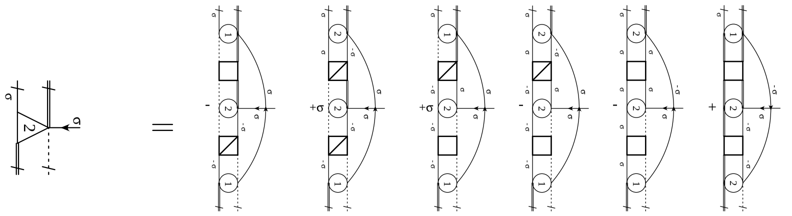

(B.88)

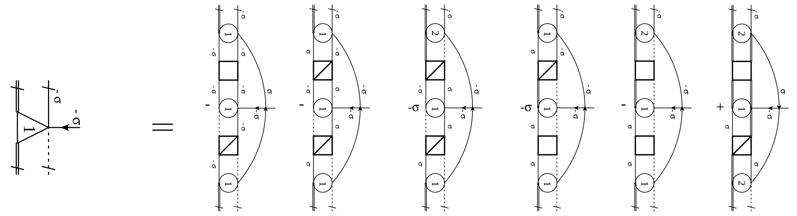

(B.89)

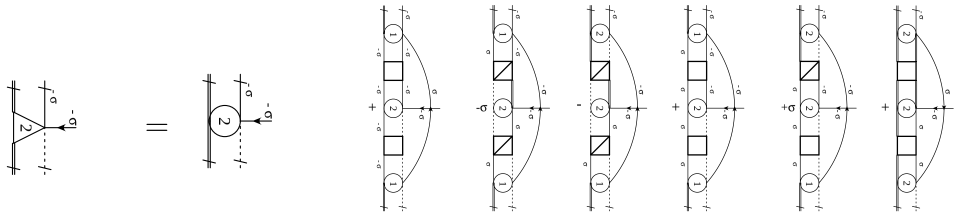

(B.90)

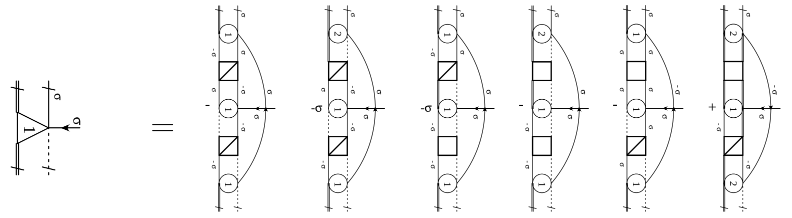

(B.91)

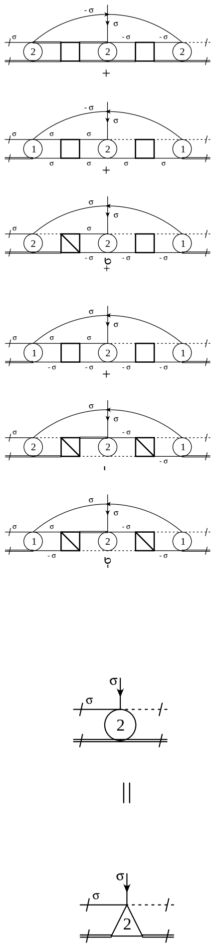

(B.92)

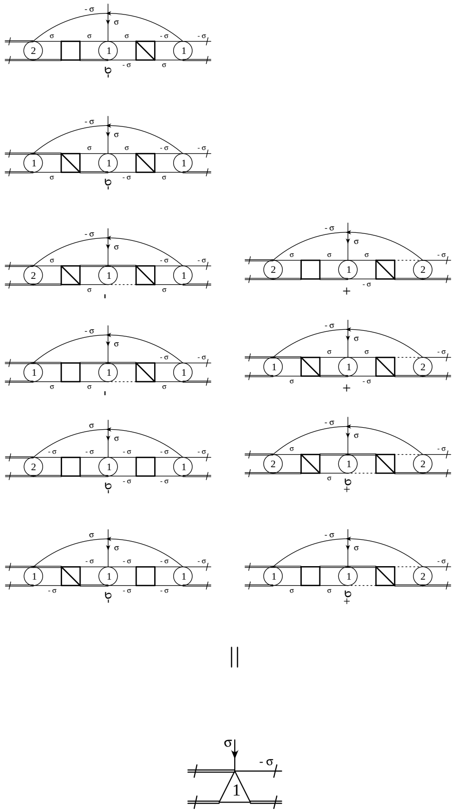

(B.93)

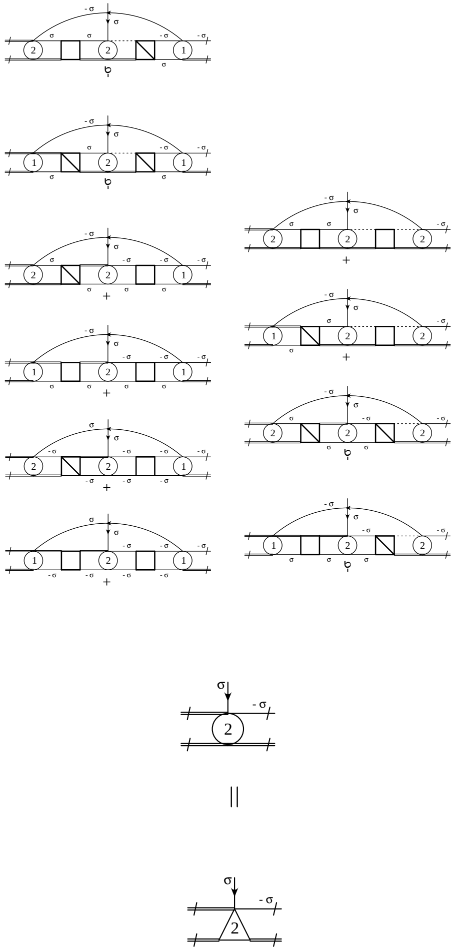

(B.94)

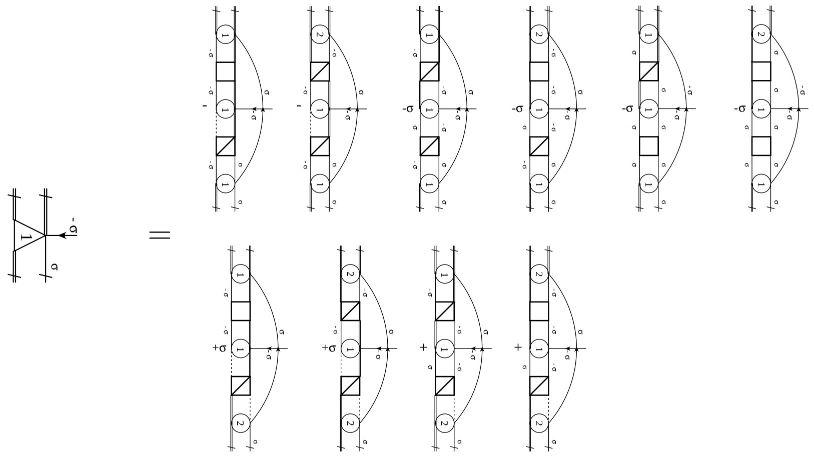

(B.95)

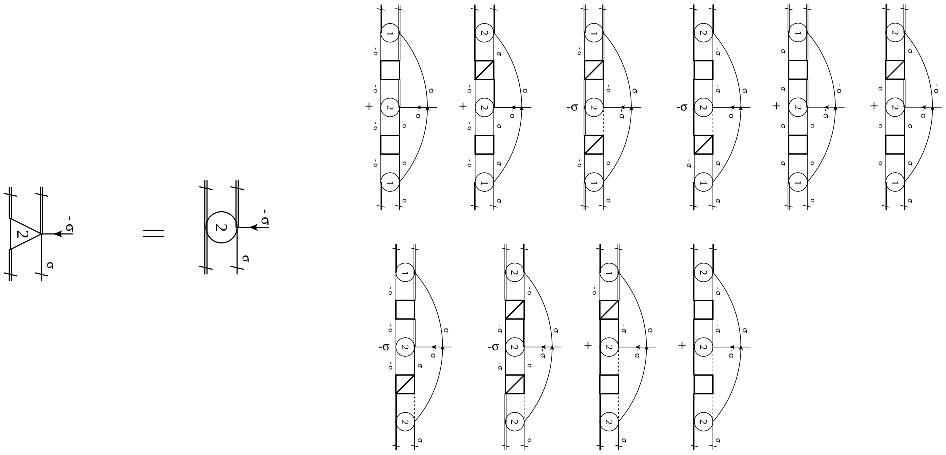

(B.96)

C Figures

C.1 Chapter 3

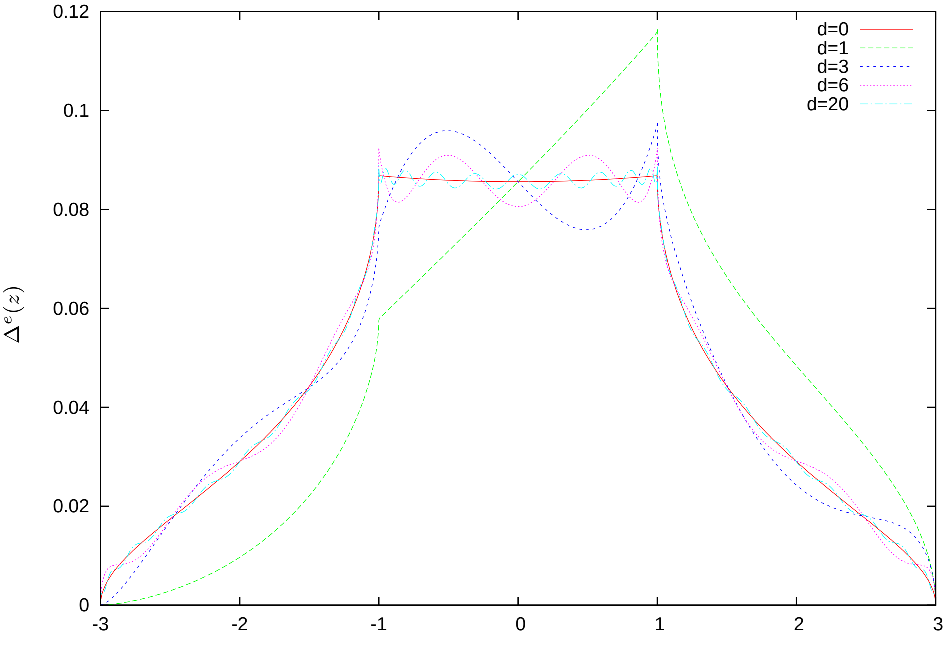
0.12
0.1
0.08
0.06
0.04
0.02
0
-3
-2
-1
0
1
2
3
$\Delta^e(z)$
ω
d=0
d=1
d=3
d=6
d=20

(a)

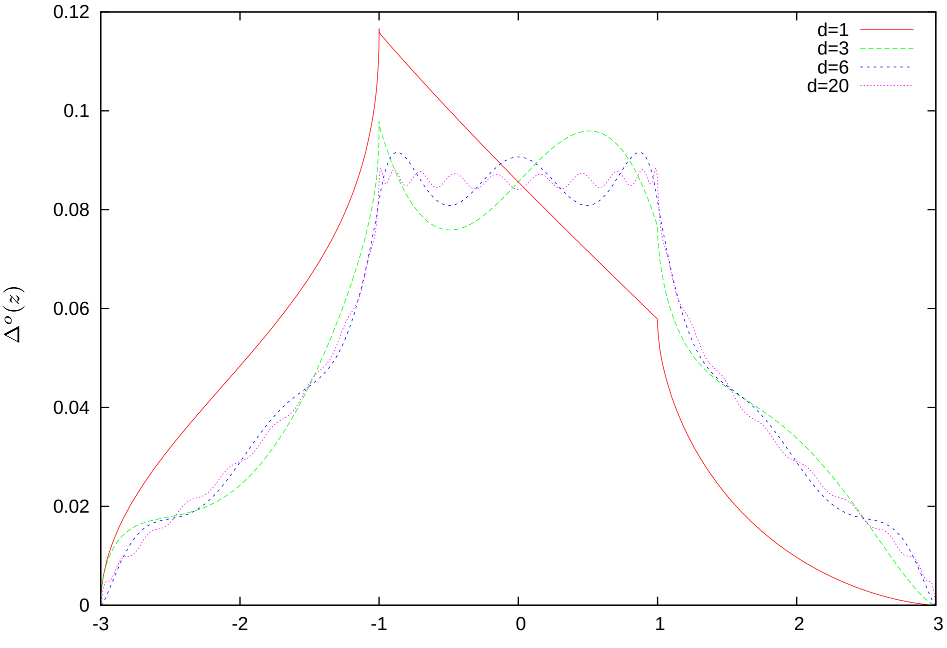
0.12
0.1
0.08
0.06
0.04
0.02
0
-3
-2
-1
0
1
2
3
$\Delta^o(z)$
ω
d=1
d=3
d=6
d=20

(b)

Figure 3.1:

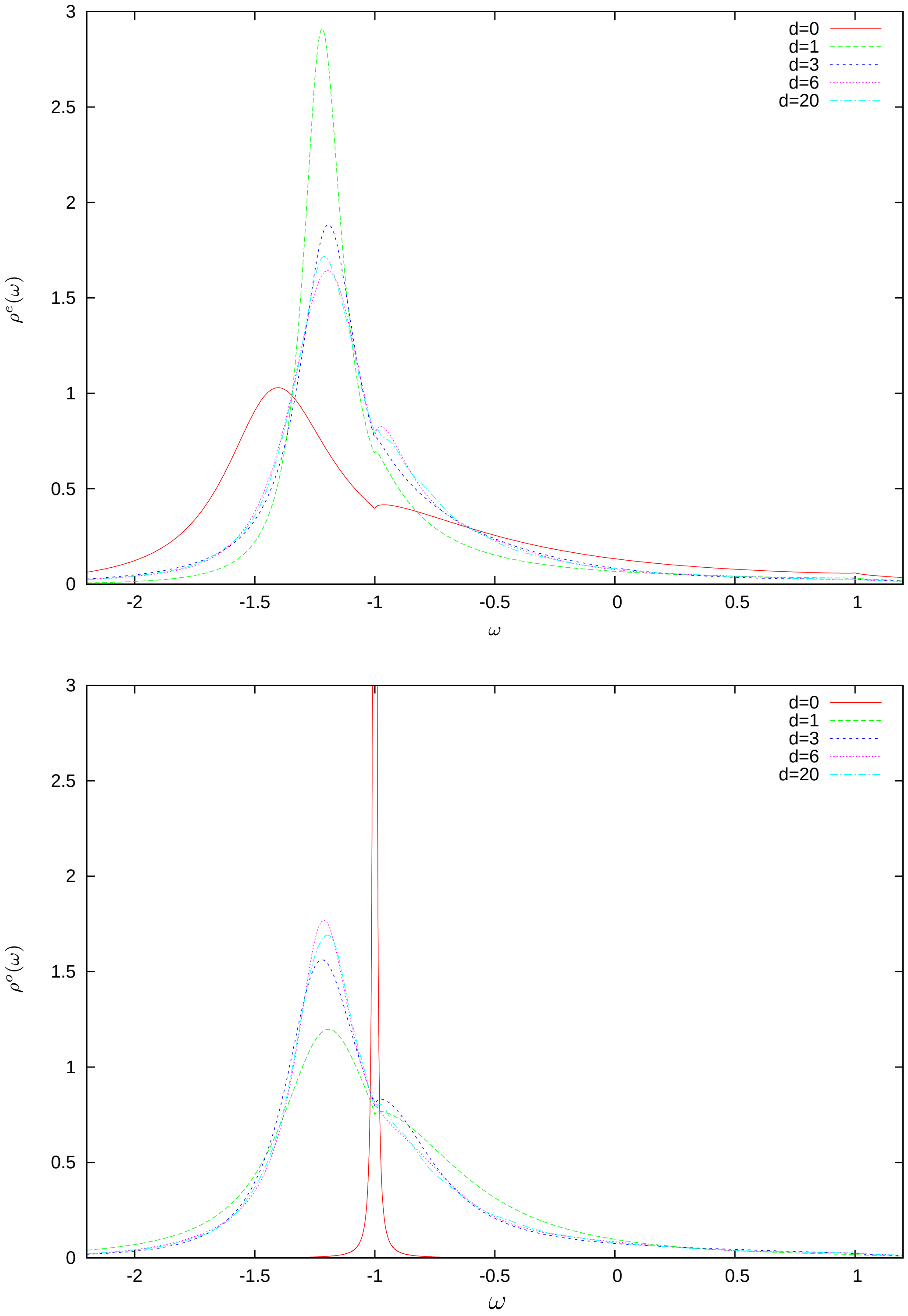
3
2.5
2
1.5
1
0.5
0
$\rho^e(\omega)$
-2
-1.5
-1
-0.5
0
0.5
1
ω
d=0
d=1
d=3
d=6
d=20
3
2.5
2
1.5
1
0.5
0
$\rho^o(\omega)$
-2
-1.5
-1
-0.5
0
0.5
1
ω
d=0
d=1
d=3
d=6
d=20

Figure 3.2:

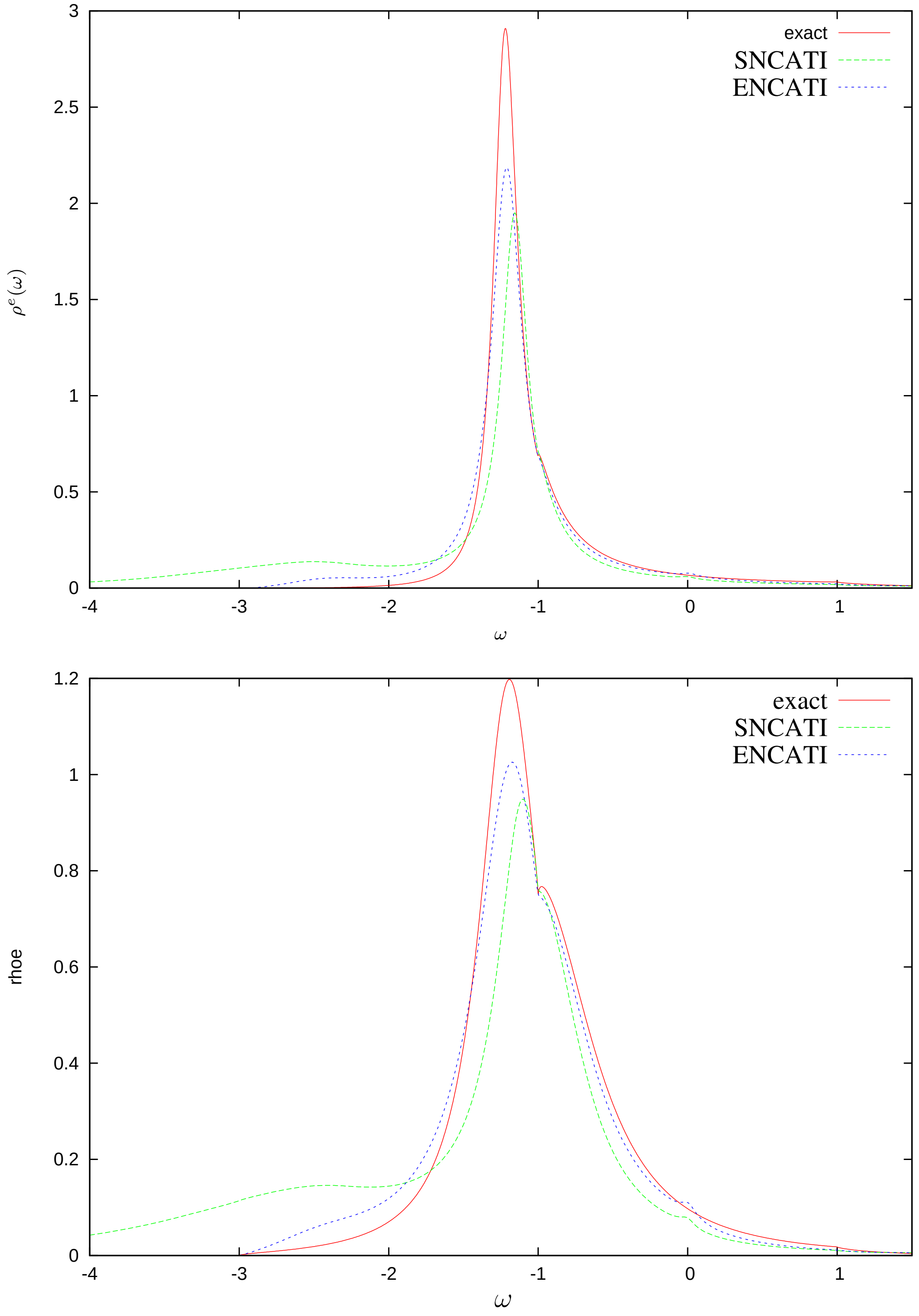

3
2.5
2
1.5
1
0.5
0
$\rho^e(\omega)$
-4
-3
-2
-1
0
1
ω
exact
SNCATI
ENCATI
1.2
1
0.8
0.6
0.4
0.2
0
rhoe
-4
-3
-2
-1
0
1
ω
exact
SNCATI
ENCATI

Figure 3.3:

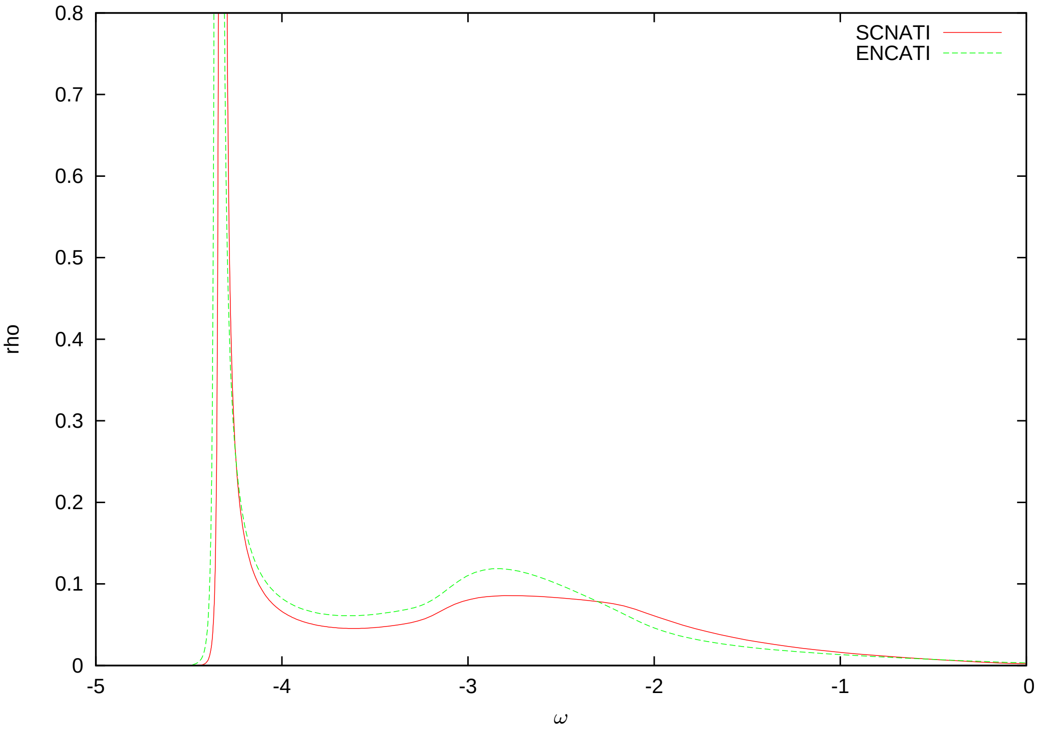

Figure 3.4:

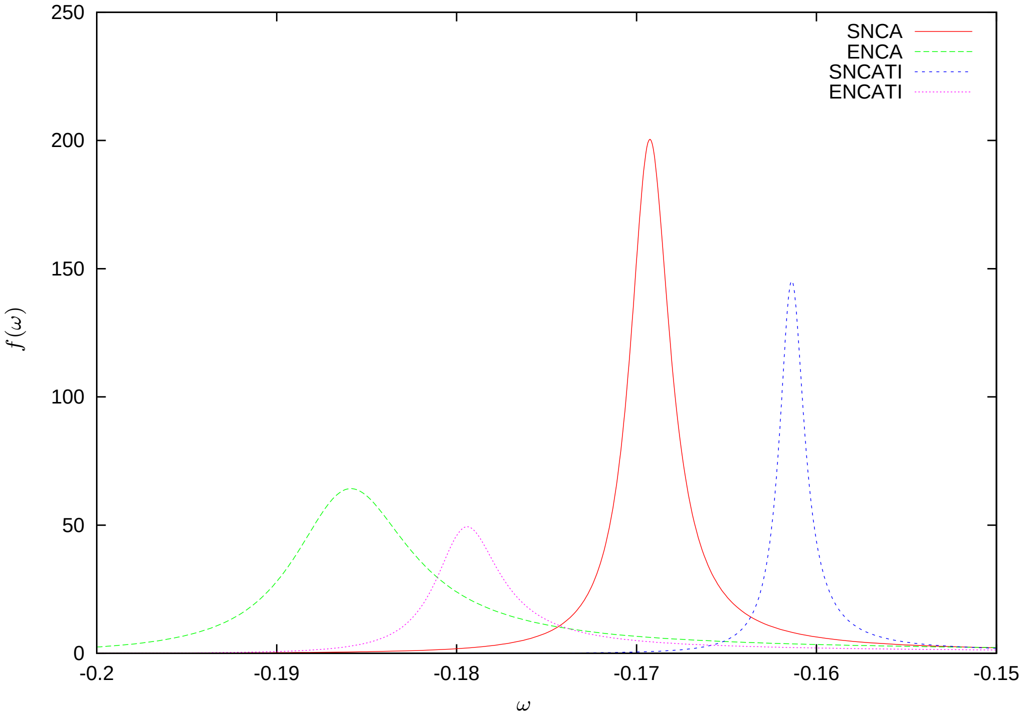

(a) $U = 3$

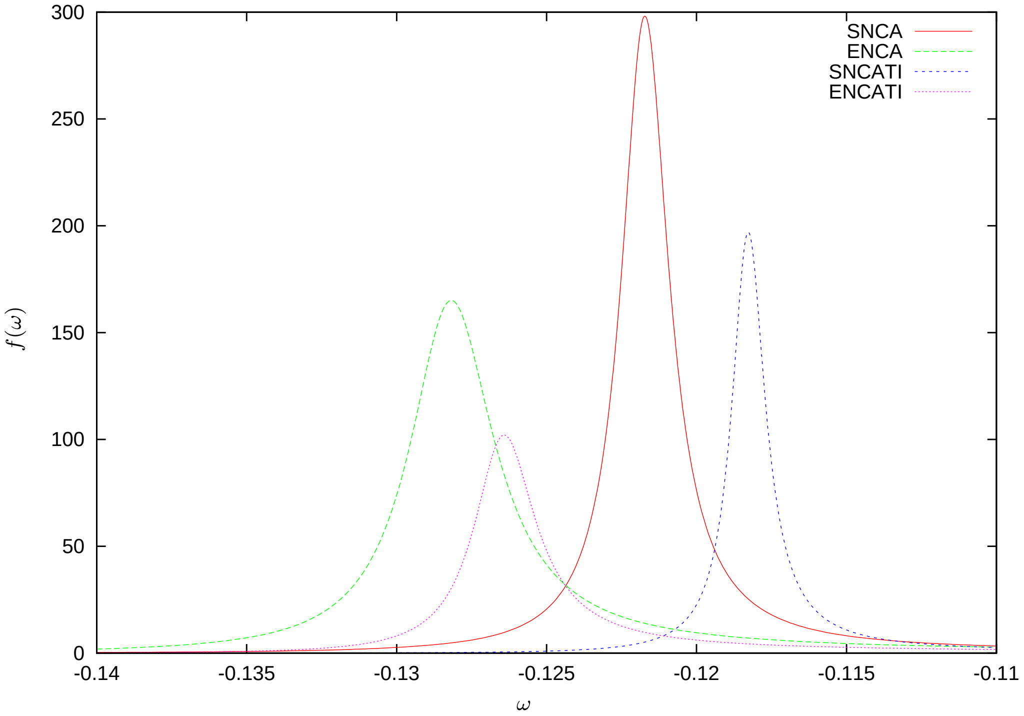

(b) $U = 6$

Figure 3.5:

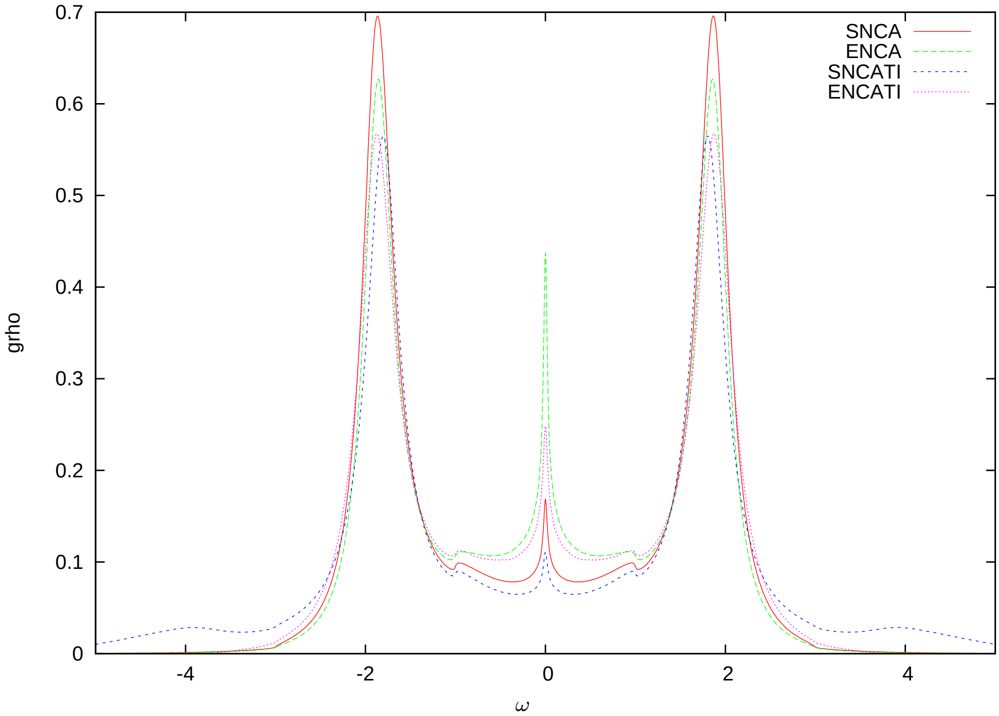

(a) $U = 3$

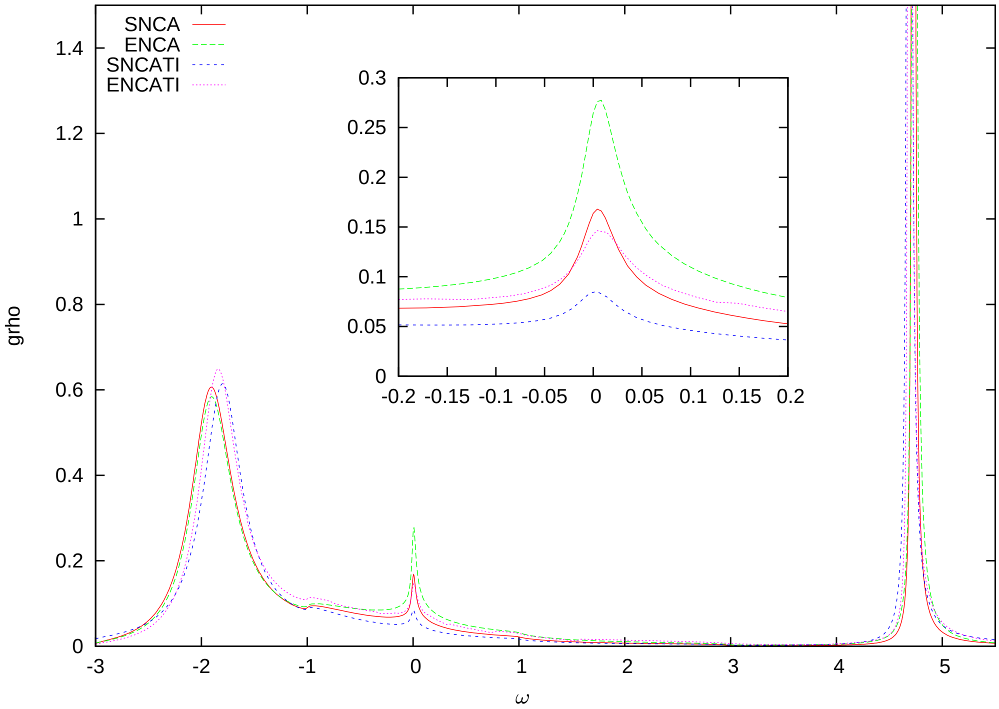

(b) $U = 6$

Figure 3.6:

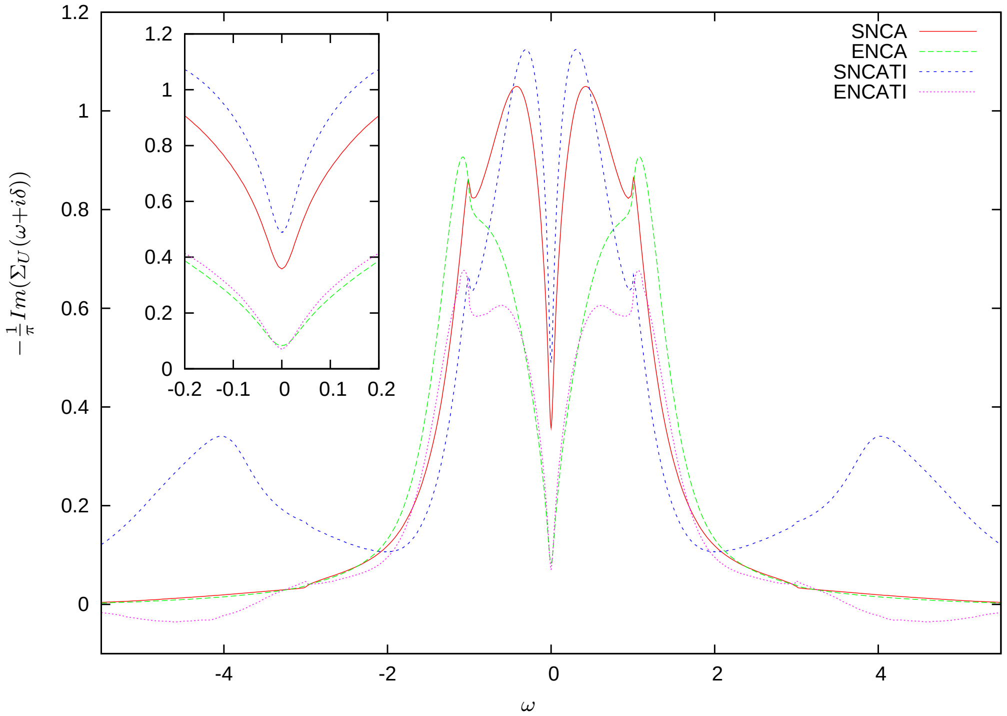

(a) $U = 3$

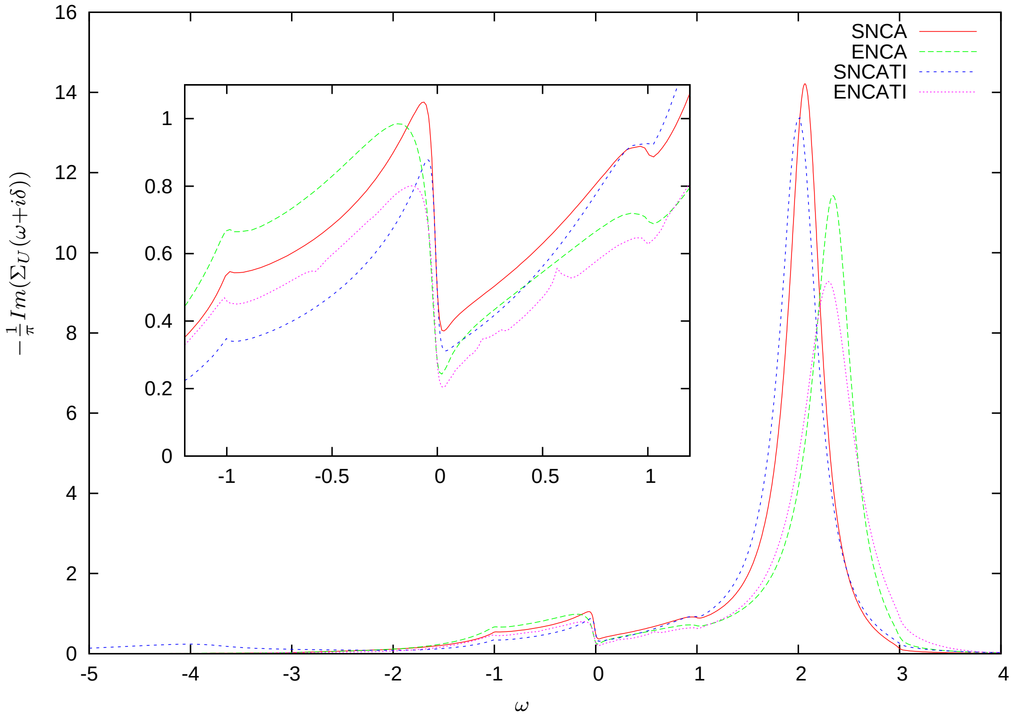

(b) $U = 6$

Figure 3.7:

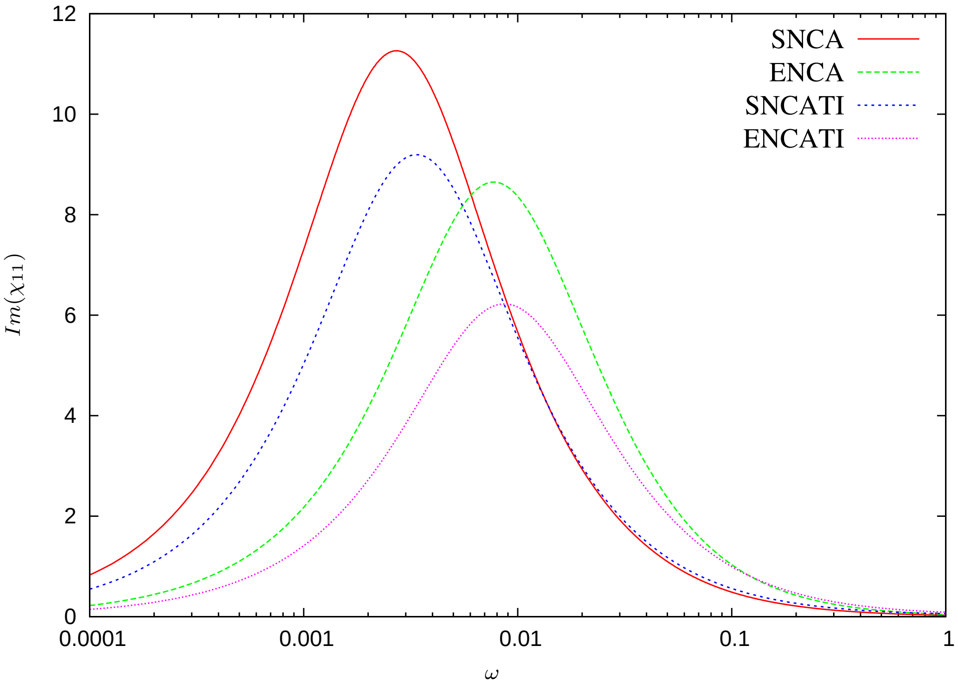

12
10
8
6
4
2
0
$Im(\chi_{11})$
0.0001
0.001
0.01
0.1
1
ω
SNCA
ENCA
SNCATI
ENCATI

(a) $U = 3$

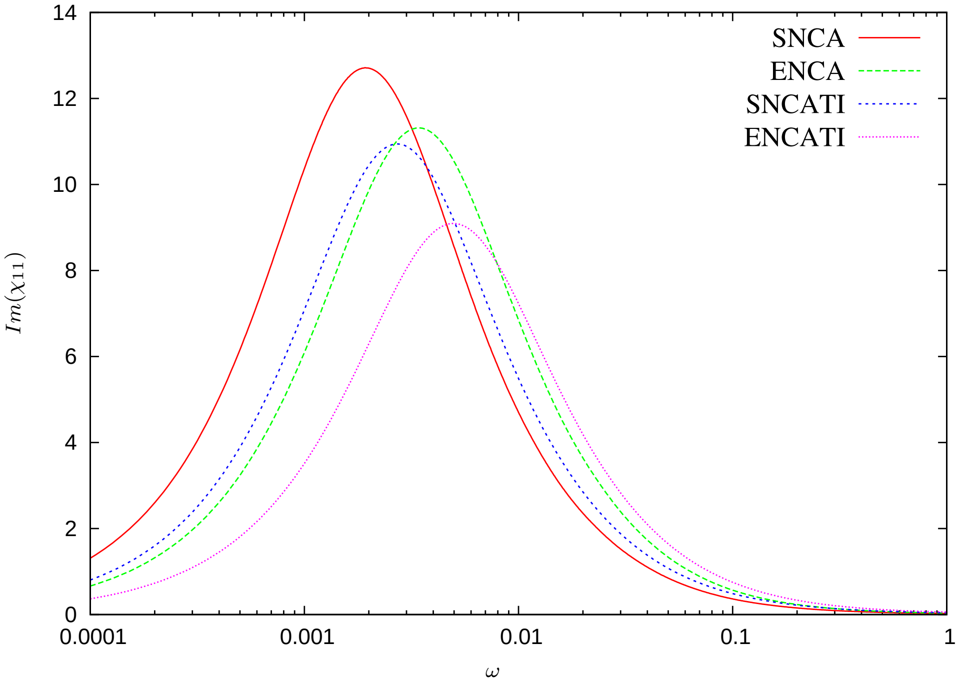

14
12
10
8
6
4
2
0
$Im(\chi_{11})$
0.0001
0.001
0.01
0.1
1
ω
SNCA
ENCA
SNCATI
ENCATI

(b) $U = 6$

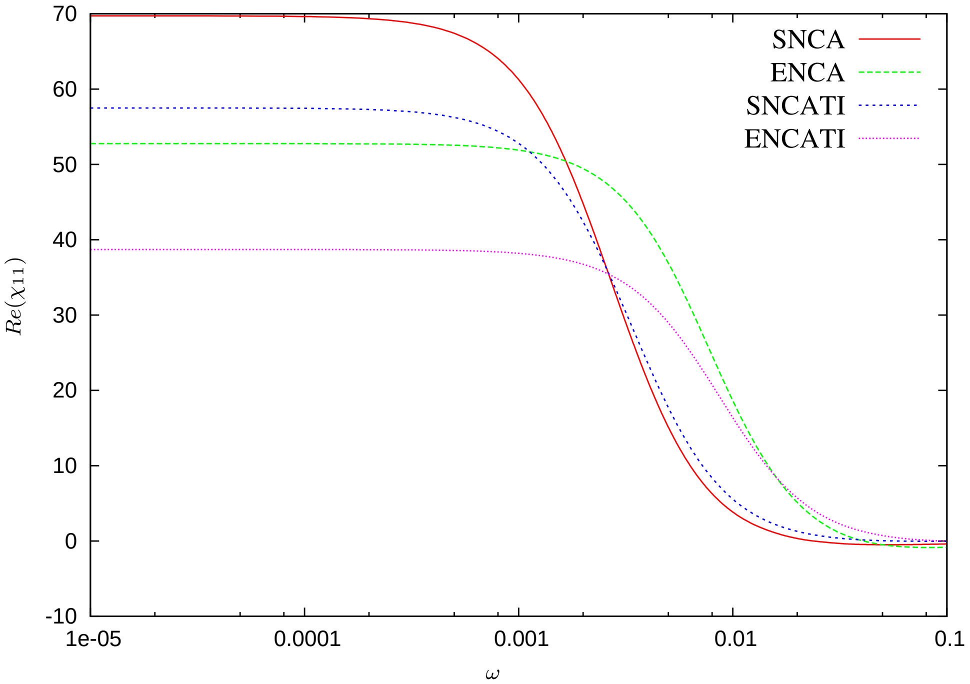

(c) $U = 3$

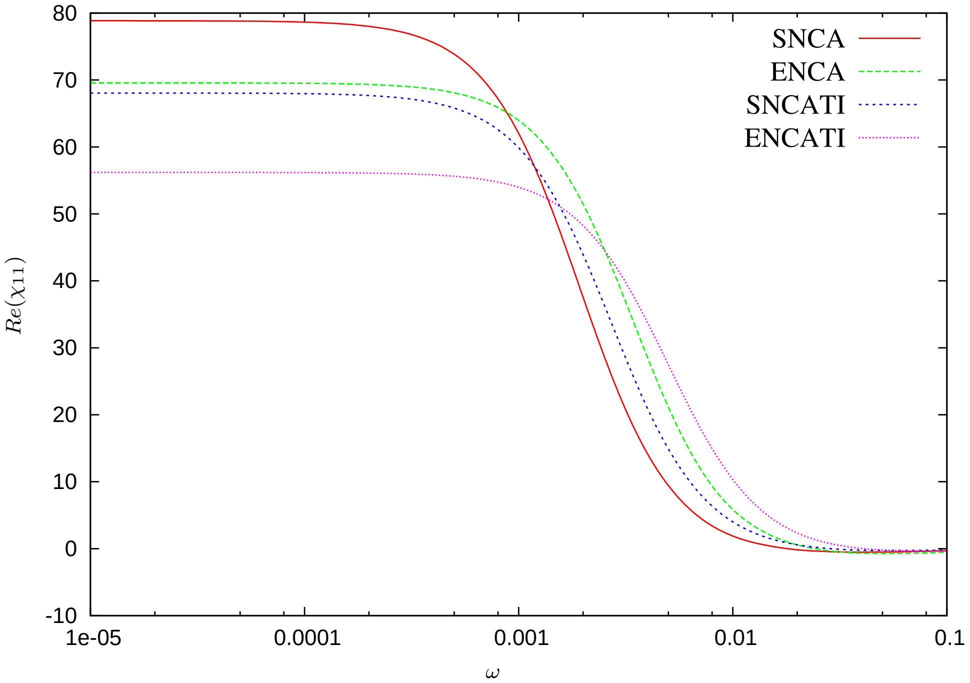

(d) $U = 6$

Figure 3.8:

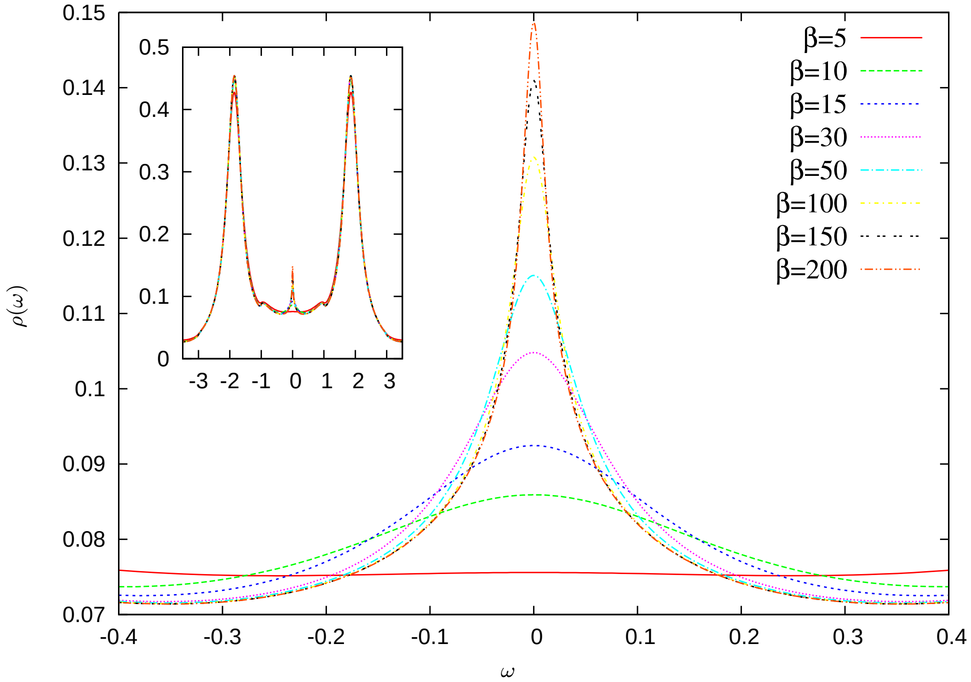

(a) SNCATI

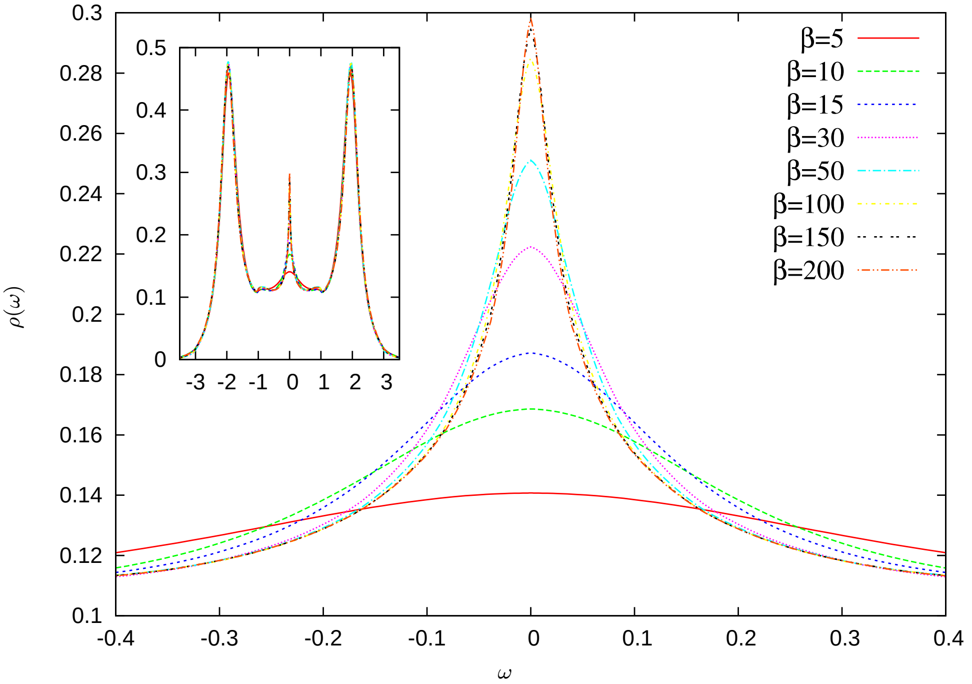

(b) ENCATI

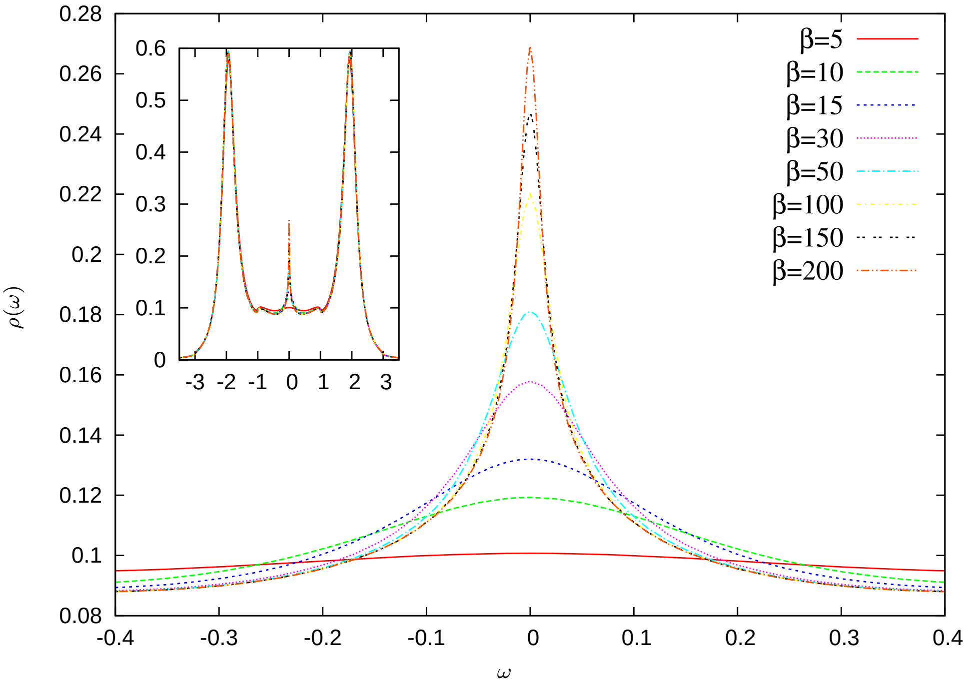

(c) SNCA

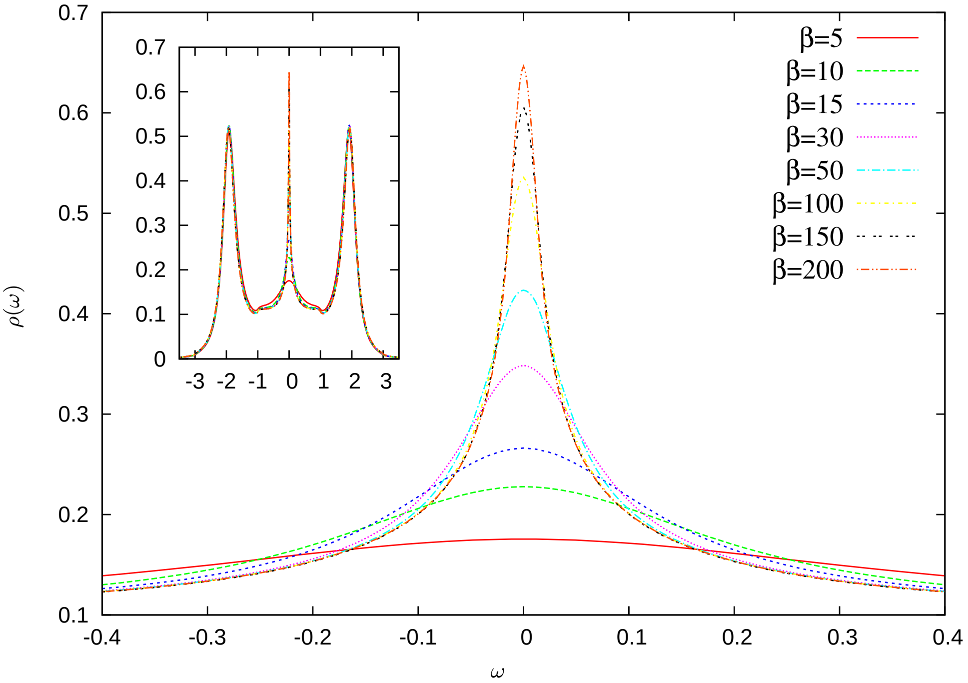

(d) ENCA

Figure 3.9:

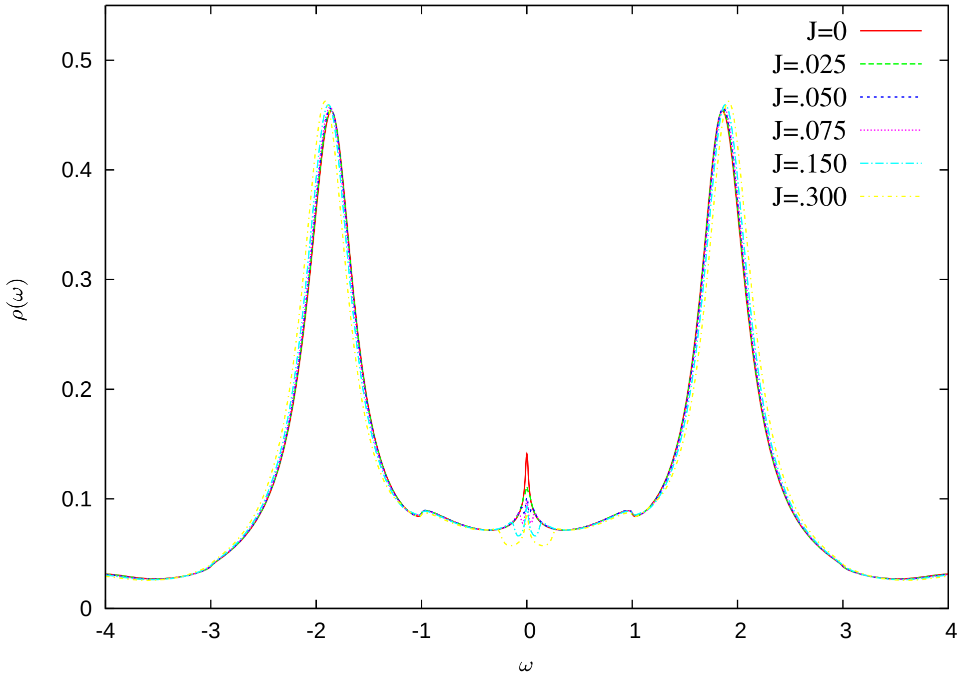

(a) SNCATI

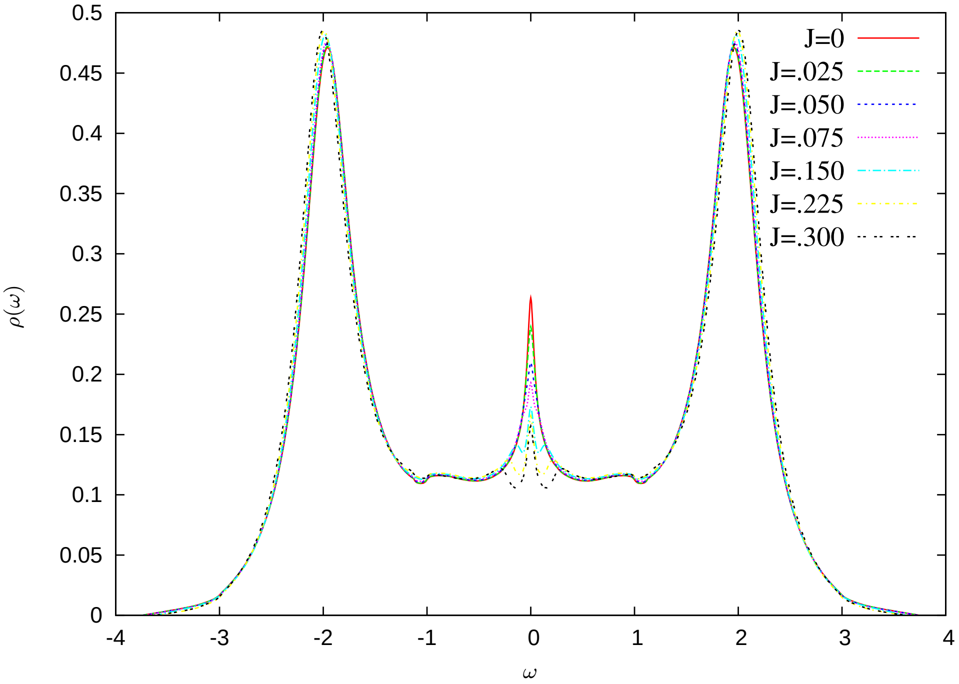

(b) ENCATI

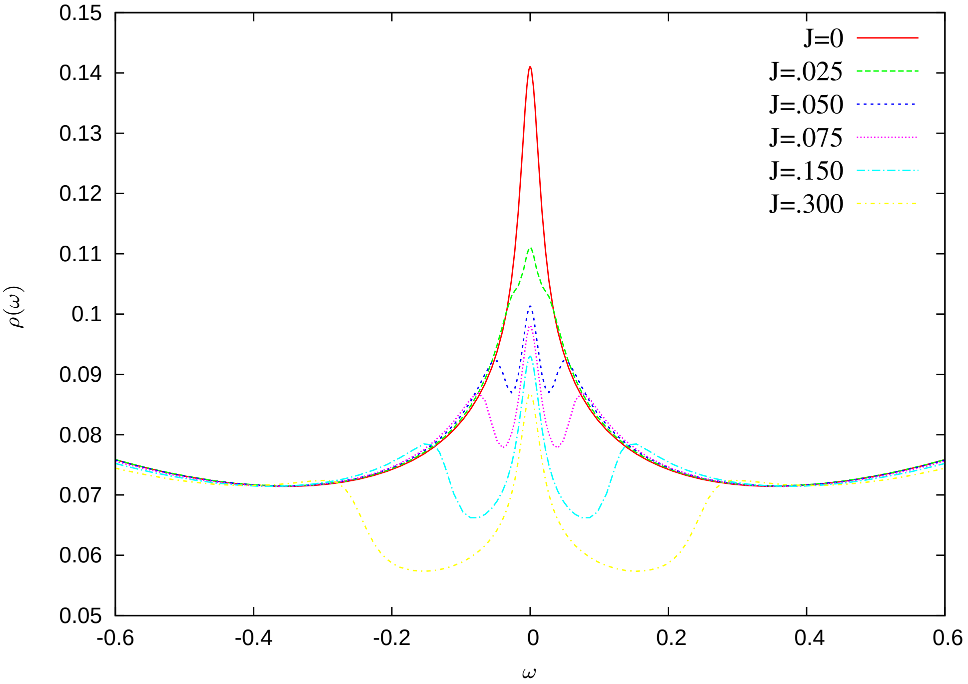

(c) SNCATI

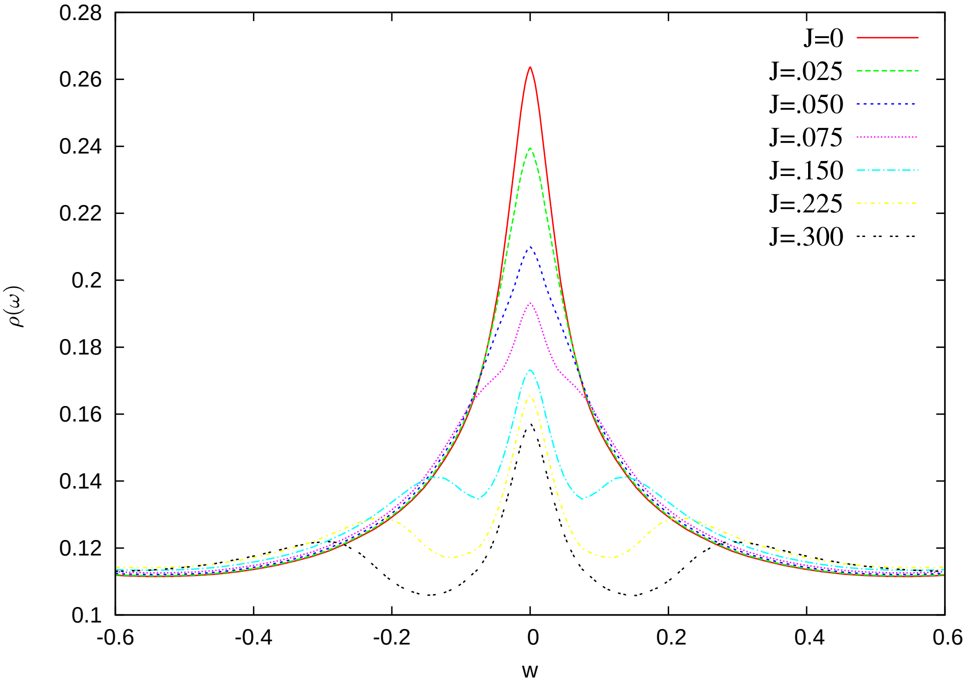

(d) ENCATI

Figure 3.10:

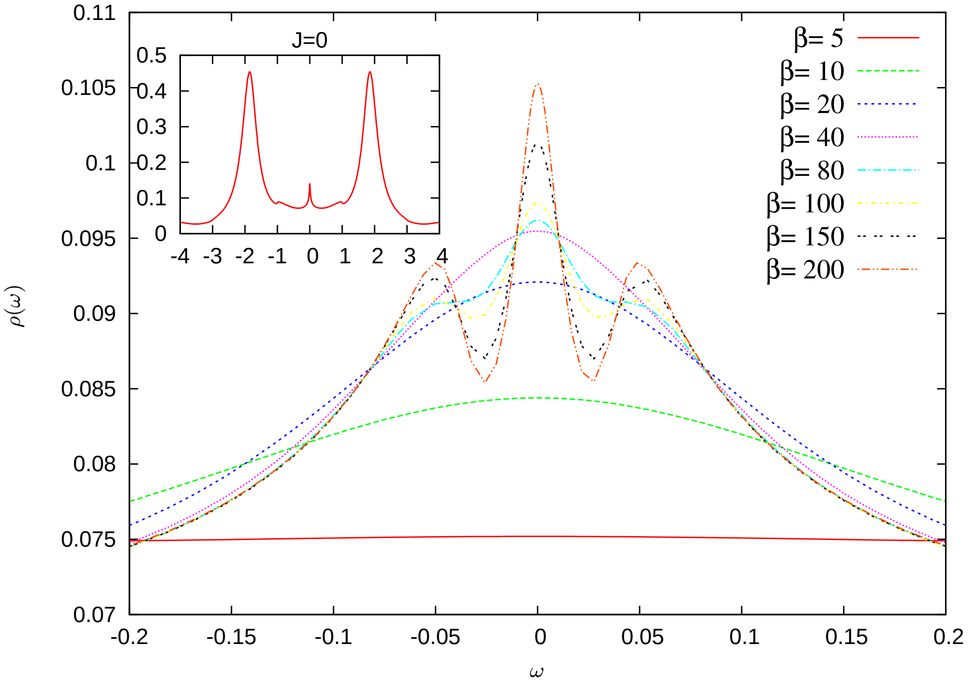

(a) SNCATI

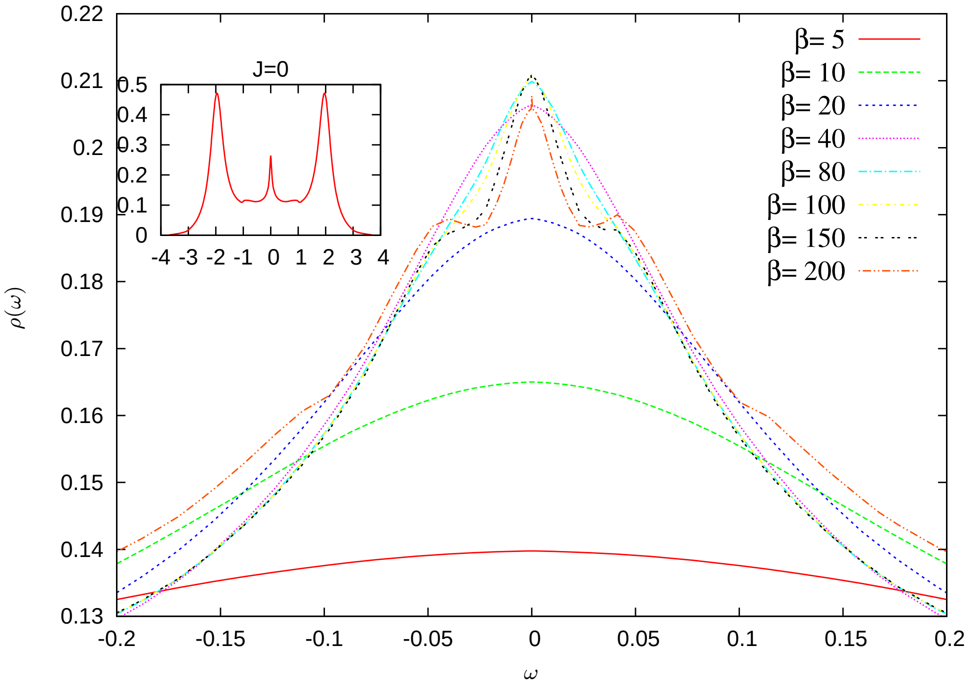

(b) ENCATI

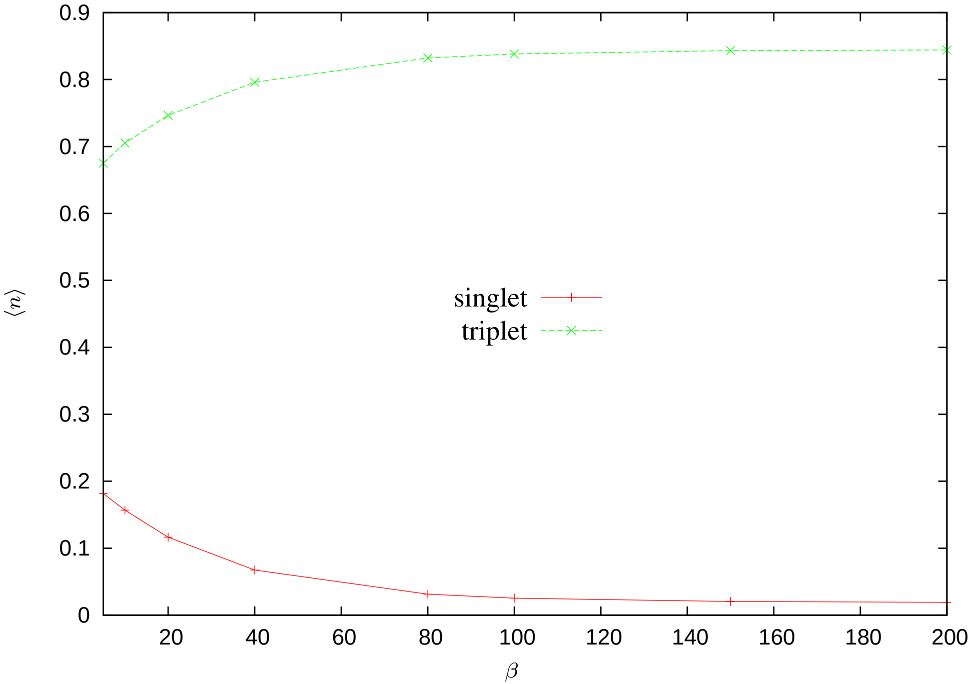

(c) SNCATI

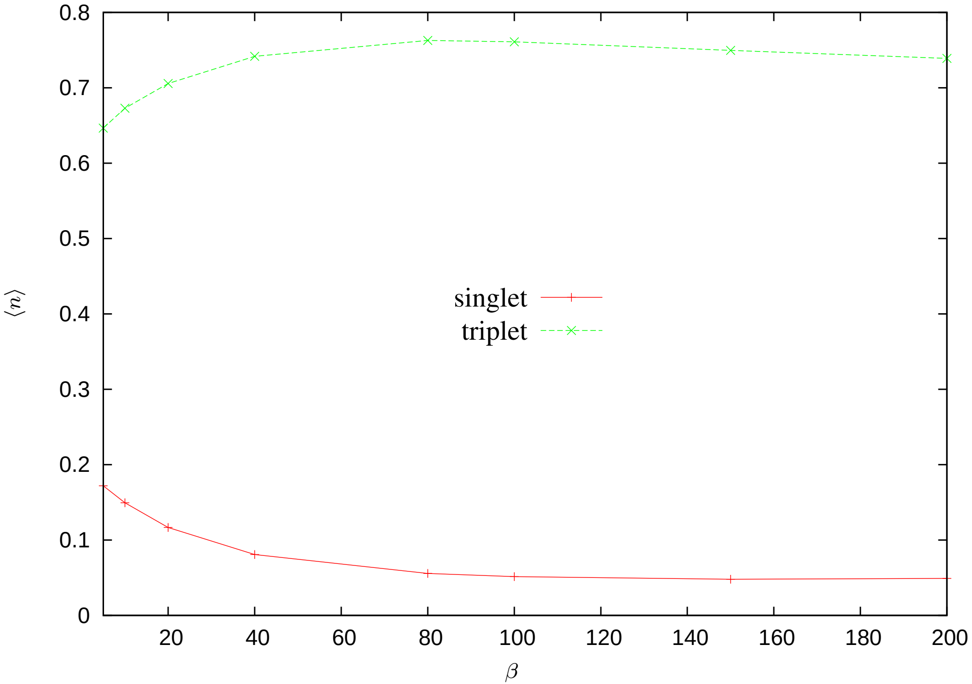

(d) ENCATI

Figure 3.11:

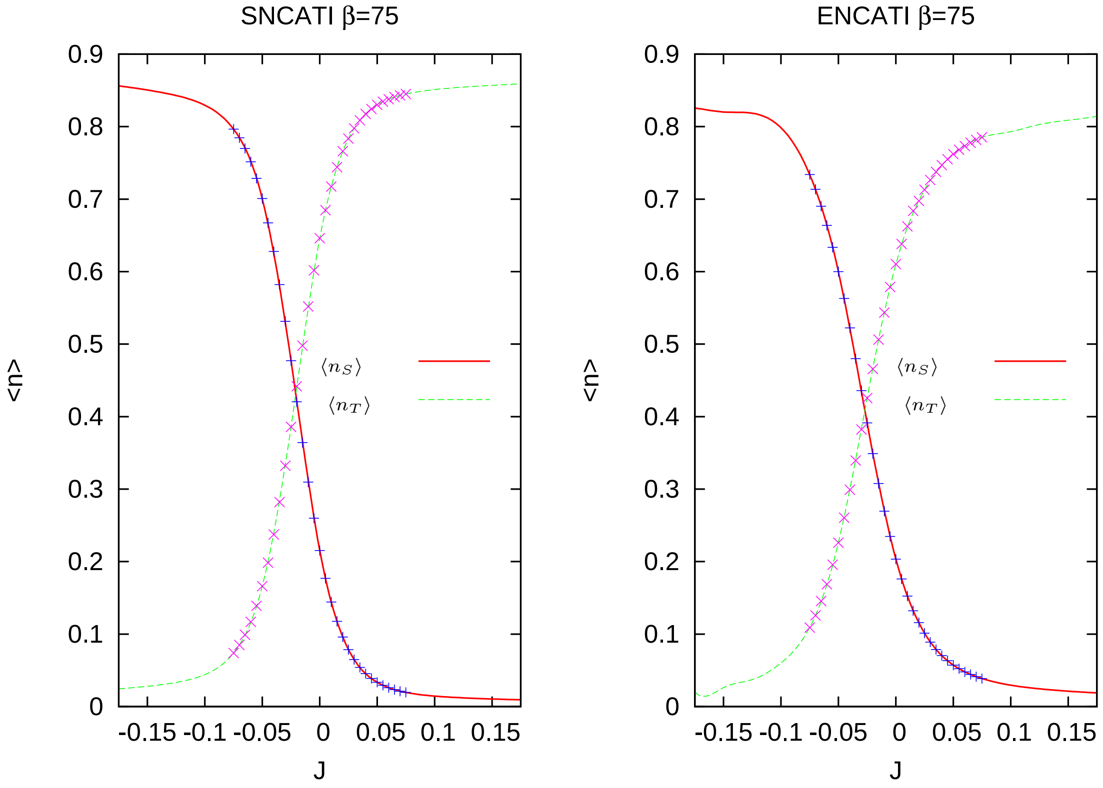
SNCATI β=75
ENCATI β=75
<n>
J
0
0.1
0.2
0.3
0.4
0.5
0.6
0.7
0.8
0.9
-0.15
-0.1
-0.05
0
0.05
0.1
0.15
$\langle n_S \rangle$
$\langle n_T \rangle$

Figure 3.12:

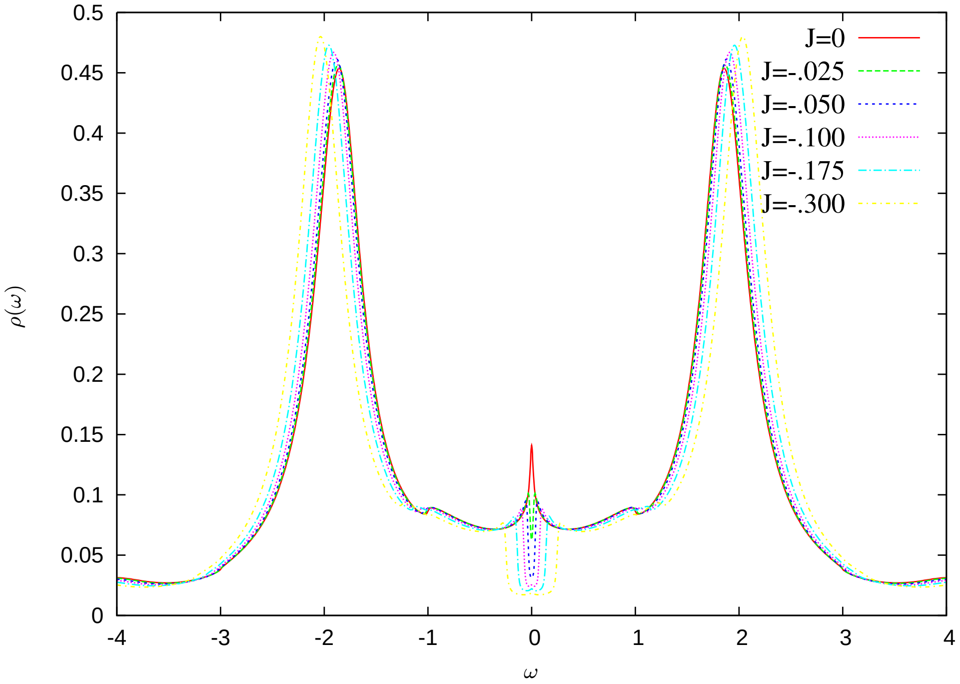

(a) SNCATI

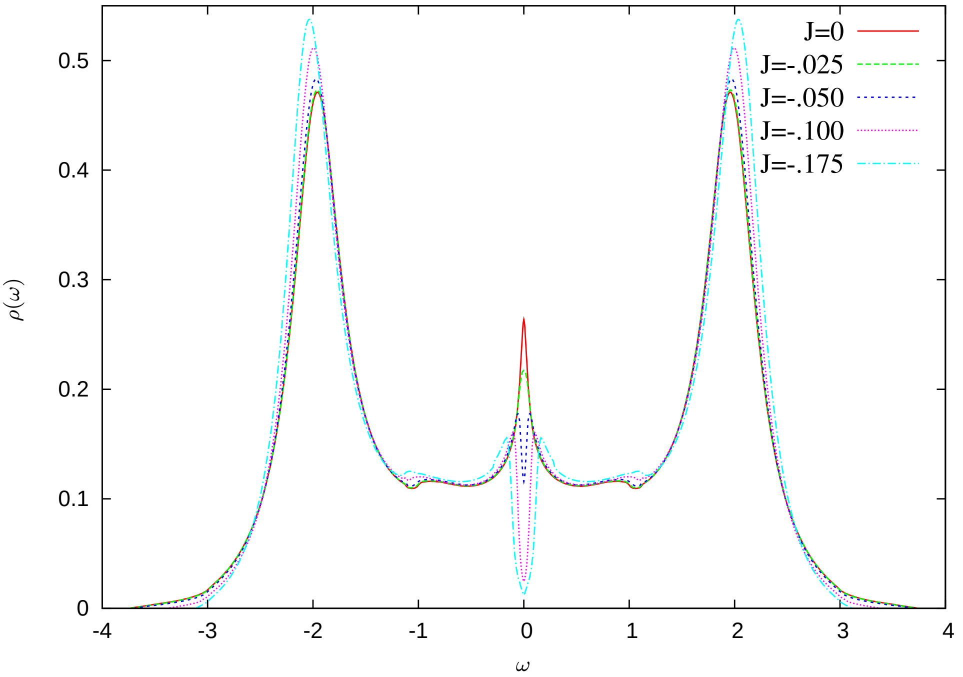

(b) ENCATI

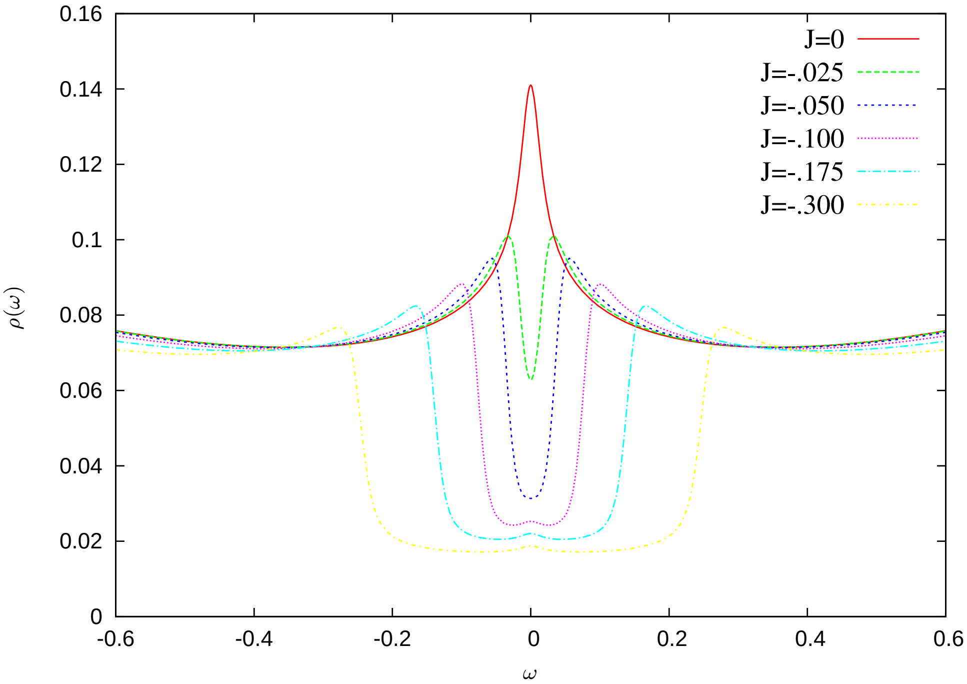

(c) SNCATI

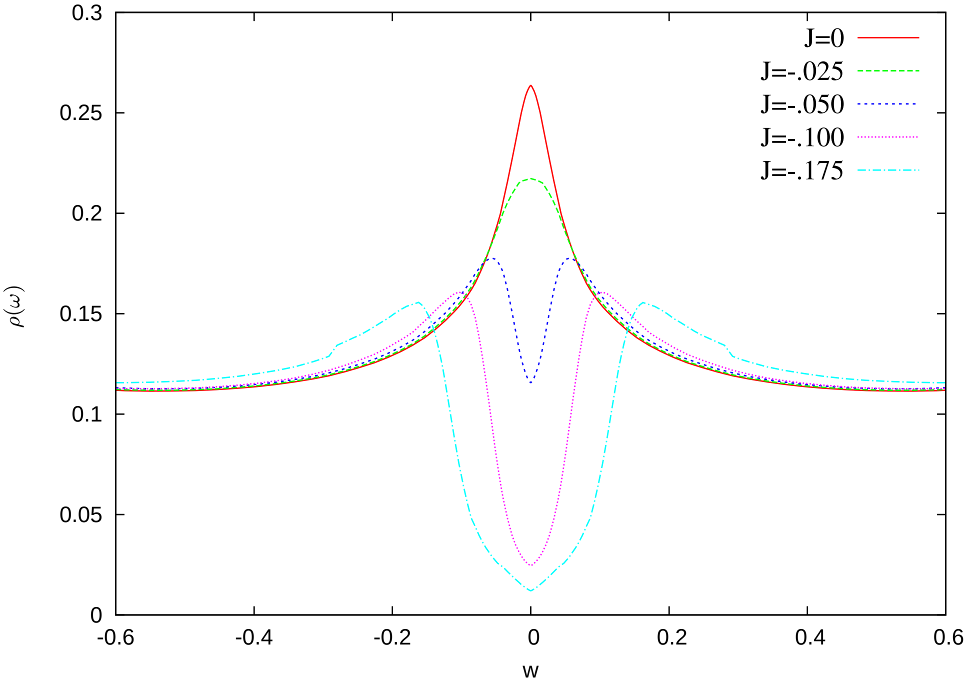

(d) ENCATI

Figure 3.13:

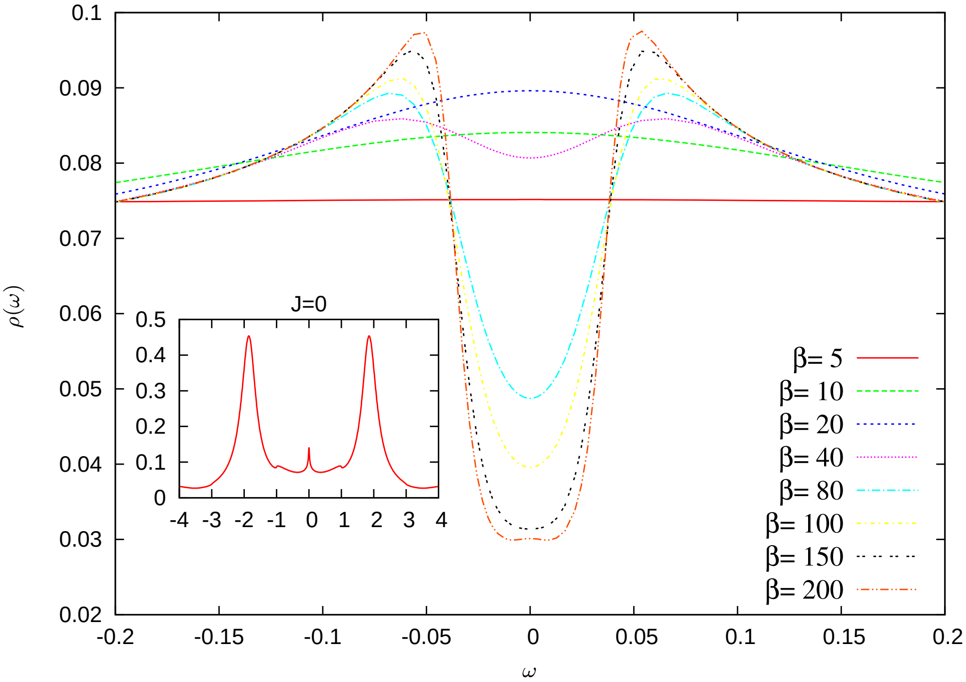

(a) SNCATI

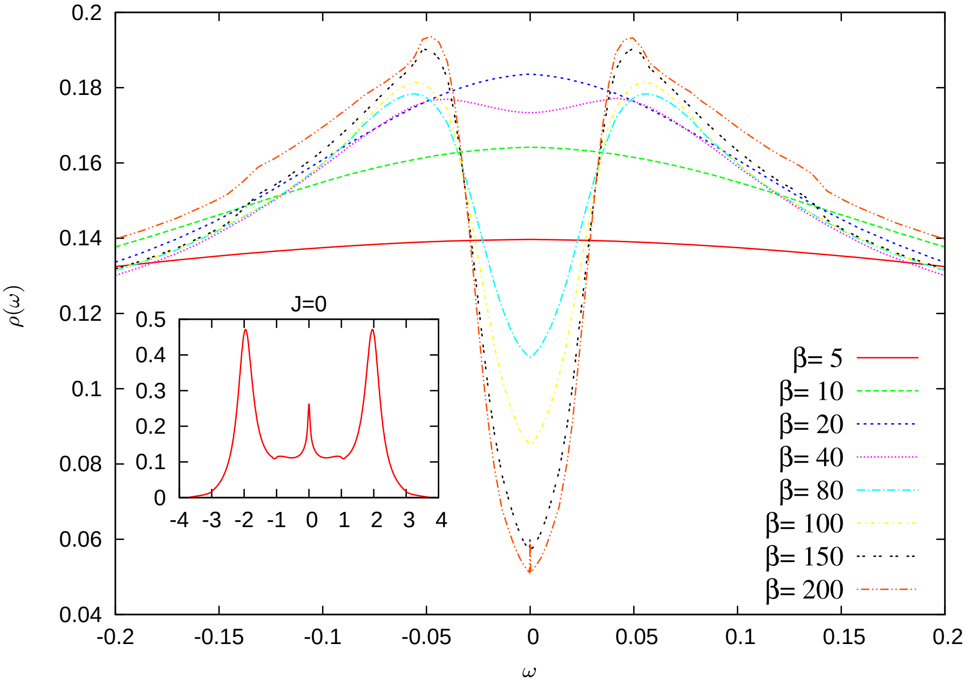

(b) ENCATI

Figure 3.14:

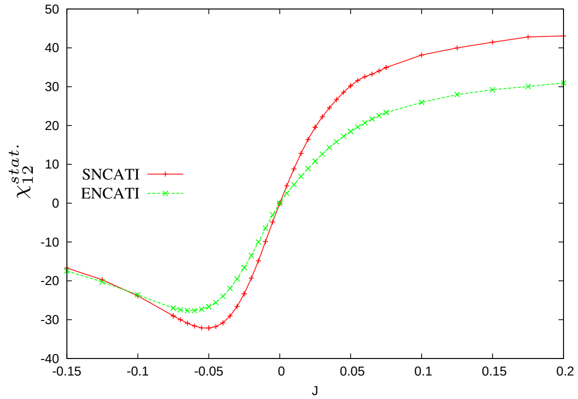

(a)

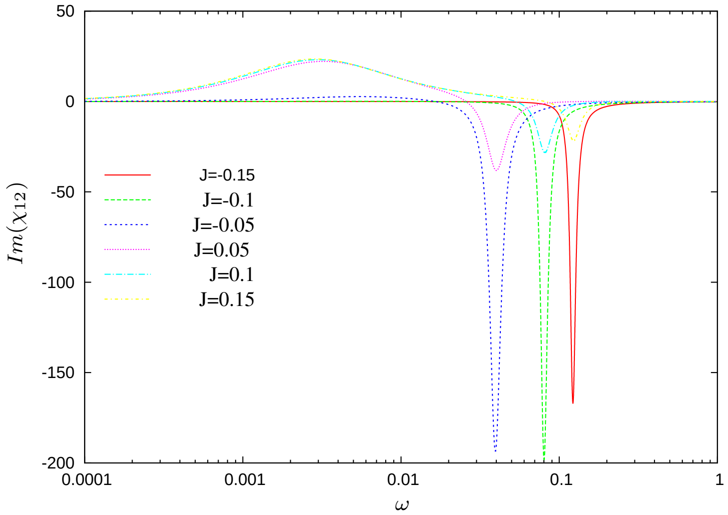

(b) SNCATI

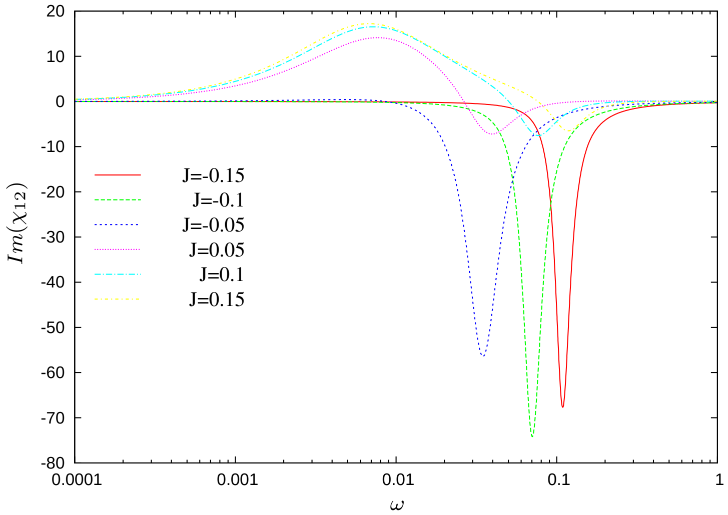

(c) ENCATI

Figure 3.15:

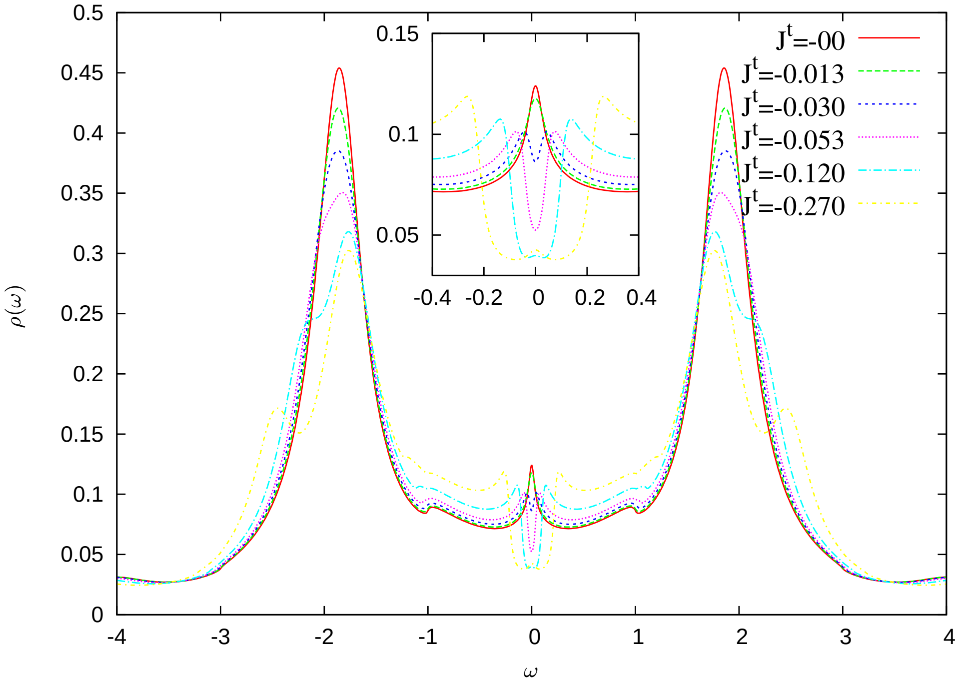

(a) SNCATI

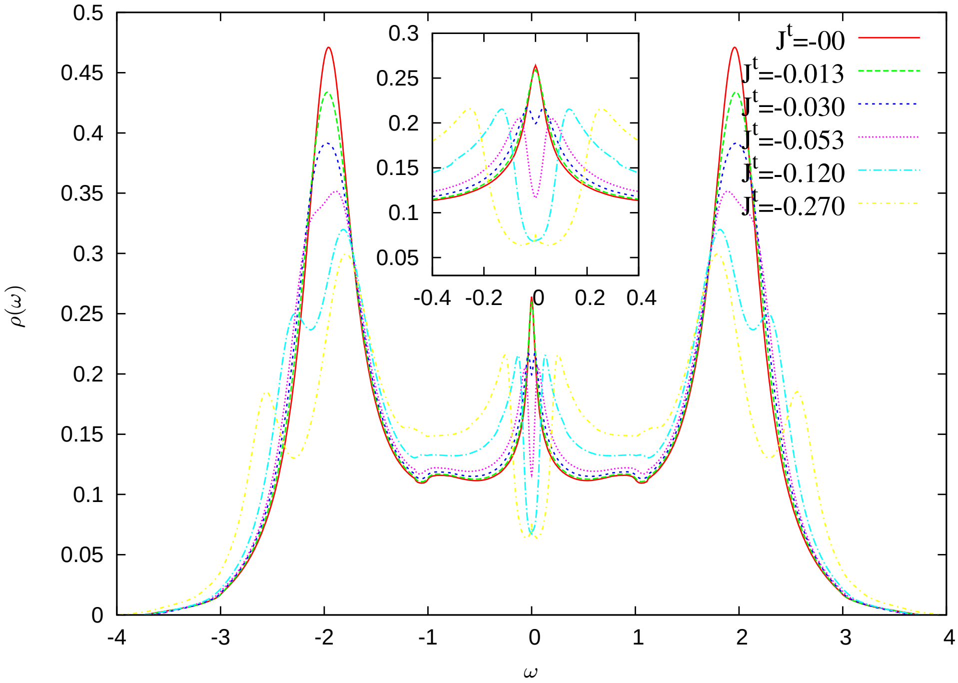

(b) ENCATI

Figure 3.17:

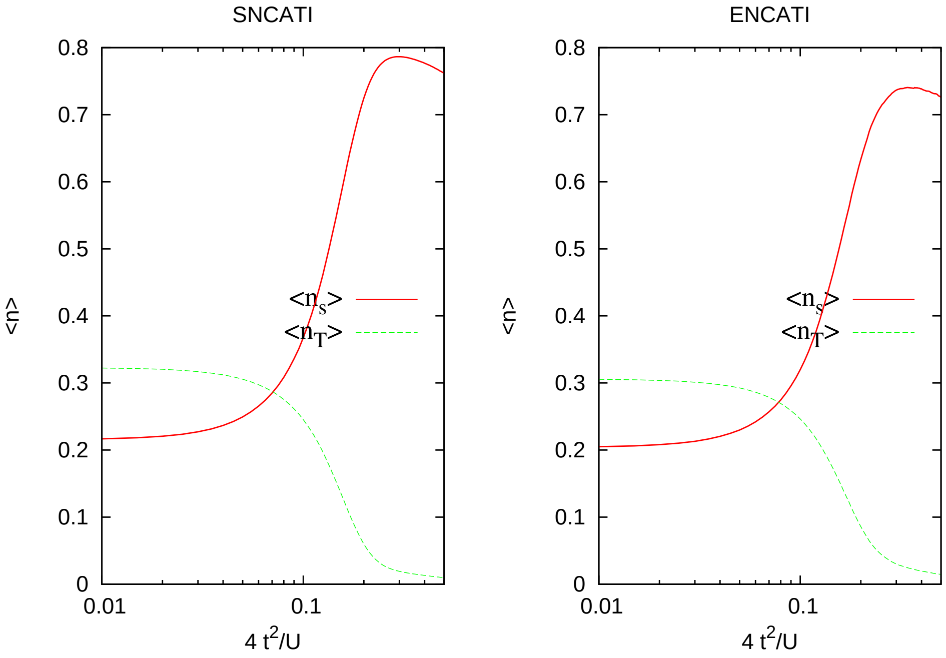

Figure 3.18:

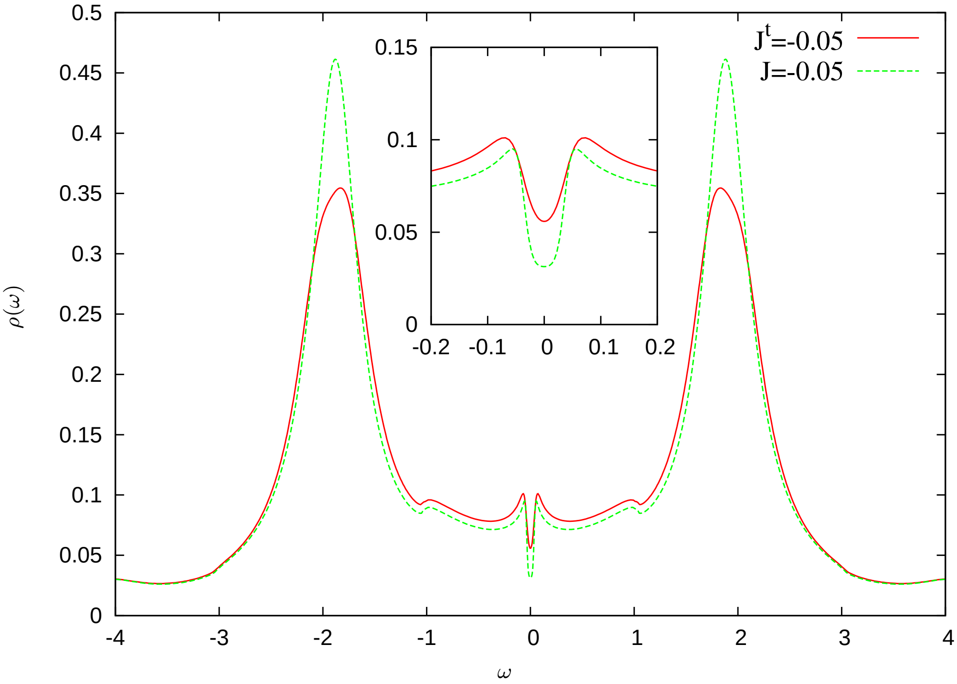

(a) SNCATI

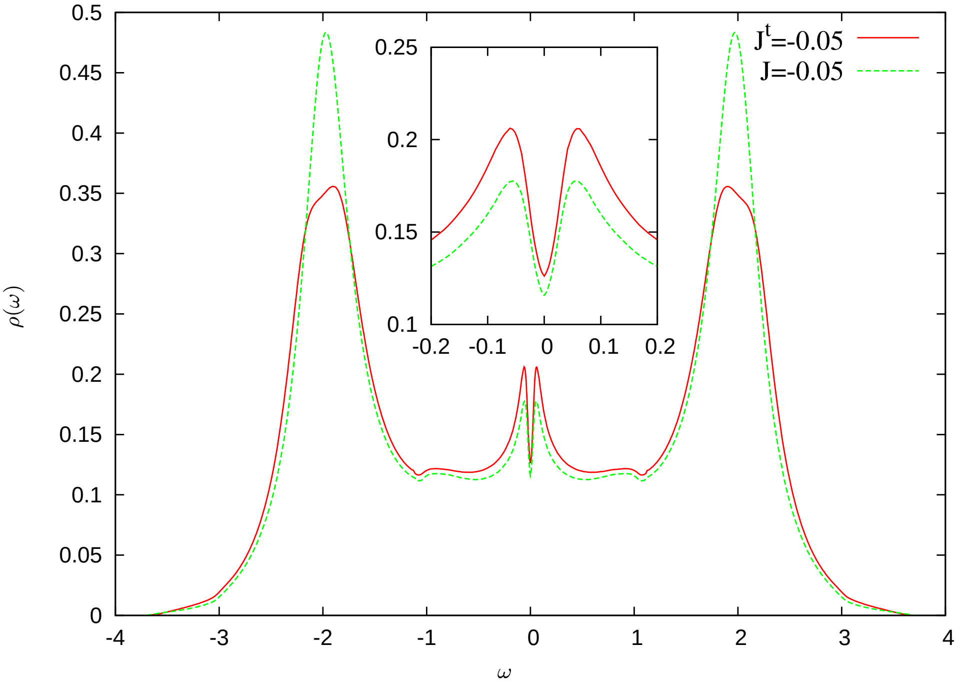

(b) ENCATI

Figure 3.19:

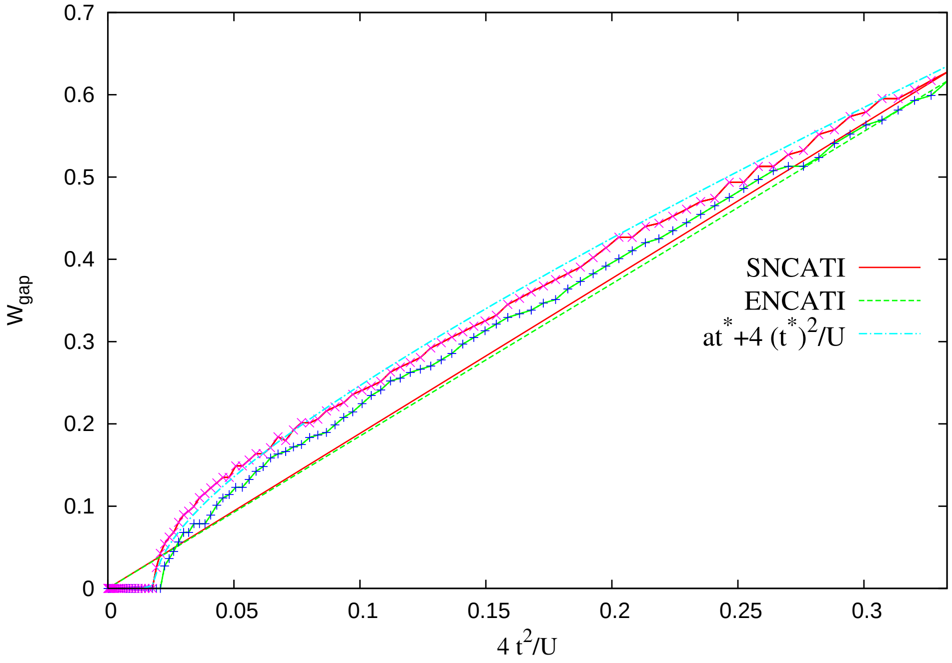
0.7
0.6
0.5
0.4
0.3
0.2
0.1
0
W_{gap}
0
0.05
0.1
0.15
0.2
0.25
0.3
$4\ t^2/U$
SNCATI
ENCATI
$at^* + 4\ (t^*)^2/U$

Figure 3.20:

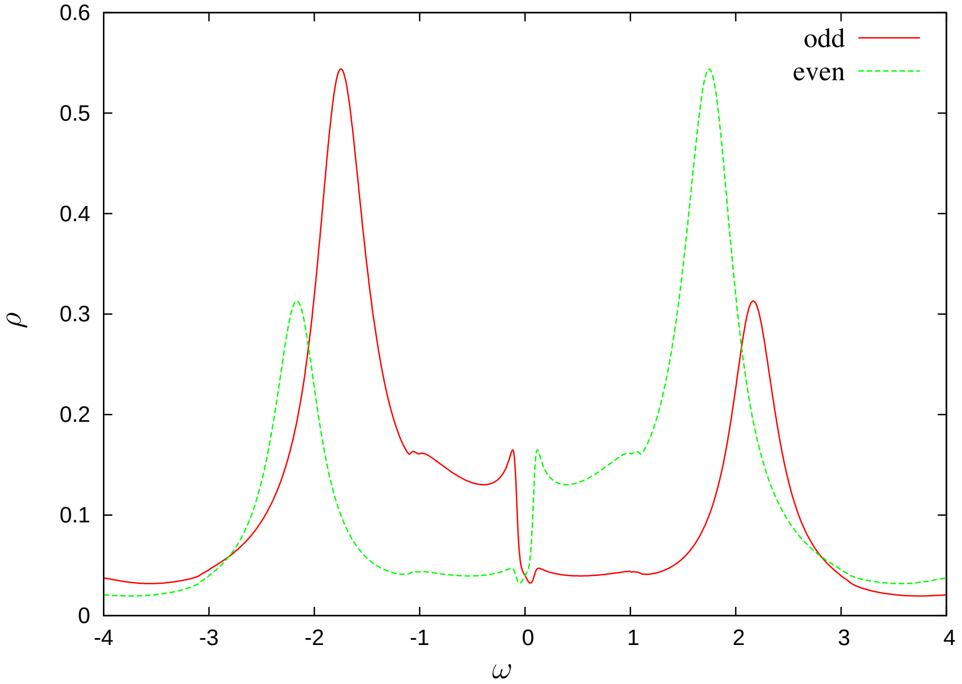

(a) SNCATI

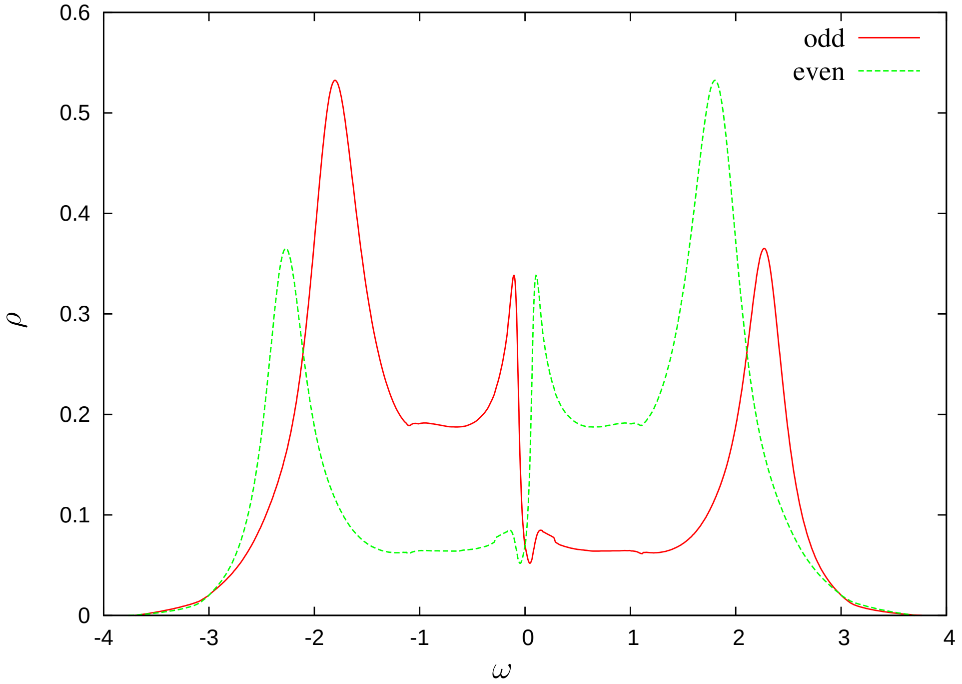

(b) ENCATI

Figure 3.21:

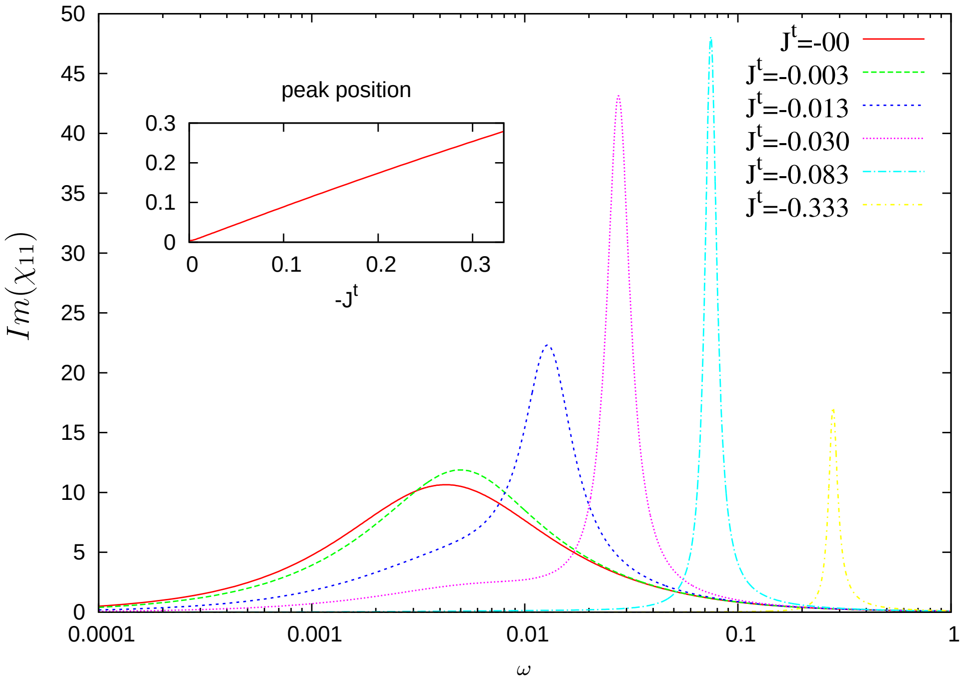

(a) SNCATI

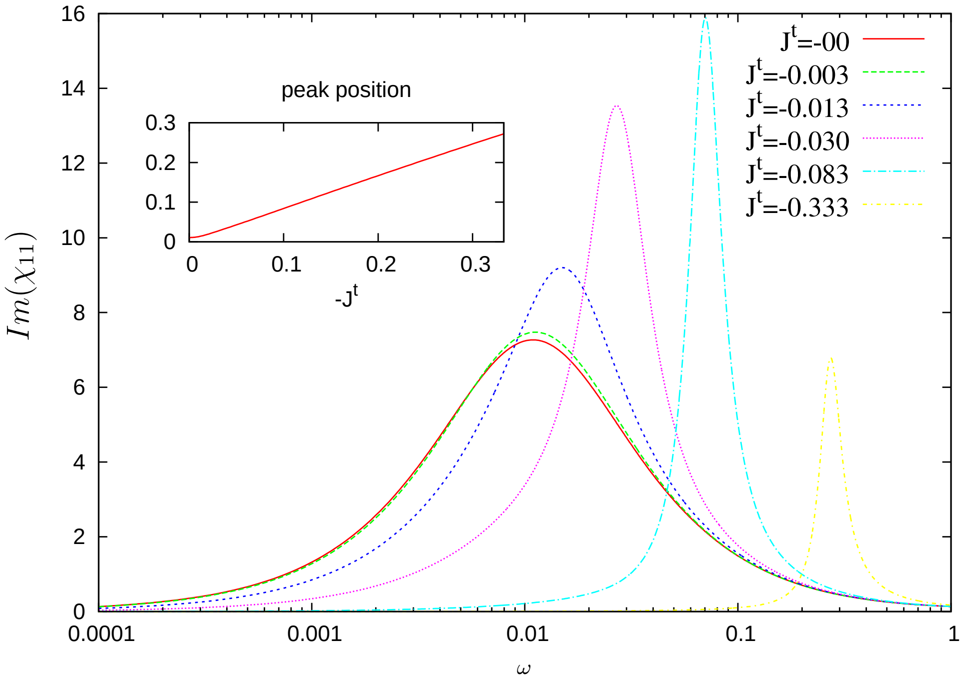

(b) ENCATI

Figure 3.22:

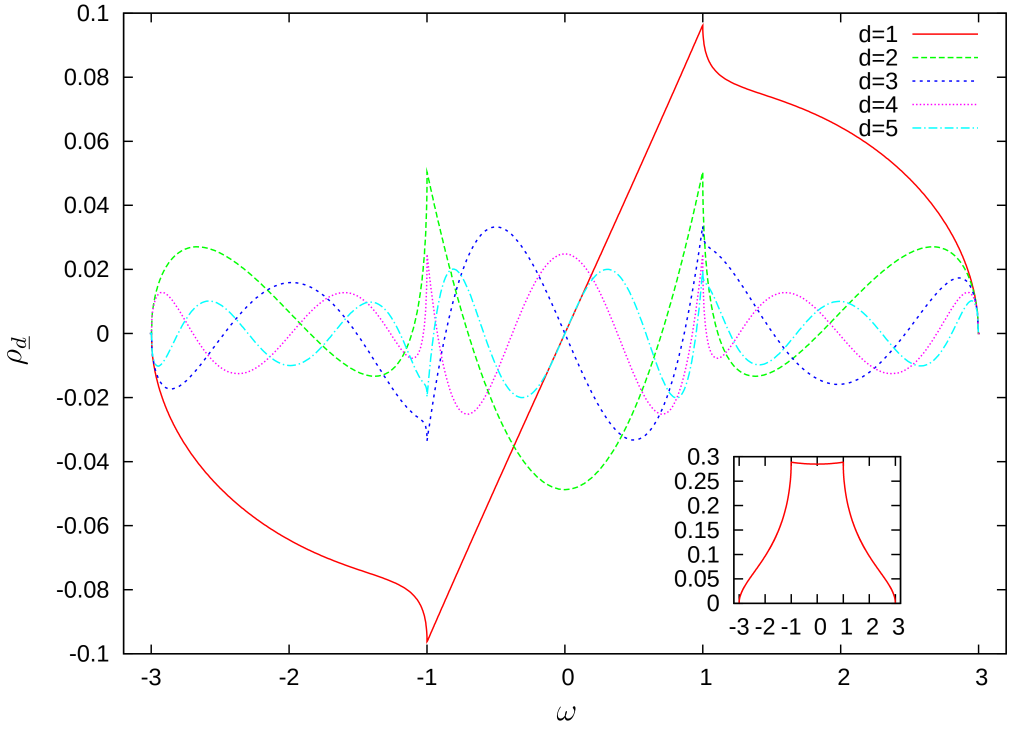
0.1
0.08
0.06
0.04
0.02
0
-0.02
-0.04
-0.06
-0.08
-0.1
$\rho_{\underline{d}}$
-3
-2
-1
0
1
2
3
ω
d=1
d=2
d=3
d=4
d=5
0.3
0.25
0.2
0.15
0.1
0.05
0
-3 -2 -1 0 1 2 3

Figure 3.23:

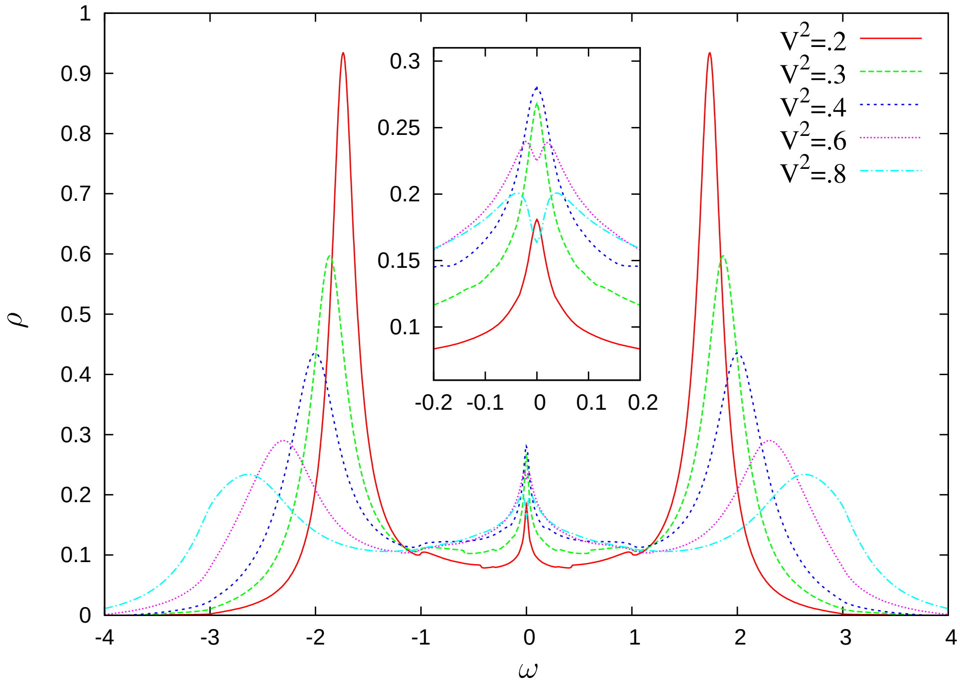

(a) $\underline{d} = 1\ \underline{e}_i$

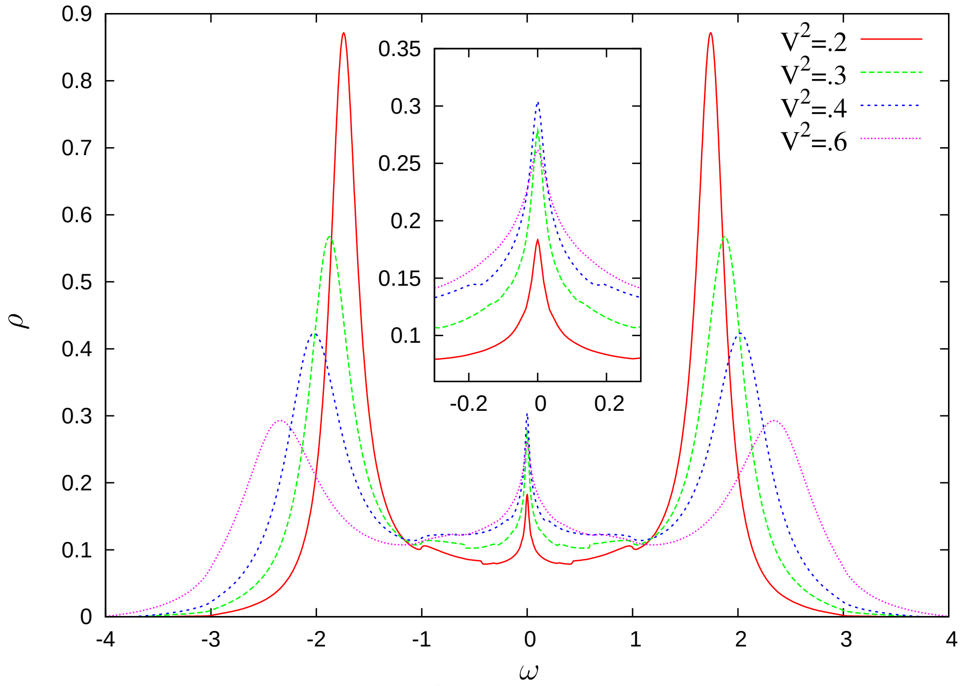

(b) $\underline{d} = 2\ \underline{e}_i$

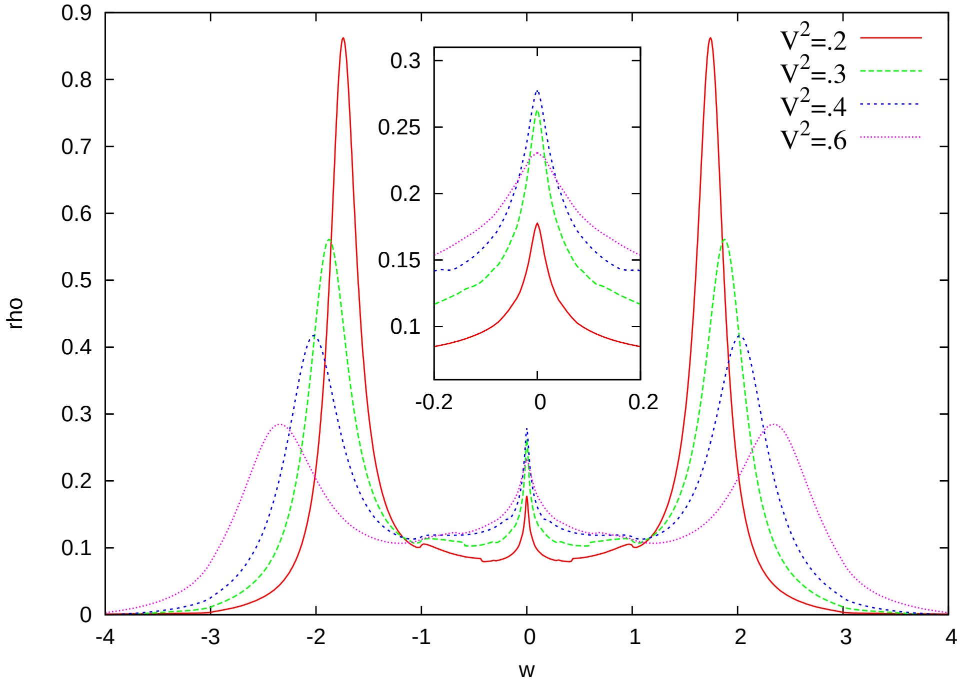

(c) $|\underline{d}| = \infty$

Figure 3.25:

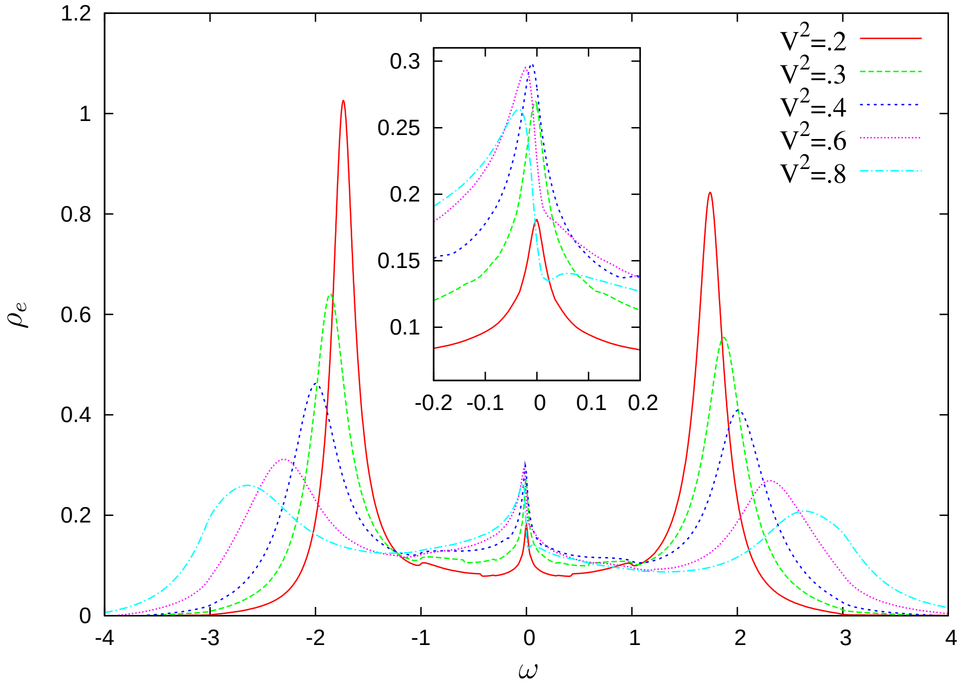

(a) $\underline{d} = 1\ \underline{e}_i$, even

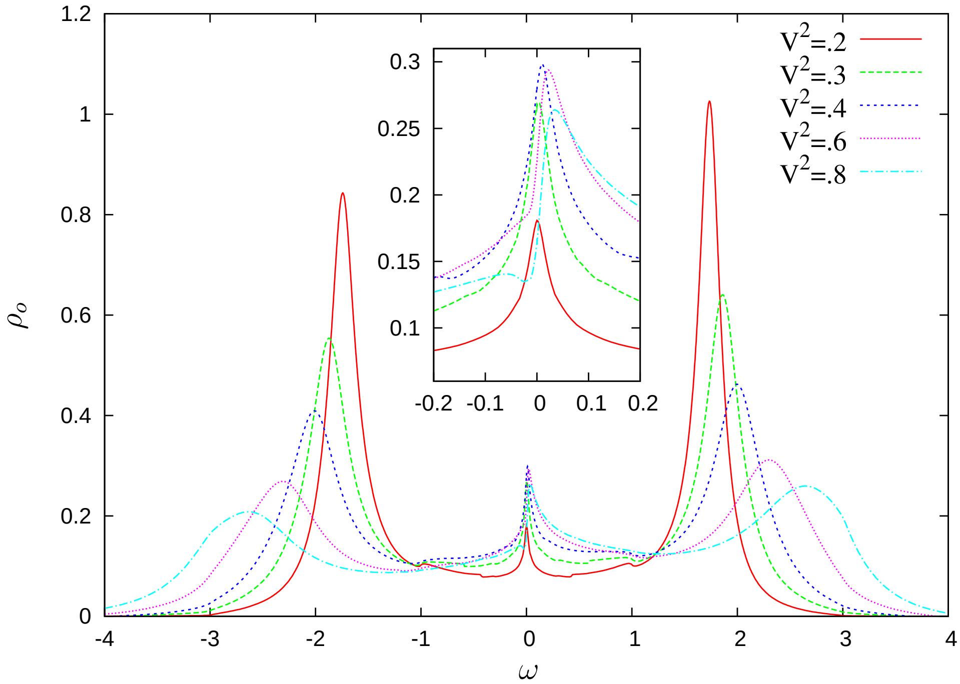

(b) $\underline{d} = 1\ \underline{e}_i$, odd

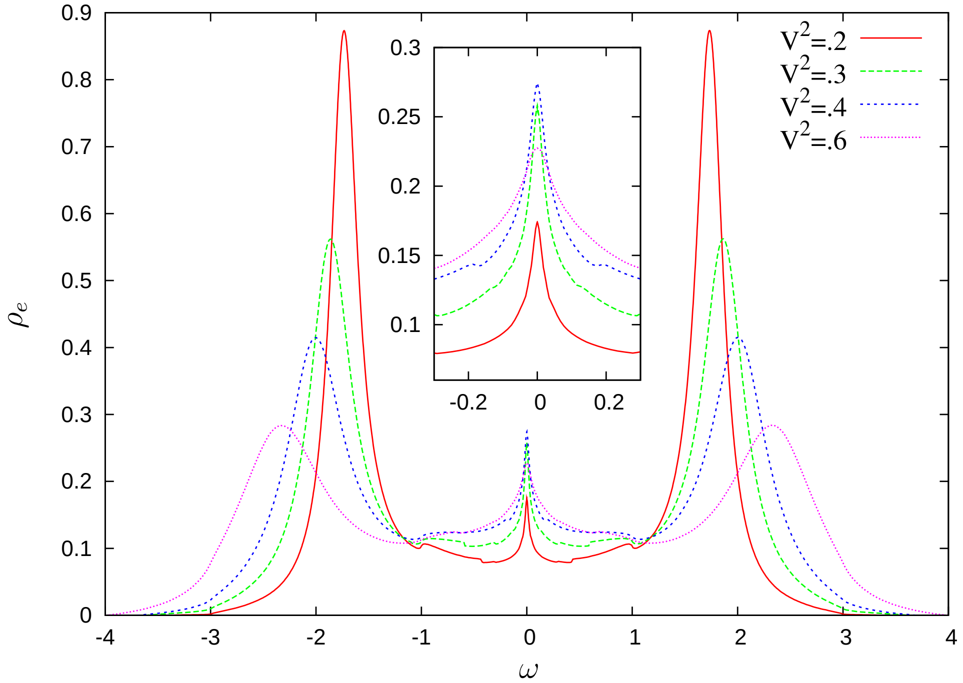

(c) $\underline{d} = 2\ \underline{e}_i$, even

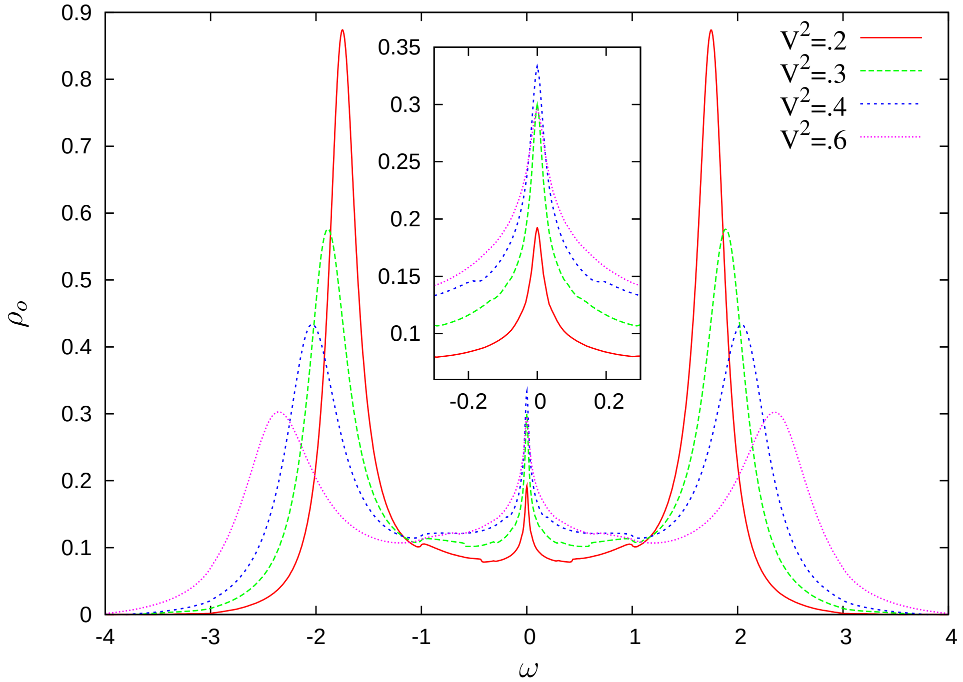

(d) $\underline{d} = 2\ \underline{e}_i$, odd

Figure 3.26:

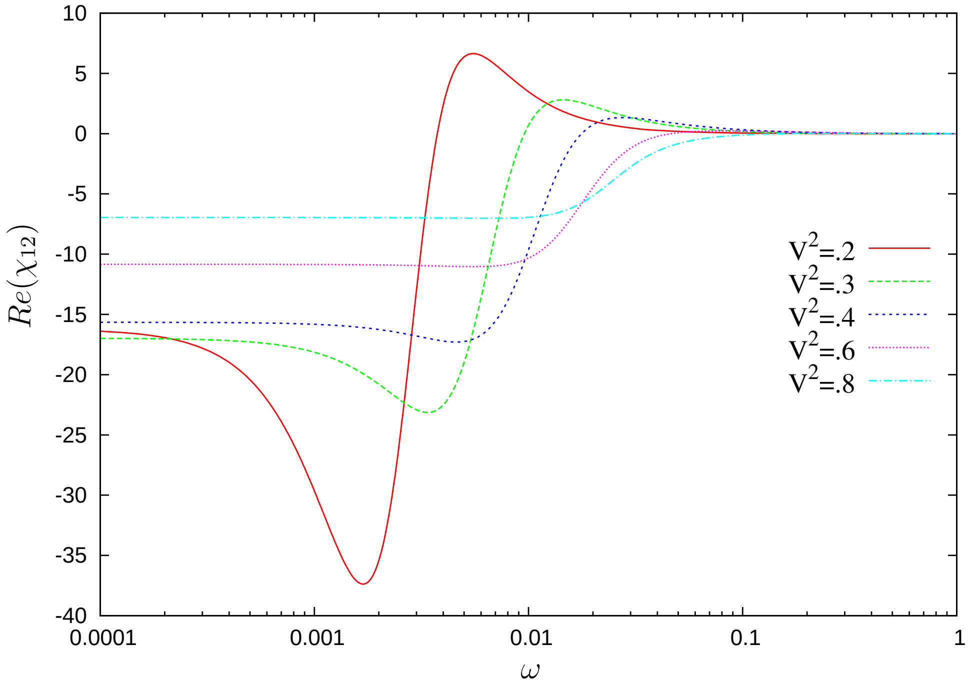

(a) $\underline{d} = 1\ \underline{e}_i$

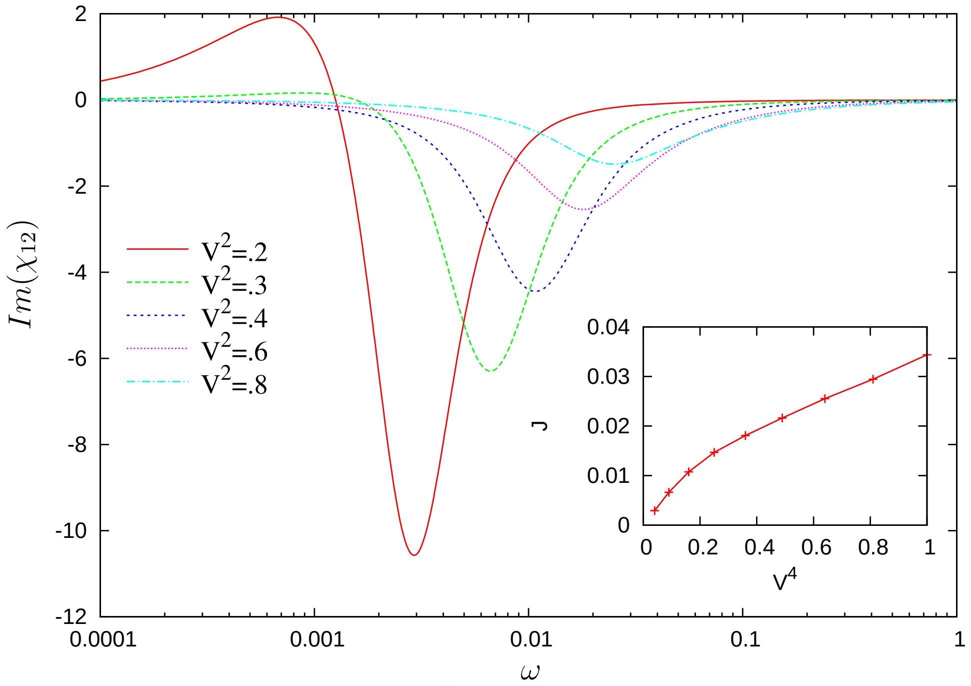

(b) $\underline{d} = 1\ \underline{e}_i$

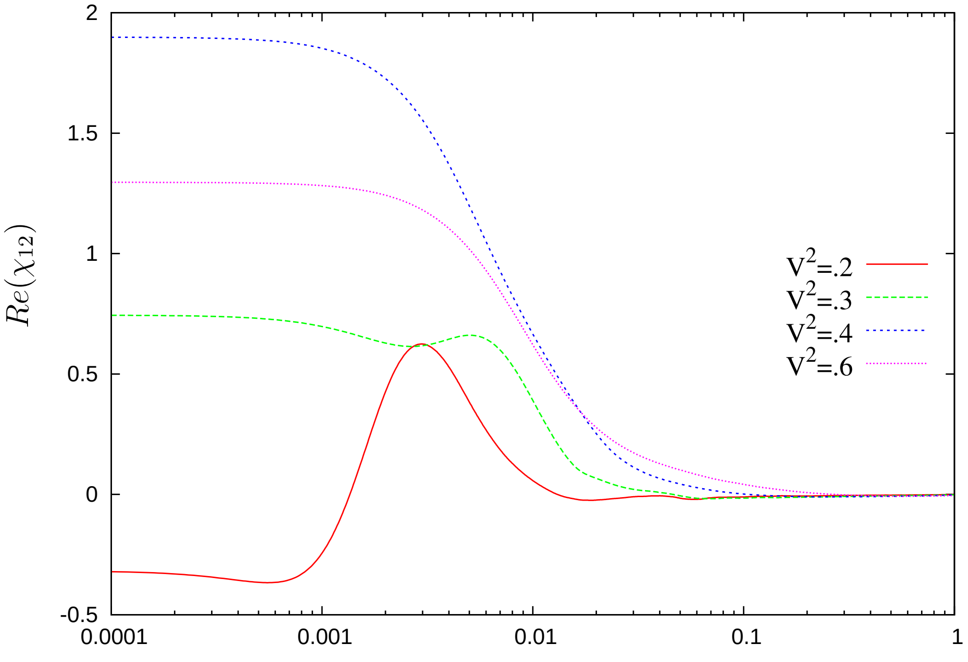

(c) $\underline{d} = 2\ \underline{e}_i$

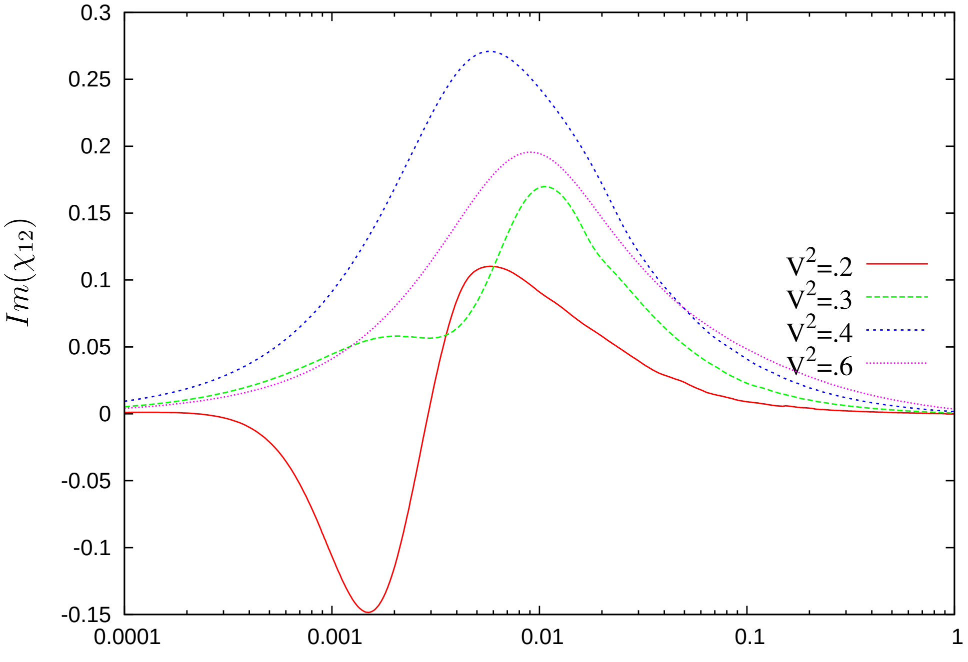

(d) $\underline{d} = 2\ \underline{e}_i$

Figure 3.27:

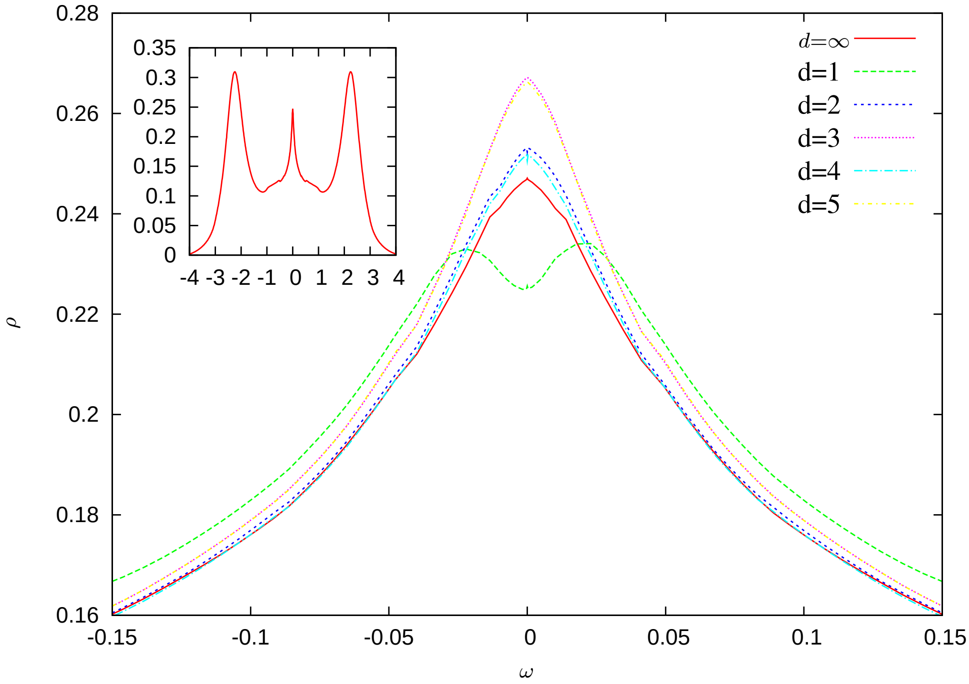

(a) $\underline{d} = 1\underline{e}_i - 5\ \underline{e}_i$

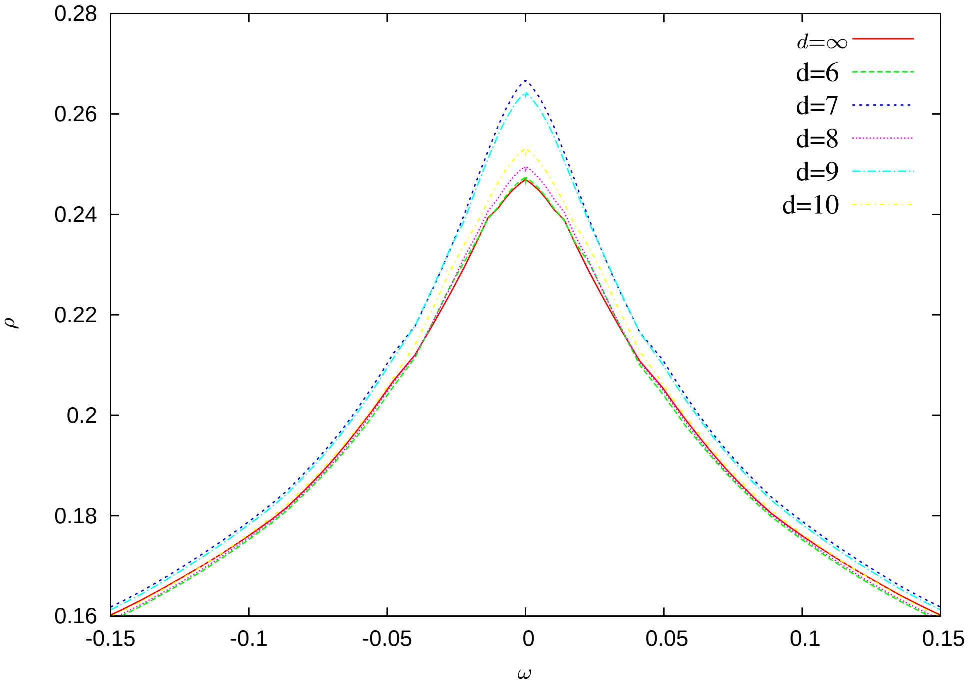

(b) $\underline{d} = 6\underline{e}_i - 10\ \underline{e}_i$

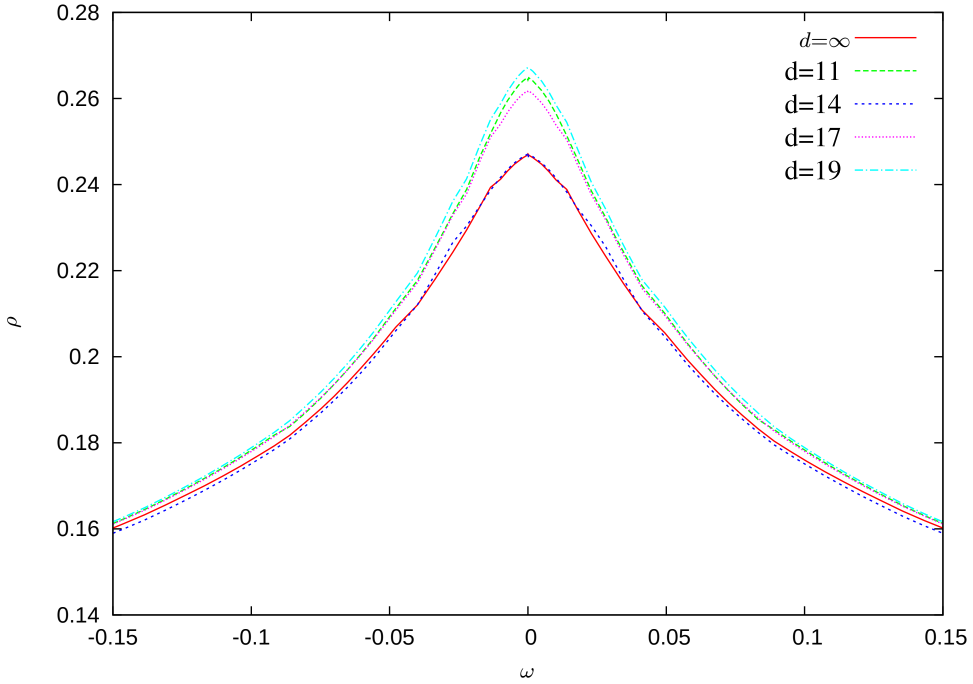

(c) $\underline{d} = 11\underline{e}_i - 19\ \underline{e}_i$

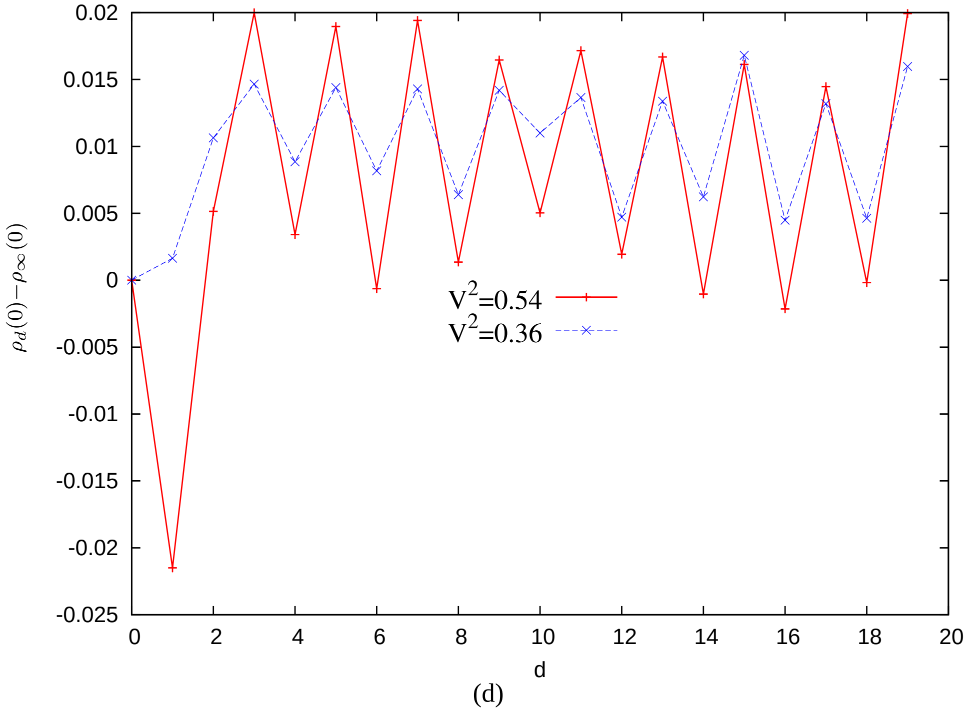

(d)

Figure 3.28:

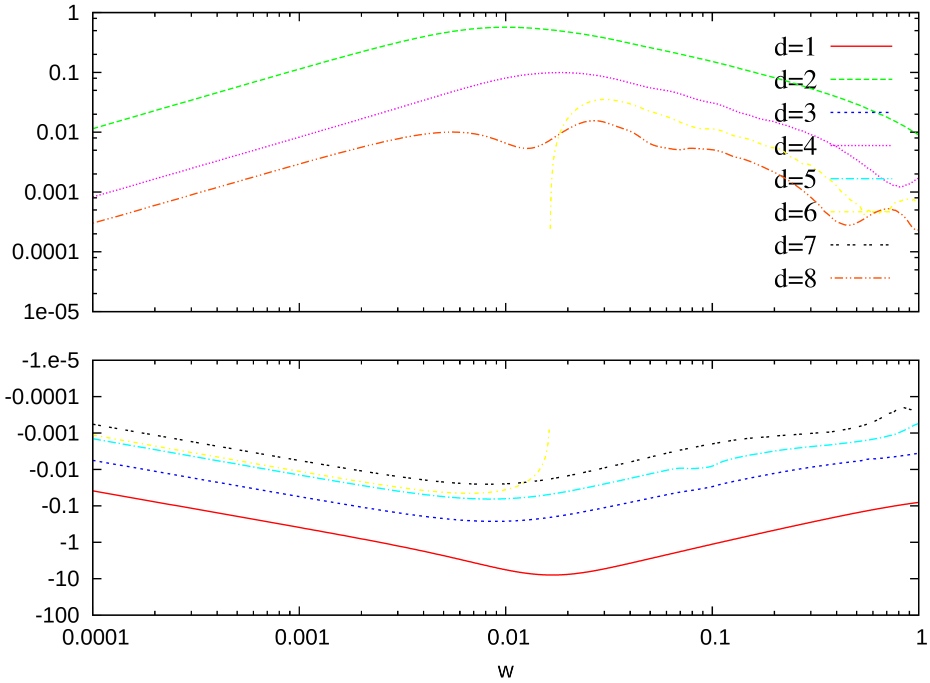

(a) $Im(\chi_{1\ 2}),\ V^2 = 0.54$

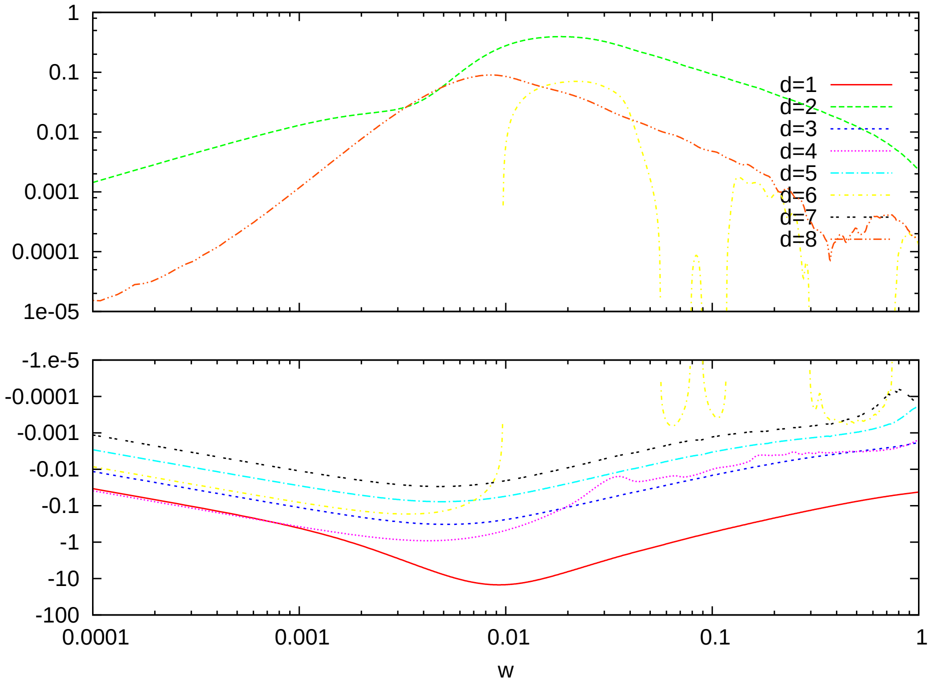

(b) $Im(\chi_{1\ 2}), V^2 = 0.36$

Figure 3.29:

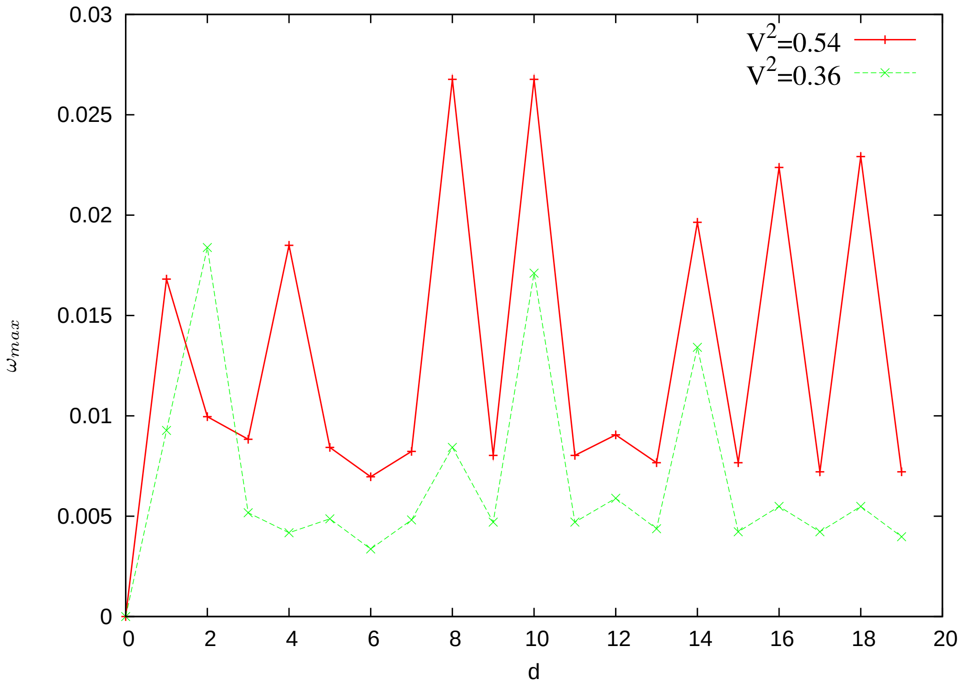

(a) resonance-peak energy

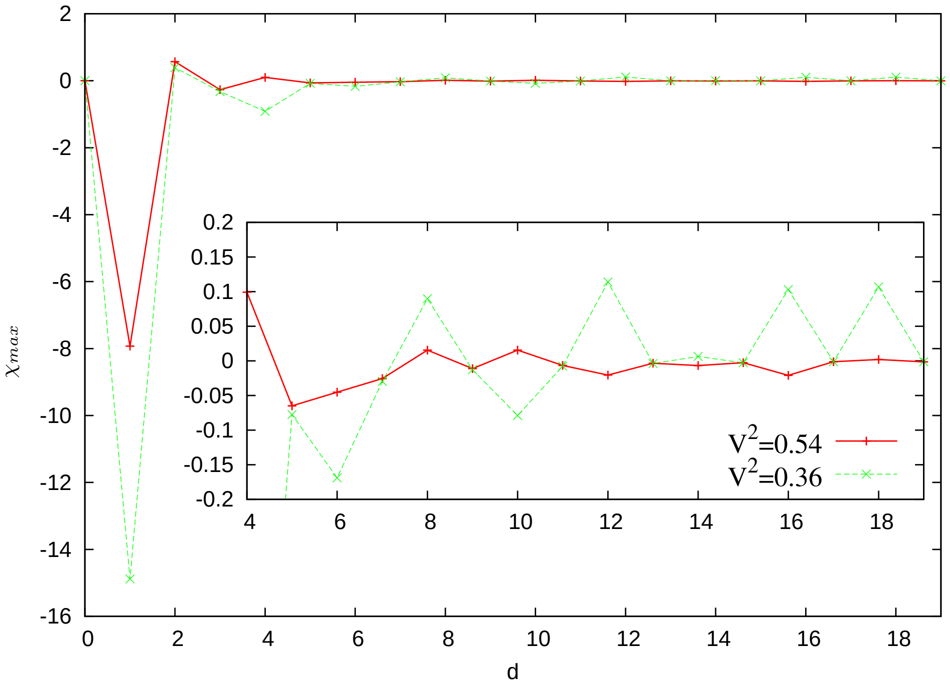

(b) resonance-peak height

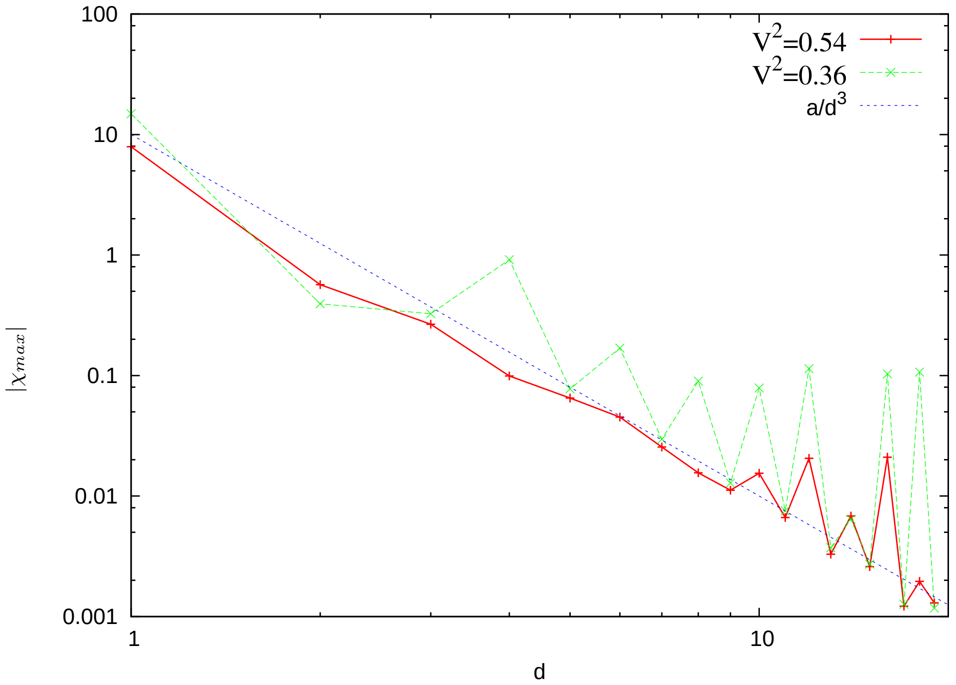

(c) logarithmic peak height

Figure 3.30:

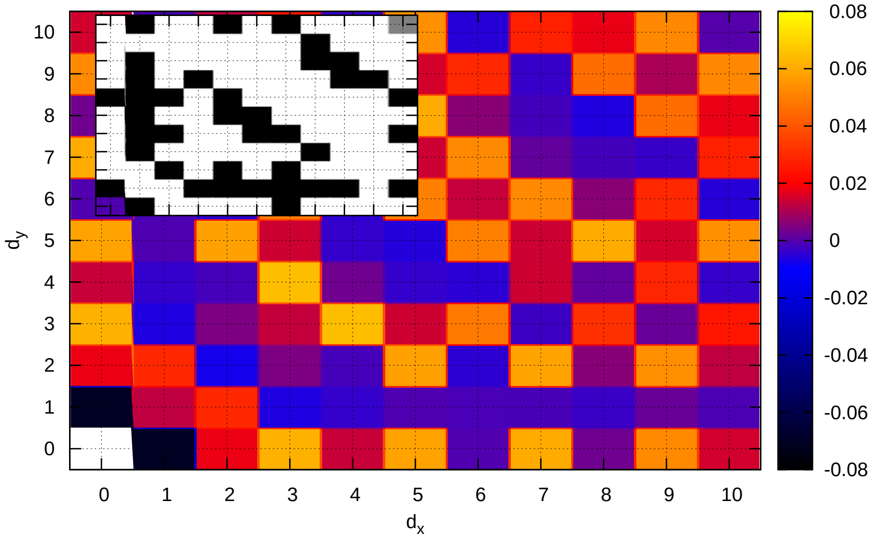

(a) $\rho_{\underline{d}}(0) - \rho_{\infty}(0), V^2 = 0.54$

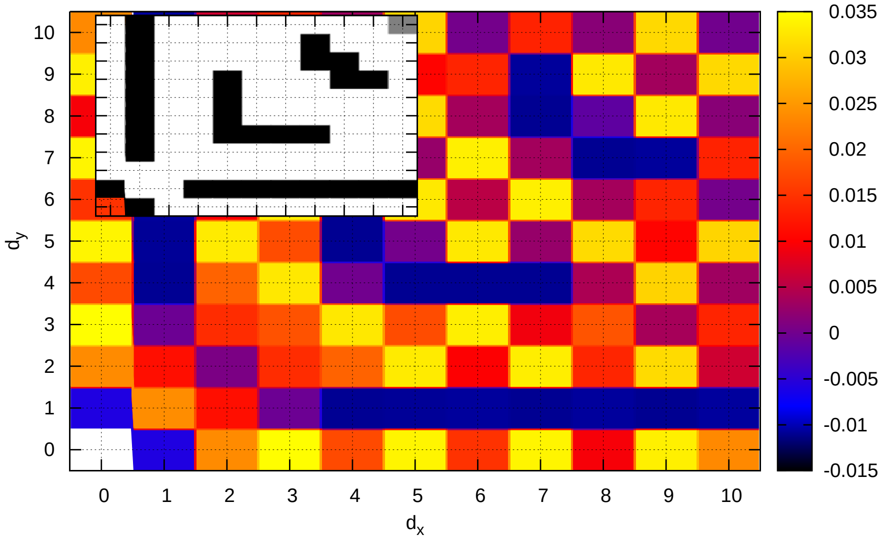

(b) $\rho_{\underline{d}}(0) - \rho_{\infty}(0), V^2 = 0.36$

Figure 3.31:

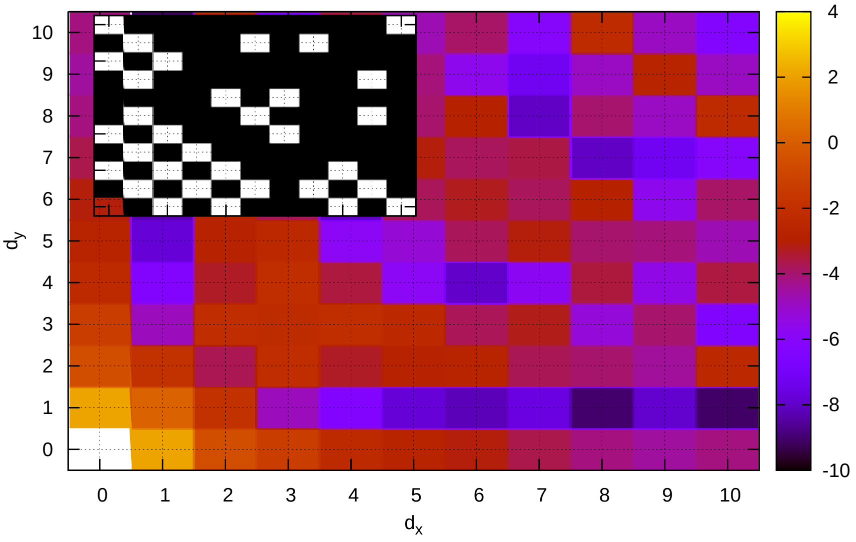

(a) $V^2 = 0.54$

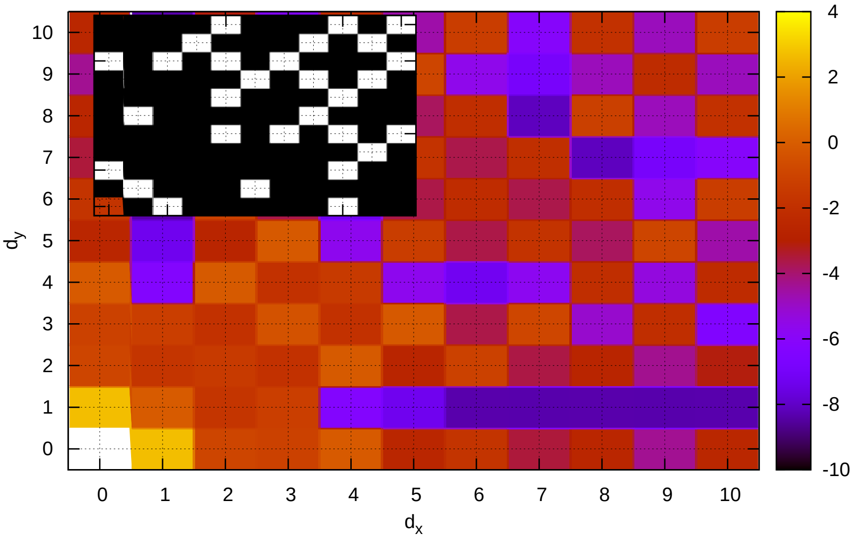

(b) $V^2 = 0.36$

Figure 3.32:

C.2 Chapter 5

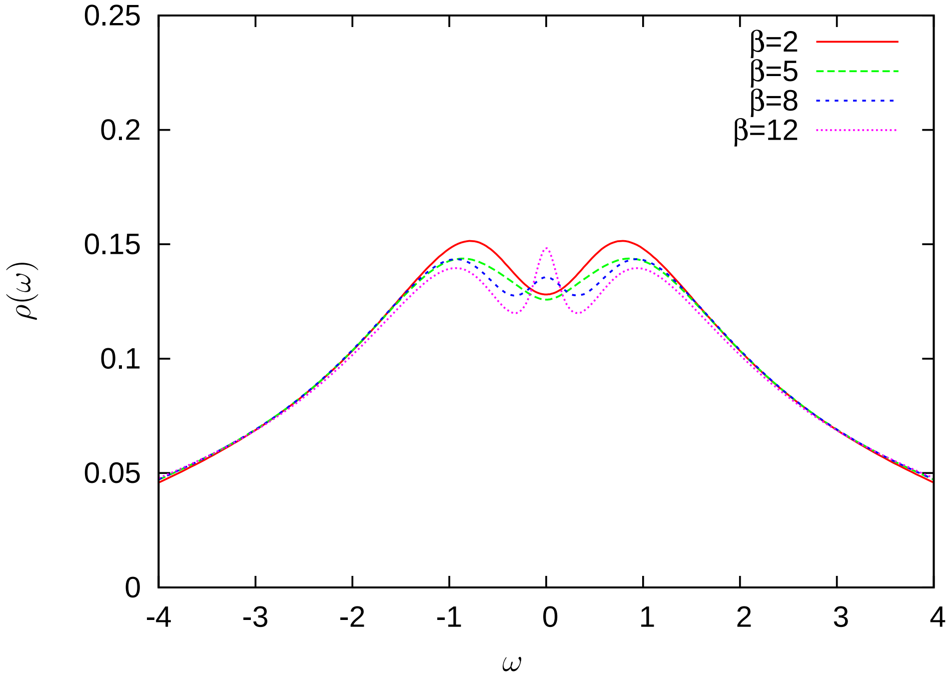

(a) DMFT/SNCATI

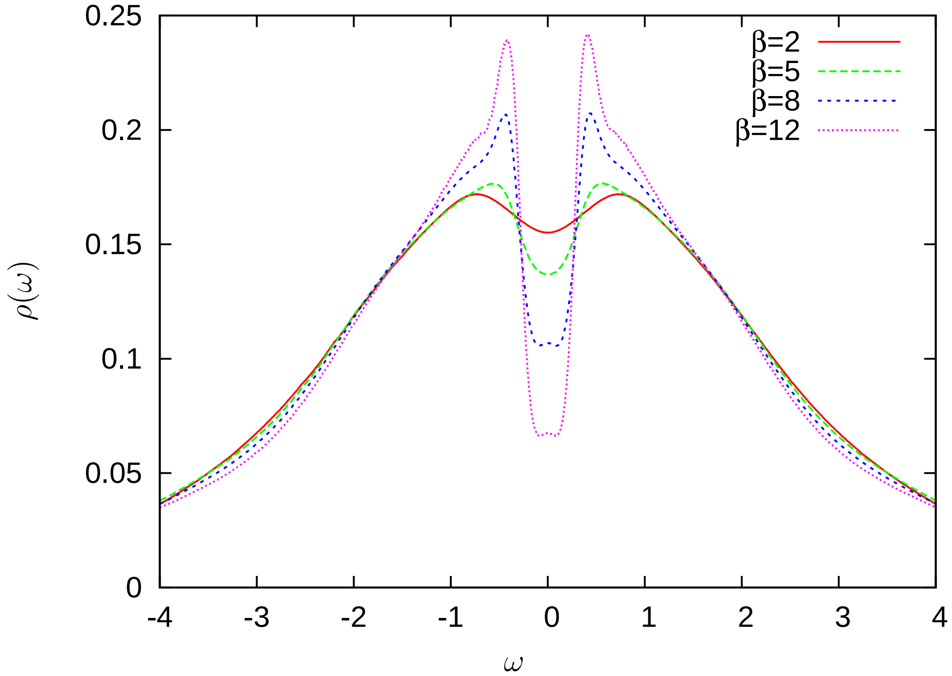

(b) DMFT2S(1)

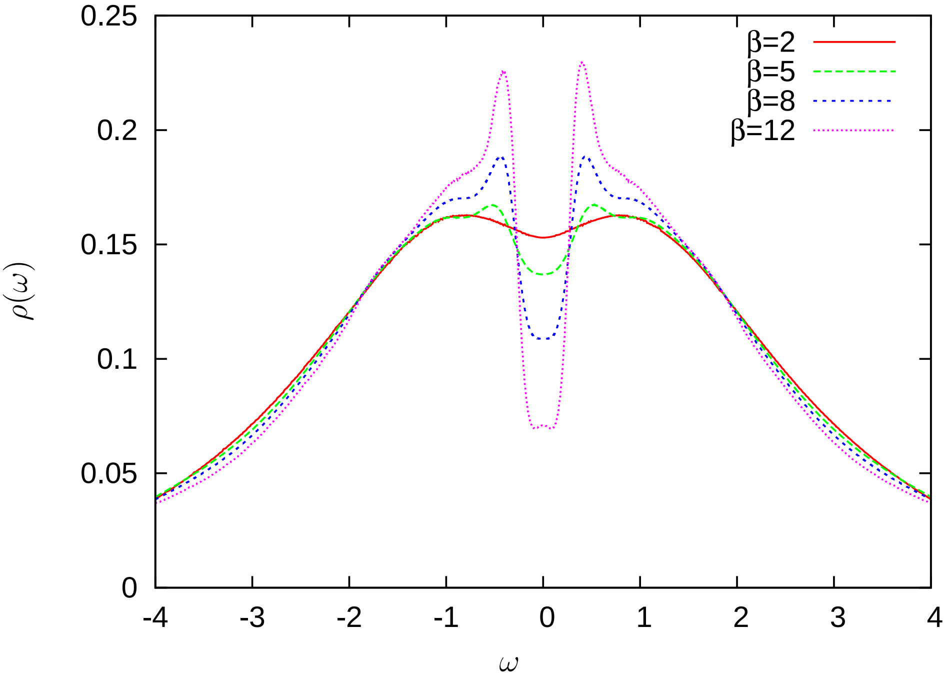

(c) DMFT2S(2)

Figure 5.1:

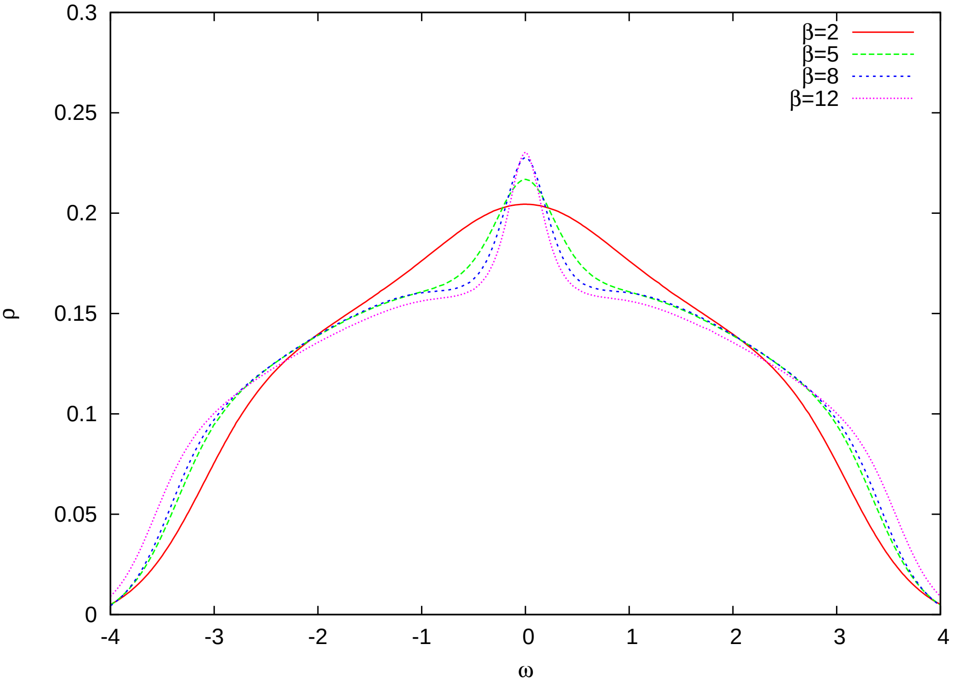

(a) DMFT/ENCATI

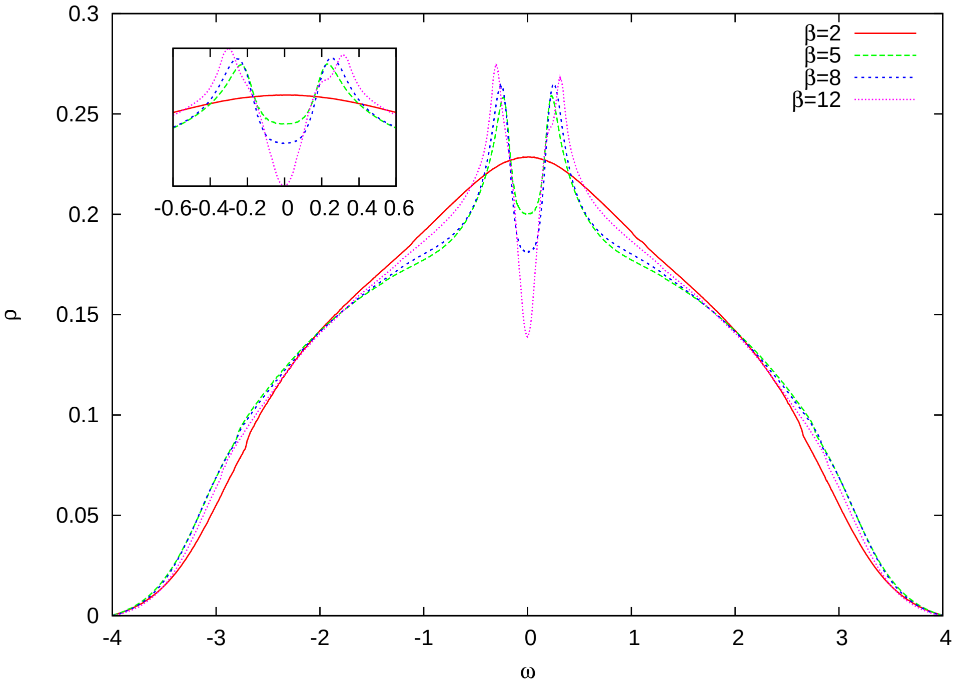

(b) DMFT2S(1)

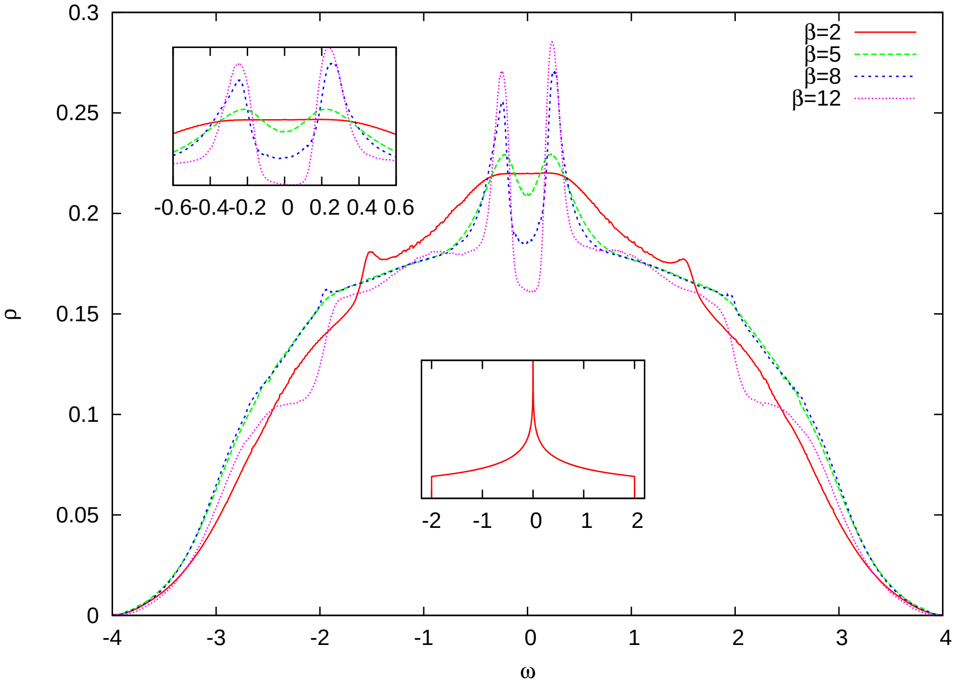

(c) DMFT2S(2)

Figure 5.2:

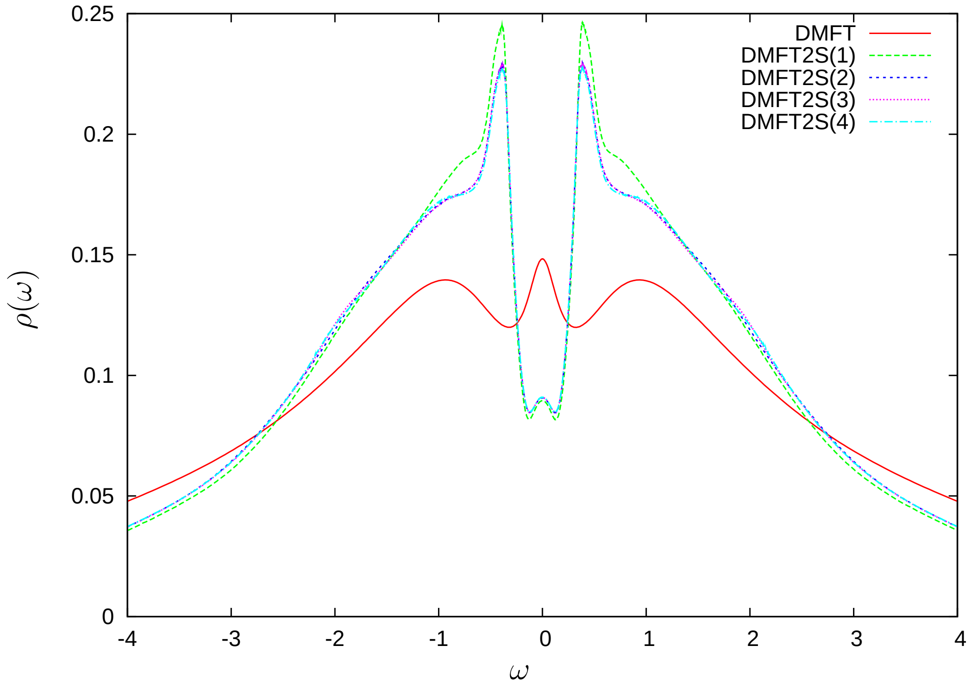

(a) DMFT2S/SNCATI

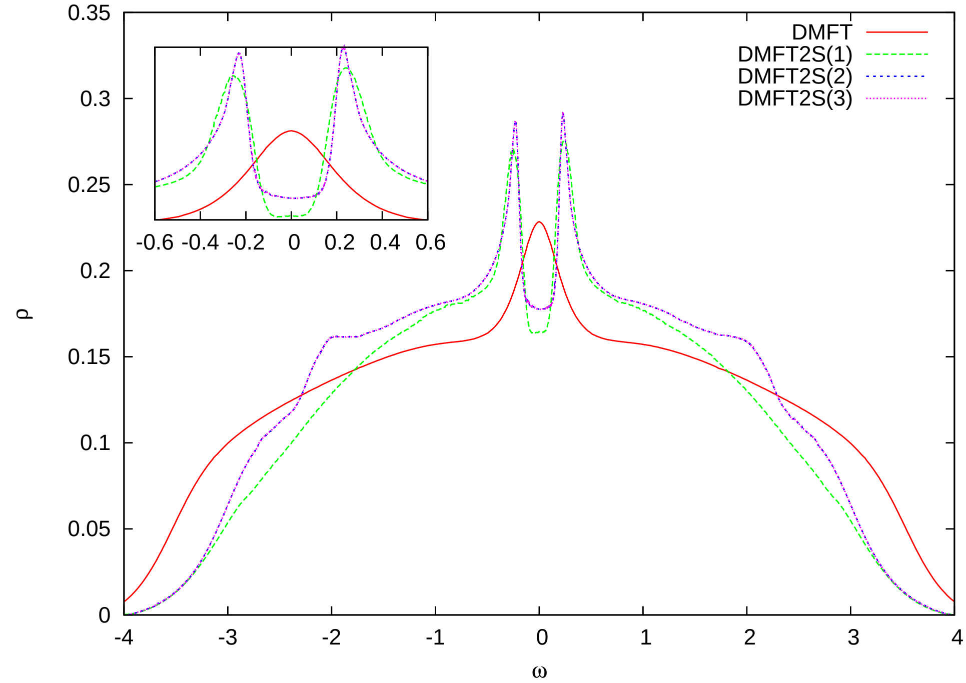

(b) DMFT2S/ENCATI

Figure 5.3:

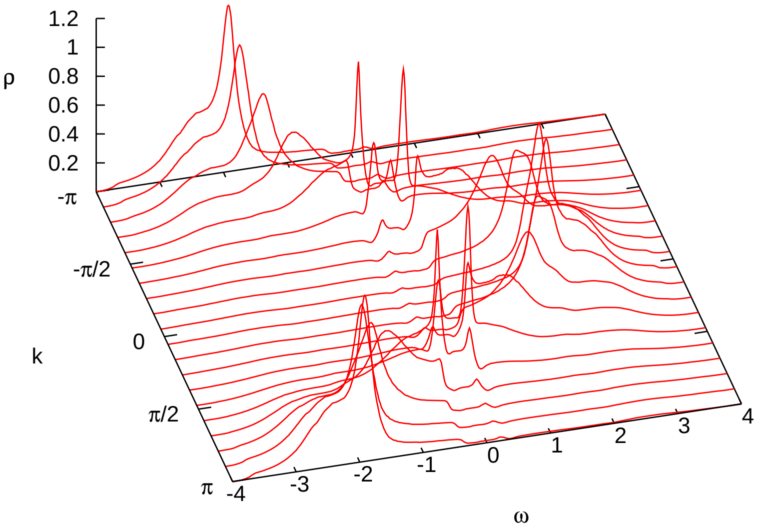
ρ
1.2
1
0.8
0.6
0.4
0.2
-π
-π/2
0
π/2
π
k
-4
-3
-2
-1
0
1
2
3
4
ω

(a)

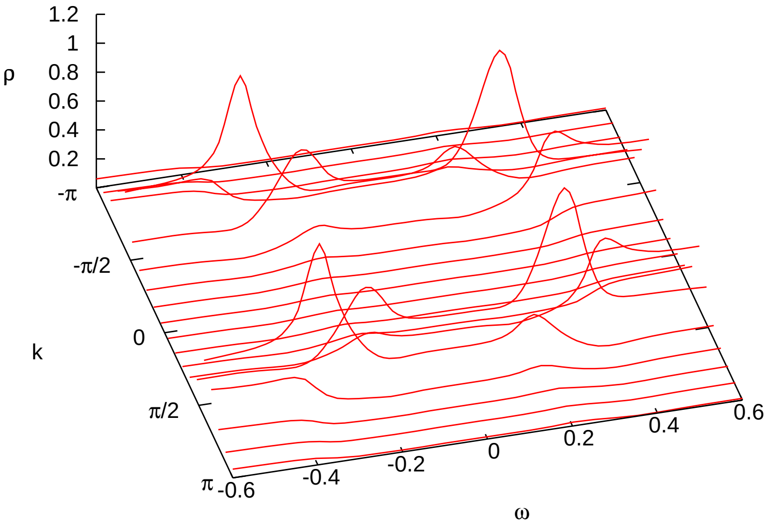
ρ
1.2
1
0.8
0.6
0.4
0.2
-π
-π/2
0
π/2
π
k
-0.6
-0.4
-0.2
0
0.2
0.4
0.6
ω

(b)

Figure 5.4:

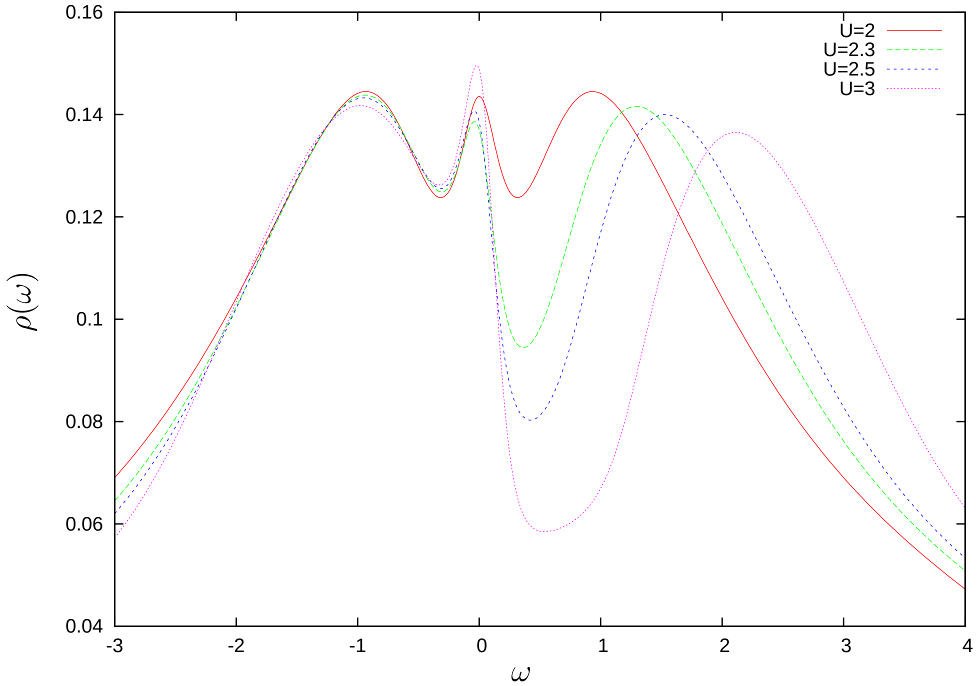

(a) DMFT/SNCATI

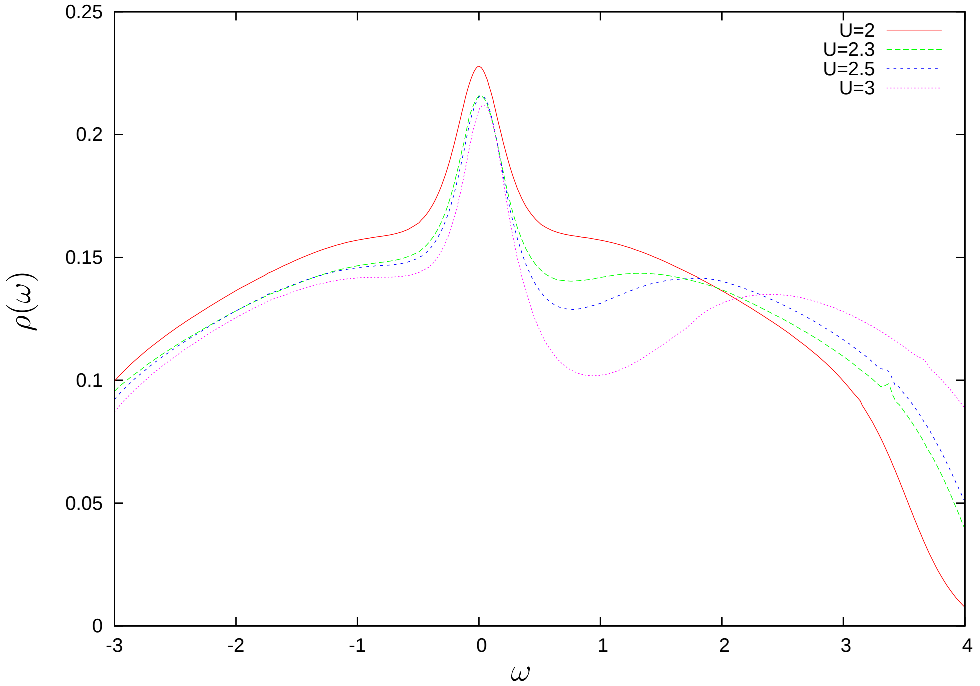

(b) DMFT/ENCATI

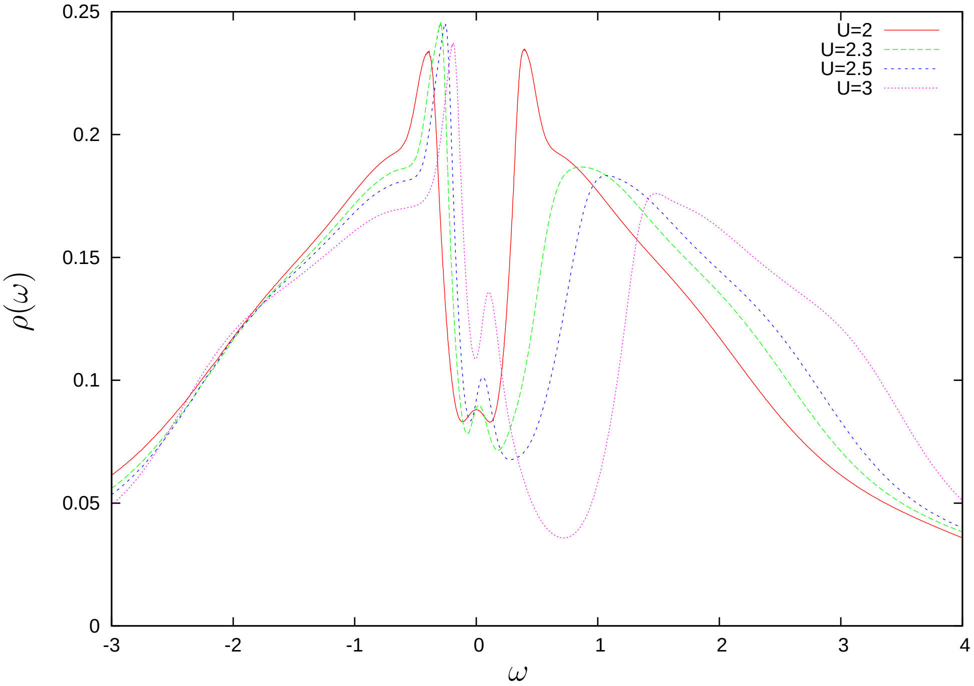

(c) DMFT2S(1)/SNCATI

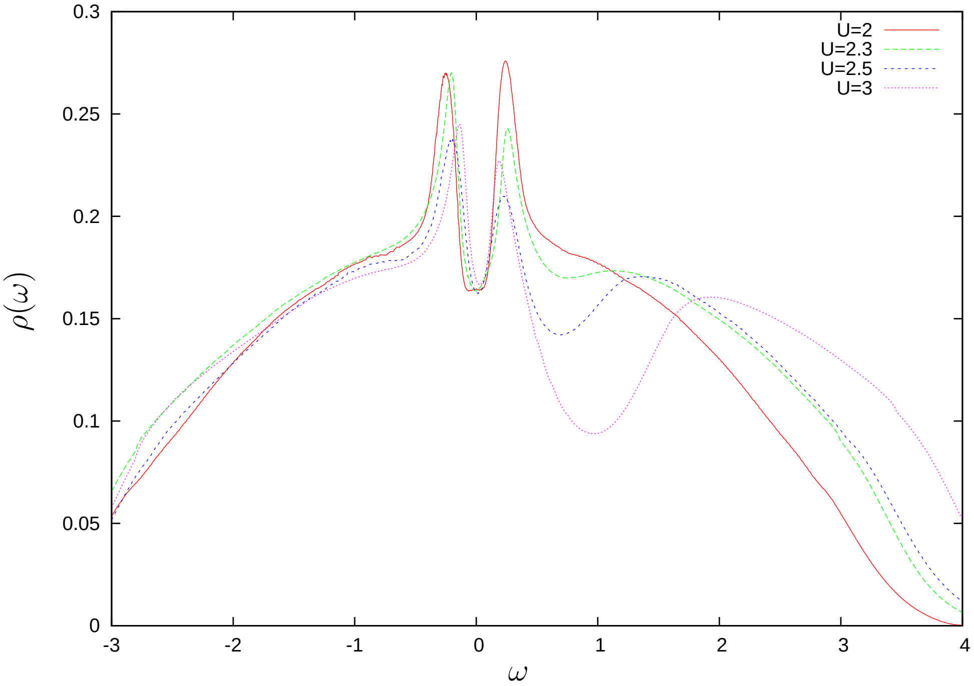

(d) DMFT2S(1)/ENCATI

Figure 5.5:

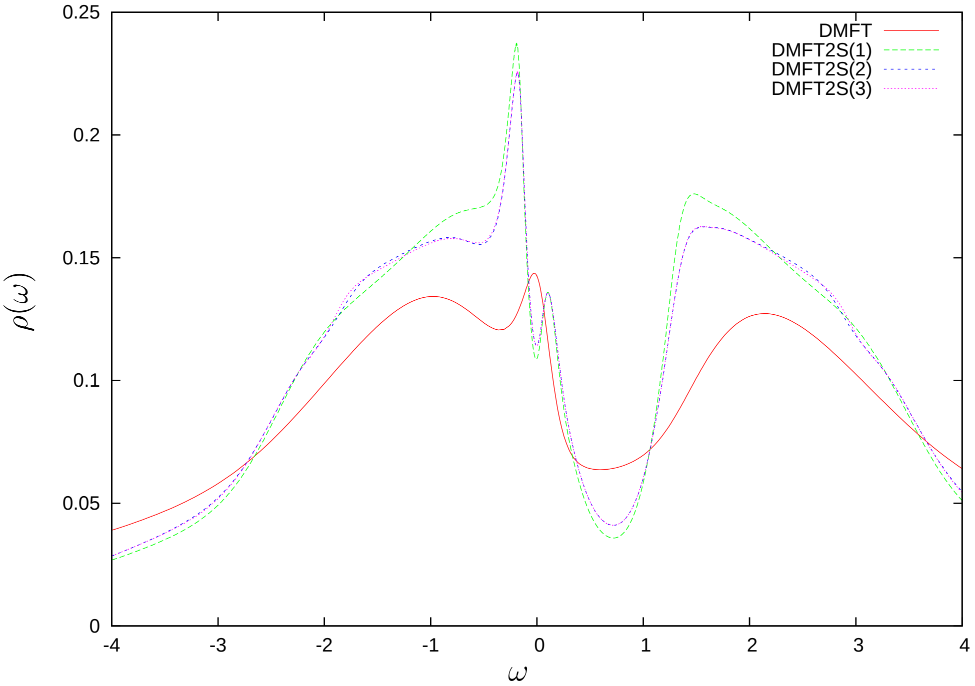

(a) DMFT2S(i)/SNCATI

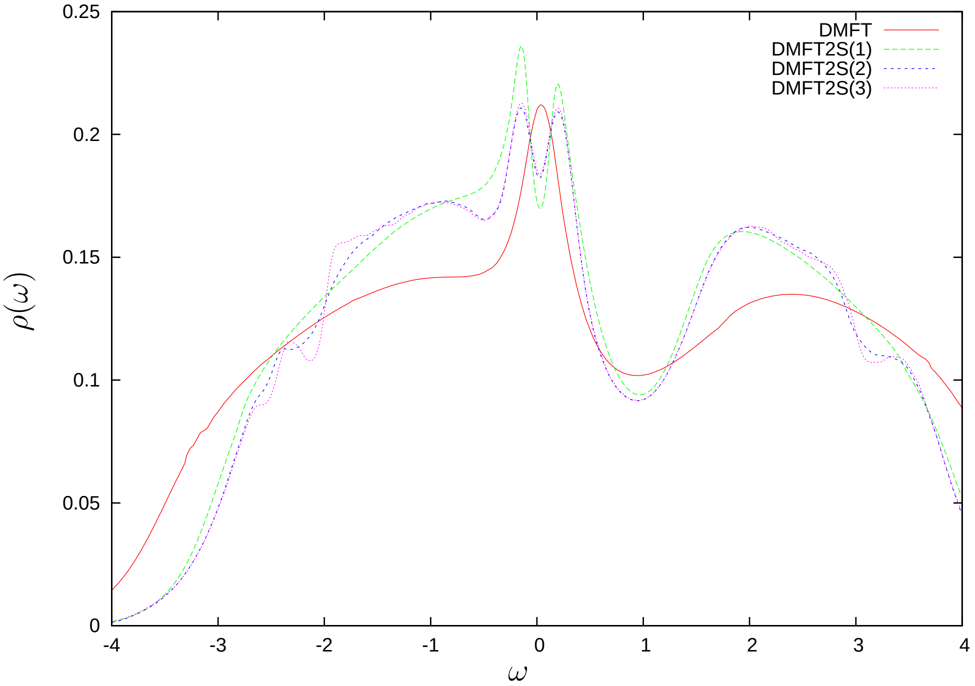

(b) DMFT2S(i)/ENCATI

Figure 5.6:

Bibliography

[A.G04] A.Georgesb, in A.Avella and F.Mancini (editors), *Lectures on the physics of highly correlated electron systems VIII*, volume 715 of *AIP Conf. Proc.*, pp. 3–74 (2004).

[Aim07] T. Aimi and M. Imada, J. Phys. Soc. Jpn. **76**, 113708 (2007).

[Ale64] S. Alexander and P. W. Anderson, Phys. Rev. **133**(6A), A1594 (1964).

[And97] P. W. Anderson, *The Theory of Superconductivity in High-Tc Cuprates*, Princeton University Press (1997).

[Bic87] N. E. Bickers, Rev. Mod. Phys. **59**(4), 845 (1987).

[Bir02] G. Biroli and G. Kotliar, Phys. Rev. B **65**(15), 155112 (2002).

[Bor09] L. Borda, M. Garst, and J. Kroha, Phys. Rev. B **79**(10), 100408 (2009).

[Bra89] U. Brandt and C. Mielsch, Z. Phys. B **75**(3), 365 (1989).

[Bre08] S. Brener, H. Hafermann, A. N. Rubtsov, M. I. Katsnelson, and A. I. Lichtenstein, Phys. Rev. B **77**(19), 195105 (2008).

[Bul06] R. Bulla, Phil. Mag. **86**, 1877 (2006), (preprint http://arxiv.org/abs/cond-mat/0412314).

[Cha04] I. H. Chan, P. Fallahi, A. Vidan, R. M. Westervelt, M. Hanson, and A. C. Gossard, Nanotechnology **15**(5), 609 (2004).

[Col84] P. Coleman, Phys. Rev. B **29**(6), 3035 (1984).

[Din96] H. Ding, T. Yokoya, J. C. Campuzano, T. Takahashi, M. Randeria, M. R. Norman, T. Mochiku, K. Kadowaki, and J. Giapintzakis, Nature **382**, 51 (1996).

[Don71] Doniach, Physica B **91**, 231 (1971).

[Eme87] V. J. Emery, Phys. Rev. B **58**, 26 (1987).

[Faz99] P. Fazekas, *Lecture Notes on Electron Correlation and Magnetism*, volume 5 of *Series in Modern Condensed Matter Physics*, World Scientific, Singapore (1999).

[FR98] D. L. F. D. S. M. A. G. L. Z.-X. S. F. Ronning, C. Kim, Science **282**, 5396 (1998).

[Fye87] R. M. Fye, J. E. Hirsch, and D. J. Scalapino, Phys. Rev. B **35**(10), 4901 (1987).

[Fye94] R. M. Fye, Phys. Rev. Lett. **72**(6), 916 (1994).

[Geg08] P. Gegenwart, Q. Si, and F. Steglich, Nature Physics **4**, 186 (2008).

[Geo96] A. Georges, G. Kotliar, W. Krauth, and M. J. Rozenberg, Rev. Mod. Phys. **68**(1), 13 (1996).

[Gre81] N. Grewe and H. Keiter, Phys. Rev. B **24**(8), 4420 (1981).

[Gre83] N. Grewe, Z. Phys. B **53**(4), 271 (1983).

[Gre91] N. Grewe and F. Steglich, *Handbook on the Physics and Chemistry of Rare Earths*, volume 14, p. 343, North-Holland (1991).

[Gre96] N. Grewe, *Eine lokale Theorie des FestkÃ¶rpers* (1996), internal Report.

[Gre05] N. Grewe, Ann. Phys. (Leipzig) **14**(9-10), 611 (2005).

[Gre08] N. Grewe, S. Schmitt, T. Jabben, and F. B. Anders, J. Phys.: Condens. Matter **20**, 365217 (2008).

[Haf08] H. Hafermann, S. Brener, A. N. Rubtsov, M. I. Katsnelson, and A. I. Lichtenstein, JETP Letters **86**(10), 677 (2008).

[Het98] M. H. Hettler, A. N. Tahvildar-Zadeh, M. Jarrell, T. Pruschke, and H. R. Krishnamurthy, Phys. Rev. B **58**(12), R7475 (1998).

[Hew93] A. C. Hewson, *The Kondo Problem to Heavy Fermions*, Cambridge University Press, Cambridge (1993).

[Hir85] J. E. Hirsch, Phys. Rev. B **31**(7), 4403 (1985).

[Hub63] J. Hubbard, Proc. Roy. Soc. A **276**, 238 (1963).

[Hus01] C. Huscroft, M. Jarrell, T. Maier, S. Moukouri, and A. N. Tahvildarzadeh, Phys. Rev. Lett. **86**, 139 (2001).

[Iva00] T. I. Ivanov, Phys. Rev. B **62**(19), 12577 (2000).

[Izu00] W. Izumida and O. Sakai, Phys. Rev. B **62**(15), 10260 (2000).

[Jar01a] M. Jarrell, T. Maier, M. Hettler, and A. Tahvildarzadeh, Europhys. Lett. **56**(4), 563 (2001).

[Jar01b] M. Jarrell, T. Maier, C. Huscroft, and S. Moukouri, Phys. Rev. B **64**(19), 195130 (2001).

[Jay81] C. Jayaprakash, H. R. Krishna-murthy, and J. W. Wilkins, Phys. Rev. Lett. **47**(10), 737 (1981).

[Jay82] Jayaprakash, Krishna-murthy, and J. Wilkins, J. Appl. Phys. **53**, 2142 (1982).

[Jeo01] H. Jeong, A. M. Chang, and M. R. Melloch, Science **293**(5538), 2221 (2001).

[Jon87] B. A. Jones and C. M. Varma, Phys. Rev. Lett. **58**(9), 843 (1987).

[Jon88] B. A. Jones, C. M. Varma, and J. W. Wilkins, Phys. Rev. Lett. **61**(1), 125 (1988).

[Kei70] H. Keiter and J. C. Kimball, Phys. Rev. Lett. **25**(10), 672 (1970).

[Kei71a] H. Keiter and J. C. Kimball, J. Appl. Phys. **42**(4), 1460 (1971).

[Kei71b] H. Keiter and J. C. Kimball, Int. J. Magn. **1**, 233 (1971).

[Kei84] H. Keiter and G. Morandi, Phys. Rep. **109**(5), 227 (1984).

[Kot01] G. Kotliar, S. Y. Savrasov, G. Pálsson, and G. Biroli, Phys. Rev. Lett. **87**(18), 186401 (2001).

[Kot04] G. Kotliar and D. Vollhardt, Physics Today **57**(3), 53 (2004).

[Kro97] J. Kroha, P. Wölfle, and T. A. Costi, Phys. Rev. Lett. **79**(2), 261 (1997).

[Kro05] J. Kroha and P. Wölfle, J. Phys. Soc. Jpn. **74**(1), 16 (2005), (preprint at http://arxiv.org/abs/cond-mat/0410273v2).

[Kur83] Y. Kuramoto, Z. Phys. B **53**, 37 (1983).

[Kur84] Y. Kuramoto and H. Kojima, Z. Phys. B **57**, 95 (1984).

[Kur85a] Y. Kuramoto, in T. Kasuka and T. Saso (editors), *Theory of heavy fermions and valence fluctuation*, volume 62 of *Springer series in solid state sciences*, pp. 152–161, Springer, Berlin (1985).

[Kur85b] Y. Kuramoto and H. Kojima, J. Magn. Magn. Mater. **47-48**(1), 329 (1985).

[Kur85c] Y. Kuramoto and E. Müller-Hartmann, J. Magn. Magn. Mater. **52**(1-4), 122 (1985).

[Kus06] H. Kusunose, J. Phys. Soc. Jpn. **75**, 054713 (2006).

[Mai00a] T. Maier, M. Jarrell, T. Pruschke, and J. Keller, Eur. Phys. J. B **13**(4), 613 (2000).

[Mai00b] K. Maiti and D. D. Sarma, Phys. Rev. B **61**(4), 2525 (2000).

[Mai05] T. Maier, M. Jarrell, T. Pruschke, and M. H. Hettler, Rev. Mod. Phys. **77**(3), 1027 (2005).

[Mai07] K. Maiti, R. S. Singh, and V. R. R. Medicherla, Physical Review B (Condensed Matter and Materials Physics) **76**(16), 165128 (2007).

[Mat98] A. Y. Matsuura, H. Watanabe, C. Kim, S. Doniach, Z.-X. Shen, T. Thio, and J. W. Bennett, Phys. Rev. B **58**(7), 3690 (1998).

[Men88] B. Menge and E. Müller-Hartmann, Z. Phys. B **73**(2), 225 (1988).

[Met89] W. Metzner and D. Vollhardt, Phys. Rev. Lett. **62**(3), 324 (1989).

[Met91] W. Metzner, Phys. Rev. B **43**(10), 8549 (1991).

[MH84] E. Müller-Hartmann, Z. Phys. B **57**(4), 281 (1984).

[MH89] E. Müller-Hartmann, Z. Phys. B **74**(4), 507 (1989).

[Nis06] S. Nishimoto, T. Pruschke, and R. M. Noack, J. Phys.: Condens. Matter **18**, 981 (2006).

[Noz69] P. Nozières and C. T. De Dominicis, Phys. Rev. **178**(3), 1097 (1969).

[Pru89] T. Pruschke and N. Grewe, Z. Phys. B **74**, 439 (1989).

[Pru01] T. Pruschke, W. Metzner, and D. Vollhardt, J. Phys.: Condens. Matter **13**, 9455 (2001).

[Pru05] T. Pruschke, Physica B **359-361**, 633 (2005).

[Ran97] M. Randeria (1997).

[Ree93] M. A. Reed, Scientific American **268**, 118 (1993).

[Rub08] A. N. Rubtsov, M. I. Katsnelson, and A. I. Lichtenstein, Phys. Rev. B **77**(3), 033101 (2008).

[Sak90] O. Sakai, Y. Shimizu, and T. Kasuya, Solid State Communications **75**(2), 81 (1990).

[Sak93] O. Sakai, Y. Shimizu, and N. Kaneko, Physica B: Condensed Matter **186-188**, 323 (1993).

[San94] G. E. Santoro and G. F. Giuliani, Phys. Rev. B **49**(10), 6746 (1994).

[Sca06] D. J. Scalapino, arXiv:cond-mat/0610710v1 p. 55 (2006).

[Sch66] J. R. Schrieffer and P. A. Wolff, Phys. Rev. **149**(2), 491 (1966).

[Sch69] K. D. Schotte and U. Schotte, Phys. Rev. **185**(2), 509 (1969).

[Sch93] A. Schiller and V. Zevin, Phys. Rev. B **47**(21), 14297 (1993).

[Sch95] A. Schiller and K. Ingersent, Phys. Rev. Lett. **75**(1), 113 (1995).

[Sch96] A. Schiller and V. Zevin, Ann. Phys. **505**, 363 (1996).

[Sch08] S. Schmitt, *Excitations, Two-Particle Correlations and Ordering Phenomena in Strongly Correlated Electron Systems from a Local Point of View*, Ph.D. thesis, TU Darmstadt (2008).

[Sim06] J. Simonin, Phys. Rev. B. **73**, 155102 (2006).

[Sla51] J. C. Slater, Phys. Rev. **82**(4), 538 (1951).

[Sle06] C. Slezak, M. Jarrell, T. Maier, and J. Deisz, cond-mat/0603421 (2006).

[Sta03] T. D. Stanescu and P. Phillips, Physical Review Letters **91**, 017002 (2003).

[Sta04] T. D. Stanescu and G. Kotliar, Phys. Rev. B **70**, 205112 (2004).

[THO98] W. G. v. d. W. T. H. Oosterkamp, T. Fujisawa, Nature **395**, 3 (1998).

[Tim99] T. Timusk and B. W. Statt, Reports on Progress in Physics **62**, 61 (1999).

[Tos07] A. Toschi, A. A. Katanin, and K. Held, Phys. Rev. B **75**(4), 045118 (2007).

[Tro05] M. Troyer and U.-J. Wiese, Phys. Rev. Lett. **94**(17), 170201 (2005).

[Tsu00] C. C. Tsuei and J. R. Kirtley, Rev. Mod. Phys. **72**(4), 969 (2000).

[Vil97] Y. Vilk and A. Tremblay, J. Phys. I **7**, 1309 (1997).

[Whi89] S. R. White, D. J. Scalapino, R. L. Sugar, E. Y. Loh, J. E. Gubernatis, and R. T. Scalettar, Phys. Rev. B **40**(1), 506 (1989).

[Zha88] F. C. Zhang and T. M. Rice, Phys. Rev. B **37**(7), 3759 (1988).

[Zha97] S.-C. Zhang, Science **275**(5303), 1089 (1997).

[Zit06] R. Zitko and J. Bonca, Phys. Rev. B **74**(4), 045312 (2006).

Acknowledgment

This work has only been possible due to the support and assistance received by several people. First of all I am sincerely grateful to my supervisor Prof. Dr. Norbert Grewe for giving me the opportunity to work on this subject, for his continuous support and many invaluable discussions. His profound insights in many fields of physics and his constant urge to look at the bottom of things, where a great and constant source of inspiration for me.

I am especially thankful to Dr. Sebastian Schmitt for years of long and hot tempered discussions, he was always willing to engage with me. Without him I surely had not overcome the many obstacles in this thesis. Almost the same can be said about Dr. Eberhard Jakobi, who helped me to understand the physics of two-impurity systems and contributed a lot to the numeric library "numpkg" developed in the last five years.

I must not fail to mention Dr. Felix Wissel and Dr. Frank Böhm, without this duo infernale my daily life in University would have been much less enjoyable. The friendship of these four - freshly baked doctors - means a lot to me.
I must also thank my non-nerd circle of friends, for helping me to stay in connection with real life issues.
I want to truly thank Caroline Stettner, for granting me asylum and support during the intense months of writing.
Last but not least, I like to thank my parents for their enduring and unconditional support.

I acknowledge generous allocation of supercomputer time by the NIC, Forschungszentrum Jülich under Project No. HDO05

Lebenslauf

Name	Torben Sven Jabben
Geburtsdatum	11. 01. 1977
Geburtsort	Frankfurt am Main
Familienstand	ledig

1983-1987	Holzhausengrundschule in Frankfurt am Main
1987-1997	Wöhlergymnasium in Frankfurt am Main
1997	Abitur am Wöhlergymnasium
1997-1998	Zivildienst beim Frankfurter Verband für Alten- und Behindertenhilfe
1998	Beginn des Studiums der Physik an der Technischen Universität Darmstadt
2003-2004	Diplomarbeit in der AG Prof. Grewe am Institut für Festkörperphysik, TU Darmstadt
2004	Beendigung des Studiums mit dem Abschluss Diplom
seit 2004	Wissenschaftlicher Mitarbeiter am Institut für Festkörperphysik der TU Darmstadt

Eidesstattliche Erklärung

Hiermit erkläre ich eidesstattlich, dass ich die vorliegende Dissertation selbständig verfasst, keine anderen als die angegebenen Hilfsmittel verwendet und bisher noch keinen Promotionsversuch unternommen habe.

Darmstadt, im Februar 2010

(Unterschrift)